The Generation and Detection of Squeezed Microwave Photons Realized using Traveling Wave Parametric Amplifiers

by

Jack Yanjie Qiu

B.A., University of California, Berkeley (2017)
S.M., Massachusetts Institute of Technology (2021)

Submitted to the Department of Electrical Engineering and Computer Science
in partial fulfillment of the requirements for the degree of

Doctor of Philosophy

at the

MASSACHUSETTS INSTITUTE OF TECHNOLOGY

February 2023

Author . . . . . .
Department of Electrical Engineering and Computer Science
January 23, 2023

Certified by . . . . . .
William D. Oliver
Professor, Electrical Engineering and Computer Science
Thesis Supervisor

Certified by . . . . . .
Kevin P. O'Brien
Assistant Professor, Electrical Engineering and Computer Science
Thesis Supervisor

Accepted by . . . . . .
Leslie A. Kolodziejski
Professor of Electrical Engineering and Computer Science
Chair, Department Committee on Graduate Students

The Generation and Detection of Squeezed Microwave Photons Realized using Traveling Wave Parametric Amplifiers

by

Jack Yanjie Qiu

Submitted to the Department of Electrical Engineering and Computer Science
on January 23, 2023, in partial fulfillment of the
requirements for the degree of
Doctor of Philosophy

Abstract

Squeezing the electromagnetic vacuum is an essential metrological technique used to reduce quantum noise in applications spanning gravitational wave detection, biological microscopy, and quantum information science. In circuit quantum electrodynamics, Josephson parametric amplifiers play a crucial role in quantum-limited amplification and squeezed microwave generation. In this thesis, we develop a dual-pump, broadband Josephson traveling-wave parametric amplifier (JTWPA) to demonstrate non-degenerate four-wave mixing using a dual-dispersion-engineered JTWPA and investigate its squeezing performance. Furthermore, the thesis extends the existing JTWPA design to a lower frequency spectrum in the hundreds of MHz regime and demonstrates broadband parametric amplification with a large gain. Capable of multiplexed readout and improved signal-to-noise ratio, the new JTWPA can be utilized in a wide range of applications in condensed matter and astrophysics.

Thesis Supervisor: William D. Oliver
Title: Professor, Electrical Engineering and Computer Science

Thesis Supervisor: Kevin P. O'Brien
Title: Assistant Professor, Electrical Engineering and Computer Science

Acknowledgments

Many people supported me through my Ph.D. journey, and I would like to acknowledge and express my gratitude to them.

I want to first thank my research advisor, Professor William Oliver, for giving me this incredible opportunity to work in an exciting field and encouraging me to explore projects of my interests. During my time in the laboratory, Will has always provided valuable and constructive feedback that inspires me to think and approach scientific tasks rigorously and effectively. I benefited tremendously under his mentorship.

I also would like to thank my other advisor Professor Kevin O'Brien. Since my undergraduate career at UC Berkeley, I have known Kevin, from whom I learned many valuable skills and techniques, such as electromagnetic simulation and numerical modeling. He inspired me to continue my graduate study in superconducting circuits, introduced me to JTWPA, and guided me through the project. I learned a lot from him, and I am grateful to have him as a mentor.

Dr. Jeff Grover has always been very supportive, from helping me address referees' comments to giving me advice on the project. I always enjoy talking with him.

Dr. Simon Gustavsson was always available for me while I was working on the experiment. I learned a lot of practical skills from him during my time in the lab.

I want to thank Professor Terry Orlando for his tremendous support and feedback on this thesis work. Terry has been very caring since my first day when I first moved here to Massachusetts. He has been an accomplished physicist himself with outstanding scientific achievements. As a student, I truly enjoyed his lectures, where I learned quantum physics and his passion for science. He is willing to help me with the research paper or thesis writing.

I doubt I would have made it this far without Arne Grimsmo and Kaidong Peng's help with their theoretical support for this project. They provided solid theoretical support throughout the project and helped me understand physics better.

The post-docs are like our big brothers and sisters in the lab, who provided much care for the graduate students. It has always been inspiring to chat with them across the work-

stations or just exchange ideas in the hallway. Always have something to learn from them.

Working with all my peer graduate students has also been a great pleasure, and I enjoyed countless hours spent together buckling down through late nights in the lab to push for an experimental result. It has also been a pleasant experience to hang out after work for movies or dinners together. I feel excited to see fresh faces in our group, and I am positive they will produce exceptional work during their time.

Chihiro and Mirabella are fantastic administrative coordinators for the lab, who facilitate research activities and organize fun group social events that made our experience memorable.

I would also like to extend my gratitude to the entire MIT community for providing a diverse and innovative research environment. Finally, I would like to thank my family and all my friends for their unconditional support and love through the ups and downs. Their trust and love encourage me to venture fearlessly into the world of scientific research.

Contents

List of Figures

Chapter 1

Introduction

Our knowledge of the universe comes from observing its cosmic complexities. Gravitational waves are extraordinarily faint signals rippling through the fabric of space and time. How can we detect them more effectively? Stealth aircraft reshaped warfare strategy in the late 20th century and remains one of the most advanced military technologies to date. It is incredibly challenging to detect stealth aircraft using current radar systems. As an potential enhancement, quantum radar promises to achieve this task and is under active study. What makes quantum radar superior in microwave sensing? The answer to these questions lies within the concept of squeezing.

Squeezed states belong to the class of *non-classical* states that cannot be described by classical electromagnetism. For example, we can observe less noise in squeezed light than in the complete absence of light (vacuum)! This paradoxical result is a direct consequence of the quantum nature of light. Heisenberg's uncertainty principle establishes the attainable measurement precision, the "standard quantum limit (SQL)," for isotropically-distributed vacuum fluctuations in the quadratures of the electromagnetic (EM) field [116, 18, 10]. Squeezing the EM field at a single frequency — single-mode squeezing — decreases the fluctuations of one quadrature below that of the vacuum at the expense of larger fluctuations in the other quadrature, thereby enabling a phase-sensitive means to beat the SQL. Squeezing can also generate quantum entanglement between observables at two distinct frequencies, producing two-mode squeezed states.

Since its first experimental demonstration in 1985 [105], squeezing the EM vacuum

has become an essential metrological technique to reduce quantum noise in diverse applications from gravitational wave [108] and dark matter detectors [64] to biological microscopy [107]. Many precision measurements rely on the interaction between squeezed light and a physical system. In this regard, superconducting microwave circuits have become one of the most promising platforms for precision sensing applications. First, generating squeezed microwaves with this platform enables a direct interface with superconducting qubits. The resulting system is ideal for tests of light-matter physics due to achievable strong coupling between qubits and microwave photons. In contrast to weak optical nonlinear interactions, superconducting circuits feature strong nonlinearity at microwave frequencies inherent to the superconducting Josephson effect [23], enabling fast quantum operations. Josephson junctions are superconducting circuit elements with an inherently strong inductive nonlinearity with respect to the current traversing them. This is the nonlinearity that enables parametric amplification in Josephson parametric amplifiers, commonly used to generate squeezed microwaves. Compared with photonic crystal waveguides, on-chip microwave circuits have less-stringent fabrication tolerance to imperfections, such as surface roughness, that can lead to excessive propagation loss. Moreover, the near-lossless electromagnetic properties of superconducting materials and their compatibility with widely-established lithographic fabrication and materials processing technology facilitate the realization of various superconducting circuit designs.

The generation and detection of squeezed microwave photons are vital to many applications in quantum information science and metrology. In the context of circuit quantum electrodynamical (cQED) systems, squeezed microwaves have been used to suppress such radiative spontaneous emission from a superconducting qubit [76], to demonstrate non-classical light-matter interactions such as resonance fluorescence from a qubit [111], and potentially to improve gate fidelity for superconducting qubits in the field of quantum computing [87]. The unique advantages of superconducting circuits enable the applications with engineered microwave amplifiers.

The resonator-based Josephson parametric amplifier (JPA) is a conventional approach to generating squeezed microwave photons. As shown in Fig. 1-1a, signal and pump photons enter the resonator and bounce around multiple times before leaving the resonator.

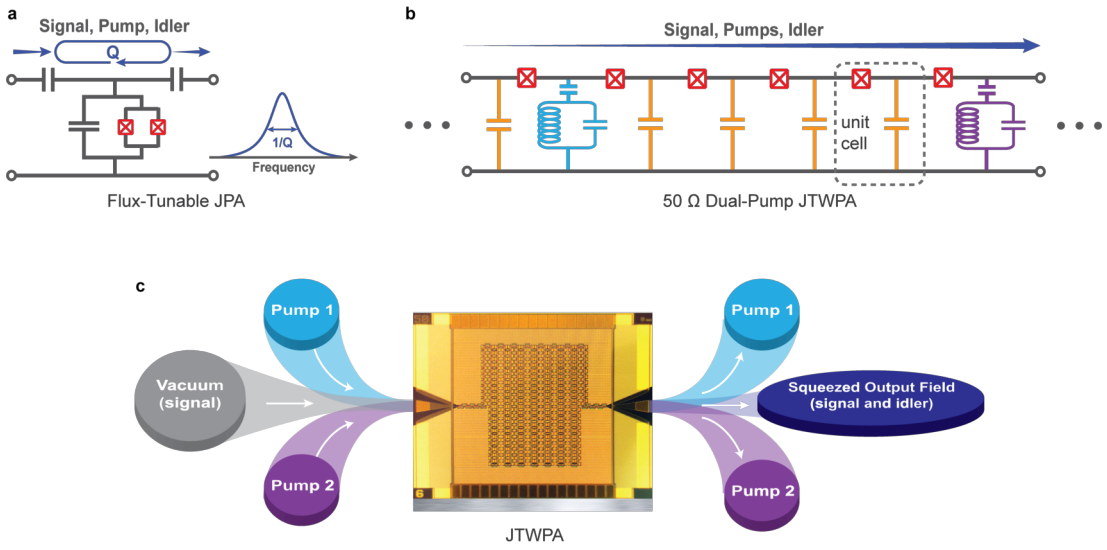

Figure 1-1. | Josephson traveling-wave parametric amplifier dispersion engineered for a bichromatic pump. a. Circuit schematic of a conventional JPA, and the crossed box represents the Josephson junction. The Q-enhancement of the field produces a narrowband frequency response. **b.** A repeating section of the dual-pump JTWPA. We can identify the L-C ladder that forms a 50 Ω transmission line from lumped elements and the two phase-matching resonators for dispersion engineering. **c.** The JTWPA in the presence of a bichromatic pump transforms the vacuum field at the input into a squeezed field at the output through non-degenerate four-wave mixing.

JPA squeezers use a narrow-band resonator and its resonant-enhanced circulating field to increase the interaction between photons and a single or few Josephson junctions. However, the relatively large circulating field in JPAs strongly drives the non-linearity of individual junctions, leading to unwanted higher-order nonlinear processes and saturation that impact squeezing performance [14, 65, 76, 69, 9, 57]. In contrast, a Josephson traveling-wave parametric amplifier (JTWPA) consists of many Josephson junctions in series (Fig. 1-1b), effectively distributing the nonlinearity across the entire device. By eliminating the resonant structure, the JTWPA can generate highly squeezed single-mode vacuum states and broadband two-mode squeezed vacuum states, circumventing the bandwidth limitations of resonator-based JPAs.

In comparison with previous work on a monochromatically pumped JTWPAs to achieve broadband amplification [62], we operate the device with a bichromatic pump to produce phase-sensitive amplification, single-mode squeezing, and two-mode squeezing through a nonlinear wave mixing process known as non-degenerate four-wave mixing (NDFWM). This dispersion-engineered JTWPA belongs to a class of amplification with the unique

characteristic of providing amplification/deamplification to input signals at select phases. A dual-pump, broadband JTWPA is developed using dispersion engineering to support NDFWM as shown in Fig. 1-1(c). Our device demonstrates the highest reported phase-sensitive extinction ratio to date for Josephson-junction-based circuits, which is useful for qubit readout in quantum computing and phase regeneration in quantum communications [89].

We also achieve single-mode squeezing with an order-of-magnitude reduction of vacuum noise, on par with the best resonator-based squeezers. We furthermore demonstrate two-mode squeezing with GHz bandwidth at microwave frequencies, almost two-orders-of-magnitude wider than that of typical resonator-based squeezers. The JTWPA is capable of creating entangled microwave photon pairs with large frequency separation, enabling new possibilities for applications including high-fidelity qubit readout, quantum illumination and teleportation. The broad bandwidth and high degree of squeezing demonstrated in our device represents a new, resource-efficient (instead of combining individual narrow-band squeezers [35]) means to generate multimode, non-classical states.

The thesis also discusses boosting the quantum efficiency and extending the operating frequency range of the JTWPA. Quantum efficiency is largely constrained by the intrinsic loss, most of which in the existing niobium-based, tri-layer JTWPAs originates from defects in the dielectric material [95]. Therefore, various aluminum-based, planar JTWPAs are designed and fabricated using a high-Q aluminum process to reduce insertion loss relative to the niobium tri-layer process. We primarily study the overall improved dielectric loss and broadband amplification in aluminum JTWPAs. The work validates design and fabrication in the process of reducing intrinsic loss. It also guides future design iterations of JTWPAs. Much of the previous amplifier work has focused on the microwave C-band (4-8 GHz) primarily due to the increasing application of quantum-limited amplifiers in quantum computing. However, broadband amplifiers play a critical role in signal processing outside the C-band. By multiplexing readout and enhancing signal-to-noise ratio, the amplifiers speed up measurement time and save amplification resources. In this thesis, we develop JTWPAs in the lower spectrum range from 500 MHz to 900 MHz and demonstrate first-of-its-kind broadband superconducting traveling-wave amplifiers with large gain

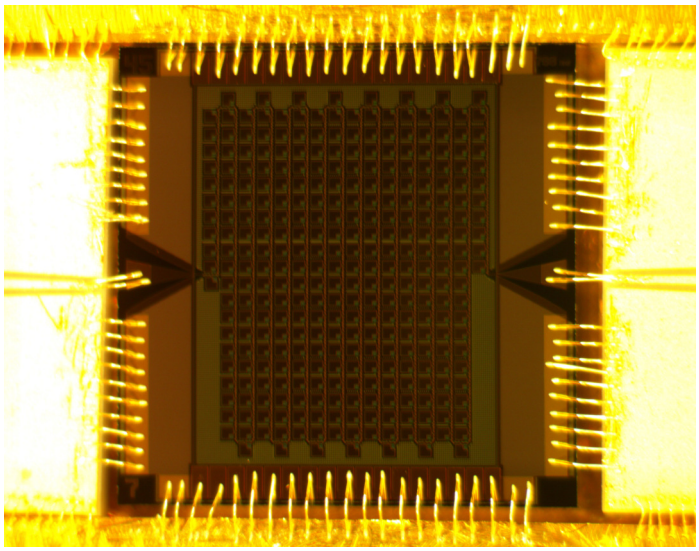

Figure 1-2. | **Low-frequency 700MHz JTWPA.** Microscopic view of a 5 mm×5 mm low-frequency JTWPA chip wire-bonded to a microwave package.

and broadband amplification performance. The amplifiers have significant applicability in spin qubit readout [48] for example, and other potential usage in condensed matter and astrophysics [108, 61].

The outline of the thesis is as follows: In Chapter 2, we will introduce concepts of squeezed states, wave-mixing processes, and the origin of the Josephson nonlinearity in superconducting circuits. These concepts will be further discussed and linked in Chapter 3 with the introduction of Josephson parametric amplifiers. Chapter 3 explores different types of Josephson parametric amplifiers and discusses various topics about them, including phase modulation, phase matching, and parametric amplification. Chapter 4 gives a quick overview of superconducting qubits and gates in quantum computing and connects to some potential applications using squeezed states. Chapter 5 focuses on the experimental setup and design parameters for different variations of JTWPAs. It also emphasizes the importance of dispersion engineering, leading to improved performance from the new JTWPAs. Chapter 6 highlights noise calibration methods used to benchmark the JTWPA performance. Noise calibration is a critical step in characterizing a squeezer as the system noise is closely associated with the measurement efficiency of the experimental setup and directly affects squeezing results. We discuss the practical aspects of their protocols including each of their unique advantages and disadvantages. The rest of the chapter presents

our latest results on operating the JTWPA in non-degenerate four-wave mixing to achieve broadband amplification and squeezed vacuum states. Finally, Chapter 7 will summarize our work and discuss the future directions.

Chapter 2

Background

This chapter introduces the concepts of squeezed light and explores the nonlinear effects specific to our system — a JTWPA — and their relation to different wave-mixing processes, including ones detrimental to the coherence of propagating signals. We also discuss the fundamentals of the Josephson junction, an essential nonlinear element in superconducting circuits, and the SQUID, a magnetic-flux-tunable nonlinear device based on Josephson junctions. These discussions set up the background for understanding Josephson parametric amplifiers and squeezed state generation in the next chapter.

2.1 Squeezed Light Generation

In this section, we start with a general discussion on electromagnetic (EM) squeezed states and introduce common terminology used to describe them quantitatively, emphasizing concepts relevant to the experiments. In Chapter 7, we shall demonstrate how to achieve these states using a JTWPA and its squeezing performance in more detail.

A classical single-mode EM field oscillating sinusoidally at frequency ω can be described with an amplitude and a phase, similar to a simple harmonic oscillator. Its electric field can be represented as a phasor, an arrow in a complex plane, or phase space represented by two conjugate variables (such as amplitude and phase or position and momentum) rotating with an angular velocity ω. In a reference frame co-rotating at the same velocity, the arrow is stationary in the complex plane used to visualize these EM signals. The static

quadrature field components are referred to as X (position) and P (momentum), or alternatively I (in-phase) and Q (quadrature). In a classical picture, the harmonic oscillator state can be depicted as a single point in phase space, as displayed in Fig. 2-1(a). Like the quantum mechanical version of a simple harmonic oscillator, the EM field is a quantized system with an equally spaced discrete energy spectrum $E_n = \hbar\omega\,(n + 1/2)$, where integer n denotes the energy level, and the quantum eigenstates are denoted by $|n\rangle$. Even in the ground state ($n = 0$), there is still a finite amount of *zero-point energy* such that the position and the momentum cannot be fully zero (different from a classical system). This ground state is known as the vacuum state for EM fields. Therefore, this vacuum state can be depicted in phase-space as an enlarged circular "blob" of fluctuation instead of a point in the classical phase-space as shown in Fig. 2-1(b). This corresponds to "quantum fluctuations" within the phase-space observables, represented by quadrature operators $\hat{X}$ and $\hat{P}$. The Heisenberg uncertainty principle states

$$\langle \Delta \hat{X}^2 \rangle \langle \Delta \hat{P}^2 \rangle \geq 1/4, \tag{2.1}$$

where $\langle (\Delta \hat{X})^2 \rangle$ and $\langle (\Delta \hat{P})^2 \rangle$ are variances for the quadrature operators. The vacuum state takes on equality in Eq. (2.1) and has the same amount of fluctuation in both quadratures, $\langle \Delta \hat{X}^2 \rangle$ = $\langle \Delta \hat{P}^2 \rangle$ = $1/2$. The vacuum state has a mean photon number $\bar{n} = 0$ or number state of $|0\rangle$; despite the void of photons, the zero-point energy in the vacuum state still contributes a noise of $\hbar\omega/2$ — "half of a photon of noise" effectively and referred to as the "standard quantum limit".

A coherent state $|\alpha\rangle$ is a specific kind of quantum state that satisfies the Heisenberg uncertainty principle with equality — the state adds $\hbar\omega/2$ of noise and assumes equal uncertainties (identical to those of a vacuum state) in both $\hat{X}$ and $\hat{P}$ quadratures. The state can be understood as a displaced vacuum state with a non-zero mean photon number $\bar{n}$ and can be expressed in the number-state basis as

$$|\alpha\rangle = e^{\left(-\frac{1}{2}|\alpha|^2\right)} \sum_{n=0}^{\infty} \frac{\alpha^n}{\sqrt{n!}} |n\rangle. \tag{2.2}$$

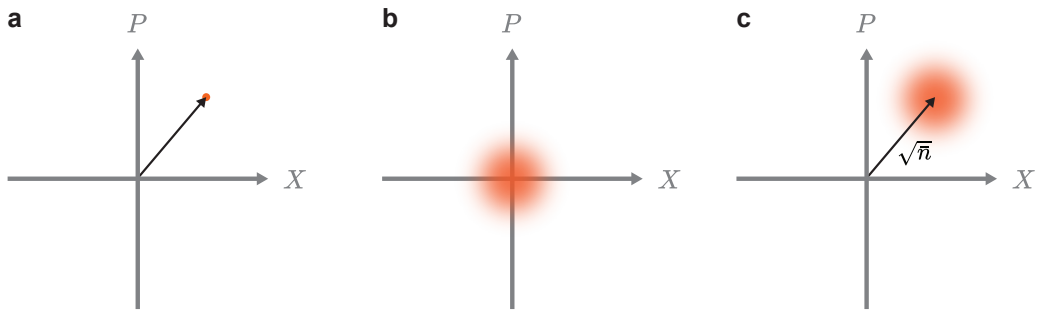

Figure 2-1. | **Phasor diagrams. a.** Illustration of a classical simple harmonic oscillator, whose state is represented as a single point in the phase space of position X and momentum P. **b.** Depiction of a quantum harmonic oscillator and in this case the vacuum state, whose state is no longer a point due to its probability distribution (quantum fluctuations). **c.** Drawing of a coherent state with amplitude of $\sqrt{\bar{n}}$ that corresponds to a mean photon number $\bar{n}$.

As shown in Fig. 2-1(b) and (c), a coherent state is generated by displacing the vacuum state by an amplitude $|\alpha| = \sqrt{\bar{n}}$, given by $|\alpha\rangle = \hat{D}(\alpha)|0\rangle$. $\hat{D}(\alpha)$ is the unitary displacement operator

$$\hat{D}(\alpha) = e^{\alpha\hat{a}^\dagger - \alpha^*\hat{a}}, \tag{2.3}$$

i.e., $\hat{D}^\dagger(\alpha) = \hat{D}(-\alpha) = [\hat{D}(\alpha)]^{-1}$. $\hat{a}^\dagger$ and $\hat{a}$ are the creation and annihilation operators. Despite the quantum nature of light, coherent states are generally considered quasi-classical states and the closest quantum mechanical analogue of a simple harmonic oscillator. This is especially true as $\bar{n}$ approaches infinity and the fractional uncertainty ($\sqrt{\bar{n}}/\bar{n}$) in the photon number reduces to zero. In other words, coherent states become relatively more localized in the phase-space with respect to the fixed quantum fluctuations and approach classical states as shown in Fig. 2-1(a) in the large $\bar{n}$ limit with a huge displacement from the origin.

2.1.1 Single-Mode Squeezed Vacuum States

In quantum-limited measurements of conjugate observables such as amplitude and phase, the precision is constrained by quantum fluctuations of the EM field [116, 18, 10]. The standard quantum limit, set by vacuum fluctuations that cannot be reduced by classical means, is described by Heisenberg's uncertainty principle. For a coherent state or vacuum state, the noise is equally distributed between the two quadratures, $\langle\Delta\hat{X}^2\rangle = \langle\Delta\hat{P}^2\rangle = 1/2$. To reach higher sensitivities, a single monochromatic mode of squeezed light has the

unique property of reduced uncertainty in one of the phase-space variables ($\hat{X}$ or $\hat{P}$) compared to the uncertainty caused by the quantum fluctuations in the vacuum state of light. It is achieved at the expense of a larger fluctuation in its conjugate observable ($\hat{P}$ or $\hat{X}$), provided it respects the uncertainty relation (Eq. (2.1)). In general, we describe that a state of EM mode exhibits (quadrature) squeezing if the variance of the position or momentum drops below $1/2$. Likewise, the other quadrature with its variance exceeding $1/2$ exhibits anti-squeezing. The ratio between the squeezed/anti-squeezed quadrature variance and the vacuum variance is defined as squeezing/anti-squeezing factor, S_- and S_+, respectively

$$S_- = \langle \Delta \hat{X}^2 \rangle / \langle \Delta \hat{X}^2_{\text{vacuum}} \rangle, \tag{2.4}$$

$$S_+ = \langle \Delta \hat{P}^2 \rangle / \langle \Delta \hat{P}^2_{\text{vacuum}} \rangle. \tag{2.5}$$

Here we assume $\hat{X}(\hat{P})$ is the squeezing (anti-squeezing) quadrature without loss of generality. It is conventional for us to express the amount of squeezing/anti-squeezing in the base-10 logarithmic value of these factors in experiments (Chapter 7). Squeezing purity can be defined as

$$\mathcal{P} = 1/\sqrt{S_- S_+}. \tag{2.6}$$

As the name suggests, it characterizes the purity of the squeezed state. The squeezing factor is equal to the anti-squeezing factor in the ideal case $\mathcal{P} = 1$. When there is some loss in the system, the squeezer will mix in vacuum noise and lead to a mixed squeezed state [96]. This effect is manifested as higher anti-squeezing than the absolute value of the squeezing, and $\mathcal{P}$ will drop below unity.

One way to visualize noise distribution of a particular state is to plot its electric field fluctuations as a function of time, as shown in Fig. 2-2(a). In that plot, the noise distribution for a vacuum state is constant for all time. However, for a squeezed vacuum state, fluctuations in the time-dependent electric field $\varepsilon(t)$ vary from a maximum value (anti-squeezing) to a minimum value (squeezing), creating a "breathing" mode. A more useful way to visualize and analyze the states is through the time-invariant phase-space representation, in which we can uniquely represent any state of light with a quasi-probability

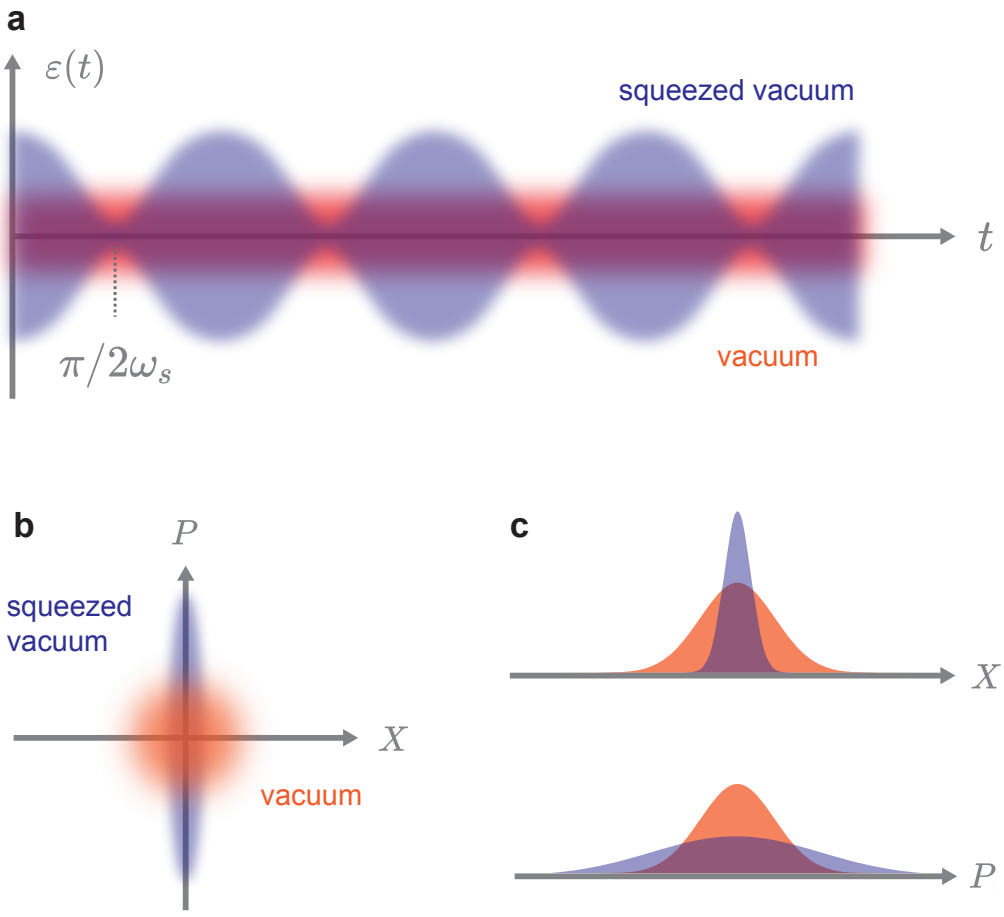

Figure 2-2. | **Illustration of single-mode squeezed states. a.** The picture shows noise in the time-dependent electric field $\varepsilon(t)$ for the vacuum (orange), and single-mode squeezed vacuum (blue) states. The latter oscillates at twice the signal frequency ω_s [71]. **b.** Phasor representation of the squeezed vacuum and vacuum noise. **c.** Gaussian distributions of the squeezed vacuum and vacuum states in the position and momentum bases.

distribution functions (they do not satisfy all the axioms of probability distributions due to quantum interference[1]). More specifically, we can represent the common case of a state with a Gaussian noise distribution that is squeezed as an ellipse (blue) in phase space, shown in Fig. 2-2(b); drawing the contour of a Gaussian Wigner function (a specific type of quasi-probability distribution) at the 1-σ level, where σ denotes the standard deviation. For instance, the vacuum state appears as an isotropic circular Gaussian in phase space with

[1]Unlike a probability distribution, it can take on negative values, and hence, the name quasi-probability distribution. However, the catch here is that the actual measurement outcome probability is never negative as one integrates or marginalizes the distribution over the orthogonal axes in phase space. A negative value from the Wigner function is a signature of quantum interference.

variance $1/2$ in every direction as displayed in Fig. 2-2.

Here let us examine the action of squeezing from a mathematical perspective on $\langle(\Delta\hat{X})^2\rangle$ and $\langle(\Delta\hat{P})^2\rangle$, two quadratures of the output state from a squeezer. The unitary squeezing operator $\hat{S}_1(\xi)$ is defined as:

$$|\mathrm{SMSV}\rangle = \hat{S}_1(\xi)|0\rangle = e^{\frac{1}{2}(\xi^*\hat{a}^2 - \xi\hat{a}^{\dagger 2})}|0\rangle, \tag{2.7}$$

for a single-mode squeezed vacuum state $|\mathrm{SMSV}\rangle$, where $\xi = re^{i\varphi}$ is the "squeezing parameter", in which r is the strength and φ is the squeezing angle that correspond to the pump strength and pump phase in the experimental setting, respectively. Similarly, the two-mode squeezed vacuum state $|\mathrm{TMSV}\rangle$ with operator $\hat{S}_2(\xi)$ is:

$$|\mathrm{TMSV}\rangle = \hat{S}_2(\xi)|0,0\rangle = e^{(\xi^*\hat{a}_s\hat{a}_i - \xi\hat{a}_s^\dagger\hat{a}_i^\dagger)}|0,0\rangle, \tag{2.8}$$

acting on the two-mode vacuum state $|0,0\rangle$. We have denoted the two modes by 's' and 'i' to refer to the signal and idler modes that we will subsequently discuss. Using an extension from the Baker-Campbell-Hausdorff (BCH) formula [43], which states

$$e^A B e^{-A} = B + [A,B] + \frac{1}{2!}[A,[A,B]] + \cdots, \tag{2.9}$$

we change the basis and get

$$\begin{aligned} \hat{S}_1^\dagger(\xi)\hat{a}\hat{S}_1(\xi) &= \hat{a}\cosh r - \hat{a}^\dagger e^{i\phi}\sinh r, \\ \hat{S}_1^\dagger(\xi)\hat{a}^\dagger\hat{S}_1(\xi) &= \hat{a}^\dagger\cosh r - \hat{a}e^{-i\phi}\sinh r, \end{aligned} \tag{2.10}$$

where $\hat{S}_1^\dagger(\xi) = \hat{S}_1(-\xi)$.

Now consider the action of the squeezing operator $\hat{S}_1(\xi)$ on an arbitrary state $|\psi\rangle$

$$|\psi_s\rangle = \hat{S}_1(\xi)|\psi\rangle. \tag{2.11}$$

In the case where $|\psi\rangle = |0\rangle$ is the vacuum state, $|\psi_s\rangle$ becomes the squeezed vacuum state $|\mathrm{SMSV}\rangle$ as we discussed in Sec. 2.1.4. In order to extract the variance of $\hat{X}$ and $\hat{P}$, we

need to find the expectation values of operator $\hat{a}$, $\hat{a}^2$, etc. As an example,

$$\langle\psi_s|\hat{a}|\psi_s\rangle = \langle\psi|\hat{S}_1^\dagger(\xi)\hat{a}\hat{S}_1(\xi)|\psi\rangle, \tag{2.12}$$

$$\langle\psi_s|\hat{a}^2|\psi_s\rangle = \langle\psi|\hat{S}_1^\dagger(\xi)\hat{a}\hat{S}_1(\xi)\hat{S}_1^\dagger(\xi)\hat{a}\hat{S}_1(\xi)|\psi\rangle. \tag{2.13}$$

The generic quadrature operator [43] can be expressed as

$$\hat{Q}(\vartheta) = \frac{1}{\sqrt{2}}\left(\hat{a}e^{-i\vartheta} + \hat{a}^\dagger e^{i\vartheta}\right). \tag{2.14}$$

We can select the two quadrature operators $\hat{X}$ and $\hat{P}$ with $\vartheta = 0$ and $\vartheta = \pi/2$, respectively, and get $\hat{X} = \frac{1}{\sqrt{2}}\left(\hat{a}^\dagger + \hat{a}\right)$ and $\hat{P} = \frac{i}{\sqrt{2}}\left(\hat{a}^\dagger - \hat{a}\right)$. These are convenient definitions for describing a time-dependent electric field with its field amplitudes oscillating out of phase with each other by $\pi/2$ and hence are in quadrature. We will discuss this more in Sec. 5.2.1. Here $\hat{X}$ and $\hat{P}$ satisfy the commutation relation $[\hat{X}, \hat{P}] = i$. Using Eq. (2.10)–Eq. (2.13), the variances of the squeezing quadrature operators are

$$\langle(\Delta\hat{X})^2\rangle = \langle\hat{X}^2\rangle - \langle\hat{X}\rangle^2 = \frac{1}{2}\left[\cosh^2 r + \sinh^2 r - 2\sinh r\cosh r\cos\varphi\right]. \tag{2.15}$$

$$\langle(\Delta\hat{P})^2\rangle = \langle\hat{P}^2\rangle - \langle\hat{P}\rangle^2 = \frac{1}{2}\left[\cosh^2 r + \sinh^2 r + 2\sinh r\cosh r\cos\varphi\right]. \tag{2.16}$$

When $\varphi = 0$, these two equations reduce to

$$\langle(\Delta\hat{X})^2\rangle = \frac{1}{2}e^{-2r}. \tag{2.17}$$

$$\langle(\Delta\hat{P})^2\rangle = \frac{1}{2}e^{2r}, \tag{2.18}$$

where r is the squeezing strength. Again, a cartoon illustration is shown in Fig. 2-2(b). We will discuss it in more detail towards the end of Sec. 2.1.

2.1.2 Squeezed Coherent States

We can give a more general description for single-mode squeezed states by applying displacement operation to Eq. (2.7):

$$|\alpha, \xi\rangle = \hat{D}(\alpha)\hat{S}_1(\xi)|0\rangle, \tag{2.19}$$

a combination of displacement and squeezing actions that transforms the vacuum state into a displaced squeezed vacuum state or squeezed coherent state. Note that the squeezing operator does not commute with the displacement operator $\hat{D}$ nor does it commute with the creation and annihilation operators. Therefore, the order of the operator actions matters. In the case of the coherent state with $\xi = 0$, we get back just a coherent state. In the less trivial case when $\xi \neq 0$, we consider the effect of displacement operator on the squeezing transformation, namely,

$$\begin{aligned} \hat{D}^\dagger(\alpha)\hat{a}\hat{D}(\alpha) &= \hat{a} + \alpha \\ \hat{D}^\dagger(\alpha)\hat{a}^\dagger\hat{D}(\alpha) &= \hat{a} + \alpha, \end{aligned} \tag{2.20}$$

where we have used the BCH formula (Eq. (2.9)) and in this case $A = \alpha^*\hat{a} - \alpha\hat{a}^\dagger$ and $B = \hat{a}$ or $\hat{a}^\dagger$. The higher-order commutators vanish since $[A, B] \in \mathbb{C}$, which commutes with other operators in the BCH expansion. Using Eq. (2.10) and Eq. (2.20), we get $\langle\hat{a}\rangle = \alpha$, which is independent of the squeezing parameter, $\langle\hat{a}^2\rangle = \alpha^2 - \sinh r \cosh r$ and $\langle\hat{a}^\dagger\hat{a}\rangle = |\alpha|^2 + \sinh^2 r$. We recover a coherent state when $r = 0$ and a squeezed vacuum state when $\alpha = 0$. Furthermore, the variance for the squeezing quadrature operators $\langle(\Delta\hat{X})^2\rangle$ and $\langle(\Delta\hat{P})^2\rangle$ follow Eq. (2.17) and Eq. (2.18). As shown in Fig. 2-3, the variance along the $\hat{X}$ quadrature of the squeezed coherent state is smaller than that of the vacuum (or coherent) state.

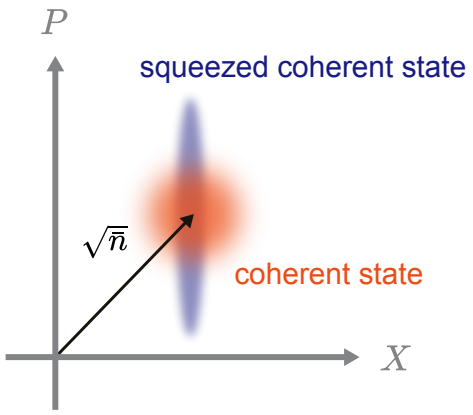

Figure 2-3. | **Squeezed coherent state.** Phase-space portrait of a coherent state of amplitude $|\alpha| = \sqrt{\bar{n}}$ and a displaced vacuum state that is the squeezed coherent state.

2.1.3 Two-Mode Squeezed Vacuum States

With the conceptual generalizations of single-mode squeezing, two-mode squeezed states exhibit correlations between the phase-space observables in the subsystem of two coupled oscillators. In other words, two-mode squeezed states can be interpreted in the context of "quantum coupling" that is the entanglement. Two-mode squeezed vacuum (TMSV) is also known as the twin-beam state [60]; photons generated at the respective two modes can be entangled. As shown in Fig. 2-4 (top row), TMSV does not imply X or P quadrature squeezing in each of its individual modes because observables in their respective quantum subspace are uncorrelated (each mode is considered in an "effective" thermal state because their photon statistics looks identical to that of an actual thermal state [60, 43]). However, the joint observables (X_1 and X_2 or P_1 and P_2) exhibit correlation or anti-correlation due to quantum entanglement. Historically, Alain Aspect's experiment in 1982 is considered to be the first quantum mechanics experiment to demonstrate the violation of Bell's inequality, further validating the principle of quantum entanglement. In his experiment, calcium atoms are excited through two-photon absorption, and at the end, pairs of photons are emitted in an entangled state and exhibit linear-polarization correlation [4]. Because of the conservation of momentum, photon pairs are always emitted in opposite directions. However, the direction of such emission is random in Aspect's experimental setup. With optical or microwave waveguides, the direction of photon propagation can be confined to

one dimension to allow better detection efficiency. Still, the entangled photons must obey physical conservation laws such as momentum and energy. The TMSV state is the basis of the famous quantum nonlocality paradox in its original formulation by Einstein, Podolsky, and Rosen (EPR) [60].

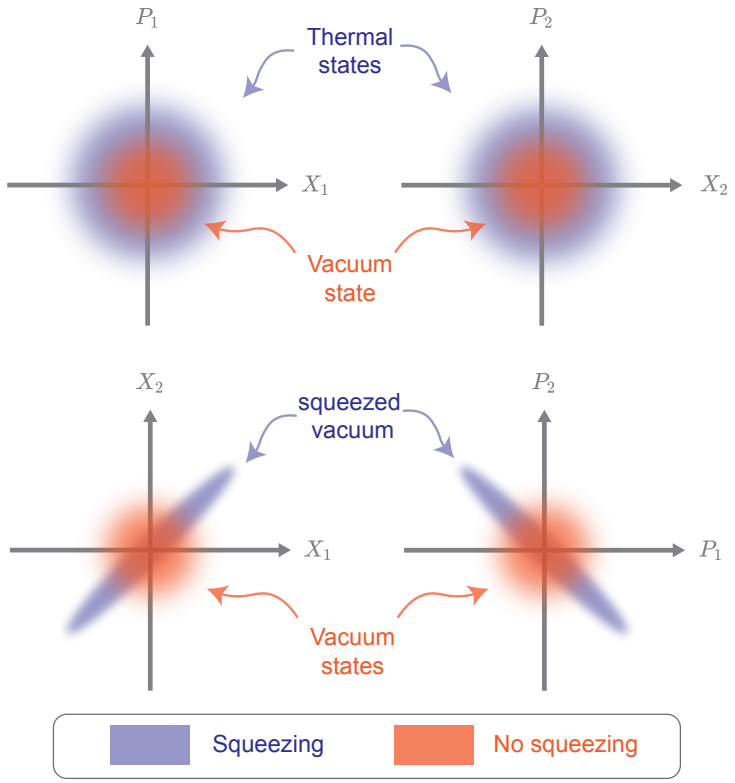

Figure 2-4. | Illustration of two-mode squeezed states. The top row displays the output field at the two modes. There is no squeezing but uncorrelated noise depicted by enlarged circular blobs. The bottom row shows two-mode squeezed and vacuum states in the position (left: X_1X_2) and momentum (right: P_1P_2) bases. For the two-mode squeezed state considered in this thesis, the position observables are correlated conventionally, while the momentum observables are anti-correlated beyond the standard quantum limit.

Here we want to extract the action of squeezing on the two quadratures of the squeezed state, similar to the single-mode example. We define the superposition of the quadrature operators $\hat{X}_1^{\mathrm{TM}}$ and $\hat{X}_2^{\mathrm{TM}}$ as the following:

$$\hat{X}_1^{\mathrm{TM}} = \frac{1}{2^{3/4}} \left(\hat{a}_s{}^{\dagger} + \hat{a}_s + \hat{a}_i{}^{\dagger} + \hat{a}_i \right), \tag{2.21}$$

$$\hat{X}_2^{\mathrm{TM}} = \frac{i}{2^{3/4}} \left(\hat{a}_s{}^{\dagger} - \hat{a}_s + \hat{a}_i{}^{\dagger} - \hat{a}_i \right). \tag{2.22}$$

One can verify that these operators satisfy the same commutation relations as for the single-mode squeezing, $[\hat{X}_1^{\mathrm{TM}}, \hat{X}_2^{\mathrm{TM}}] = i$, given that $[\hat{a}_s, \hat{a}_i] = 0$.

Applying the same BCH formula, we get similar expressions as for the single-mode case,

$$\hat{S}_2^\dagger(\xi)\hat{a}_s\hat{S}_2(\xi) = \hat{a}_s \cosh r - \hat{a}_i^\dagger e^{i\varphi} \sinh r \tag{2.23}$$

$$\hat{S}_2^\dagger(\xi)\hat{a}_i\hat{S}_2(\xi) = \hat{a}_i \cosh r - \hat{a}_s^\dagger e^{i\varphi} \sinh r. \tag{2.24}$$

Using these results, we can show that $\langle \hat{X}_1^{\mathrm{TM}} \rangle = \langle \hat{X}_2^{\mathrm{TM}} \rangle = 0$, and

$$\langle (\Delta \hat{X}_1^{\mathrm{TM}})^2 \rangle = \frac{1}{2} \left[\cosh^2 r + \sinh^2 r - 2 \sinh r \cosh r \cos \varphi \right]. \tag{2.25}$$

$$\langle (\Delta \hat{X}_2^{\mathrm{TM}})^2 \rangle = \frac{1}{2} \left[\cosh^2 r + \sinh^2 r + 2 \sinh r \cosh r \cos \varphi \right]. \tag{2.26}$$

When $\varphi = 0$,

$$\langle (\Delta \hat{X}_1^{\mathrm{TM}})^2 \rangle = \frac{1}{2} e^{-2r}. \tag{2.27}$$

$$\langle (\Delta \hat{X}_2^{\mathrm{TM}})^2 \rangle = \frac{1}{2} e^{2r}, \tag{2.28}$$

These are the same mathematical results, but the interpretation is different since we have a superposition of modes in the two-mode squeezed vacuum states instead of the individual mode in the single-mode case.

2.1.4 Effective Squeezing Operators in the JTWPA

In superconducting circuits, the typical scheme for generating squeezed states uses a parametrically driven nonlinear medium, producing an interaction that is quadratic in the annihilation and creation operators of the field mode [43]. For example, the Hamiltonian for the non-degenerate four-wave mixing process in a JTWPA can be expressed as

$$\hat{H} = \hbar\omega_s \hat{a}_s^\dagger \hat{a}_s + \hbar\omega_i \hat{a}_i^\dagger \hat{a}_i + \hbar\omega_{\mathrm{p1}} \hat{b}_1^\dagger \hat{b}_1 + \hbar\omega_{\mathrm{p2}} \hat{b}_2^\dagger \hat{b}_2 + i\hbar\chi^{(3)} \left(\hat{a}_s \hat{a}_i \hat{b}_1^\dagger \hat{b}_2^\dagger - \hat{a}_s^\dagger \hat{a}_i^\dagger \hat{b}_1 \hat{b}_2 \right), \tag{2.29}$$

where the first and second terms represent the signal and idler fields with mode operators $\hat{a}_s$ and $\hat{a}_i$, while the third and fourth terms denote the two pump fields with mode operators $\hat{b}_1$ and $\hat{b}_2$. The last term is the interaction Hamiltonian presuming a $\chi^{(3)}$, the leading nonlinear susceptibility of this system. We will discuss the origin of this interaction in further detail in the following section. In general, Eq. (2.29) describes the two-mode scenario, and in the special case when the signal frequency equals the idler frequency, i.e. $\omega_s = \omega_i$, the Hamiltonian describes single-mode operation. As shown in Fig. 2-5, squeezing always involves two modes, a "signal" and an "idler". We note that there are finite bandwidths associated with measurement in experimental settings. To clarify the terminology used in the thesis and draw comparison with other previous works, we define "two-mode" as when the signal and idler are non-degenerate and their mode separation is much larger than the measurement bandwidth $|\omega_\mathrm{s} - \omega_\mathrm{i}| \gg B_\mathrm{meas}$, and "single-mode" as when the signal and idler are both nominally degenerate and within the measurement bandwidth $|\omega_\mathrm{s} - \omega_\mathrm{i}| \leq B_\mathrm{meas}$.

Figure 2-5. | **Single-mode vs. two-mode. a.** We define "single-mode" when the two modes, signal and idler, are degenerate. **b.** When the signal and idler are non-degenerate, we have "two-mode".

From the last term in Eq. (2.29), one identifies the pair-wise photon creation and annihilation operators that are effectively the same as the squeezing operator $\hat{S}_1(\xi)$ and $\hat{S}_2(\xi)$. Intuitively, when $\omega_s = \omega_i$, the output signal and idler can interfere, leading to constructive or destructive interference depending on their relative phase. This gives rise to phase sensitivity in the parametric amplification process and single-mode squeezing. As discussed earlier, when the signal and idler are non-degenerate, the nonlinear wave mixing process produces entangled states that result in two-mode squeezing. In an ideal squeezer that generates both single-mode and two-mode squeezed vacuum states, the squeezing levels are the same if the squeezing parameter ξ is the same for both cases.

Returning to Eq. (2.29), we consider the interaction Hamiltonian

$$\hat{H}_{\text{int}} = i\hbar\chi^{(3)}\left(\hat{a}_s\hat{a}_i\hat{b}_1^\dagger\hat{b}_2^\dagger - \hat{a}_s^\dagger\hat{a}_i^\dagger\hat{b}_1\hat{b}_2\right). \tag{2.30}$$

Transforming to a time-dependent interactive frame with strong, undepleted (i.e. the field does not decay as it propagates in space) pump fields $\hat{b}_1 = \gamma_1 e^{-i\omega_1 t}$ and $\hat{b}_2 = \gamma_2 e^{-i\omega_2 t}$.

$$\hat{H}_{\text{int}} = i\hbar\chi^{(3)}\left[\hat{a}_s\hat{a}_i\gamma_1^*\gamma_2^* e^{i(\omega_1+\omega_2-\omega_s-\omega_i)t} - \hat{a}_s^\dagger\hat{a}_i^\dagger\gamma_1\gamma_2 e^{-i(\omega_1+\omega_2-\omega_s-\omega_i)t}\right]. \tag{2.31}$$

Here we explicitly include the time-dependence for signal and idler mode operators. Under the nonlinear wave mixing process ($\omega_1 + \omega_2 - \omega_s - \omega_i = 0$), we have

$$\hat{H}_{\text{int}} = i\hbar\chi^{(3)}\left(\hat{a}_s\hat{a}_i\gamma_1^*\gamma_2^* - \hat{a}_s^\dagger\hat{a}_i^\dagger\gamma_1\gamma_2\right). \tag{2.32}$$

Its associated unitary evolution operator is

$$\hat{U}_{\text{int}}(t,0) = e^{-i\hat{H}_{\text{int}}t/\hbar} = e^{\chi^{(3)}\left(\hat{a}_s\hat{a}_i\gamma_1^*\gamma_2^* - \hat{a}_s^\dagger\hat{a}_i^\dagger\gamma_1\gamma_2\right)t}, \tag{2.33}$$

which has the same form as the squeezing operator $\hat{S}_{1,2}(\xi)$ in Eq. (2.7) and Eq. (2.8). Comparing the two, we can extract

$$\xi = \chi^{(3)}\gamma_1\gamma_2 t = r \tag{2.34}$$

with $\varphi = 0$. As we can see, the squeezing parameter r is only related to the interaction time t (constrained by the coupling between the pump and the signal), nonlinearity $\chi^{(3)}$, and pump strengths $\gamma_{1,2}$, properties either intrinsic to the nonlinear medium itself or related to the external setup and control.

In short, to generate squeezing, we need to create interactions that result in correlations between photons, either at a single mode or two modes. Moreover, it requires energy (pump sources) to generate photons. Both indicate that we need a mechanism to create these photon conversion processes, achievable through a nonlinear medium, upon which the squeezing performance is highly dependent.

2.2 Nonlinear Refraction & Phase Modulation

In this section, we will present the concepts of nonlinear optical processes based on Reference [1]. Consider an ideal linear dielectric medium under an external electric field $\mathbf{E}$. The induced polarization $\mathbf{P}$ is

$$\mathbf{P} = \epsilon_0 \bar{\boldsymbol{\chi}} \cdot \mathbf{E}, \tag{2.35}$$

where $\bar{\boldsymbol{\chi}}$ is the material susceptibility and is in general a tensor to capture the full extent of the polarization response to an applied electric field. This is not to be confused with the polarization (direction) of the electric field. The polarization of the nonlinear medium (dipole moment per unit volume) $\mathbf{P}$ propagates together with the EM field in the form of a polarization wave. Going beyond linear systems, with larger field magnitude $|\mathbf{E}|$, higher-order terms in the polarization expression become more important, and in general, can be expressed as

$$\mathbf{P} = \epsilon_0 \left(\boldsymbol{\chi}^{(\mathbf{1})} \cdot \mathbf{E} + \boldsymbol{\chi}^{(\mathbf{2})} : \mathbf{EE} + \boldsymbol{\chi}^{(\mathbf{3})} \vdots \mathbf{EEE} + \cdots \right), \tag{2.36}$$

where vertical dots represent tensor multiplication and $\boldsymbol{\chi}^{(\boldsymbol{i})}$ is the i'th order susceptibility. In the case of a JTWPA, the medium is centrosymmetric, meaning it is isotropic with spatial inversion symmetry. Therefore, the second-order susceptibility $\boldsymbol{\chi}^{(\mathbf{2})}$ vanishes, leaving $\boldsymbol{\chi}^{(\mathbf{3})}$ the higher-order term in Eq. (2.36). The third-order susceptibility essentially leads to many nonlinear effects of interest, including four-wave mixing in the parametric amplification process.

Now let us think about the case when there is more than one wave propagating through the nonlinear medium. Since microwave waveguide systems generally have a fixed polarization, this simplifies the description of wave propagation by grouping all of the $\boldsymbol{\chi}^{(\mathbf{3})}$ elements into one scalar term $\chi^{(3)}_{\mathrm{xxxx}}$. For example, by the superposition principle, four waves each oscillating at each frequency ω_j can be expressed as

$$E = \frac{1}{2} \sum_{j=1}^{4} E_j e^{ik_j z - \omega_j t} + c.c., \tag{2.37}$$

with wavevector $k_j = \tilde{n}_j \omega_j / c$, where $\tilde{n}_j$ is the nonlinear refractive index for mode j. By substituting this expression into Eq. (2.35) and expanding the sum, one can find terms that involve the product of three electric fields. The resulting polarization of wave at frequency ω_4 can be expressed as

$$P^{(3)} = \frac{3\epsilon_0}{4}\chi^{(3)}_{xxxx}[|E_4|^2 E_4 + 2(|E_1|^2 + |E_2|^2 + |E_3|^2)E_4 + 2E_1 E_2 E_3 e^{i\phi_+} + 2E_1 E_2 E_3^* e^{i\phi_-} + \cdots], \tag{2.38}$$

where $\phi_+ = (k_1 + k_2 + k_3 - k_4)z - (\omega_1 + \omega_2 + \omega_3 - \omega_4)t$ and $\phi_- = (k_1 + k_2 - k_3 - k_4)z - (\omega_1 + \omega_2 - \omega_3 - \omega_4)t$. Again, since the system is centrosymmetric, there are no second-order nonlinear interactions. Therefore, $\boldsymbol{\chi^{(3)}}$ is the leading nonlinear susceptibility of the system. Moreover, we are only interested in one of the tensor components, as the JTWPA can be largely approximated as a 1-dimensional nonlinear transmission line with waves propagating in $\pm\hat{z}$ and the electric fields oriented in $\pm\hat{x}$.

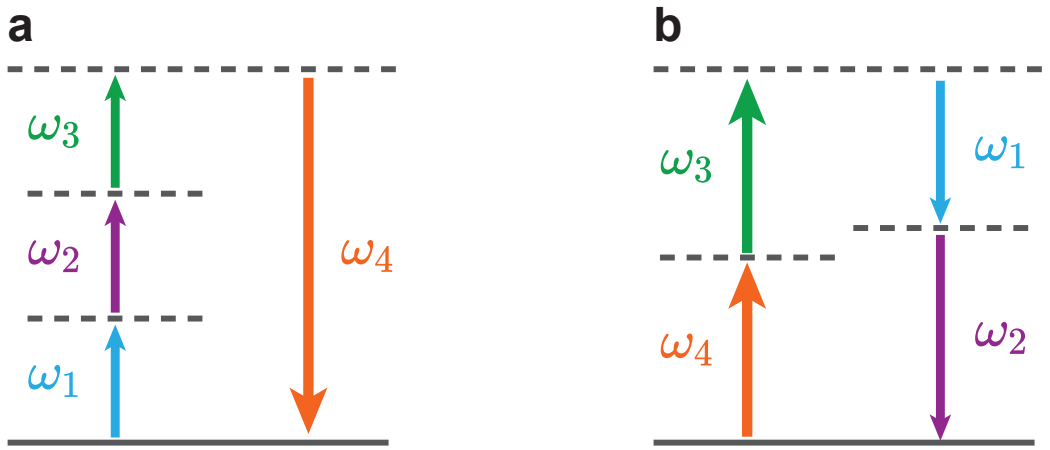

Figure 2-6. | **Energy-level description. a.** Third-harmonic generation when $\omega_1 = \omega_2 = \omega_3$. **b.** Non-degenerate four-wave mixing. When $\omega_3 = \omega_4$, the process is called degenerate four-wave mixing.

The term proportional to $|E_4|^2 E_4$ can be identified as self-phase modulation (SPM), and the term proportional to $(|E_1|^2 + |E_2|^2 + |E_3|^2)E_4$ represents cross-phase modulation (XPM). The field intensity ($I \sim |E|^2$) modifies the nonlinear refractive index according to $\tilde{n}(|E|^2) = n + n_2|E|^2$; the $|E|^2$ generates an intensity-dependent phase shift, and n_2 is known as the intensity-dependent refractive index. In our example, $n_2 = \frac{3}{8n}\mathrm{Re}(\chi^{(3)}_{xxxx})$,

where n is the linear refractive index for the material. When $\phi_{\pm} = 0$, the third and fourth terms in the bracket of Eq. (2.38) reduce to (1) third harmonic generation[2] when $\omega_1 = \omega_2 = \omega_3$, where three photons are converted to one photon at frequency $\omega_4 = \omega_1 + \omega_2 + \omega_3$, and (2) four-wave mixing, in which case two photons combine to produce two other photons $\omega_3 + \omega_4 = \omega_1 + \omega_2$, respectively. In the special case when the two input modes coincide in frequency space, the process is typically called degenerate four-wave mixing (DFWM). When this condition does not hold, it is called non-degenerate four-wave mixing (NDFWM). The latter process will be discussed in full detail in later chapters.

2.3 Superconducting Nonlinear Elements

2.3.1 Josephson Junction

An essential nonlinearity within superconducting circuits comes from the Josephson junction, a superconductor-insulator-superconductor (SIS) junction, named after Brian David Josephson, who predicted the mathematical relationships for the current and voltage across the junction in 1962 [52]. This section aims to motivate the AC and DC Josephson relations to demonstrate the nonlinear inductance inherent to a Josephson junction, crucial for many superconducting circuit devices, including the JTWPA.

A Josephson junction consists of two superconductors separated by a thin insulating material, as shown in Fig. 2-7. The wavefunction of the superconducting state can be described as:

$$\Psi_j(x,t) = |\Psi_j(x,t)|e^{i\theta_j(x,t)},\ j \in \{1,2\}, \tag{2.39}$$

where we define $|\Psi_j(x,t)|^2$ as the density of Cooper pairs, and $\theta_j(x,t)$ as the phase factor of the wavefunction [22]. Josephson discovered two important constituent relations between voltage, current, and phase across the junction, which we will introduce within the context of identical superconductors separated by an infinitely thin insulator.

The DC Josephson relation describes the relationship between the current I and the

[2]Third harmonic generation is a special case that also involves four photons, while four-wave mixing is a more general description.

phase difference across the junction ϕ. The quantum mechanical expression for the probability current of Cooper pairs in one dimension with position x is given by

$$I = \frac{i\hbar(-2e)}{4m_e}\left(\Psi^*\frac{\partial\Psi}{\partial x} - \Psi\frac{\partial\Psi^*}{\partial x}\right), \tag{2.40}$$

where m_e is the mass of a single electron. As the barrier thickness decreases, the spatial derivative of the wavefunction at junction should be proportional to the difference between Ψ_1 and Ψ_2, while the spatial symmetry requires the wavefunction to take the mean value $\Psi = (\Psi_1 + \Psi_2)/2$, leading Eq. (2.40) to

$$I \propto \frac{\left(e^{-i\theta_1} + e^{-i\theta_2}\right)\left(e^{i\theta_2} - e^{i\theta_1}\right)}{2} - \frac{\left(e^{i\theta_1} + e^{i\theta_2}\right)\left(e^{-i\theta_2} - e^{-i\theta_1}\right)}{2} = \left(e^{i\phi} - e^{-i\phi}\right), \tag{2.41}$$

where $\phi = \theta_2 - \theta_1$, the phase difference across the junction barrier. After identifying the proportionality constant in Eq. (2.40) as the junction critical current I_0 — the maximum supercurrent the barrier can sustain, which is dependent on the barrier and the properties of the superconductor — we can obtain the current phase relation

$$I = I_0 \sin\phi. \tag{2.42}$$

So far, the derivation assumes no voltage applied to the junction, and Eq. (2.42) suggests a DC current may tunnel across the Josephson junction in the absence of an external voltage. This is known as the DC Josephson effect.

Now, in the case when there is external voltage V applied across the junction, the total energy difference between the two regions of superconductors is given by $2eV$, assuming the Kirchoff's current rule still applies and the Cooper pair density $|\Psi(x,t)|^2$ is approximately independent of position x. As a function of time, an additional phase difference $\phi = 2eVt/\hbar$ will occur per the time-dependent Schrödinger equation [30]. The time derivative of this phase difference yields the AC Josephson relation,

$$\frac{\partial\phi}{\partial t} = \frac{2\pi V}{\Phi_0}, \tag{2.43}$$

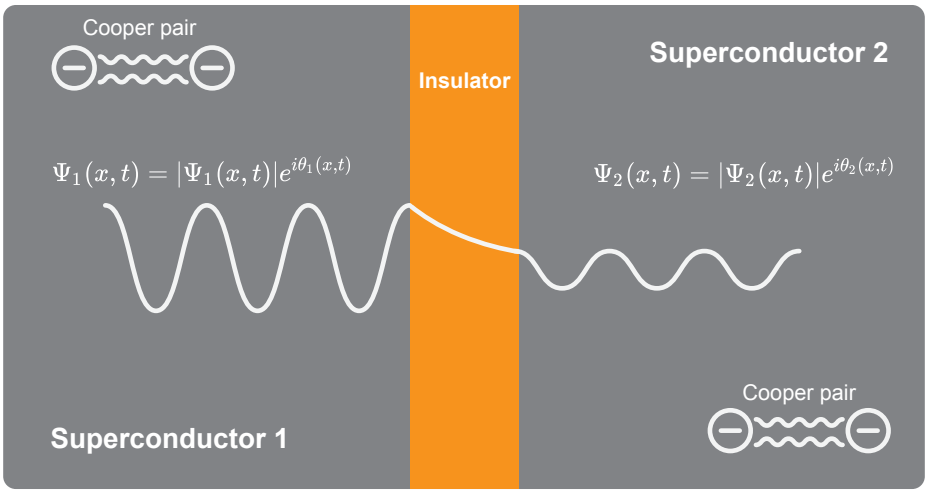

Figure 2-7. | **Josephson junction.** An illustrative drawing of a superconductor-insulator-superconductor (SIS) Josephson junction, typically made out of aluminum and aluminum oxide. A single wavefunction can describe Cooper pairs in a superconductor in the absence of a current. When a thin insulating layer separates two superconductors, quantum mechanical tunneling can occur for the Cooper pairs.

where $\Phi_0 = h/2e$ is the magnetic flux quantum. The AC Josephson relation implies that a DC voltage across the junction would cause the tunneling of a Cooper pair and emit or absorb a photon at frequency $\omega = V/\Phi_0$. This is the important result of the AC response, which allows physicists to experimentally determine this ratio of fundamental constants h and e. Combining Eq. (2.43) and Eq. (2.42), one can obtain the Josephson inductance

$$L_j = V\left(\frac{\partial I}{\partial t}\right)^{-1} = \frac{\Phi_0}{2\pi I_0 \cos(\phi)} = \frac{\Phi_0}{2\pi\sqrt{I_0^2 - I^2}}. \tag{2.44}$$

Clearly, the junction has a nonlinear inductance with respect to the current traveling through it, which is crucial to the development of superconducting circuit technology.

2.3.2 DC SQUID

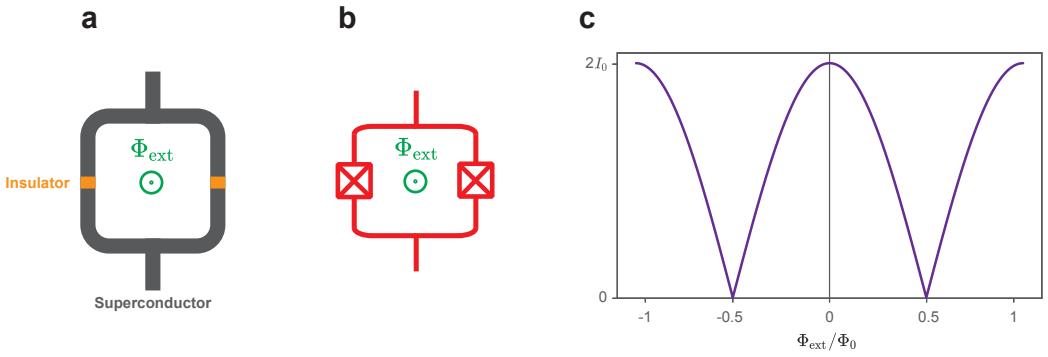

Figure 2-8. | **DC SQUID. a.** An illustrative drawing of a DC SQUID with two identical Josephson junctions. An external magnetic flux threads through the loop. **b.** A circuit representation of the SQUID with an external magnetic field; red squares with "X"s represent Josephson junctions. **c.** Dependence of the critical current of a symmetric, two-junction SQUID on the applied flux.

To construct a tunable Josephson inductance, one can form a superconducting loop with two Josephson junctions as shown in Fig. 2-8, a configuration called DC Superconducting Quantum Interference Device, or DC SQUID for short. Despite the terminology involving "DC" for historical reasons, there is no intrinsic low-frequency limitation to DC SQUIDs as they often readily exhibit dynamics at tens of GHz. The total current passing through the SQUID is the sum of currents through each single junction,

$$I = I_{0,\mathrm{L}} \sin\phi_{\mathrm{L}} + I_{0,\mathrm{R}} \sin\phi_{\mathrm{R}}, \tag{2.45}$$

where $I_{0,\mathrm{L/R}}$ and $\phi_{\mathrm{L/R}}$ are the critical current and phase drop across the left/right Josephson junction, respectively. If we assume the junctions are identical, the SQUID becomes symetric with $I_{0,\mathrm{L}} = I_{0,\mathrm{R}} = I_0$ and Eq. (2.45) can be expressed as

$$I = 2I_0 \cos(\phi_-) \sin(\phi_+), \tag{2.46}$$

where we define $\phi_- = (\phi_{\mathrm{L}} - \phi_{\mathrm{R}})/2$ and $\phi_+ = (\phi_{\mathrm{L}} + \phi_{\mathrm{R}})/2$. One can thread an external magnetic flux Φ_{ext} through the superconducting junction loop to tune the device. Due to the magnetic flux quantization in the superconducting circuit loop, the phase difference must

adhere to the relation

$$\phi_{\mathrm{R}} - \phi_{\mathrm{L}} - \frac{2\pi\Phi_{\mathrm{ext}}}{\Phi_0} = 2\pi n, \tag{2.47}$$

where n is an integer. Choosing $n = 0$, we get $\phi_{\mathrm{R}} = \phi_{\mathrm{L}} + (2\pi\Phi_{\mathrm{ext}}/\Phi_0)$ and substitute it in Eq. (2.46) to obtain

$$I(\Phi_{\mathrm{ext}}) = 2I_0 \cos\left(\frac{\pi\Phi_{\mathrm{ext}}}{\Phi_0}\right) \sin\phi_+, \tag{2.48}$$

where $I(\Phi_{\mathrm{ext}})$ is the current through the SQUID as a function of the applied magnetic flux. Notice its similar expression to the current-phase relation Eq. (2.42) for a single Josephson junction. Therefore, the SQUID can be regarded as a single Josephson junction with a tunable critical current $I_c(\Phi_{\mathrm{ext}}) = 2I_0 \left|\cos\left(\frac{\pi\Phi_{\mathrm{ext}}}{\Phi_0}\right)\right|$. This relationship is plotted in Fig. 2-8(c). In the limit where the loop geometric inductance L_g is much smaller than the individual Josephson inductance L_j, the presence of a magnetic flux inside the SQUID loop induces a circulating current that reduces the effective critical current of the SQUID. The effective inductance of the SQUID becomes

$$L_{\mathrm{SQUID}} = \frac{\Phi_0}{4\pi I_0 \cos\left(\frac{\pi\Phi_{\mathrm{ext}}}{\Phi_0}\right) \cos\phi_+}. \tag{2.49}$$

The inductance can be modulated by varying the externally applied magnetic flux Φ_{ext} or by running an oscillating current through the SQUID to cause ϕ_+ to change. These two cosine factors can be used in flux pumping or current-pumping schemes [30] when operating SQUID-based Josephson parametric amplifiers. The flux-tunability of the SQUID is also exploited to construct frequency-tunable transmon qubits in the noise characterization protocol in Chapter 4.

So far, we have introduced the fundamental concepts behind squeezing, wave-mixing processes, and Josephson junctions. In Chapter 5, we will piece together these elements and discuss using Josephson nonlinearity to generate parametric amplification and produce squeezed states.

Chapter 3

Qubits and Quantum Control

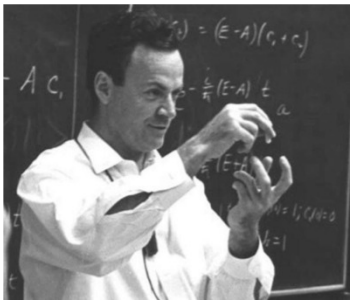

"Nature isn't classical, dammit, and if you want to make a simulation of nature, you'd better make it quantum mechanical..."

Richard Feynman

3.1 Introduction

The idea of quantum computing was broadly conceived in the 1980s, primarily by Richard Feynman, a well-known Nobel physicist. The obstacle he faced at the time was to simulate quantum systems that are very challenging to simulate via classical means with binary bits such as 0 and 1 — the number of classical bits needed grows exponentially with the size of the quantum system. Feynman realized that to simulate nature, we need to use something quantum mechanical. The fundamental building block in this construct is a qubit, short for a quantum bit. Unlike a classical bit, which takes on binary values of 0 or 1, a qubit is a quantum state $|\psi\rangle$ in a superposition of both the 0-state $|0\rangle$ and the 1-state $|1\rangle$, expressed as $|\psi\rangle = a|0\rangle + b|1\rangle$ or represented by the column vector $\left[\begin{smallmatrix} a \\ b \end{smallmatrix}\right]$. Here a and b are quantum amplitudes related to the probability of measuring the qubit in either state.

Coupling two qubits together allows us to form states such as

$$|\psi\rangle_{mn} = \frac{1}{2}\left(|0\rangle_m|0\rangle_n + |1\rangle_m|1\rangle_n\right), \tag{3.1}$$

where subscript m and n denote two different single qubits. $|\psi\rangle_{mn}$ cannot be expressed by the product states of individual qubits. In fact, such state is called an entangled state, which we have also discussed earlier in the context of photons in Chapter 2. A fully-coupled quantum computer could understand 2^N computations, where N is the number of qubits used. This leads to the expansion of information space exponentially — with only $N = 300$ qubits, the total number of information bits exceeds the number of particles in the universe. The goal of quantum computing is to do computations faster than could be done classically. The power of quantum computers is unparalleled if they can be realized. Some of the

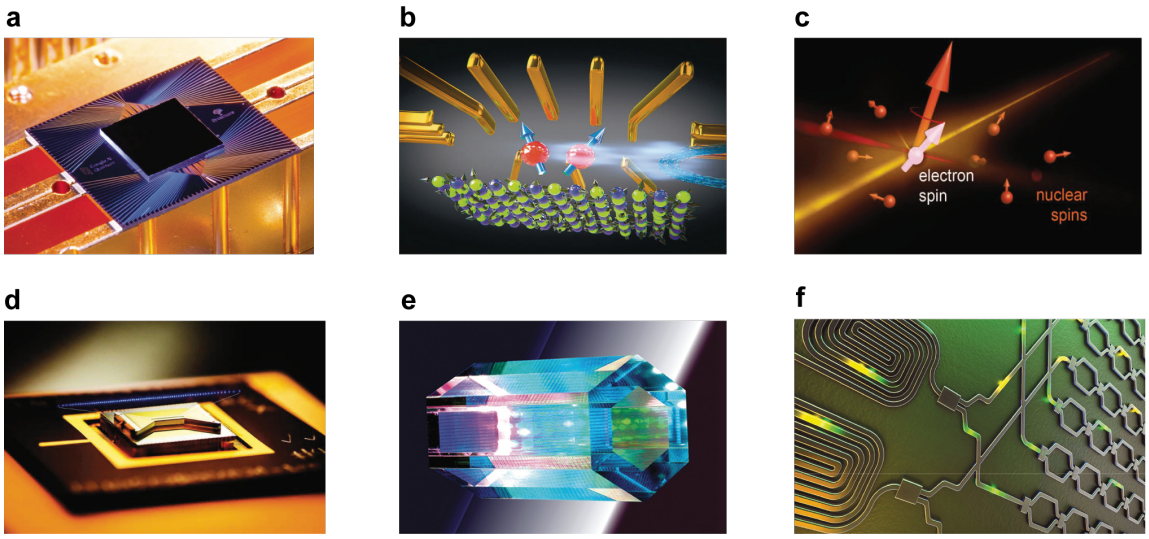

Figure 3-1. | **Exemplary qubit platforms. a.** Superconducting circuits [3]. **b.** Quantum dots [115]. **c.** Electron/Nucleus spins [98]. **d.** Trapped ions [27]. **e.** Neutral atoms [118]. **f.** Photonic modes [88].

prominent applications are quantum simulation, optimization, and cryptography. For example, 1.2% of the world's total energy output annually is used to produce fertilizer [119], and this relies on a process developed in the early 1900s that is extremely energy intensive. However, we know that a tiny anaerobic bacteria in the roots of plants performs this same process every day at low energy cost using a specific molecule—nitrogenase. This molecule is beyond the abilities of our largest supercomputers to analyze but would be

within reach of a moderate-scale quantum computer. Efficient carbon capture (to combat global warming) is in the same class of problem. The search for high-temperature superconductors is another example.

To date, there are a variety of qubit modalities that large organizations and research institutes pursue. As shown in Fig. 3-1, a few exemplary qubit platforms are commonly explored. At the present moment, the field of quantum computing is still in its infancy. Compared to the early work in the 1930s with classical computing architecture, researchers are determining the most effective candidate for qubit architecture. The field is still looking for an equivalent to transistors in a quantum computer. Nevertheless, what is clear is that because the quantum state is fragile, most of these qubits require a cryogenic or UHV system to help reduce noise, which we will discuss later.

3.2 Superconducting Qubits

To approximate an artificial atom, we need a qubit 1) with uniquely addressable energy levels and 2) that is dissipation-less. The former is to encode the logical information (0 or 1) into the physical states and to address them with discrete energy pulses to induce transitions. The latter is to preserve the quantum information long enough to carry out computational tasks. In superconducting circuits, we can construct a quantized system using electrical components like capacitors and nonlinear inductors that typically utilize Josephson junctions. The qubit will be mainly in its ground state when it is situated at a physical temperature such that $k_B T \ll \hbar\omega$, where ω is at the qubit frequency. One can control it using an external photon source that drives the transitions between different energy levels. Over the years, a variety of superconducting qubits have been developed, including but not limited to the Copper-pair box [13], the persistent-current flux qubit [80, 73], the C-shunt flux qubit [123, 124], and the transmon [55]. We focus on the transmon for the rest of the thesis.

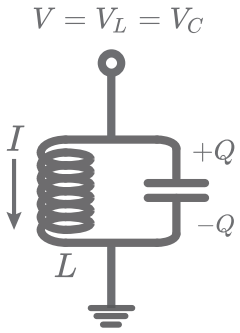

Figure 3-2. | **An LC oscillator with its quantities and coordinates.** Q represents the charge on the capacitor, L is the inductance in the oscillator with the current I traversing through it.

3.2.1 Quantization of an LC Circuit

An LC oscillator in the ground state (cooled down to a very low temperature) and operated in the lossless regime (no energy dissipation) becomes an ideal quantum system. In the previous chapter, we have seen the LC oscillator and its circuit schematic in the context of Josephson parametric amplifiers. As shown in Fig. 3-2, the classical electromagnetic equation conventionally describes an LC oscillator with voltage and current as the generalized coordinates. In contrast, it is more convenient to adopt the charge on the capacitor Q and the flux through the inductor as the coordinates in a quantum treatment of the oscillator. The reason is that the number of charge carriers on a metal island or the quanta of superconducting flux threading through a loop turn out to be good quantum numbers [62]. The total energy of an oscillator can be expressed in a standard way as

$$E = \frac{1}{2}CV^2 + \frac{1}{2}LI^2. \tag{3.2}$$

By converting to flux and charge with the relations $\Phi = LI$ and $Q = VC$, the classical Hamiltonian of the LC oscillator can be written as

$$H = \frac{\Phi^2}{2L} + \frac{Q^2}{2C}. \tag{3.3}$$

Expressing Hamilton's equations of motion, we obtain

$$\frac{\partial H}{\partial \Phi} = \frac{\Phi}{L} = -\dot{Q} \tag{3.4}$$

$$\frac{\partial H}{\partial Q} = \frac{Q}{C} = L\dot{I} = \dot{\Phi}, \tag{3.5}$$

from which we can right away identify Φ as a generalized position and Q as a generalized momentum, analogous to the classical equation of motion for a particle which has position and momentum as the generalized coordinates. Converting them to quantum operators $\hat{\Phi}$ and $\hat{Q}$, we write their commutation relation as

$$[\hat{\Phi}, \hat{Q}] = i\hbar \tag{3.6}$$

in analogy to the commutation for a particle which has $[\hat{X}, \hat{P}] = i\hbar$. Therefore, like the quantum harmonic oscillator, we introduce the raising and lowering operators defined in terms of $\hat{\Phi}$ and $\hat{Q}$ as

$$\hat{a}^\dagger = \frac{1}{\sqrt{2\hbar Z}} \left(\hat{\Phi} - iZ\hat{Q} \right), \tag{3.7}$$

$$\hat{a} = \frac{1}{\sqrt{2\hbar Z}} \left(\hat{\Phi} + iZ\hat{Q} \right), \tag{3.8}$$

where $Z = \sqrt{L/C}$ is the definition of the oscillator impedance. The quantum LC circuit follows the dynamics of a quantum harmonic oscillator with raising and lowering operators $\hat{a}^\dagger$ and $\hat{a}$ and a Hamiltonian $\hat{H} = \hbar\omega(\hat{a}^\dagger\hat{a} + 1/2)$. Here we have the characteristic frequency $\omega = 1/\sqrt{LC}$, and the expected energy of the LC circuit corresponds to the number of photons at ω multiplied by the energy per photon, in addition to the zero-point energy $\hbar\omega/2$.[1] Unfortunately, using a harmonic oscillator system as our qubit would be challenging. This is because all the energy levels would be evenly spaced, so any radiation that drives the transition within our quantum mechanical subspace — the ground and first excited states — would excite the qubit to other levels as shown in Fig. 3-3(a). To store quantum information, we need a quantum mechanical system with uneven energy spacing — such as an

[1] In reality, the physical model involves more degrees of frequency and experiences different sources of dissipation. A more detailed discussion can be found in references [56].

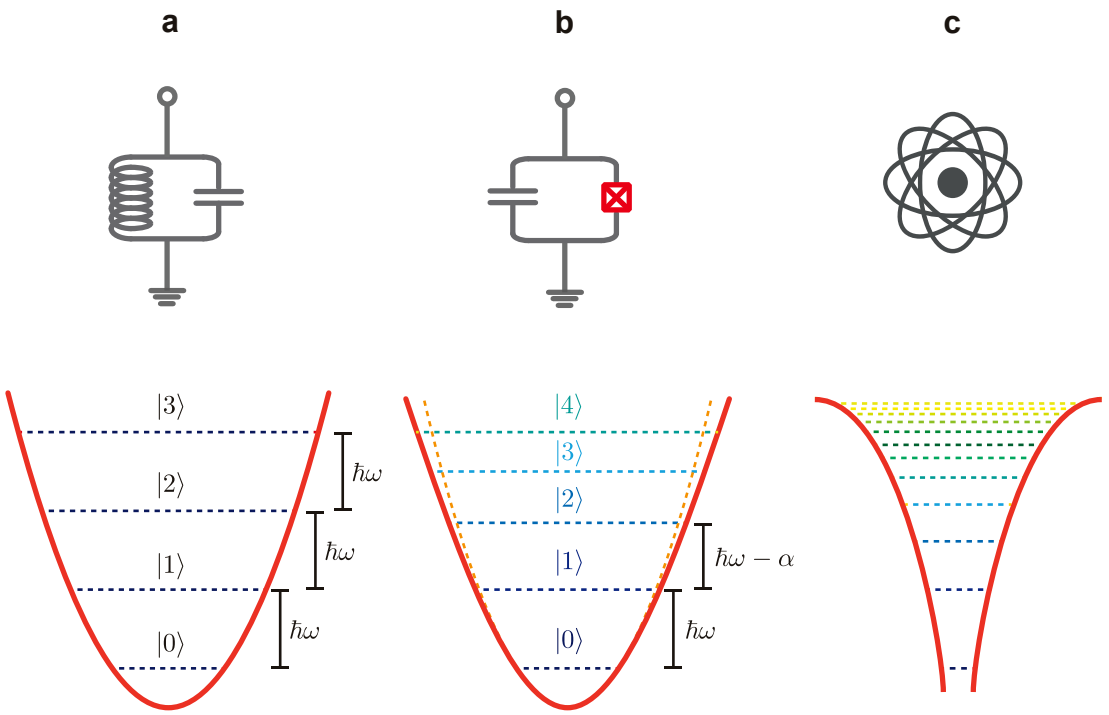

Figure 3-3. | **Energy levels of harmonic and anharmonic systems. a.** Harmonic oscillator potential with equal energy level spacing of $\hbar\omega$. **b.** Harmonic potential (dashed orange line) with a softening correction (solid red line), showing reduced energy level spacing by the anharmonicity parameter α as the energy level increases. **c.** A rough illustration of the potential of a highly anharmonic system such as a physical atom. In general, the anharmonicity in an atomic system is quite significant as the potential is far distinct from that of a harmonic oscillator.

anharmonic oscillator (Fig. 3-3(b)). As introduced in Chapter 2, a Josephson junction is a nonlinear inductor with its junction energy expressed as

$$U = E_J(1 - \cos\phi), \tag{3.9}$$

where $E_J = \Phi_0 I_0/2\pi = \hbar I_0/2e$ is defined as the characteristic Josephson energy scale, and ϕ is the gauge-invariant phase across the Josephson junction as discussed in Eq. (2.41). The junction potential energy is a cosine function with a characteristic scale determined by the junction critical current. ϕ is related to the magnetic flux variable Φ as $\phi = 2\pi\Phi/\Phi_0$ given by Eq. (2.43). The nonlinear Hamiltonian Eq. (3.3) can be rewritten as

$$H = \frac{\hat{Q}^2}{2C} + E_J\left[1 - \cos\left(\frac{2\pi\hat{\Phi}}{\Phi_o}\right)\right]. \tag{3.10}$$

Therefore, a Josephson junction embedded inside the LC oscillator is capable of creating an anharmonic potential for a qubit. This means the energy spectrum of potential is no longer degenerate. Therefore, we are able to create an addressable qubit by identifying the two-level quantum subspace labeled as $|0\rangle$ and $|1\rangle$ as shown in Fig. 3-3(b).

3.2.2 Cavity QED

Having constructed a qubit by modeling the two lowest levels of the supercondcuting circuit in the above equation, we can now couple these qubits to a cavity system, a paradigm of cavity quantum electrodynamics (cavity QED). Cavity QED has been discussed extensively in the literature, and we follow Ref. [104] for this part of the derivation. The Hamiltonian $H = H_q + H_{\text{res}} + H_{\text{int}}$ for a transmon typically involves three terms: a

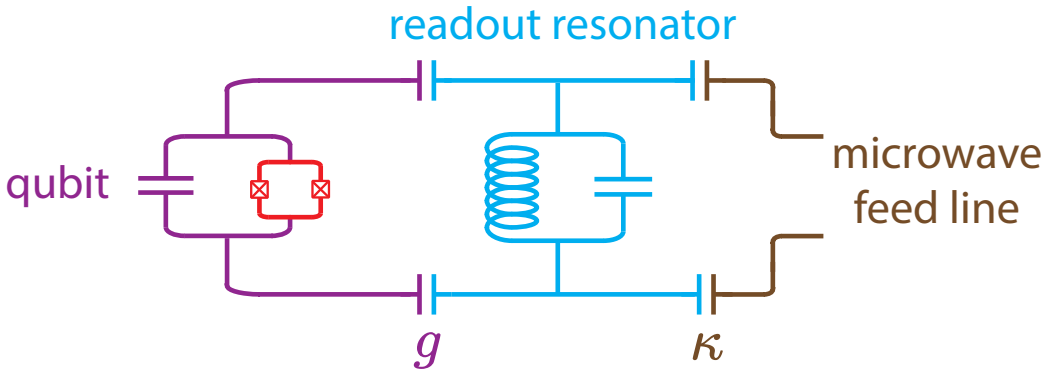

Figure 3-4. | **Schematic of a cavity QED system.** g is the coupling strength between the qubit and the readout resonator; κ is the coupling between the readout resonator and the microwave feed line.

qubit term, a resonator term, and an interaction term between the two, and can be expressed as

$$H = \frac{\hbar\omega_q}{2}\hat{\sigma}_z + \hbar\omega_r\left(\hat{a}^\dagger\hat{a} + \frac{1}{2}\right) + \hbar g\left(\hat{a} + \hat{a}^\dagger\right)\left(\hat{\sigma}_+ + \hat{\sigma}_-\right), \tag{3.11}$$

where ω_q and ω_r denote the qubit and resonator frequencies, and σ_+ and σ_- are the qubit raising and lowering operators, respectively given by $\sigma_+ = |1\rangle\langle 0|$ and $\sigma_- = |0\rangle\langle 1|$. Note that we treat the resonator as a harmonic oscillator for simplicity. In this system, we assume energy conservation, considering the qubit and resonator energies are large compared to the available thermal energy from the environment. We can make the rotating wave ap-

proximation of the Hamiltonian and discard terms that do not conserve energy, such as the term $\hat{a}^\dagger\sigma_+$ because it adds energy to both the qubit and resonator. After the approximation, Eq. (3.11) becomes

$$H = \frac{\hbar\omega_q}{2}\hat{\sigma}_z + \hbar\omega_r\left(\hat{a}^\dagger\hat{a} + \frac{1}{2}\right) + \hbar g\left(\hat{a}^\dagger\hat{\sigma}_- + \hat{a}\hat{\sigma}_+\right). \tag{3.12}$$

Eq. (3.12) is known as the Jaynes-Cummings Hamiltonian, and the interaction term can be interpreted as the excitation exchange between the atom and the resonator. The simplicity of this Hamiltonian makes cavity QED systems a popular choice in implementing coherent control of the quantum degrees of freedom of a qubit.

Dispersive Regime and QND Measurement

Now let's take a step further and consider the coupling in the dispersive limit, i.e. $g \ll \Delta \equiv \omega_q - \omega_{\rm res}$. In this limit, no energy is exchanged between the qubit and the resonator, and the eigenstates of the cQED system can be well approximated by the product states of the qubit and resonator. By performing a perturbation expansion in the small parameter g/Δ, we approximate the Eq. (3.12) in the dispersive limit as

$$H_{\rm disp} = \frac{\hbar}{2}\left(\omega_q + \frac{g^2}{\Delta}\right)\hat{\sigma}_z + \hbar\omega_r\left(\hat{a}^\dagger\hat{a} + \frac{1}{2}\right) + \frac{\hbar g^2}{\Delta}\hat{a}^\dagger\hat{a}\hat{\sigma}_z. \tag{3.13}$$

The additional term g^2/Δ represents the Lamb shift caused by the qubit and the zero-point energy of the resonator field. The last term in Eq. (3.13) describes the interaction between the qubit state and the resonator field. To see the effect of the qubit on the resonator, we rearrange the terms and express the Hamiltonian as

$$H_{\rm disp} = \frac{\hbar}{2}\omega_q\hat{\sigma}_z + \hbar\left(\omega_r + \frac{g^2}{\Delta}\hat{\sigma}_z\right)\left(\hat{a}^\dagger\hat{a} + \frac{1}{2}\right). \tag{3.14}$$

Here we see the resonator frequency depends on the qubit state $\hat{\sigma}_z$, and thereby probing the resonator frequency gives us information on the qubit state. This shift between the two qubit-state-dependent resonator frequencies, $\omega_{\rm r}(|0\rangle)$ and $\omega_{\rm r}(|1\rangle)$ corresponds to the so-called dispersive shift, denoted by 2χ, where $\chi = g^2/\Delta$. As we see in Fig. 3-5, one can

use the dispersive shift to determine the qubit states. In either reflection or transmission measurement of the resonator phase, it changes rapidly as one goes through the resonance. The resonator linewidth is denoted by κ representing the coupling between the resonator to the microwave feedline as shown in Fig. 3-4. By probing the resonator at ω_{d} — halfway between $\omega_{\mathrm{r}}(|0\rangle)$ and $\omega_{\mathrm{r}}(|1\rangle)$ indicated by the brown dashed line, one can achieve the maximum contrast between the two states with $2\chi = \kappa$ [41]. Similarly, the shift can also be observed in the transmission profile $|S_{21}|$ of the resonances, allowing us to distinguish the two qubit states.

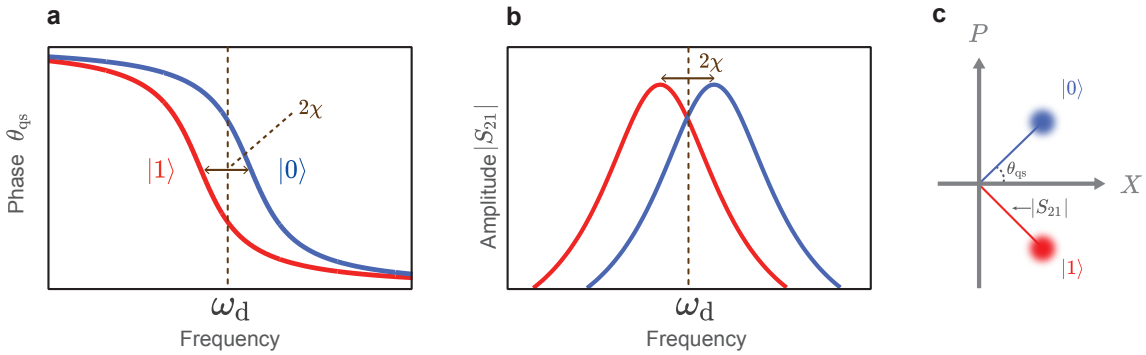

Figure 3-5. | **cQED readout. a.** Qubit-state-dependent phase response θ_{qs} of the resonator, when the qubit is in its ground state $|0\rangle$ (blue) and excited state $|1\rangle$ (red). **b.** The corresponding transmission amplitude $|S_{21}|$ **c.** The complex plane representation of the qubit states. One can obtain the maximum contrast between the two states by probing/driving the resonator at the middle of the two resonances at ω_{d} (dashed line in (a) and (b)).

Decoherence Channels

The qubit state can be thus mapped out at any given time by probing the resonator, allowing us to examine the qubit coherence. It is characterized with metrics such as longitudinal relaxation time T_1 associated with its rate $\Gamma_1 \equiv 1/T_1$ and transverse relaxation time T_2 with its corresponding dephasing rate $\Gamma_2 \equiv 1/T_2 = \Gamma_1/2 + \Gamma_\varphi$, where Γ_φ represents the pure dephasing rate. The types of relaxation refer to the dynamics of the qubit state that can be represented on a Bloch sphere — a description of a quantum two-level system [56]. The measurements for these quantities are well studied methodologically from nuclear magnetic resonance and atomic physics and require many repetitions of a given experiment, referred to as ensemble measurements.

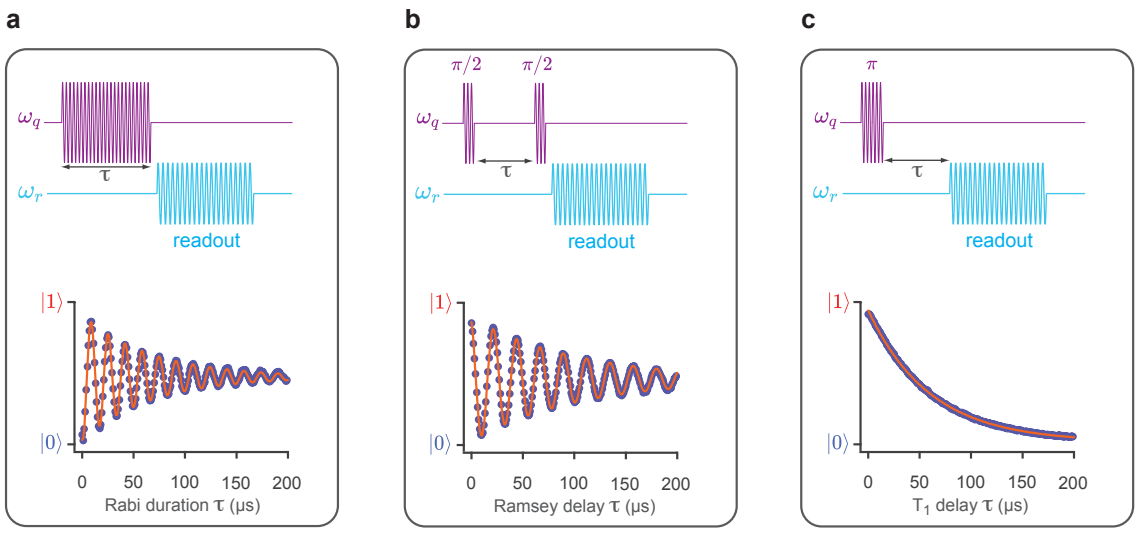

Figure 3-6. | Qubit coherence measurement protocols for Rabi, Ramsey and T_1. Qubit coherence measurement protocols for Rabi, Ramsey and T_1. The top panels show pulse sequences for the Rabi, Ramsey, and T_1 experiments. The purple trace indicates pulses at the qubit frequency ω_q, while the blue trace indicates pulses at the readout frequency ω_r. The bottom panels show typical experimental Rabi, Ramsey, and T_1 traces. More specifically, the red lines in (a) and (b) correspond to a sine wave with an exponentially decaying envelope and a fit to a decay exponential in (c).

As displayed in Fig. 3-6(a), we typically commence with measuring Rabi oscillations of the qubit. This is achieved by sending a variable-width pulse at the qubit frequency ω_q and measuring the qubit's state after the pulse. The experiment is repeated several times for different pulse durations τ and averaged each time for a given τ. The result is a decaying sinusoidal Rabi oscillation, as shown in the picture. The Rabi frequency Ω_{Rabi} depends on the amplitude of the Rabi drive and also on the detuning of the Rabi drive from the qubit frequency $\Delta\omega$ as $\Omega_{\text{Rabi}} = \sqrt{\Omega^2 + (\Delta\omega)^2}$, where Ω is the Rabi frequency at zero detuning. Rabi measurement gives us several valuable pieces of information. First, it indicates the qubit frequency location by fixing the Rabi drive amplitude and varying the drive frequency until the minimum Rabi frequency is observed. Secondly, Rabi oscillations give us a calibration for the Π pulse — a pulse with duration and amplitude necessary to a transition between qubit states $|0\rangle$ and $|1\rangle$. The name corresponds to rotating the qubit state vector on the Bloch sphere by π radian. Moreover, the decay of Rabi oscillations is related to qubit dephasing and, more specifically, to noise-induced variations in the Rabi frequency. Considering Rabi oscillations as an ensemble measurement, the noise leads to

different phases at longer pulse duration for individual measurements. Therefore, one can use the Rabi decay as a probe of the qubit noise. The envelope of the Rabi oscillations alters from exponential to Gaussian, depending on the noise spectrum [50].

We measure the Ramsey fringes to obtain information about the qubit frequency and its dephasing time T_2. As shown in Fig. 3-6(b), the protocol involves sending two $\pi/2$ pulses (thanks to the Rabi measurement) to the qubit with a varying time delay τ between the pulses and then measuring the state of the qubit. Similarly, we repeat this measurement for each time delay and extract the average measured qubit state as a function of time delay τ. Oscillations will occur — in this case, called Ramsey fringes — if the qubit drive is detuned from the unperturbed qubit frequency. The bottom of Fig. 3-6(b) shows a typical Ramsey fringe, whose decay envelope can be fitted with an exponential $e^{-\Gamma_2 t}$, with a time constant given by $T_2 = 1/\Gamma_2$. Since the Ramsey frequency is equal to the detuning between the qubit drive and the true qubit frequency, a Ramsey measurement is a precise way to extract the qubit frequency and even beyond to monitor low-frequency fluctuations (e.g., caused by flux noise) by continuously measuring Ramsey fringes to extract the qubit frequency over time. The Ramsey frequency has a linear dependence on drive detuning and, thereby, gives a more sensitive way to extract the qubit frequency in contrast to Rabi oscillations, whose frequency has a quadratic detuning dependence.

After calibrating ω_q and the π pulse with Rabi and Ramsey measurements, we can characterize the qubit's longitudinal relaxation time T_1. We prepare the qubit in the excited state $|1\rangle$ with a π pulse, wait for a variable amount of time τ, and then measure the qubit state. Again, we perform an ensemble measurement of the experiment as a function of τ. As a result, we can observe ensemble decay of the qubit state as shown in Fig. 3-6(c) and extract the time constant T_1 by fitting the decay with an exponential function $e^{-\Gamma_1 t}$.

The coherence measurements essentially inform us of the time for the qubit to transform into a classical bit, serving as a quality check of the quantum mechanical system. On the other hand, they provide us with information regarding the coupling of the qubit to its environment and the amount of environmental noise the qubit experiences. Using such information can turn the qubit into a sensor to characterize, for example, the noise in the system. We will discuss this more in the upcoming chapter.

3.2.3 Waveguide Quantum Electrodynamics (wQED)

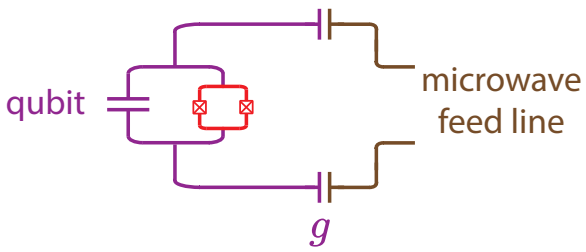

Figure 3-7. | **Waveguide coupled to a qubit.** The qubit has a DC SQUID, so its frequency can be tuned via an external magnetic flux bias. The qubit also couples to a $50\,\Omega$ microwave feedline.

Unlike cavity QED, waveguide quantum electrodynamics (wQED) deals with a system where the atoms or qubits couple to a waveguide containing a continuum of propagating photonic modes that emulates one-dimensional free space. In these systems, atoms can directly absorb or release their excitations in the waveguide as photons, as shown in Fig. 3-8(b). Because wQED focuses on emissive phenomena, its architecture is ideal for observing interference phenomena that involve atom-photon interaction, in addition to quantum communication applications [54]. Our discussion of this topic pivots on the usage of wQED as a noise calibration source, which we will discuss further in the next chapter.

In systems with a qubit coupled to a waveguide (Fig. 3-8(b)), the qubit will reflect weak incident coherent tones ($\bar{n} = |\alpha|^2 \ll 1$, where $|\alpha|$ is the amplitude of the coherent state) in the transmission line [54]. In the limit $\bar{n} \ll 1$, the probability of two or more photons is negligible. The qubit absorbs a single photon from the coherent drive and emits the photon isotropically in the forward and reverse directions with a π phase shift. As a result, the forward direction destructively interferes with the transmitted driving field, while the reverse direction constructively interferes with the reflected field. Therefore, under ideal conditions, all photons are reflected and no photons are transmitted. This perfect destructive interference is modified by the presence of decoherence, which changes the transmission coefficient. Each qubit can be treated independently as long as they are far-detuned from each other, when $|\omega_i - \omega_j| \gg \Gamma_{i,i}, \Gamma_{j,j}$, where ω_i is the qubit i's frequency, and $\Gamma_{i,i}$ is its self-decoherence rate due to the transmission line. A vector-network analyzer (VNA) — an instrument that measures the scattering parameter of electrical networks — can be used to measure the transmission of coherent signals $\langle V_{\text{out}} \rangle / \langle V_{\text{in}} \rangle$. The transmission coefficient

is [72, 54]

$$t = 1 - \frac{\xi_w \Gamma_1}{2\Gamma_2} \frac{1 - \frac{i\Delta}{\Gamma_2}}{1 + \left(\frac{\Delta}{\Gamma_2}\right)^2 + \frac{\Omega^2}{\Gamma_1 \Gamma_2}}. \tag{3.15}$$

Using this equation, we can calibrate the absolute power at the device with independently

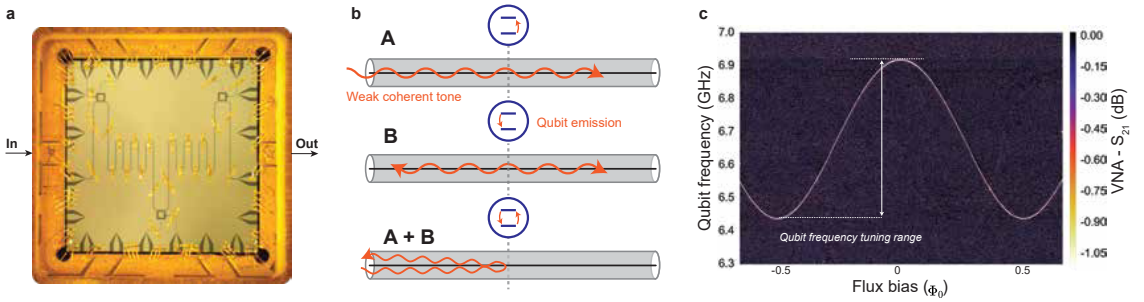

Figure 3-8. | **Waveguide coupled to a qubit as a noise power reference. a.** A microscopic image of the wQED device, where three qubits coupled to a meandering transmission line are visible. **b.** A schematic illustrating the interference effect between a qubit and a weak coherent tone. Process A: in the limit $\bar{n} < 1$, the qubit absorbs a photon from the coherent driving field. Process B: the qubit emits the photon isotropically in the forward and reverse directions with a π phase shift. As a result (A+B), the emission from the qubit causes a destructive interference with the forward propagating field and results in the reflection of the signal [54]. **c.** Qubit spectrum measured by scanning DC magnetic flux bias and measuring its transmission profile at large drive. The noise temperature characterization is performed at various qubit frequencies between its two sweet spots (marked between the white dashed lines).

measured parameters: Γ_1 is the spontaneous emission rate of the qubit into the transmission line, $\Gamma_2 = \Gamma_1/2 + \Gamma_\phi$ is the transverse decoherence of the qubit, and Γ_ϕ is the qubit dephasing rate; Ω is the drive amplitude in the unit of Hz at the input of the qubit. These are similar to the quantities in cavity QED. Moreover, Δ is the qubit-drive detuning; ξ_w is the ratio of emission to the waveguide compared to all loss channels, and within the SNR of the data, it is assumed to be unity since the qubit is considered to be strongly coupled to the waveguide so that the decay into the waveguide dominates all the other decay channels. Finally, the drive power at the qubit is given by [72]

$$P = \pi \hbar \omega_i \Omega^2 / 2\Gamma_1, \tag{3.16}$$

which can be used to plot the transmission coefficient versus power by substituting Ω in the equation. The power dependence of the transmission calibrates the absolute power at the qubit, which enables us to further calibrate the noise power.

3.3 Qubit control

Quantum gates are essential operations to manipulate qubits' states and implement quantum algorithms. π and $\pi/2$ pulses introduced in the earlier section are examples of single-qubit quantum gates. Like classical logic gates, the quantum gates can change qubit states conditionally.

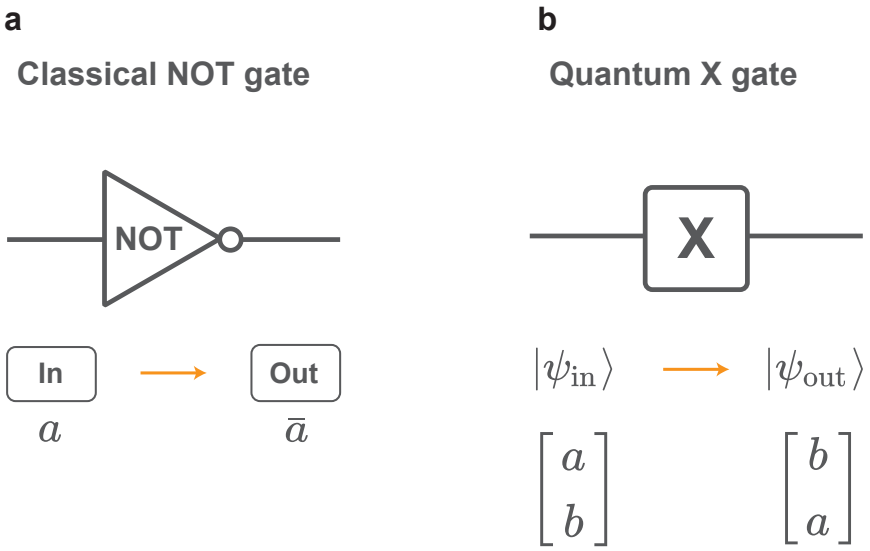

Figure 3-9. | Comparison between the classical inverter (NOT) gate and the quantum bit flip (X) gate. a. The classical NOT gate inverts the input state of a classical bit. **b.** The quantum X gate flips the amplitudes of the two components of a quantum bit.

3.3.1 Single-Qubit Gates

For example, shown in Fig.3-9 is a comparison of the classical inverter (*NOT*) gate and quantum bit flip (*X*) gate. The classical *NOT* gate inverts the state of a classical bit. Analogously, the quantum *X* gate flips the amplitudes of the two components of a quantum bit from $|\psi_{\text{in}}\rangle = \left[\begin{smallmatrix} a \\ b \end{smallmatrix}\right]$ to $|\psi\rangle_{\text{out}} = \left[\begin{smallmatrix} b \\ a \end{smallmatrix}\right]$. Unlike the classic logic gates, quantum gates can alter the phase of qubit states. For instance, a *Z* gate — a single-qubit phase shift gate — rotates a qubit state about the z-axis by $180°$. During the operation, the qubit acquires a global phase $e^{i\pi}$, but there is no change to the probability of measuring a $|0\rangle$ or a $|1\rangle$. The *Z* gate

circuit representation is displayed in Fig. 3-10, and its matrix form is:

$$\mathrm{Z} = \begin{pmatrix} 1 & 0 \\ 0 & e^{i\pi} \end{pmatrix} \tag{3.17}$$

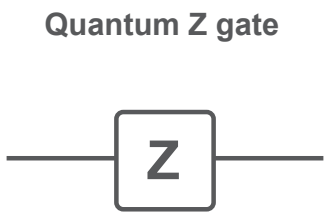

Figure 3-10. | **Quantum Z gate.** The quantum Z gate rotates the qubit state by π radian about z-axis.

3.3.2 Two-Qubit Gates

Going beyond single-qubit operation, the controlled phase (*cPhase*) gate is a two-qubit entangling operation that can take product states of individual qubit states and outputs entangled states. An exemplary two-qubit product state can be expressed as $(a_1|0\rangle + b_1|1\rangle) \otimes (a_2|0\rangle + b_2|1\rangle) = a_1a_2|00\rangle + a_1b_2|01\rangle + b_1a_1|10\rangle + b_1b_2|11\rangle$. Depending on the control state, the gate induces a phase ϕ on the state of the target qubit, such as $|1\rangle \rightarrow e^{i\phi}|1\rangle$. Again, this is a global phase for the quantum state and does not change the probability of measuring $|1\rangle$.

$$\mathrm{CPHASE}(\phi) = \begin{pmatrix} 1 & 0 & 0 & 0 \\ 0 & 1 & 0 & 0 \\ 0 & 0 & 1 & 0 \\ 0 & 0 & 0 & e^{i\phi} \end{pmatrix} \tag{3.18}$$

Equation 3.18 represents the two-qubit *cPhase* gate with respect to its computational basis, and only shifts the phase of the $|11\rangle$ state, i.e., the coefficient $b_1b_2 \rightarrow b_1b_2e^{i\phi}$ while all the other coefficients remain the same. In the special case that $\phi = \pi$, we have the so-called

CZ gate that with the matrix form of

$$\mathrm{CZ} = \begin{pmatrix} 1 & 0 & 0 & 0 \\ 0 & 1 & 0 & 0 \\ 0 & 0 & 1 & 0 \\ 0 & 0 & 0 & -1 \end{pmatrix}. \tag{3.19}$$

Its quantum circuit representation is shown in Fig. 3-11, where the CZ gate is achieved by applying a Z-gate to the target qubit if the control qubit is in state $|1\rangle$

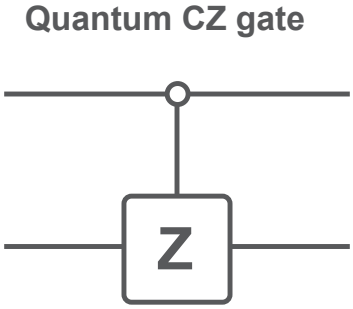

Figure 3-11. | **Quantum CZ gate.** The CZ gate in this case applies a Z-gate operation to the target qubit if the control qubit is in state $|1\rangle$.

A quick remark: there are many other types of two-qubit gates and even multiqubit gates. In this thesis, we will focus on the two-qubit cPhase gate mediated through a common resonator bus.

To realize the *cPhase* gate, we need a longitudinal interaction, which is purely diagonal (e.g., magnetic dipole coupling). A longitudinal interaction can affect the energy level splitting and generate entangled states without energy exchange. In the next section, we will discuss how to engineer effective longitudinal coupling using the native transverse interaction between transmons.

3.3.3 Resonator-Induced Phase Gate

A *cPhase* gate can be achieved with two qubits coupled to a resonator bus with an effective ZZ-type longitudinal interaction. Such a gate is known as the Resonator-Induced Phase gate (RIP gate).

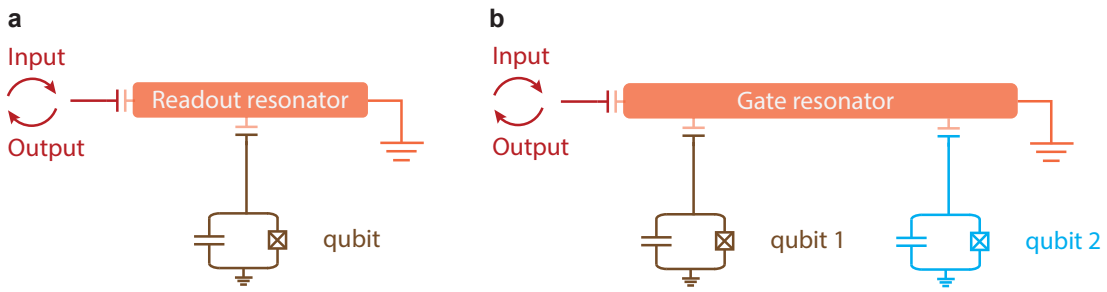

Figure 3-12. | **RIP gate circuit schematic. a.** A typical circuit representation of a qubit coupled to a quarter-wave resonator for dispersive readout measured in a reflection setup. **b.** Schematic of the RIP gate with two fixed-frequency qubits coupled to a common quarter-wave resonator bus in a reflection setup.

This gate was studied recently by IBM [81], and we now summarize their discussion and experiments before suggesting improvements to the RIP gate in the next section. By adiabatically applying and removing an off-resonant pulse to the resonator, the resonator state evolves from its initial vacuum state by following a qubit-state-dependent closed loop in phase space — this trajectory is sometimes referred to as 'which-path' information. After this joint qubit-resonator evolution, the resonator returns to vacuum state, and the qubits are left unentangled from the resonator but with an acquired a non-trivial phase, which corresponds to the global phase we have seen in equation 3.18. A cartoon illustration is shown in Fig. 3-13.

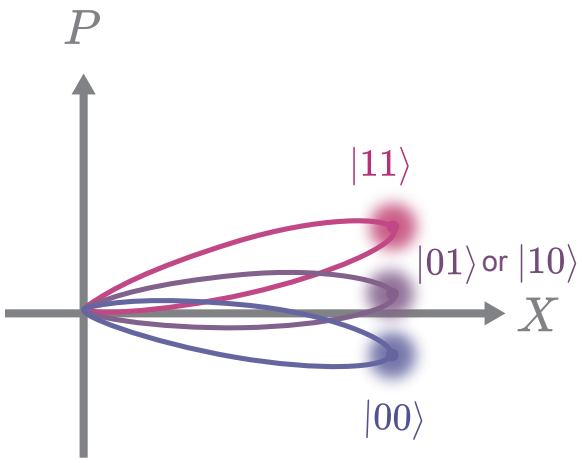

Figure 3-13. | **RIP gate phase evolution.** The illustration depicts qubit-state dependent trajectories with the gate resonator under a coherent drive.

Paik et al. from IBM demonstrated this effect experimentally using a 3D transmon system, where fixed-frequency transmon qubits were dispersively coupled to a resonator bus. There were two sets of 4-qubit devices as shown in Fig. 3-14, which were coupled to a superconducting high-Q aluminum resonator with a decay rate $\kappa/2\pi = 7.7\,\mathrm{kHz}$. Qubits have consistent lifetimes in the tens of microseconds. Paik et al. performed two-qubit randomized benchmarking between pairs of qubits in a four-qubit device with frequency differences spanning 0.38 GHz to 1.8 GHz, all with fidelities in the range 0.96-0.98 and gate times in the range 285 to 760 ns.

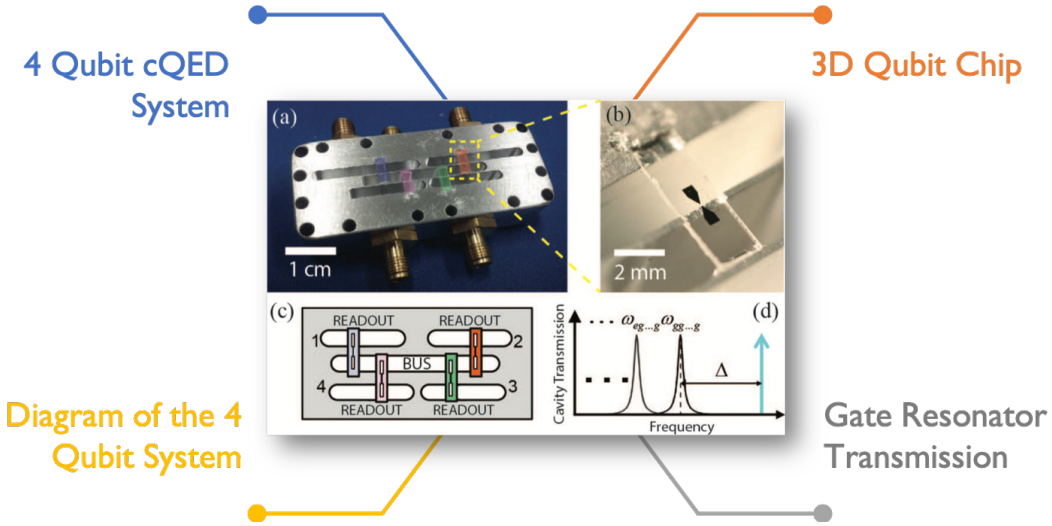

Figure 3-14. | **IBM RIP gate setup.** Figure credit to Ref. [81]. **a.** Photo of IBM's superconducting 4-qubit 3D cQED system with five resonators (four are for individual qubit dispersive readout, and the common one coupling all the qubits is the gate resonator bus. **b.** A close-up picture of a 3D qubit chip. **c.** Diagram of the 4-qubit 3D cQED system with 5 cavities. **d.** Illustration of gate resonator transmission. The microwave drive for the RIP gate (cyan arrow) is blue-detuned by frequency Δ from the dressed cavity resonance $\omega_{gg\ldots g}$.

The four-qubit system can be described by a sum of Duffing oscillator Hamiltonians coupled to the resonator bus, with a microwave drive term for the RIP gate. When the qubit frequencies are well-separated, the qubit-qubit interactions become diagonal in the qubit computational basis, with a static component and dynamical interactions activated by the resonator drive. The qubit interactions can therefore be described in terms of Z operators. Depending on the Pauli weight p on Z interactions (ZZ, ZZZ or ZZZZ), the

phase accumulation rates are different and can be expressed as the following:

$$\dot{\theta}_{Z_iZ_j} = -\frac{|\tilde{\epsilon}_0|^2\chi^2}{8\Delta(\Delta+2\chi)(\Delta+4\chi)}, \tag{3.20}$$

$$\dot{\theta}_{Z_aZ_bZ_c} = -\frac{3|\tilde{\epsilon}_0|^2\chi^3}{16\Delta(\Delta+\chi)(\Delta+3\chi)(\Delta+4\chi)}, \tag{3.21}$$

$$\dot{\theta}_{Z_1Z_2Z_3Z_4} = -\frac{3|\tilde{\epsilon}_0|^2\chi^4}{8\Delta(\Delta+\chi)(\Delta+2\chi)(\Delta+3\chi)(\Delta+4\chi)}, \tag{3.22}$$

where Δ is the detuning of the drive frequency to the dressed bus resonator with all qubits in their ground state. Here we assume each qubit has the same dispersive coupling χ. As one can see, when the RIP gate drive is activated, all Z interactions are turned on at the same time automatically, which is converse to the objective of exerting control over individual qubit-qubit interactions. Fortunately, the phase accumulation rate scales with $(\chi/\Delta)^p$, so the multi-body interaction rate becomes slower as the Pauli weight increases under the condition $\chi/\Delta < 1$. Generally speaking, there are several unique advantages of the RIP gate. The first is its all-to-all connectivity originating from qubits sharing the same resonator bus. It has potential application in fault-tolerant error correction using the gauge color code or digital quantum simulations. Secondly, due to the nature of the geometric phase, the RIP gate is insensitive to phase fluctuations of the drive as long as the area enclosed loop remains invariant. Therefore, the gate itself is largely immune to imperfections and practical limitations within the microwave sources that drive the RIP gate. Thirdly, frequency crowding is less of an issue by accommodating larger differences in qubit frequencies compared to other microwave activated gates such as cross-resonance gate.

There are also noticeable drawbacks to the existing RIP gate scheme. First, the gate time (>200 ns) is slow in comparison with the *cPhase* gate implementation using tunable transmons (<50 ns) [6]. The long gate time is detrimental to the overall gate fidelity as it determines the number of operations within the qubit coherence limit; the fidelity of a single qubit gate would also be worse. One remedy to this is to drive the gate stronger or

decrease the drive-resonator detuning, which is equivalent to increasing $\tilde{\epsilon}_0$ or decreasing Δ in equations Eq. (3.20) to Eq. (3.22). Both can enhance the gate speed, but gate fidelity will suffer from worsening measurement-induced dephasing associated with enhanced photon shot noise in the resonator. It has been proposed to counter this effect by driving the gate resonator with a squeezed coherent state [87], and it is one of the many applications of squeezed light in a qubit system, which we will discuss in the final chapter.

Chapter 4

Experimental Setups and Measurement Protocols

As we discussed in Chapter 5, measuring quantum mechanical signals requires a series of amplification stages, and it is paramount to characterize their noise performance as an integral part of the signal processing. For instance, the measurement efficiency of the output chain needs to be determined accurately to extract squeezing levels at the output of the JTWPA. However, the experiments are primarily conducted at milliKelvin temperatures in a vacuum, presenting a fundamental challenge for direct access to the cryogenic setups. Calibrating at room temperature by passing a signal through the entire setup is insufficient, as the insertion loss for the input and the overall transmission of the output changes dramatically with temperature. Therefore, it requires an in-situ noise power calibration device at the mixing chamber. In this chapter, we will discuss a few commonly used approaches to calibrate the noise such as the AC Stark shift from a cQED qubit [99], the Y-factor method [38], the shot noise from a voltage-biased tunnel junction [106]. In addition, we will explore a fourth method using a wQED device to characterize the system noise temperature [72, 54].

4.1 Cryogenic setup and control instrumentation

Superconducting quantum experiments must operate at milliKelvin temperatures to reduce the thermal photon population at the qubit frequency. The dilution refrigerator is an essential workhorse in conducting experiments on superconducting circuits. The physical temperature of the metal needs to drop below its critical temperature T_c for it to transition into a lossless superconducting state. Heinz London first proposed the concept of a dilution refrigerator in the early 1950s, which was realized experimentally in 1964 at Leiden University. Over more than five decades, state-of-the-art dilution refrigerators have developed into commercially available items, capable of reaching below 10 mK with outstanding reliability. A dilution refrigerator has different temperature stages set by the physical limits of different cooling mechanisms. This marvelous cryogenic technology has enabled many exciting pieces of research, including two Nobel-Prize-winning experiments (the discovery of superfluidity in $^3\mathrm{He}$ in 1971 by Lee, Osheroff, and Richardson, as well as the discovery of fractional quantum hall effect in 1981 by Daniel Tsui, Horst Störmer and Robert Laughlin).

In the lab, a typical dilution refrigerator can reach a temperature of 20 mK or lower, which at a frequency of 8 GHz contributes to an average thermal photon number $\bar{n} < 0.0006$ [122], limited by the input and output lines, assuming they receive proper attenuation and filtering to reduce thermal photons from the high-temperature environment. Generally speaking, a superconducting quantum experiment requires carefully designed input and output control.

There are three common wiring categories inside a dilution refrigerator: DC lines, RF input lines, and RF output lines (some dilution refrigerators may feature optical fibers, etc.). For the input, to prevent extrinsic noise contamination, whether it arises from thermal fluctuations or the control instruments, heavy filtering and attenuation are necessary to remove unwanted noise. Stainless steel cables are typically used as RF input lines to the mixing chamber stage. They provide an electrical connection between different temperature stages with a low thermal conductivity that helps reduce the thermal load on the cooling unit of a dilution refrigerator. In table 4.1, we list the major experimental components

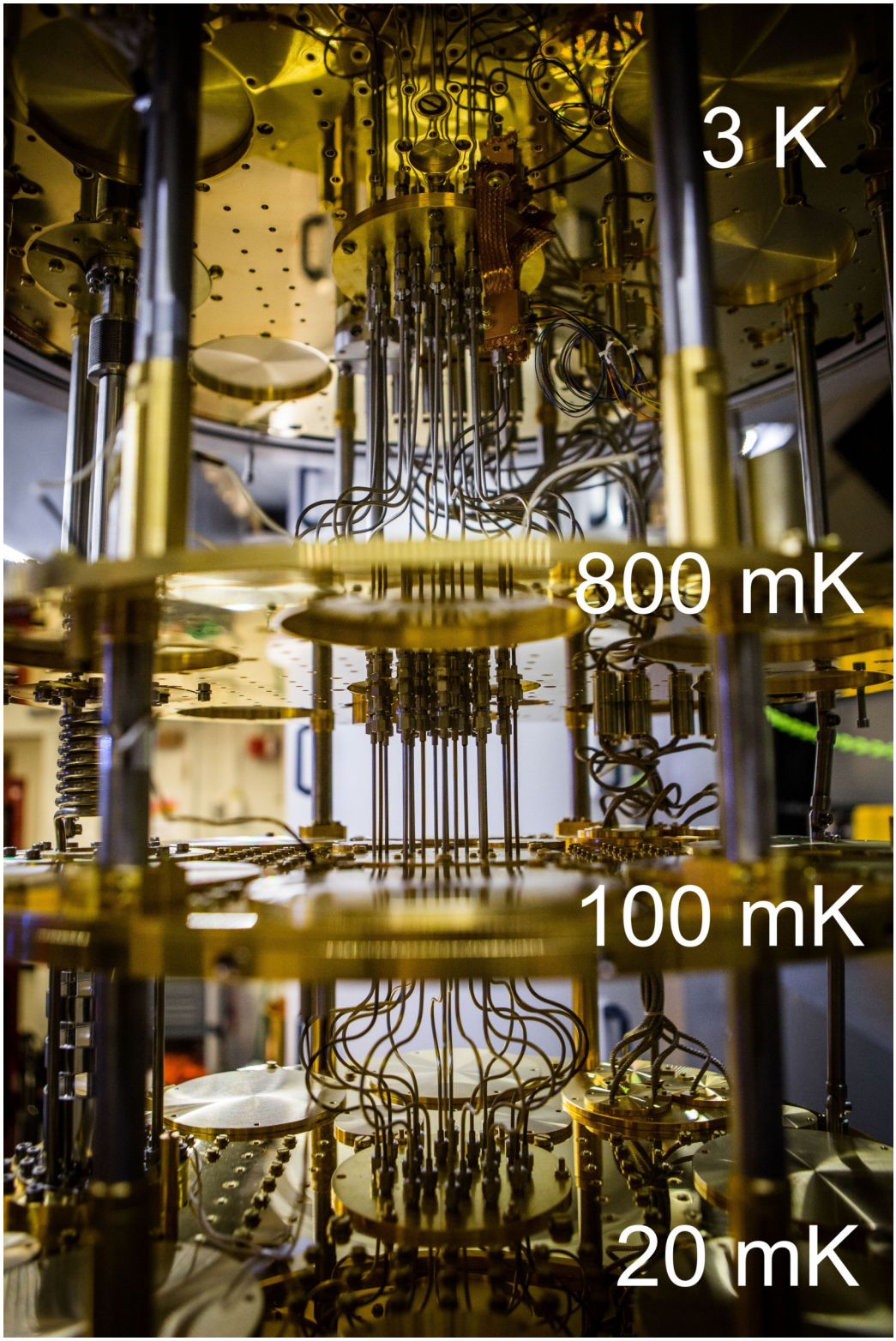

Figure 4-1. | **Dilution refrigerator.** Different temperature stages and cryogenic wirings are visible. Image credit: MIT EQuS Group.

used in the experiment, and Fig. 4-2 shows the overall wiring diagram for the experiments conducted in a Leiden CF450 dilution refrigerator with a base temperature around 30 mK. The pumps and probe signal generated by RF sources (Rhode and Schwarz SGS100A) are combined at room temperature (290 K) and sent via semi-rigid microwave coaxial cable to the squeezer (SQZ), a Josephson traveling-wave parametric amplifier (JTWPA). The line is attenuated by 20 dB at the 3 K stage, 10 dB at the still, and 33 dB at the mixing chamber to ensure proper thermalization of the line and attenuation of thermal photons from higher-temperature stages. In addition, coaxial cables and other components from the input line contribute around 8 dB loss. A Cryoperm-10 shield magnetically shields the samples. We use Radiall single-pole-6-throw (SP6T) microwave switches to transmit the signal from either the squeezer, the shot-noise tunnel junction (SNTJ), or the waveguide QED (wQED) qubit to the measurement chain. The microwave signal at the output of the SP6T switch propagates through two 50 Ohm-terminated circulators, a combination of a 3 GHz high-pass and a 12 GHz low-pass filter, and then into a superconducting NbTi coaxial cable that connects the 30 mK and 3 K stages. The NbTi cable allows high electrical and low thermal conductivity to minimize attenuation and heat transfer between different temperature stages.

Component	Manufacturer	Type
Control Chassis	Keysight	M9019A
AWG	Keysight	M3202A & 33250A
ADC	Keysight	M3102A
RF source	Rohde & Schwarz	SGS100
Refrigerator	Leiden	CF450
DC Bias	Yokogawa	GS 200

Table 4.1. Major experimental equipment used in the experiment.

For the output, the signal strength from a device at the mixing chamber[1] is often too small to be measured directly by a room temperature instrument such as a spectrum analyzer. Hence, the measurement electronics in the dilution refrigerator needs several amplification stages to bring the signal above the instrumental noise floor; it typically requires a

[1]Mixing chamber is the temperature stage inside a dilution fridge that is around 20 mK in the setup of this work. It is where the ^{3}He and ^{4}He mixture undergoes the dilution process.

high electron mobility transistor (HEMT, e.g., Low Noise Factory LNF-LNC4_8C) amplifier at 3 K to give 35-40 dB gain with a noise temperature around 2 K. Room temperature amplifiers (e.g., MITEQ, AMP-5D-00101200-23-10P) then boost the signal by another 35 dB. Finally, low-frequency amplifiers amplify the baseband signals after further signal processing steps (e.g., frequency downconversion, filtering, etc.). In the squeezing experiment, the pump tones are band-pass filtered (and reflected into the 50 Ohm termination of the room-temperature isolators) before the signal enters the IQ mixer for downconversion to avoid saturating the setup. In addition, the pump phase drift with 1 GHz clock reference is negligible compared to the measurement noise in the squeezing quadrature data. We also preemptively minimize any potential experimental drifts with our interleaved acquisition method described in Chapter 7.

DC wires come in different forms depending on the usage. For instance, it would require two pairs of DC wires to accurately measure the resistance of a thermometer (four-terminal sensing method); superconducting wires with NbTi cladding (usually in the form of twisted pairs) are frequently used in flux bias of SQUID-based systems such as qubit or cavity-based Josephson parametric amplifiers. In the thesis work, Fig. 4-2 shows an example of the DC wiring setup. The frequency of the wQED qubit is controlled with a global flux line filtered at the 3 K stage, using a DC source (Yokogawa GS200) at room temperature.

We use an arbitrary waveform generator (AWG Keysight 33250A) to bias the SNTJ. The AWG sends a low-frequency triangle wave with an amplitude V_{bias} through a 993 $\mathrm{k}\Omega$ resistor at room temperature to current bias the device in the μA range. The current then passes through a stainless steel thermocoax to attenuate microwave and infrared noise. The resistance of the SNTJ at base temperature is measured in-situ to allow accurate extraction of the bias voltage across the junction. Additionally, to ensure no spurious resonance due to the package design that can affect the noise temperature measurement, S_{11} of the SNTJ is characterized using a vector network analyzer (VNA) as shown in Sec. 4.1. From the measurement, we observe that SNTJ has its S_{11} consistently below -17 dB overall from 4 GHz to 8 GHz, which means $< 2\%$ power coming from the SNTJ is reflected. In addition, S_{11} of a 50 Ω and a circulator are characterized as a comparison.

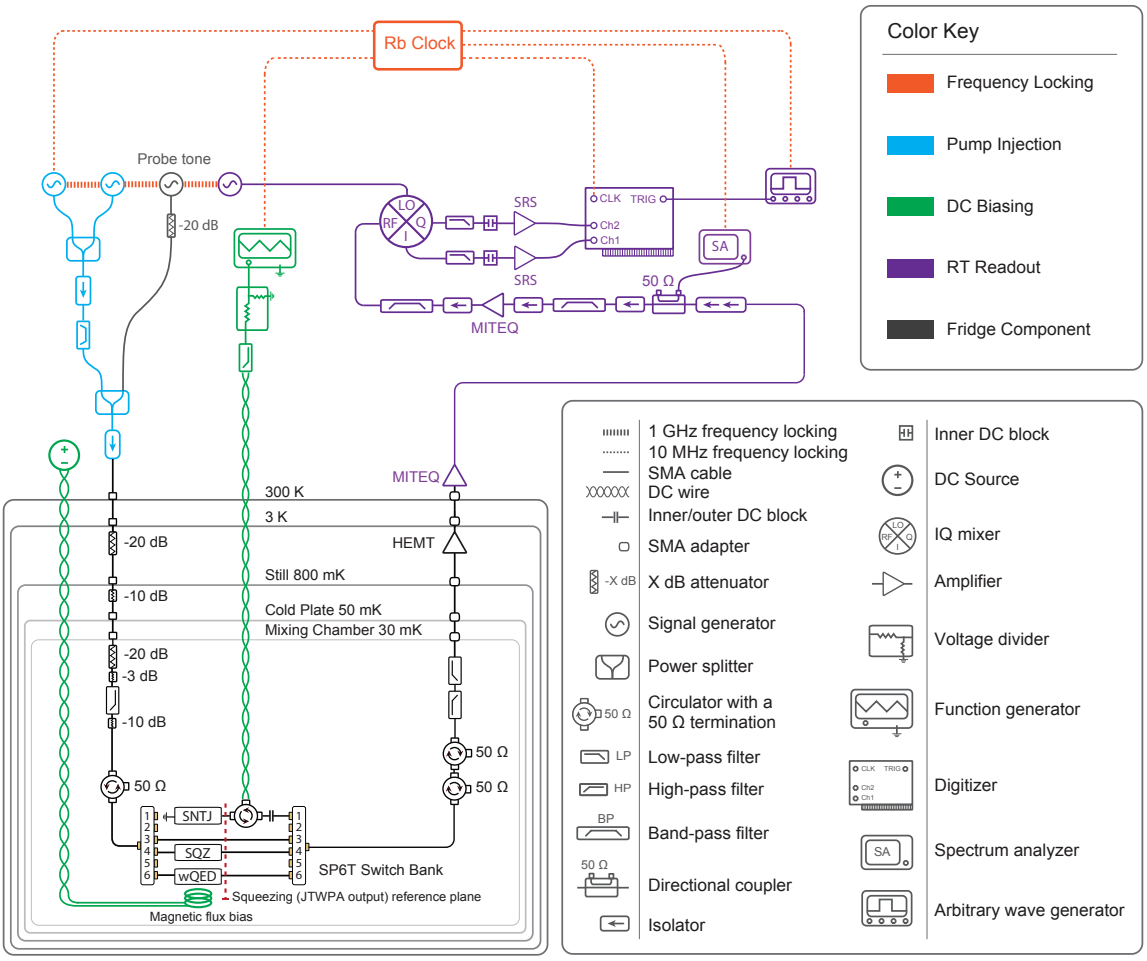

Figure 4-2. | **Cryogenic setup and wiring diagram.** The diagram is color-coded to illustrate individual functional groups. The blue circuit shows the JTWPA pump sources with additional components including power combiner, isolator, and bandpass filter. The purple circuit represents the data acquisition setup that includes a spectrum analyzer and a digitizer with several filters and amplifiers. The green circuit is the DC biasing of shot-noise tunnel junction (SNTJ) and wQED qubit in the noise temperature characterization.

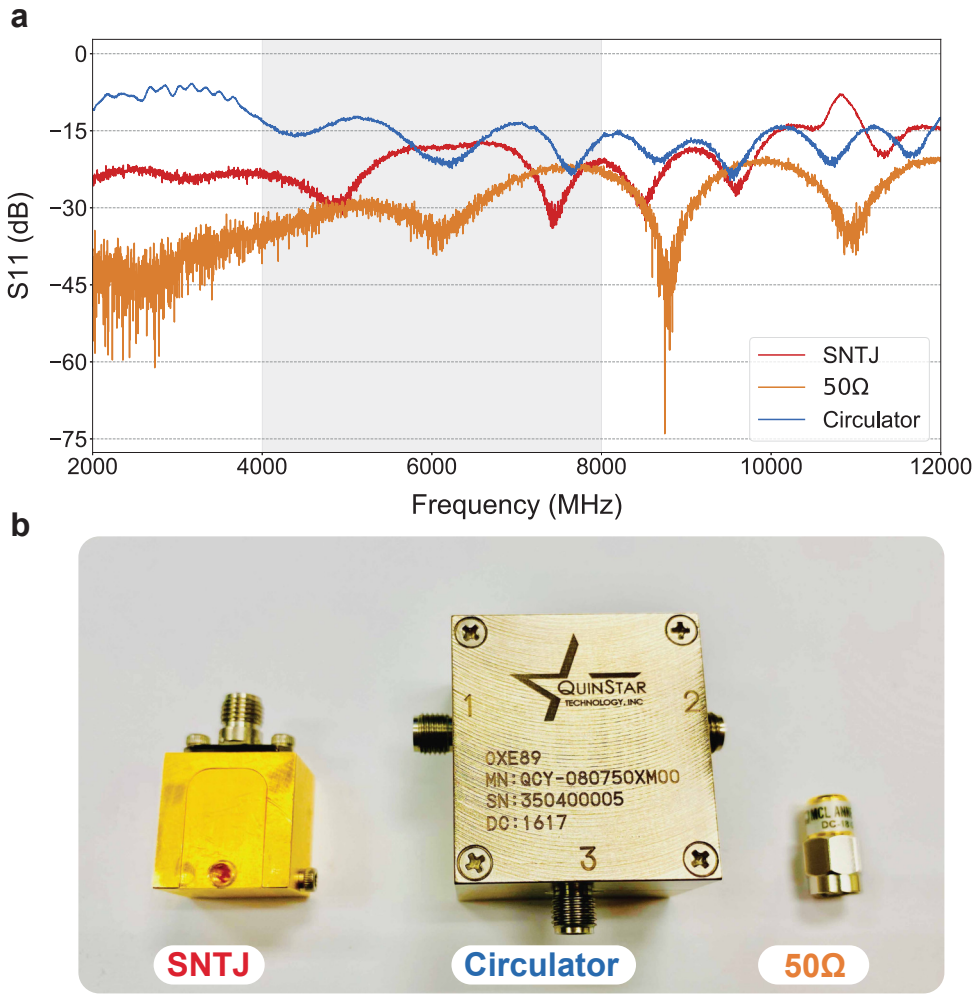

Figure 4-3. | **Room temperature return loss. a.** S_{11} of different components measured at room temperature. **b.** Device pictures.

4.2 System Noise Calibration

4.2.1 cQED AC Stark Shift

To use a cQED qubit as a noise calibration device, let us revisit the dispersive Hamiltonian Eq. (3.13) from the perspective of the qubit and examine the effect of resonator photons on the qubit as

$$H_{\text{disp}} = \frac{\hbar}{2}\left(\omega_q + \frac{2g^2}{\Delta}\hat{a}^\dagger\hat{a} + \frac{g^2}{\Delta}\right)\hat{\sigma}_z + \hbar\omega_r\hat{a}^\dagger\hat{a}. \tag{4.1}$$

Eq. (4.1) shows that the qubit frequency shifts due to the presence of photons in the resonator, a phenomenon known as the AC Stark shift. This is the basis for the noise calibration protocol using a qubit-resonator system.

Populating the resonator with photons shifts the qubit frequency, corresponding to

$$\Delta\omega_{\text{ac}} = 2\frac{\kappa^2}{\kappa^2 + \chi^2}\chi\bar{n}, \tag{4.2}$$

where the number of photons is given by $\bar{n} = \hat{a}^\dagger\hat{a}$. In the case $\chi \ll \kappa$, it can be simplified to

$$\Delta\omega_{\text{ac}} = 2\chi\bar{n}. \tag{4.3}$$

We extract κ and χ values from the resonator's Lorentzian response and from π pulse calibration through Rabi oscillation measurement. The pulse calibration method serves as a check for more accurate measurement of χ using a photon-induced dephasing process, i.e.,

$$\Gamma_\phi = \frac{8\chi^2}{\kappa}\bar{n}. \tag{4.4}$$

This is a simplified result from Ref. [42], where we again assume $\chi \ll \kappa$. The characterization process involves injecting photons during a Ramsey measurement as shown in Fig. 4-4.

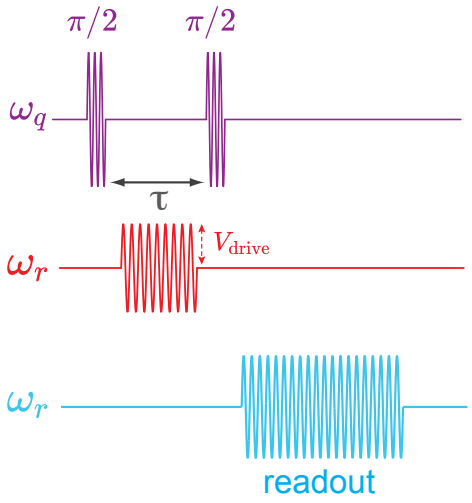

Figure 4-4. | **Photon induced dephasing measurement sequence.** Compared with regular Ramsey measurement (Fig. 3-6(b)), here we insert an additional drive tone at the resonator frequency with drive amplitude V_{drive} in-between the two $\pi/2$ pulses.

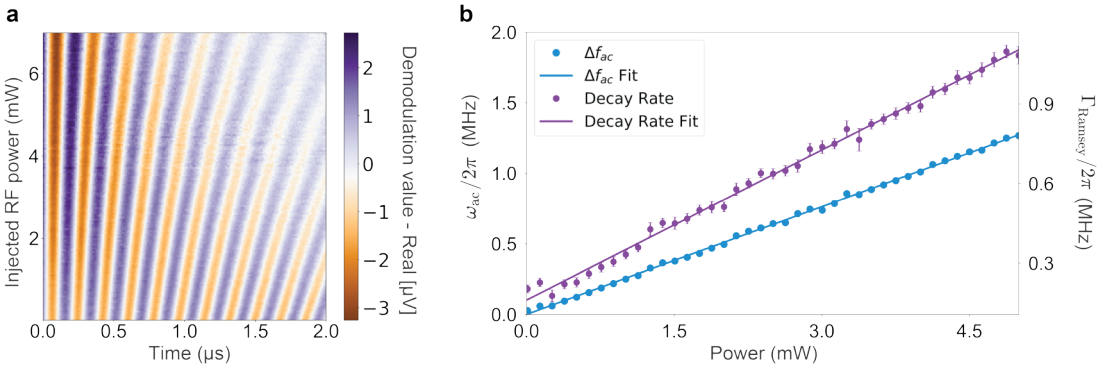

Figure 4-5. | **Measurement of qubit frequency shift and dephasing due to increasing photon number in the resonator. a.** The photon number in the resonator increases as we ramp up the RF power. We perform Ramsey measurement as a function of time at each given drive power. **b.** From the left plot, we can extract Ramsey decay rates and AC Stark shift as a function of RF power.

From the qubit frequency shift and dephasing measurements, we can extract χ fairly accurately by performing a linear fit on both $\Delta\omega_{\mathrm{ac}}$ and Γ_ϕ. We did not use this method in the thesis work, and more details can be found in [62]. We can continue to calibrate the photon number inside the resonator and use it as a calibrated noise source. The exact protocol will be discussed in Sec. 4.2.4.

In general, the AC Stark shift method has been commonly used in cQED for noise characterization because it utilizes the same experimental setup — a qubit system followed by an amplifier in most cases. It does not require additional calibration resources as the qubit-resonator system acts as the source. However, a shortcoming of this method is the bandwidth limit. The procedure only works effectively within a narrow range around the resonator frequency; the resonator will bandpass filter input power, restricting a broadband application, such as broadband two-mode squeezing characterization.

4.2.2 Y-Factor Method

Y-factor method utilizes the Johnson noise generated from a resistive load at a temperature T at thermal equilibrium. Its output noise spectrum to a matched load in a waveguide is given by

$$P_{\mathrm{noise}} = \frac{hf}{2B_{\mathrm{Y}}} \coth\left(\frac{hf}{2k_{\mathrm{B}}T}\right), \tag{4.5}$$

- f is the frequency of the measurement.
- B_{Y} is the measurement bandwidth,
- T is the physical temperature,
- k_{B} is the Boltzmann constant,
- h is the Planck constant.

The Y-factor method uses two $50\ \Omega$ matched resistors at different temperature values T_1 and T_2 ($T_2 > T_1$ without loss of generality) to output two different thermal noise powers P_1 and P_2. The effective noise temperature as defined in Chapter 5 of the device under test

is

$$T_e = \frac{T_2 - YT_1}{Y - 1}, \tag{4.6}$$

where $Y = P_2/P_1$ is the ratio of the output power measurements. More details of the derivation can be found in Ref.[86]. This method has been used frequently to characterize the noise performance in the regime $hf \gg k_{\mathrm{B}}T$ and noise power $P_{\mathrm{noise}} = k_{\mathrm{B}}B_{\mathrm{Y}}T$ varies with temperature T. There are a few drawbacks to this method. First of all, it needs a microwave switch to change between a high thermal load and a low thermal load. Alternatively, it requires an additional heater to vary the physical temperature of the resistor if one forgoes the microwave switch. Both of these are additional experimental complexities that could bring uncertainty to the characterization result. Second, the $1/f$ noise in the system can cause a drift in the overall noise power given that the measurement speed is slower compared to other aforementioned methods.

4.2.3 Shot-Noise Tunnel Junction (SNTJ)

A shot-noise tunnel junction [106] is a superconductor-insulator-superconductor aluminum junction, with the superconducting Al operated in the normal state via the strong magnetic field from an in-situ neodymium magnet.

With a matched load, the noise power at frequency f generated by a voltage-biased SNTJ at temperature T is [106]

$$\begin{aligned} N = Gk_{\mathrm{B}}B_{\mathrm{SNTJ}}\Bigg\{ T_N + \frac{1}{2}\Bigg[\left(\frac{eV + hf}{2k_{\mathrm{B}}}\right) \coth\left(\frac{eV + hf}{2k_{\mathrm{B}}T}\right) \\ + \left(\frac{eV - hf}{2k_{\mathrm{B}}}\right) \coth\left(\frac{eV - hf}{2k_{\mathrm{B}}T}\right) \Bigg\}, \end{aligned} \tag{4.7}$$

where V is the voltage bias across the shot noise tunnel junction, B_{SNTJ} is the measurement bandwidth for the SNTJ noise measurement, G is the system gain, and T_{N} is the system noise temperature.

In the limit $eV \ll hf$, Eq. (4.7) is dominated by thermal and quantum noise. When $eV \gg hf$, the noise is dominated by the Poissonian shot noise of the electron current

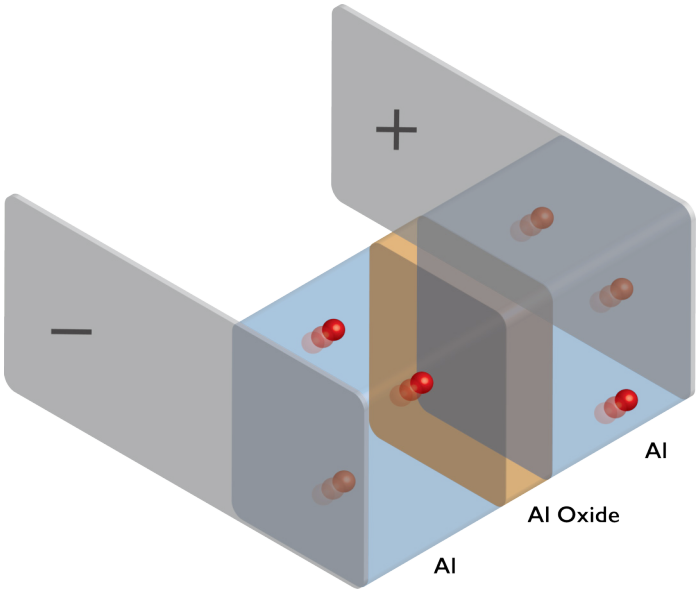

Figure 4-6. | **A simplified illustration of shot-noise tunnel junction.** The "+" and "-" represent the gate voltage applied to the junction such that the electrons (red) can tunnel through the thin Al-oxide barrier.

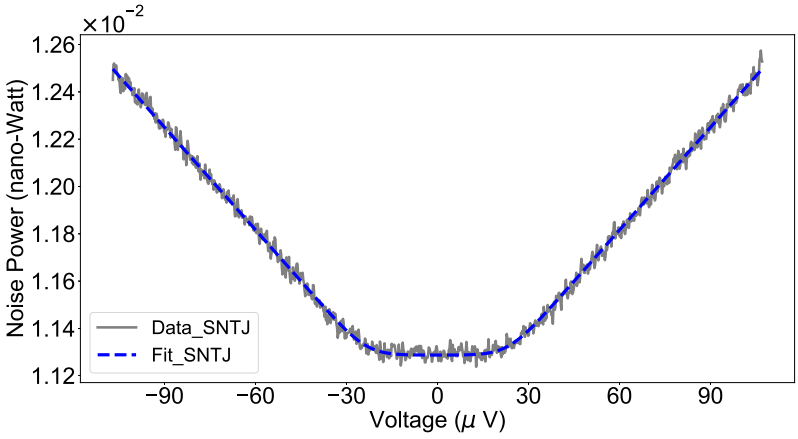

Figure 4-7. | **"Noise mustache curve" generated from a SNTJ.** Experimental data plotted together with the fit using Eq. (4.7). The x-axis is the voltage across the tunnel junction, and the y-axis shows the noise power coming out from the SNTJ. We can see the "double-coth" feature and a flat quantum noise bottom — the reason people jokingly refer to this curve as the "noise mustache."

through the tunnel junction. Dilution refrigerators with a base temperature 20-30 mK are sufficient to reach the quantum noise floor within the frequency range of interest here — 4-8 GHz represented by the plateau in the vicinity of 0 V junction voltage as shown in Fig. 4-7. It is worth noting that using a SNTJ, the data set can be collected in tens of milliseconds, effectively mitigating drift by $1/f$ noise. From the fit, we can extract both the system noise temperature T_N as well as the temperature of the noise source T. We adopt this method in the experiment for noise calibration as well as the protocol we introduce next.

4.2.4 wQED System Power Calibration

In Sec. 3.2.3, we introduced the wQED system and its power dependence of the transmitivity. Here we continue to explore its application in noise calibration. From Eq. (3.15), we have

$$t = 1 - \frac{\xi_w \Gamma_1}{2\Gamma_2} \frac{1 - \frac{i\Delta}{\Gamma_2}}{1 + \left(\frac{\Delta}{\Gamma_2}\right)^2 + \frac{\Omega^2}{\Gamma_1 \Gamma_2}}. \tag{4.8}$$

Note that the transmission coefficient through the qubit is normalized by subtracting the

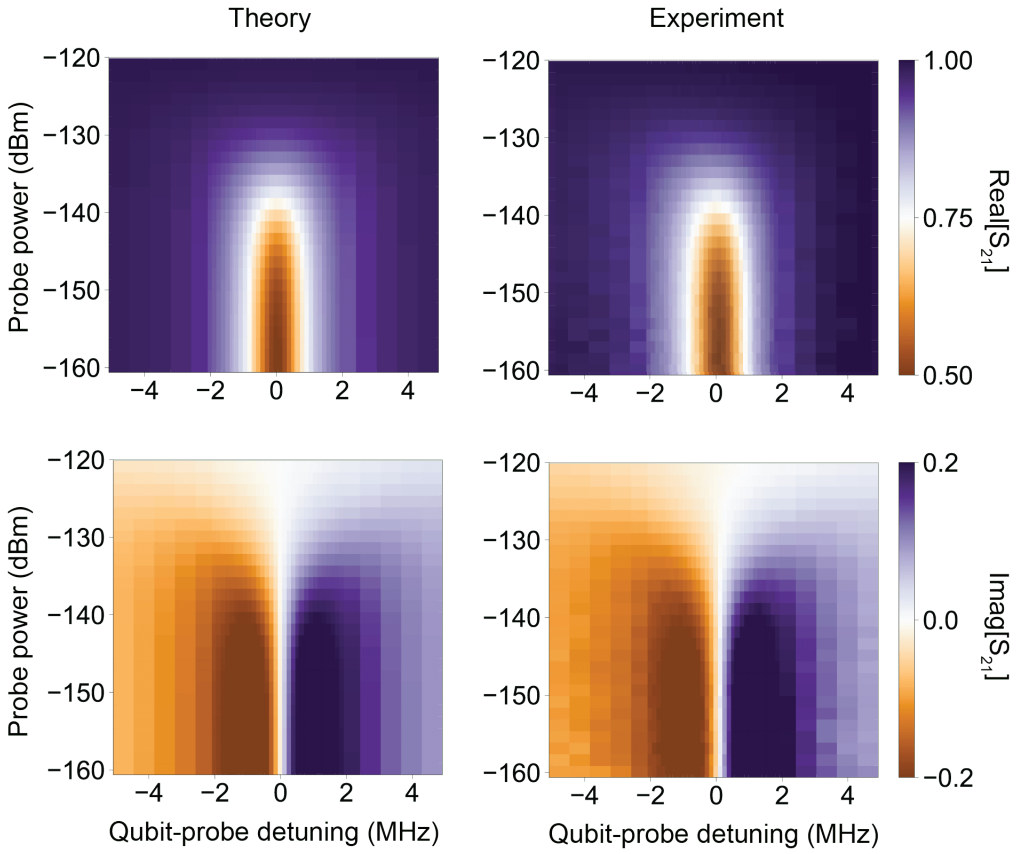

Figure 4-8. | Transmission scan of a qubit as a function of input power and qubit-probe detuning. Real and imaginary parts of the experimental data (right) and theory (left) are plotted together as a comparison.

background (without the qubit resonance, determined by detuning the qubit away). Next, we perform the same VNA measurement while also sweeping the input power. The input of a coherent state $|\alpha\rangle$ is mostly reflected at low power ($\bar{n} = |\alpha|^2 \ll 1$) due to interference between the input field and the qubit emission. As we increase the input power, the coherent state $|\alpha\rangle$ will have more contributions from higher number states $|n\rangle$, where $(n > 1)$,

while the qubit can only perfectly reflect up to a single photon. As a result, the resonant transmission increases and approaches unity at sufficiently high power.

S_{21} measured by a VNA corresponds to the complex transmission t as defined in Eq. (4.8). Fig. 4-9 compares the real and imaginary parts of the data (points) with the theory (line). Fitting is performed over the entire 2D scan, as shown in Fig. 4-8. In Fig. 4-9(c), we show the transmittance $|t|^2$ as a function of power at zero frequency detuning $\Delta = 0$ from the resonance. Fitting the entire 2D scan enables us to extract Ω and Γ_1. Using Eq. (3.16), we can extract powers at the qubit given the preset powers at refrigerator input at room temperature. As a result, this method also gives us the information for the setup input attenuation from the signal source to the qubit. The data shown in Fig. 4-9 are fitted nicely with $\Gamma_1 = 934\,\mathrm{kHz} \pm 11\,\mathrm{kHz}$ and $\Gamma_2 = 755\,\mathrm{kHz} \pm 14\,\mathrm{kHz}$. The decay rates of our wQED qubit are (and are expected to be) relatively large compared with a typical cQED qubit due to its direct coupling to a $50\,\Omega$ waveguide.

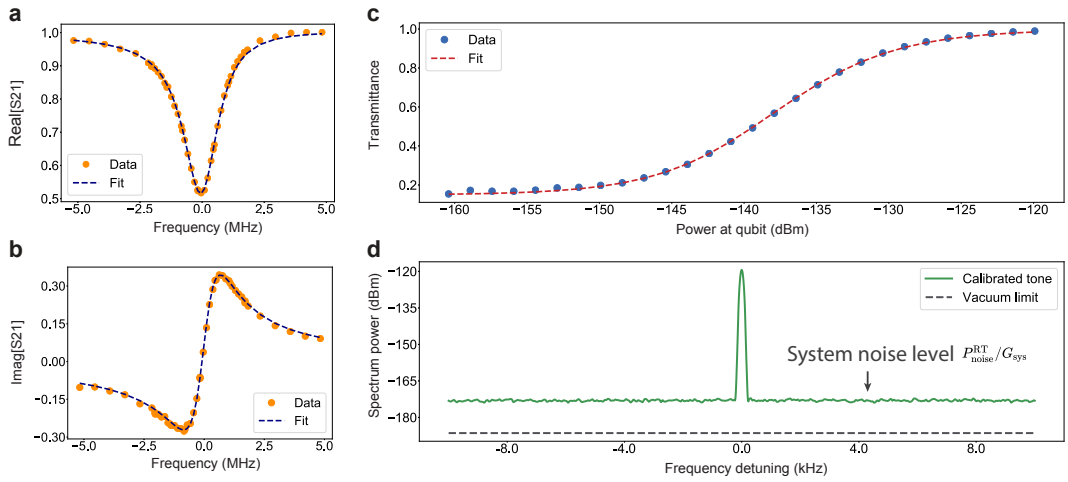

Figure 4-9. | **Transmission profiles and photon number calibration.** Experimental and theory fits are plotted together. **a. & b.** Real and imaginary part of the transmission coefficient as a function of input power. **c.** Resonant transmittivity as a function of input power. **d.** System noise extracted using a spectrum analyzer. The system noise is shown as a raised noise floor from the vacuum limit.

After calibrating the power at the qubit, we characterize the output noise spectrum shown in Fig. 4-9(d). The same method was performed in Ref [61]. To calibrate the system noise level, we first extract the system gain by sending a calibrated input field through the qubit-waveguide system — $P^{\mathrm{MXC}}_{\mathrm{OTL}}$ — power at the wQED reference plane at the mixing

chamber (MXC), and measure its output — $P_{\mathrm{OTL}}^{\mathrm{RT}}$ — power at room temperature using a spectrum analyzer [61]. The system gain $G_{\mathrm{sys}} = P_{\mathrm{OTL}}^{\mathrm{RT}}/P_{\mathrm{OTL}}^{\mathrm{MXC}}$ is then used to obtain the system noise temperature

$$T_{\mathrm{sys}} = P_{\mathrm{noise}}^{\mathrm{RT}}/G_{\mathrm{sys}}k_{\mathrm{B}}B, \tag{4.9}$$

where $P_{\mathrm{noise}}^{\mathrm{RT}}$ is the noise level measured at the spectrum analyzer. At frequency $\omega = 6.7\,\mathrm{GHz} \times 2\pi$, $P_{\mathrm{noise}}^{\mathrm{RT}}$ = -109.63 dBm, G_{sys} = 65.06 dB and measurement bandwidth $B = 100\,\mathrm{Hz}$, giving a system noise temperature T_{sys} = 2.46 K using Eq. (4.9). The corresponding measurement efficiency η_{meas} using the definition [63] is given by

$$\eta_{\mathrm{meas}} = \frac{\hbar\omega}{2k_{\mathrm{B}}T_{\mathrm{sys}}}, \tag{4.10}$$

where k_{B} and $\hbar$ are Boltzmann and reduced Planck constants respectively. In this case, we have a measurement efficiency $\eta_{\mathrm{meas}} = \hbar\omega/2k_{\mathrm{B}}T_{\mathrm{sys}} = 6.53\,\%$.

4.2.5 Comparison Between the wQED (primary) and the SNTJ (secondary) Calibration Methods

We have employed two different methods — the primary wQED qubit power calibration technique and the secondary SNTJ method — to cross-check the measurement results. We perform the noise temperature characterization using both methods from 6.5 GHz to 6.9 GHz as shown in Fig. 4-10. Given the identical setup after the SP6T switch, the difference between the two curves most likely arises from the insertion loss ΔA imposed by the additional components required to operate the SNTJ (highlighted in red color in the figure). Based on this assumption, the overestimated noise temperature can be corrected by accounting for ΔA and scaling the noise temperature accordingly. The adjusted results can be seen from Fig. 4-11. In other words, we calibrate the SNTJ using the wQED. The latter, in principle, gives a more accurate system noise characterization for the squeezing measurement without additional circuit components as employed for the former. In this experiment, one drawback of the wQED method is its limited frequency range (6.5-6.9 GHz). However, it can be readily addressed with different qubit designs to target a particular fre-

quency band.

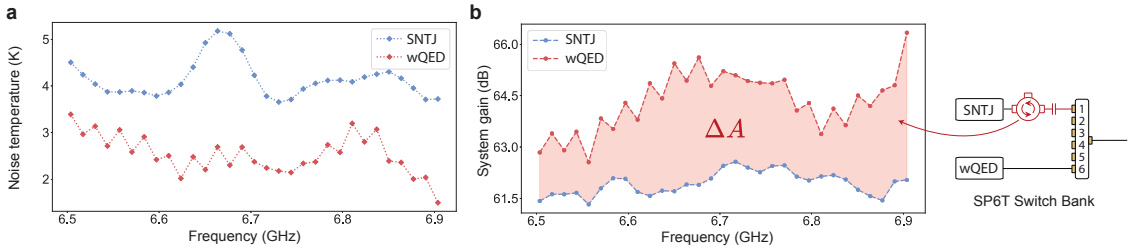

Figure 4-10. | Uncorrected noise temperature characterization and system gain. a. Noise temperature as a function of frequency from 6.5 GHz to 6.9 GHz measured using the SNTJ and the wQED device separately. **b.** System gain measured using the two methods. Due to the finite difference in their RF transmission ΔA, the extracted system gains are different. In other words, we are using the wQED (primary) to calibrate the SNTJ and isolator loss (secondary). We use this to correct the system noise in panel (a) independently.

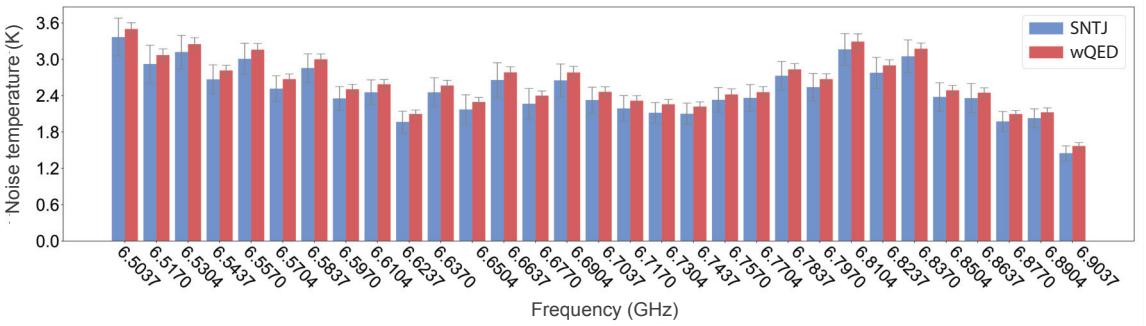

Figure 4-11. | SNTJ calibrated using wQED. The SNTJ noise temperature has been corrected here while the wQED measurement values remain unchanged.

At the time of the experiment, no suitable quantum-limited amplifiers were available with superior noise performance than the HEMT that can tolerate the output power and the strong pump tones from the squeezer (JTWPA). The HEMT suffices but requires extensive averaging and background subtraction for this experiment and most others in the literature of squeezed microwave generation in superconducting circuits. The overall measurement efficiency can benefit from an additional quantum-limited amplifier like a JTWPA before the HEMT, allowing a faster data acquisition rate and better signal-to-noise ratio.

Chapter 5

Josephson Parametric Amplifiers

This chapter starts with the origin and characteristics of noise in quantum mechanical systems and the effect of noise propagation in a circuit. The discussion highlights the importance of amplification, including phase-preserving and phase-sensitive amplifiers. We then explore the mechanism behind parametric amplification, a phenomenon that exists in both the quantum and classical worlds. We will overview different superconducting parametric amplification technologies focusing on the Josephson-junction-based parametric amplifiers and examine both resonant and traveling-wave architectures.

5.1 Noise and the Necessity of Amplification

Manipulating quantum mechanical systems often involves a weak signal at cryogenic temperatures with only a single to a few photons, while the measurement and data recording of such a signal occurs at room temperature. The presence of thermal noise can easily drown out the signal, not to mention the non-negligible transmission loss that further worsens the signal-to-noise ratio (SNR)[1]. To put the comparison in perspective, a typical signal coming out of a resonator in superconducting circuits can be represented as a Gaussian coherent state as introduced in Chapter 2. Assuming the resonant frequency and its FWHM bandwidth are 6 GHz and 6 MHz, respectively, in addition to a

[1]The loss of a transmission medium is highly dependent upon its frequency spectrum and specific setup. For example, loss can be a more pronounced issue in microwave coaxial cables compared to optical fiber due to the skin effect of the conductor.

typical intracavity coherent drive field with mean cavity occupation $\bar{n} \sim 1$, the output power is $P = \hbar\omega\kappa\bar{n} \sim 1 \times 10^{-16}\,\mathrm{W} = -130\,\mathrm{dBm}$. In contrast, a typical analog microwave signal entering the measurement apparatus at room temperature is on the order of $10^{-7}\,\mathrm{W} = -40\,\mathrm{dBm}$. The sheer scale of 9-orders-of-magnitude difference in the signal power levels accentuates the necessity of amplification to bridge the quantum mechanical and the classical worlds.

However, there is a price to pay for amplifying the signal: the additional noise associated with the amplification process. Chapter 2 discussed inherent quantum limit on measurement. Likewise, amplification is essentially a form of measurement that correlates the output signal with the input [62]. Through the amplification process, the uncertainty relation constrains how well the output can be correlated to the input. The manifestation of the uncertainty relation is characterized as the amplifier noise. In physics, one typically works with linear amplification[2] where the output signal power is linearly related to the input power by a gain factor the G (or $\sqrt{G}$ in amplitude). It can described as

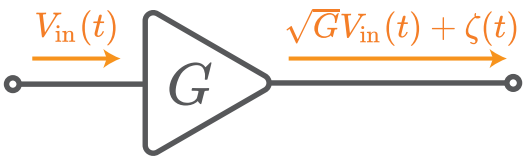

Figure 5-1. | **Input and output of a generic amplifier** An amplifier characterized by its power gain G. The input signal with amplitude $V_{\mathrm{in}}(t)$ gets amplified by $\sqrt{G}$ along with the additional noise $\zeta(t)$.

$$V_{\mathrm{out}}(t) = \sqrt{G}V_{\mathrm{in}}(t) + \zeta(t), \tag{5.1}$$

where $V_{\mathrm{in}}(t)$, $V_{\mathrm{out}}(t)$ are the input and output signal amplitudes, respectively, and $\zeta(t)$ is the additional uncorrelated noise introduced by the amplifier. Typically, we characterize the time-varying noise $\zeta(t)$ in its Fourier domain using the power spectral density $S(\omega)$, the noise intensity as a function of frequency ω. It can be expressed as the Fourier transform

[2]The terminology can sometimes cause confusion. The linearity refers to the amplifier transfer function, i.e., the output is proportional to the input by a fixed gain factor. The amplification process is mainly due to the nonlinearity intrinsic to the amplifier itself. In addition, there does exist nonlinear amplification that can be useful. Still, it is not commonly used in superconducting circuits. It is more straightforward to treat linear amplification mathematically [104].

of the noise signal

$$S(\omega) = \int_{-\infty}^{\infty} \langle \zeta(t)\zeta(0) \rangle e^{-i\omega t} dt. \tag{5.2}$$

The $S(\omega)$ carries units of a^2/Hz, where a is the unit of the fluctuations in current, flux, or voltage.

All practical devices such as coaxial cables, waveguides, amplifiers, and their associated connections introduce a finite amount of both resistive and reactive loss between the input and the output. The passive, resistive loss leads to Johnson-Nyquist noise, named after the people who discovered and explained it. In thermal equilibrium at temperature T with resistance R, it has a voltage noise spectral density of $\sqrt{4k_{\mathrm{B}}TR}$ $[\mathrm{V}/\sqrt{\mathrm{Hz}}]$ and a current noise spectral density $\sqrt{4k_{\mathrm{B}}T/R}$ $[\mathrm{A}/\sqrt{\mathrm{Hz}}]$. When we multiply these two expressions and integrate them over a finite bandwidth B, the overall noise power in the resistor R is given by $P = 4k_{\mathrm{B}}TB$. Connecting the noisy resistor with a load resistor R gives the maximum power transfer. The noise power dissipated in a matched load within the bandwidth B is given by

$$P = \left(\frac{\zeta_{\mathrm{rms}}}{2R}\right)^2 R = \frac{\zeta_{\mathrm{rms}}^2}{4R} = k_{\mathrm{B}}TB, \tag{5.3}$$

where ζ_{rms} is the rms voltage of the time-varying noise $\zeta(t)$ defined in Eq. (5.1), or equivalently as the power spectral density

$$S(\omega) = k_{\mathrm{B}}T. \tag{5.4}$$

The classical noise occurs due to the thermal fluctuations of charge carriers and displays a frequency-independent behavior often referred to as "white" noise. Note that the above linear equations serve as an approximation that does not work well for very high frequencies (so-called ultraviolet catastrophe historically, and Planck's blackbody radiation law must be used in this case) or very low temperatures, which we will discuss in a moment. Nonetheless, this is a significant result as it suggests that smaller bandwidth comes with less noise power. In addition, as temperature T decreases, the noise power P decreases accordingly. This implies the colder devices and components generate less noise power, which is a motivation for using a dilution refrigerator to cool them down to a lower temperature.

As mentioned, the simple relation of the noise spectral density becomes invalid when quantum mechanical effects take place. Considering the quantum effects by using the fluctuation-dissipation theorem (FDT), the noise spectral density becomes the following [24]:

$$S(\omega) = \frac{\hbar\omega}{2} \coth\left[\frac{\hbar\omega}{2k_{\mathrm{B}}T}\right]. \tag{5.5}$$

We will not discuss FDT in the thesis, but the theorem quantifies the connection between fluctuations in a physical system about its equilibrium and susceptibility to external perturbations. Further details can be found in Ref.[24]. Here we draw some intuition from Eq. (5.5) by considering it as a composition of both the classical and quantum parts. First, Eq. (5.5) can be expressed in exponential form

$$S(\omega) = \frac{\hbar\omega}{2}\left(\frac{e^{\hbar\omega/2k_{\mathrm{B}}T} + e^{-\hbar\omega/2k_{\mathrm{B}}T}}{e^{\hbar\omega/2k_{\mathrm{B}}T} - e^{-\hbar\omega/2k_{\mathrm{B}}T}}\right) \tag{5.6}$$

$$= \frac{\hbar\omega}{2}\left(\frac{e^{\hbar\omega/k_{\mathrm{B}}T} + 1}{e^{\hbar\omega/k_{\mathrm{B}}T} - 1}\right) \tag{5.7}$$

$$= \frac{\hbar\omega}{2}\left(\frac{e^{\hbar\omega/k_{\mathrm{B}}T} - 1 + 2}{e^{\hbar\omega/k_{\mathrm{B}}T} - 1}\right) \tag{5.8}$$

$$S(\omega) = \hbar\omega\left(\frac{1}{e^{\hbar\omega/k_{\mathrm{B}}T} - 1} + \frac{1}{2}\right). \tag{5.9}$$

One can recognize the first term in the parenthesis as the photon occupancy $\bar{n}$ with Bose-Einstein statistics that describes the classical thermal contribution, while the second term is the quantum mechanical zero-point energy. If we examine the limits of Eq. (5.9), we will find the following. First, in the high-temperature, classical limit where $\hbar\omega \ll k_{\mathrm{B}}T$, $e^{\hbar\omega/k_{\mathrm{B}}T} - 1 \sim \hbar\omega/k_{\mathrm{B}}T$. Therefore, $S(\omega) \approx k_{\mathrm{B}}T$, reproducing the original classical result from Eq. (5.4). We verify that Eq. (5.5) gives the same result since $\coth\beta \approx 1/\beta$ for small β. Second, in the low-temperature limit where $\hbar\omega \gg k_{\mathrm{B}}T$, the Planck term in Eq. (5.9) goes to zero, leaving the quantum part $\hbar\omega/2$. We can also verify Eq. (5.5) gives

$$S(\omega) = \frac{\hbar\omega}{2}, \tag{5.10}$$

considering $\lim_{\beta\to\infty} \coth(\beta) = 1$. The low-temperature result can be recognized as the zero-

point energy of the EM field — there still exist quantum fluctuations even at zero temperature, which give a lower bound of noise in our qubits and readout experiments at few-tens-of-milli-Kelvin temperatures.

Speaking of temperature, we can model a noise power N_0 over the bandwidth of interest B as an equivalent thermal noise source with an *effective noise temperature* T_e as

$$T_\mathrm{e} = \frac{N_0}{k_\mathrm{B} B}. \tag{5.11}$$

For example, in a qubit experiment with readout frequencies of 7 GHz, the effective (noise) temperature $T_\mathrm{e} = S(2\pi \times 7\,\mathrm{GHz})/k_\mathrm{B} = \hbar\omega/2k_\mathrm{B} = 168\,\mathrm{mK}$, even though the physical temperature might be near 20 mK. The effective noise temperature must not be confused with the physical temperature of a system that describes the thermodynamic equilibrium. At absolute zero temperature, there is no macroscopic thermal energy. The zero-point energy cannot be used to drive an atomic transition like ordinary EM radiation. Still, it is responsible for quantum mechanical phenomena such as spontaneous emission and the Casimir effect.

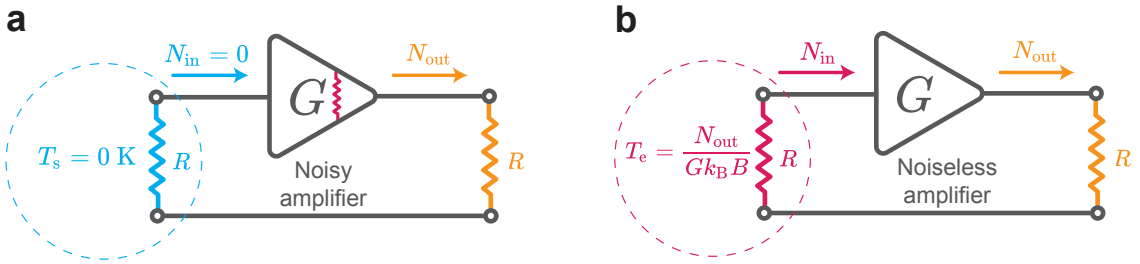

Figure 5-2. | **Equivalent noise temperature of a noisy amplifier. a.** An illustrative drawing of a noisy amplifier. If the source resistor (blue) is at a hypothetical temperature of $T_\mathrm{s} = 0\,\mathrm{K}$, then the input power to the amplifier would be zero, $N_\mathrm{in} = 0$. The output noise power N_out would be solely due to the noise generated by the amplifier itself. **b.** An equivalent model with a noiseless amplifier. Instead, we assume the takes on an input noise N_in generated by the source resistor at an effective temperature T_e.

Amplifiers have effective noise temperatures associated with them as well that characterize the amount of added noise, even though they do not necessarily represent actual temperatures (although it can be affected by the physical temperature of the amplifier). Consider a noisy amplifier as shown in Fig. 5-2(a) with bandwidth B, gain G and matched to an input resistor at a hypothetical source temperature $T_\mathrm{s} = 0\,\mathrm{K}$. The amplifier adds a

noise with power N_{out}. In regards to the overall output noise, it is equivalent to modeling the system as driving a noiseless amplifier with the source resistor at an input-referred temperature

$$T_{\text{e}} = \frac{N_{\text{out}}}{Gk_{\text{B}}B} \tag{5.12}$$

as displayed in Fig. 5-2(b) such that the output noise power remains the same as $N_{\text{out}} = Gk_{\text{B}}T_{\text{e}}B$. Hence, we define T_{e} as the effective input-referred noise temperature of the amplifier. The definition of T_{e} also applies to multiple amplifiers. It is often difficult to quantify the noise performance of different amplifier chains by comparing the total output noise N_{out} when their system gain might be different. Referring to the effective noise temperature allows people to normalize the output noise with respect to the system gain and scale the added noise back to the input of the system.

In most experimental settings, one would need a series of different amplifiers in the output path to boost the signal strength to the classical level. At the same time, the noise is continually getting added to the system and even amplified as it propagates through the amplification chain. Next, we are going to quantify the overall effective noise temperature of the cascaded chain of amplifiers — commonly referred to as system noise temperature T_{sys}. First, consider a microwave amplifier connected to a impedance-matched source with

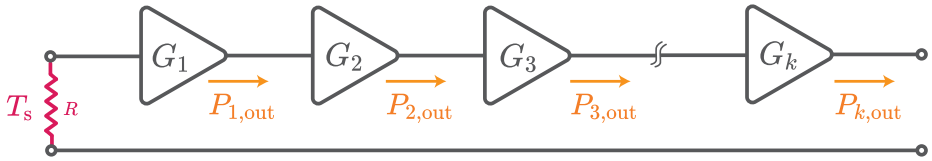

Figure 5-3. | **Noise propagation in a cascade of amplifiers.** An illustrative drawing of a chain of noisy amplifiers.

an effective temperature T_{s} at the input shown in Fig. 5-3, and the added noise by the first amplifier T_{n1}. The noise power at the output is given by

$$P_{1,\text{out}} = G_1 k_{\text{B}} \left(T_{\text{s}} + T_{\text{n1}}\right) B. \tag{5.13}$$

Experimentally, we can determine the amplifier noise temperature T_{n1} by measuring the output noise power $P_{1,\text{out}}$, the gain G_1 with the understanding of source temperature T_{s} and

measurement bandwidth B. Back to the amplification chain, the first amplifier's output now becomes the second's input. Therefore, adding the noise contribution of the second amplifier $T_{\mathrm{n}2}$, we can write down its output noise as

$$P_{2,\mathrm{out}} = G_2 \left[G_1 k_{\mathrm{B}} \left(T_{\mathrm{s}} + T_{\mathrm{n}1} \right) B + k_{\mathrm{B}} T_{\mathrm{n}2} B \right]. \tag{5.14}$$

Continuing with the third stage of amplification with added noise $T_{\mathrm{n}3}$, we obtain

$$P_{3,\mathrm{out}} = G_3 \left(G_2 \left[G_1 k_{\mathrm{B}} \left(T_{\mathrm{s}} + T_{\mathrm{n}1} \right) B + k_{\mathrm{B}} T_{\mathrm{n}2} B \right] + k_{\mathrm{B}} T_{\mathrm{n}3} B \right). \tag{5.15}$$

This product rule of noise propagation goes on through all the stages. At the output of the final stage, we would like to refer back to the input of the amplification chain to quote an effective noise temperature for the whole system:

$$T_{\mathrm{sys}} = T_{\mathrm{n}1} + \frac{T_{\mathrm{n}2}}{G_1} + \frac{T_{\mathrm{n}3}}{G_1 G_2} + \cdots + \frac{T_{\mathrm{n}k}}{G_1 G_2 \cdots G_{k-1}}, \tag{5.16}$$

where G_k, $T_{\mathrm{n}k}$ are the power gain and added noise for the k-th amplifier, respectively. To obtain Eq. (5.16), we divide both sides of Eq. (5.15) by $G_{\mathrm{sys}} k_{\mathrm{B}} B$, where the system gain $G_{\mathrm{sys}} = G_1 G_2 \cdots G_k$, and subtract the original effective source temperature T_{s} to isolate out the system noise. Eq. (5.16) is called the Friis formula, named after the Danish-American electrical engineer Harald T. Friis. A very important observation from the formula is that for large gain $G_{\mathrm{k}} \gg 1$, there is less amplifier noise contribution to the overall system noise temperature from later stages. In other words, the overall T_{sys} can be almost solely dependent upon the first amplifier if its gain is large enough to diminish the rest of the amplifier noises. To put this in the context of superconducting circuits, state-of-the-art cryogenic semiconductor microwave amplifiers have noise temperatures around 2 K and a power gain of 30-40 dB in a logarithmic scale or equivalently, $10^3 - 10^4$ in linear units. This suggests that as long as the next amplifier has a noise temperature $T_{\mathrm{n}} \ll 2000\,\mathrm{K}$, the value of T_{sys} is primarily set by the cryogenic amplifier. Moreover, if one can make an amplifier with a noise temperature of $T_{\mathrm{n}} \approx 170\,\mathrm{mK}$ (around half a photon of noise at 7 GHz) and a power gain $G \geq 20\,\mathrm{dB}$ ($\geq 100\times$ in linear units), the system noise temperature will

approach the standard quantum limit, which is half a photon.

This observation is a cornerstone for the amplifier work in this thesis to engineer a superior amplifier. To a large extent, the Friis formula played an essential role in shaping the quantum readout schemes in different scientific disciplines and will keep motivating the development of amplification technologies.

5.2 Quantum Limit on Amplifications

In the previous section, we discussed that quantum mechanics sets a fundamental limit on the amplification processes, namely the standard quantum limit. The Heisenberg uncertainty principle constrains the measurement precision on non-commuting observables such as X and P, manifested as an uncertain "blob" in phase space. As shown in Fig. 5-4, the amplification process "stretches" the state vector while maintaining its phase but adds additional noise (dashed circle) to the noise present at the input state vector. This type of amplification is often referred to as phase-preserving amplification (PPA) or phase-insensitive amplification (PIA). We can heuristically describe PPA as a process that simultaneously copies and enlarges both quadratures of the input signal. However, the process introduces additional noise; therefore, amplification never makes a perfect, enlarged copy of the input signal but rather a noisier version. This interpretation [104] suggests a way to amplify without adding noise if we are only interested in one quadrature — the premise of phase-sensitive amplification (PSA). In the following two sections, we will examine PPA and PSA mathematically following the derivation by Caves [19], based on earlier work by Haus and Mullen [45].

5.2.1 Phase-Preserving Amplifiers

A classical signal $E(t)$ oscillating at frequency ω takes the general form

$$E(t) \propto \left(ae^{-i\omega t} + a^* e^{i\omega t}\right), \tag{5.17}$$

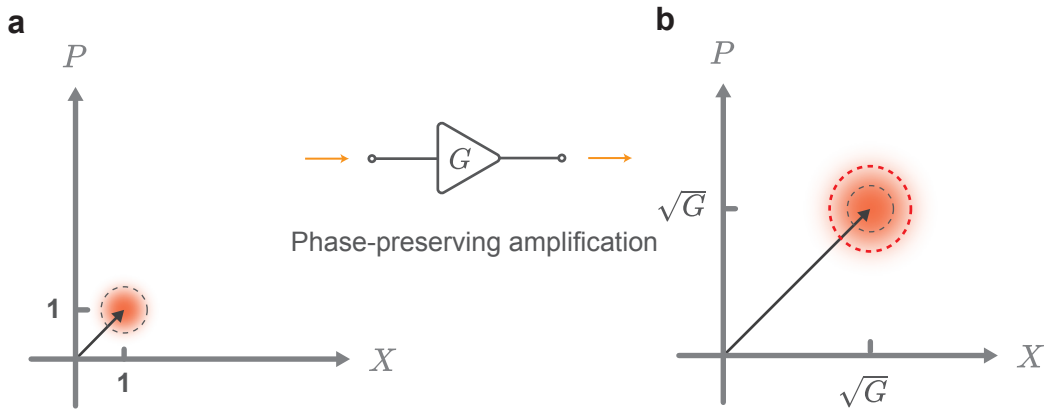

Figure 5-4. | **Phase-preserving amplification. a.** Diagram of an input coherent state vector in the phase space. The uncertainty "blob" represents vacuum fluctuations, and the dashed circle denotes the input noise. **b.** The phase-preserving amplifier with a power gain G amplifies the input state vector while maintaining its phase. The process also introduces additional noise represented by the enlarged "blob," and the red dashed circle representing the output noise.

where a and its complex conjugate a^* define the two quadrature components of the signal. The in-phase component I is the real part of a, $\mathrm{Re}\{a\} = (a + a^*)/2$, and the quadrature component Q is the imaginary part of a, $\mathrm{Im}\{a\} = (a - a^*)/2i$. For a quantum mechanical signal, the a and a^* transform into the annihilation $\hat{a}$ and creation $\hat{a}^\dagger$ operators for the EM field. We then consider just one bosonic mode for the input $\{\hat{a}_{\mathrm{in}},\ \hat{a}^\dagger_{\mathrm{in}}\}$ and output $\{\hat{a}_{\mathrm{out}},\ \hat{a}^\dagger_{\mathrm{out}}\}$ of the amplifier. The input and output operators obey the bosonic commutation relations,

$$[\hat{a}_{\mathrm{in}},\ \hat{a}^\dagger_{\mathrm{in}}] = 1,\ [\hat{a}_{\mathrm{out}},\ \hat{a}^\dagger_{\mathrm{out}}] = 1. \tag{5.18}$$

Naively, one would think the action from the amplifier enlarges both quadratures simultaneously as

$$\hat{a}_{\mathrm{out}} = \sqrt{G}\hat{a}_{\mathrm{in}},\ \hat{a}^\dagger_{\mathrm{out}} = \sqrt{G}\hat{a}^\dagger_{\mathrm{in}}. \tag{5.19}$$

However, the expression violates the commutation relations in Eq. (5.18). Therefore, we introduce an additional mode $\hat{\mathcal{F}}$ such that

$$\hat{a}_{\mathrm{out}} = \sqrt{G}\hat{a}_{\mathrm{in}} + \hat{\mathcal{F}},\ \hat{a}^\dagger_{\mathrm{out}} = \sqrt{G}\hat{a}^\dagger_{\mathrm{in}} + \hat{\mathcal{F}}^\dagger. \tag{5.20}$$

Physically, the operator $\hat{\mathcal{F}}$ represents the added noise by the amplifier, which originates from the source to enable the power gain G and is uncorrelated with the input signal $\hat{a}$. This implies $[\hat{\mathcal{F}}, \hat{a}] = [\hat{\mathcal{F}}^\dagger, \hat{a}^\dagger] = 0$, and $\langle \mathcal{F} \rangle = \langle \mathcal{F}\hat{a}_{\rm in} \rangle = \langle \mathcal{F}\hat{a}_{\rm in}^\dagger \rangle = 0$ since $\mathcal{F}$ is a random noise. Now by enforcing the commutation relations Eq. (5.18) on the output field $\hat{a}_{\rm out}$, we get

$$[\hat{\mathcal{F}},\ \hat{\mathcal{F}}^\dagger] = 1 - G. \tag{5.21}$$

The output noise can be expressed as the mean-square fluctuations $(\Delta\hat{a}_{\rm out})^2$,

$$(\Delta\hat{a}_{\rm out})^2 = \frac{1}{2}\langle\{\hat{a}_{\rm out},\ \hat{a}_{\rm out}^\dagger\}\rangle - \langle\hat{a}_{\rm out}\rangle\langle\hat{a}_{\rm out}^\dagger\rangle. \tag{5.22}$$

A similar expression can be given for $(\Delta\hat{a}_{\rm in})$. This is a result from Ref. [19], where Caves uses a series of useful commutation and anti-commutation (denoted with curly brackets $\{\}$) relations, in addition to the relations between $\hat{\mathcal{F}}$ and $\hat{a}$ above. We can express Eq. (5.22) as

$$(\Delta\hat{a}_{\rm out})^2 = G(\Delta\hat{a}_{\rm in})^2 + \frac{1}{2}\langle\{\hat{\mathcal{F}},\ \hat{\mathcal{F}}^\dagger\}\rangle. \tag{5.23}$$

Using the generalized uncertainty principle $\left|\Delta\hat{\mathcal{F}}\right|^2 \geq \frac{1}{2}\left|\langle[\hat{\mathcal{F}},\ \hat{\mathcal{F}}^\dagger]\rangle\right|$ and the fact that $\langle\hat{\mathcal{F}}\rangle = 0$, Eq. (5.23) becomes

$$(\Delta\hat{a}_{\rm out})^2 \geq G(\Delta\hat{a}_{\rm in})^2 + \frac{1}{2}\left|\langle[\hat{\mathcal{F}},\ \hat{\mathcal{F}}^\dagger]\rangle\right| \tag{5.24}$$

$$\geq G(\Delta\hat{a}_{\rm in})^2 + \frac{|G-1|}{2}. \tag{5.25}$$

We can rewrite the inequality as

$$\frac{(\Delta\hat{a}_{\rm out})^2}{G} \geq (\Delta\hat{a}_{\rm in})^2 + \frac{1 - 1/G}{2}, \tag{5.26}$$

where we divide both sides by G and refer to the amplifier input.

- In the limit of no gain ($G = 1$), $(\Delta\hat{a}_{\rm out})^2 = (\Delta\hat{a}_{\rm in})^2$ — no additional noise is introduced by the amplifier.

- When taking G to the large gain limit such that $G \approx G - 1$,

$$\frac{\left(\Delta\hat{a}_{\text{out}}\right)^2}{G} \geq (\Delta\hat{a}_{\text{in}})^2 + \frac{1}{2}. \tag{5.27}$$

  This result signifies that phase-preserving amplification must add at least half a quantum (or half of a photon) of noise in the large gain limit.

- In the case of greater-than-unity, small gain, the minimum number of added noise quanta is given by $(1 - 1/G)/2$, which can be arbitrarily small. It might be tempting to ask, is it possible to evade the SQL by reducing the gain? The answer is no. As we discussed at the beginning of the chapter, a massive power gap exists for the quantum signal to make up (with amplifiers) before reaching the classical level for signal processing, or as Caves puts it, "we can lay our grubby, classical hands on" (Caves, 1982). Using the Friis formula derived in the previous section, it is a relatively simple task to show that feeding the input signal first into a low-gain amplifier and then to the following booster amplifiers produces an asymptotic overall added noise of half a photon. Therefore, high gain is still necessary for quantum signal amplification, and the SQL always applies as the signal strength approaches the classical level. Hence, the term "quantum-limited amplification."

As we have briefly discussed, the operator $\hat{\mathcal{F}}$ is associated with additional degrees of freedom beyond the input and output channels during the amplification process. To examine the role of this extra degrees of freedom, we first notice the RHS of Eq. (5.21) becomes negative when $G > 1$. To address this mathematically, one easy solution is to transform $\hat{\mathcal{F}}$ and $\hat{\mathcal{F}}^\dagger$ into

$$\hat{\mathcal{F}} = \sqrt{G-1}\hat{d}^\dagger,\ \hat{\mathcal{F}}^\dagger = \sqrt{G-1}\hat{d}, \tag{5.28}$$

where $\hat{d}$ and $\hat{d}^\dagger$ denote a single additional mode for the amplification process. By introducing two additional modes instead of one, one can show that the overall added noise is larger than the minimum half-quantum of noise at high gain [24]. It can be interpreted as a waste of information, as the extra degrees of freedom are not monitored during the measurement process, and therefore, the information becomes lost. With the new definition of $\hat{\mathcal{F}}$, we can

write the amplifier input-output/scattering relation Eq. (5.20) as

$$\hat{a}_{\text{out}} = \sqrt{G}\hat{a}_{\text{in}} + \sqrt{G-1}\hat{d}^{\dagger}. \tag{5.29}$$

5.2.2 Phase-Sensitive Amplifiers

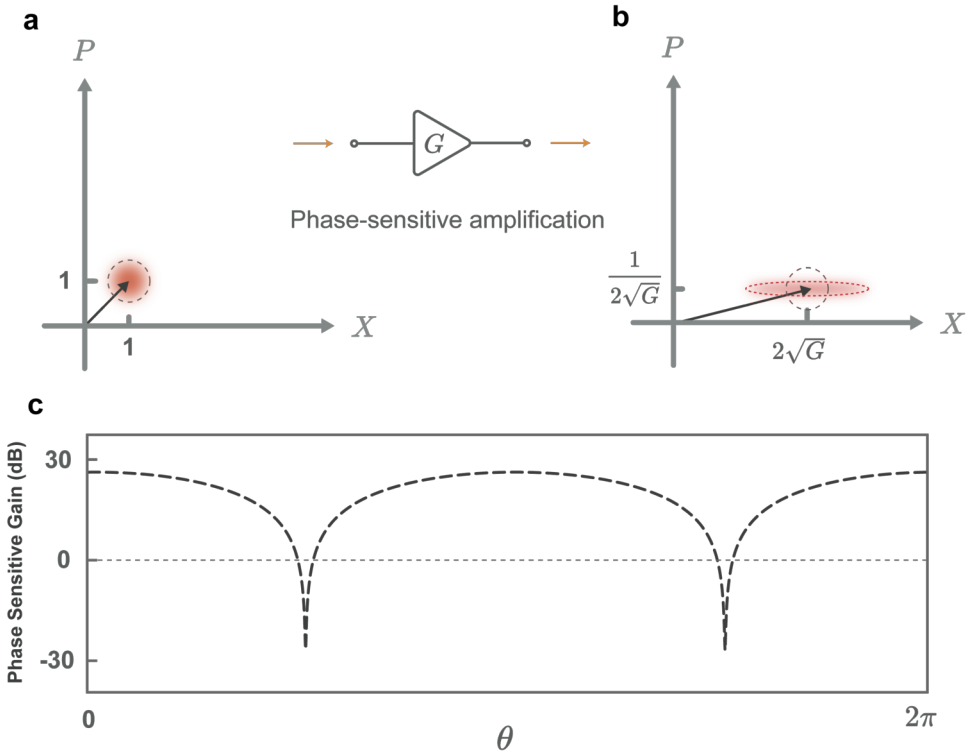

Figure 5-5. | **Phase-sensitive amplification. a.** Diagram of an input coherent state vector in phase space. The uncertainty "blob" represents vacuum fluctuations, and the dashed circle denotes the input noise. **b.** Phase-sensitive amplification along the X quadrature. The signal amplitude and fluctuations are increased along the X quadrature and decreased along the P quadrature. **c.** Phase-sensitive gain as a function of phase, in which the amplification depends on the relative phase θ between the pump and the signal, providing either amplification or de-amplification of the quadrature.

In a phase-preserving amplifier, the signal and idler gains are insensitive to the phase of the incoming signals, and the amplifier equally amplifies the I and Q components of the signals. At exact degenerate pumping, $\omega_{\text{p}} = 2\omega_{\text{s}}$, the signal and idler frequencies coincide in frequency, leading to a correlation between their amplified counterparts as well. The resultant output field becomes sensitive to the relative phase θ between the incoming signal and the pump phase as shown in Fig. 5-5(c). As we have seen in the previous section,

the idler mode can transfer its associated fluctuations to the signal mode from which the amplifier noise originates. Bringing the signal and idler frequencies together in frequency means fluctuations in both modes can now interfere. This is the basis for phase-sensitive amplifiers. The phase sensitivity in the amplification process implies that a fixed phase relationship exists between the pump and the signal — they interfere constructively (phase-sensitive amplification) and destructively (phase-sensitive de-amplification). Equivalently and without loss of generality, there will be an amplified (or anti-squeezing) quadrature $\hat{a}_{\mathrm{out}}^{\dagger}$ and a de-amplified (or squeezed) quadrature $\hat{a}_{\mathrm{out}}$,

$$\hat{a}_{\mathrm{out}}^{\dagger} = 2\sqrt{G}\hat{a}_{\mathrm{in}}^{\dagger}, \quad \hat{a}_{\mathrm{out}} = \frac{1}{2\sqrt{G}}\hat{a}_{\mathrm{in}}, \tag{5.30}$$

where the factor of 2 comes from the interference between the signal and idler. If the input mode is a vacuum state, this suggests we can suppress the fluctuation amplitude $2\sqrt{G}$ times smaller than the vacuum. While the amplifier treats the two quadratures differently, the commutation relation can be satisfied without the extra degrees of freedom and added noise as needed in the phase-preserving amplification. The result suggests noiseless amplification is possible if we are only interested in measuring one-half of a pair of non-commuting observables since there is no fundamental limit to how well we can measure it. This is advantageous for quantum metrology applications, e.g., the qubit state measurement, since its information can be mapped to a phase shift. One caveat for phase-sensitive amplification is maintaining phase coherence between the signal and pump sources. We will see how we can achieve that in an experiment in Chapter 6. From a different perspective, the pump tone plays the role of a clock in a phase-sensitive amplifier, with the pump phase picking out the quadrature of the signal to be amplified.

5.3 Parametric Amplification

Time-dependent parameters in a physical system typically result in resonant responses at specific modulation frequencies. This generic parametric resonance occurs in a significant number of both quantum mechanical and classical systems. In the latter case, a

representative example is a playground swing set. The parents often drive the motion of a child by pushing them, directly contributing energy to the swing's motion. Sometimes, the children swing themselves higher by standing up and bending their knees at the right moment. Physically, the children modulate their center of mass at twice the swing's natural frequency, as shown in Fig. 5-6. This is a mechanical "pumping" action — adding energy to the swing's motion and amplifying the initial conditions — a classical illustration of parametric amplification.

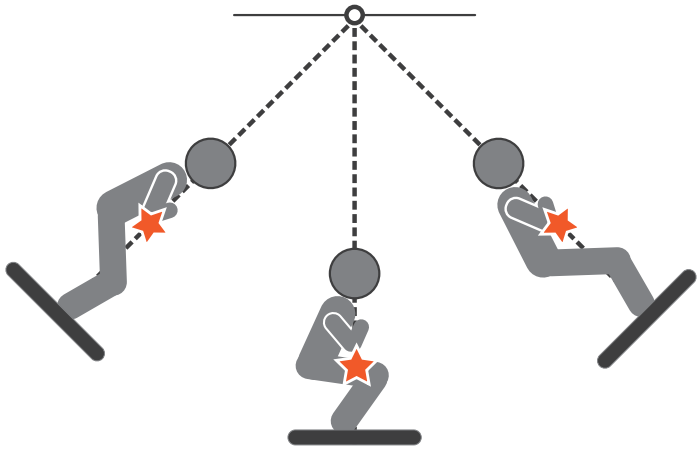

Figure 5-6. | Parametric amplification of pendulum motion by a child standing on a swing. The amplification is driven by changing the center of mass (star), and thus effective length of the pendulum at twice the swing's natural frequency.

Like the swing example where the children need an initial push from the parents or kick themselves off the ground at their first swing, a classical system must initially be displaced from the equilibrium state as a condition for parametric amplification. There are many sources of fluctuations that can break the equilibrium. Still, in principle, classical mechanics allows the oscillator's position and momentum to become zero simultaneously, which sharply contrasts with a quantum mechanical oscillator where the uncertainty relation inhibits the absence of motion. This suggests vacuum noise that corresponds to the ground state of the quantized oscillator may be parametrically amplified. Consequently, it may intensify the overall system noise in quantum readout applications. However, the action of amplification on quantum fluctuations leads to the squeezing effect, a purely quantum mechanical manifestation of parametric amplification.

Parametric amplifiers operate by periodically modulating specific parameters of a dy-

namical system. The modulation tone, or pump, produces amplification of a signal mode incident on the system at a different frequency rather than directly transferring energy to the signal. In general, the parametric process involves a pump tone at a frequency ω_{p} that couples at least two other modes, traditionally called the signal and the idler at frequencies ω_{s} and ω_{i}, respectively. Energy from the pump gets transferred to the signal mode via the creation of an idler. Parametric amplification is a fundamental wave-mixing process that typically occurs through either a three-wave-mixing process (TWM) or a four-wave-mixing process (FWM). The wave-mixing relationship is essentially a statement of energy conservation. In TWM, the relationship is given by

$$\omega_{\mathrm{p}} = \omega_{\mathrm{s}} + \omega_{\mathrm{i}}, \tag{5.31}$$

where one pump photon is converted to one signal and one idler photon. In 4WM,

$$\omega_{\mathrm{p1}} + \omega_{\mathrm{p2}} = \omega_{\mathrm{s}} + \omega_{\mathrm{i}}, \tag{5.32}$$

where two pump photons (same frequency) are converted to one signal and one idler. This is called the NDFWM process as defined in Sec. 2.2 or DFWM when $\omega_{\mathrm{p1}} = \omega_{\mathrm{p2}}$. In either case, if the signal and idler modes are degenerate with $\omega_{\mathrm{s}} = \omega_{\mathrm{i}}$, ω_{s} will be an integer multiple of ω_{p}, indicating a well-defined phase relationship between the pump and the signal. Thus, only the in-phase component of the signal concerning the pump will be amplified. In other words, a degenerate parametric amplifier can support phase-sensitive amplification. In most of the thesis, I will focus on 4WM processes, as none of the devices operate in a 3WM model.

5.4 A Brief History of Superconducting Parametric Amplifiers

In nonlinear optics, a crystal with a nonlinear index of refraction is used as the amplifier system, such that a coherent pump tone will periodically modulate the index of refraction.

When a material with nonlinear polarization is excited with an intense electromagnetic field, a weak signal field can get amplified via the interaction with the medium. An analogous device can be realized in an electrical circuit by modulating the impedance. For microwave parametric amplification, the role of the nonlinear medium can be played by the nonlinear inductance of a superconducting circuit composed, for example, of Josephson junctions. Josephson amplifiers reaching near quantum-limited performance were first demonstrated by Bernard Yurke's work in the late 1980s [126, 125]. The squeezing of vacuum fluctuations has also been observed [74]. In the early 2000s, many groups started and continued their research on microwave quantum-limited amplifiers due to a strong interest in cQED devices [114, 11, 116], especially in the field of quantum computing. The goal of achieving single-shot and high-fidelity qubit readout in cQED motivated the development of these superconducting Josephson amplifiers. Josephson bifurcation amplifiers (JBA) [100, 67] reached an initial breakthrough result by exploiting the bi-stable regime of an RF-driven Josephson junction. Afterward, Castellanos-Beltran et al. observed amplification and quadrature squeezing of an input signal with resonant Josephson parametric amplifiers [17]. Since then, tremendous progress has been made towards improving the amplifier bandwidth [77, 94], saturation point [16, 85], circuit schemes [121, 92, 32, 40], frequency tunability [101] and non-reciprocity [70, 59].

Even with these remarkable improvements, the resonant circuit architecture constrains the bandwidth for JPAs, significantly hindering broadband applications, such as multiplexed readout of many qubits or broadband squeezed microwave photon generation. These limitations propelled the development of traveling-wave parametric amplifiers (TWPAs), a more generic category for the Josephson-TWPA (JTWPA) introduced earlier in Chapter 1. Early theoretical and experimental work on TWPAs emerged in the 70s-90s [104] with technologies such as heterostructure transistors and vacuum tubes. With superconducting circuits, TWPAs have the advantage of operating over a much larger fractional bandwidth compared with optical amplifiers with nonlinear optical fibers [1]. Some of the early superconducting TWPAs demonstrations were realized with modern nano-fabrication techniques, exploiting nonlinear elements such as kinetic inductance of disordered superconductors [47] or Josephson junctions. In 2015, the first demonstration of near quantum-

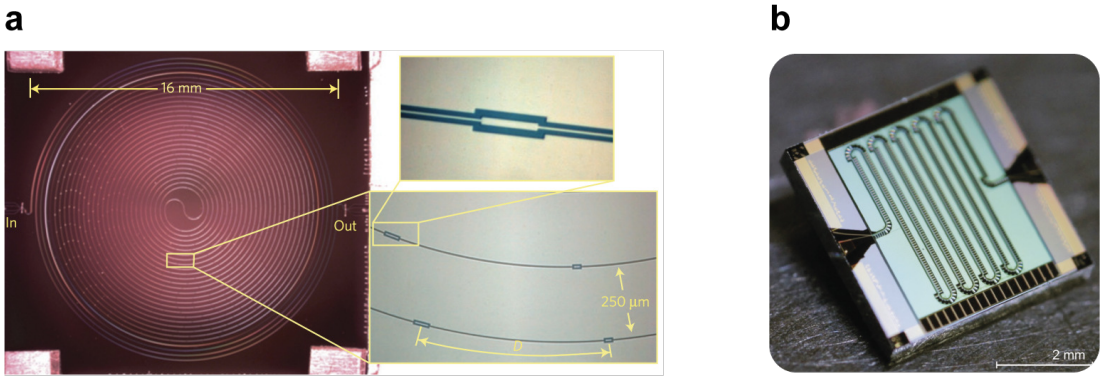

Figure 5-7. | **Traveling-wave parametric amplifiers with superconducting circuits. a.** The picture shows the kinetic-inductance-based TWPA in the form of a long NbTiN CPW line arranged in a double spiral. The line is periodically loaded by widening a short section, producing the stop band and dispersion characteristics [47]. **b.** Photograph of a Josephson-TWPA consisting of a chain of Josephson junctions [61].

noise-limited JTWPA was accomplished [61], and it serves as a blueprint for the JTWPA work in this thesis. On a broader scope, these are crucial experimental hallmarks for exploring TWPA technology based on the kinetic inductance of superconducting thin films and Josephson metamaterials.

The signal gain can be enhanced by increasing the interaction time in the nonlinear medium via two main strategies. The first one, resonant amplification, consists of placing the nonlinear medium in a cavity; in this way, the interaction time will be as long as the inverse of the cavity linewidth. This approach, however, puts a constraint on the amplification bandwidth, which also depends on the cavity linewidth. The second strategy, traveling wave amplification, consists in optimizing the gain by increasing the physical length of the nonlinear medium, removing the constraint on the amplification bandwidth given by the presence of a cavity. Next, we will mathematically examine the system dynamics of two types of amplifier.

5.5 Resonant Josephson Parametric Amplifiers

Although various resonant implementations of parametric systems exist, we here focus on the resonator-based Josephson parametric amplifier (JPA). In realizing a parametric amplifier using superconducting circuits, we modulate the impedance with a time-varying

circuit element — a Josephson junction. When the junction is driven with a pump wave oscillating at $\omega_{\rm p}$, the Josephson inductance L_j varies approximately as $I_{\rm p}(t)^2$, the square of the current traversing through the junction. Since $I_{\rm p}(t)^2$ is always positive, the inductance is effectively modulated at frequency $\omega_{\rm p}$. To realize a JPA (Fig. 5-8), the junction is embedded inside an lumped-element LC resonator that resembles a superconducting transmon qubit. The JPA is a nonlinear oscillator similar to the transmon except with a much weaker anharmonicity and effectively behaves as a classical nonlinear oscillator. To tune the resonant frequency of a JPA, we replace the nonlinear inductor with a dc SQUID, which acts as a single Josephson junction with a flux-tunable critical current (recall Eq. (2.49)). The small-signal resonant frequency of this circuit is given by

$$\omega_0 = \frac{1}{\sqrt{L_{\rm SQUID} C}}, \tag{5.33}$$

where $L_{\rm SQUID}$ is the effective inductance of the SQUID given by Eq. (2.49), namely, $L_{\rm SQUID} = \Phi_0 \left[4\pi I_0 \cos\left(\pi\Phi_{\rm ext}/\Phi_0\right) \cos\phi_+\right]^{-1}$. The inductance can be increased by either applying a flux through the SQUID loop(s) to induce a circulating current in the SQUID(s) or driving current across the SQUID(s) directly. Therefore, as shown in Fig. 5-8, the JPA resonance can be modulated by a flux-pump at $2\omega_0$ (orange) or a direct current-pump at ω_0 (green), leading to parametric gain and squeezing. Several other pumping schemes exist, including sideband pumping (or "double-pumping" — a technique we exploit in the dual-pump JTWPA) [14] and even subharmonic pumping [75]. A resonant geometry is essential to enhance the coupling between the signal wave and the modulation of the Josephson junction. Much like a child on a swing pumping their legs to go higher, a small signal amplifies by parametrically modulating the resonance frequency of the JPA with a pump tone.

We will not give the detailed derivation of JPA dynamics because it is not a major focus of the thesis, and a more in-depth treatment has been discussed extensively in other works [15, 33]. Nevertheless, it is crucial to understand the limitations of the resonator-based JPA and the motivations for developing a traveling-wave approach. Due to the resonant structure, the JPA amplifies signals within a finite frequency bandwidth, B, about its resonance frequency. In the linear regime, where no amplification occurs, the bandwidth is

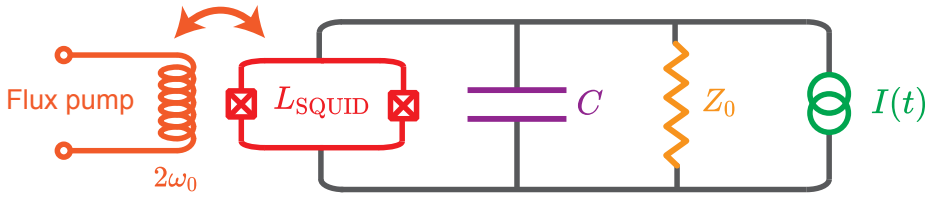

Figure 5-8. | Circuit diagram for a Josephson parametric amplifier. The nonlinear resonator is formed with the dc SQUID and shunt capacitor, loaded by a transmission line modeled as a lumped impedance Z_0 and driven by an ideal current source $I(t)$ model for the pump source or a flux pump oscillating at twice the resonance frequency.

determined by the quality factor of the resonator $Q = \omega_0 Z_0 C$, set by the choice of circuit parameters such as the shunt capacitor C and the lumped impedance Z_0 of the feedline. Equivalently, $B \sim \omega_0/Q$. As the drive power increases toward the critical power of the JPA $\sim I_0^2$, the gain increases, and the resonance steepens, effectively decreasing the amplification bandwidth. This trade-off is known as the *gain-bandwidth product*, and is loosely defined as

$$B\sqrt{G} \propto \frac{1}{Q}. \tag{5.34}$$

Thus, it is possible to increase both the gain and the bandwidth independently by lowering the Q. However, we cannot make Q arbitrarily small, as eventually higher-order nonlinear processes become dominant and destabilize amplifier operation. Typical gain-bandwidth products for JPAs are on the order of $100\,\mathrm{MHz}$, implying $B = 10\,\mathrm{MHz}$ with $20\,\mathrm{dB}$ gain [17]. Some devices demonstrate gain-bandwidth products on the order of $1\,\mathrm{GHz}$ [77].

The gain-bandwidth product is one of the most challenging design constraints in improving the JPA performance. Moreover, there are further tradeoffs associated with the saturation point (or input compression power). The nonlinear dynamics of the resonator limit the input compression power, typically constrained to be $5 - 10\%$ of the critical current [104]. Lowering the shunt capacitance C is a way to reduce the quality factor Q. However, keeping the JPA resonant frequency invariant requires a fixed ratio of I_0/C. Thus, we also need to reduce the critical current, which decreases the compression power.

One possible way to avoid this problem is by decreasing the environmental loading impedance Z_0 via an impedance transformer to convert the standard $50\,\Omega$ environment to

a smaller value. One such device has been demonstrated with $Z_0 = 50\,\Omega$ and achieved a much larger bandwidth [94, 77], although the small numbers of junctions inside the JPA still curbs the saturation point. We need to eliminate the resonator and enhance the nonlinear interaction through a different approach to address the fundamental limitations of the JPA.

5.6 Josephson Traveling-Wave Parametric Amplifiers

With the nonlinear inductor that is the Josephson junction, we can construct a nonlinear transmission line shown in Fig. 5-9(c) and start deriving the coupled wave equations to achieve parametric amplification in a traveling-wave amplifier. We will show the overall gain is dependent not only on the pump strength but also on the phase-matching condition. More information can be found in Yaakobi's paper [120]. For the section on parametric amplification, we shall closely follow the derivation in the paper by O'Brien et al. [78].

5.6.1 Continuum Wave Equation

Let us start our discussion with the most basic model of a lossless distributed transmission line consisting of linear serial inductance L and capacitance to ground C_0 per length a along the transmission line as displayed in Fig. 5-9(a). Applying Kirchhoff's voltage and current laws, we get a set of coupled partial differential equations — the so-called telegrapher's equations — that describe the voltage $V(x,t)$ and current $I(x,t)$ at position x and time t.

$$\begin{cases} \dfrac{\partial}{\partial x}V = -\dfrac{L}{a}\dfrac{\partial}{\partial t}I & \text{(5.35a)} \\ \dfrac{\partial}{\partial x}I = -\dfrac{C_0}{a}\dfrac{\partial}{\partial t}V. & \text{(5.35b)} \end{cases}$$

Substituting Eq. (5.35b) into Eq. (5.35a) and taking the second derivative with respect to x, we get the voltage wave equation

$$a^2\frac{\partial^2}{\partial x^2}V - LC_0\frac{\partial^2}{\partial t^2}V = 0, \tag{5.36}$$

whose solution describes a forward and a backward voltage traveling wave through the

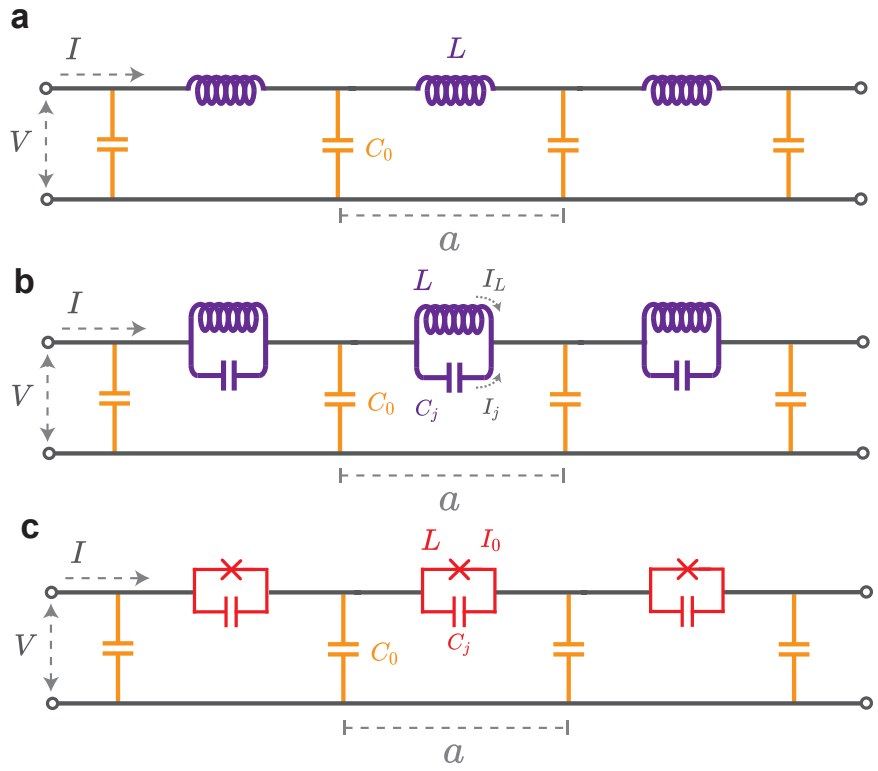

Figure 5-9. | **Different transmission line models. a.** A linear transmission line model with inductance L and capacitance C_0. **b.** Linear transmission line model with an additional shunting capacitance in parallel with the inductance. **c.** Josephson nonlinear transmission line model. The "X" symbol denotes a Josephson junction. a denotes the length of a unit cell, and I_0 is the critical current of the Josephson junction.

transmission line with linear dispersion $k = \frac{\omega\sqrt{C_o L}}{a}$, i.e., a pulse propagating along this transmission line retains its shape as a function of time. This is due to the fact the group delay dispersion is zero — $\mathrm{d}^2\omega/\mathrm{d}k^2 = 0$ — for a linear-dispersion system, which also means the group velocity $\mathrm{d}\omega/\mathrm{d}k$ remains constant.

Next, we will consider the model with an additional shunting capacitor C_j in parallel with the linear inductor L as shown in Fig. 5-9(b). The modified coupled partial differential equations are given by

$$\begin{cases} \dfrac{\partial}{\partial x}V = -\dfrac{L}{a}\dfrac{\partial}{\partial t}I_L & \text{(5.37a)} \\ \dfrac{\partial}{\partial x}I = -\dfrac{C_0}{a}\dfrac{\partial}{\partial t}V & \text{(5.37b)} \\ \dfrac{\partial}{\partial t}\left(L\dfrac{\partial}{\partial t}I_L\right) = \dfrac{\partial}{\partial t}\left(\dfrac{q_j}{C_j}\right) = \dfrac{I_j}{C_j} & \text{(5.37c)} \\ I_j + I_L = I, & \text{(5.37d)} \end{cases}$$

where Eq. (5.37a) and Eq. (5.37b) are the modified voltage and current relations according to Kirchhoff's laws, while we take the first derivative with respect to time of the equal voltage drop across L and C_j (q_j — charge on C_j) in Eq. (5.37c), and Eq. (5.37b) reflects the conservation of current. Solving this set of equations gives us a new voltage wave equation

$$C_0\frac{\partial^2}{\partial t^2}V - \frac{a^2}{L}\frac{\partial^2}{\partial x^2}V - a^2 C_j\frac{\partial^4}{\partial x^2\partial t^2}V = 0. \tag{5.38}$$

The equation has an additional term compared with Eq. (5.36) due to the presence of the shunting capacitance C_j. Consequently, the dispersion $k = \frac{\omega\sqrt{C_o L}}{a\sqrt{1-C_j L\omega^2}}$ can no longer remain linear with frequency because of the additional C_j. However, when $\omega \ll \omega_{\mathrm{J}}$ as defined below, the dispersion can be approximated to be linear as $C_j L\omega^2$ becomes negligible, meaning that in the context of a JTWPA, we can still treat the dispersion as linear within the frequency range of interest (4 - 8 GHz) below the junction plasma frequency (around 30 GHz) — its natural oscillation frequency given by $\omega_{\mathrm{J}} = 1/\sqrt{LC_j}$.

Finally, consider the nonlinear transmission line model replacing the linear inductance with a Josephson junction, as shown in Fig. 5-9(c). Because the junction is composed of two superconducting regions separated by a thin insulator, a more realistic junction model

would be a nonlinear inductor L shunted by its self-capacitance C_j. More specifically, as shown in Fig. 5-9(c), C_0 is the capacitance to ground, L is the junction inductance, C_j is the junction capacitance, I_0 is the critical current of the junction, a is the unit cell length, and ϕ is the phase across the junction. Based on the previous linear transmission line model Eq. (5.38) as well as the AC Josephson relation, the nonlinear wave equation describing the dynamics of JTWPA in terms of phase across the junction ϕ is the following

$$C_0\frac{\partial^2\phi}{\partial t^2} - \frac{a^2}{L}\frac{\partial^2\phi}{\partial x^2} - a^2C_j\frac{\partial^4\phi}{\partial x^2\partial t^2} = \frac{a^4}{2I_o^2L^3}\frac{\partial^2\phi}{\partial x^2}\Big(\frac{\partial\phi}{\partial x}\Big)^2. \tag{5.39}$$

The terms on the left-hand side represent the weakly dispersive linear system similar to Eq. (5.38), and the term on the right-hand side stands for the cubic nonlinearity from the junction. The equation is expressed in circuit parameters such as C_j and C_0. It can be shown that the combination of the weak dispersion and the cubic nonlinearity gives rise to parametric amplification via degenerate four-wave mixing (DFWM).

JTWPA Gain

We now proceed to show that the solution to this equation can be mapped on to the equations for an optical parametric amplifier that exists prior to a JTWPA. To solve the nonlinear wave equation, we propose an ansatz that the solutions shall be forward propagating waves in the form of

$$\phi = \frac{1}{2}\left[A_p(x)e^{i(k_px+\omega_pt)} + A_s(x)e^{i(k_sx+\omega_st)} + A_i(x)e^{i(k_ix+\omega_it)} + c.c.\right], \tag{5.40}$$

where subscripts i, s, p stands for idler, signal and pump respectively, and A_{m} is the amplitude of the slowly varying amplitude. To clarify the terminology used here: a pump can be considered as an external energy source to the system, e.g., a laser or a microwave tone; a signal represents an input we wish to amplify; an idler carries the energy difference between the absorbed pump and the amplified signal, and it plays an important role in nonlinear conversion processes such as squeezed light generation.

In order to achieve a solution to the parametric amplification model, we continue to

solve the nonlinear equation by substituting the expression for ϕ into Eq. (5.39) and making the slowly varying envelope approximation (SVEA) that neglects the second derivatives of A_{m}, i.e., we assume $|\frac{\partial^2 A_{\mathrm{m}}}{\partial x^2}| \ll |k_{\mathrm{m}} \frac{\partial A_{\mathrm{m}}}{\partial x}|$. In addition, we will neglect the first derivatives of A_{m}, i.e., we assume $|\frac{\partial A_{\mathrm{m}}}{\partial x}| \ll |k_{\mathrm{m}} A_{\mathrm{m}}|$. The wavevector k_{m} is defined as $\frac{\omega_{\mathrm{m}}\sqrt{C_o L}}{a\sqrt{1-C_j L \omega_{\mathrm{m}}^2}}$ using circuit parameters, where $\mathrm{m} \in p, s, i$. In the end, we can separate out the terms associated with pump, signal and idler respectively.

$$\frac{\partial A_p}{\partial x} - \frac{i a^4 k_p^5}{16 C_o I_o^2 L^3 \omega_p^2} A_p^2 A_p^* = 0 \tag{5.41}$$

This is the equation of propagation for the pump. The terms involving amplitudes for the signal and idler are neglected as they are small compared to the strong pump field. For the signal and idler, we also ignore terms that are quadratic in the signal and idler amplitudes, leaving:

$$\frac{\partial A_s}{\partial x} - \frac{i a^4 k_p^2 k_s^3}{8 C_o I_o^2 L^3 \omega_s^2} A_p A_p^* A_s = \frac{i a^4 k_p^2 (2k_p - k_i) k_s k_i}{16 C_o I_o^2 L^3 \omega_s^2} A_p^2 A_i^* e^{i \Delta k_L x} \tag{5.42}$$

$$\frac{\partial A_i}{\partial x} - \frac{i a^4 k_p^2 k_i^3}{8 C_o I_o^2 L^3 \omega_i^3} A_p A_p^* A_i = \frac{i a^4 (2k_p - k_s) k_s k_i}{16 C_o I_o^2 L^3 \omega_s^3} A_p^2 A_s^* e^{i \Delta k_L x}, \tag{5.43}$$

where $\Delta k_L = 2k_p - k_s - k_i$ is the phase mismatch term for DFWM process. Using Eq. (5.41), we can solve for the pump amplitude assuming no loss and an undepleted pump, meaning $A_p(x) A_p^*(x) = A_{p,0}^2$, where $A_{p,0}$ is the pump field amplitude entering the JTWPA at the beginning of the device.

$$A_p(x) = A_{p,0} e^{i \frac{a^4 k_p^5 A_p A_p^*}{16 C_o I_o^2 L^3 \omega_p^2} x}. \tag{5.44}$$

If we substitute $A_s = a_s e^{i\alpha_s x}$, $A_i = a_i e^{i\alpha_i x}$ and the above expression of A_p into Eq. (5.42) and Eq. (5.43), we have the coupled amplitude equations for the signal and idler:

$$\frac{\partial a_s}{\partial x} - i\kappa_s a_i^* e^{i(\Delta k_L + 2\alpha_p - \alpha_s - \alpha_i)x} = 0, \tag{5.45}$$

$$\frac{\partial a_i}{\partial x} - i\kappa_i a_s^* e^{i(\Delta k_L + 2\alpha_p - \alpha_s - \alpha_i)x} = 0, \tag{5.46}$$

The couplings α_m and κ_m between waves are defined as:

$$\alpha_p = \frac{\kappa_p k_p^3 a^2}{LC_0\omega_p^2}, \;\; \kappa_p = \frac{a^2 k_p^2 A_{p,0} A_{p,0}^*}{16 I_0^2 L^2}, \tag{5.47}$$

$$\alpha_s = \frac{\kappa_p k_s^3 a^2}{LC_0\omega_s^2}, \;\; \kappa_s = \frac{\kappa_p (2k_p - k_i) k_s k_i a^2}{LC_0\omega_s^2}, \tag{5.48}$$

$$\alpha_i = \frac{\kappa_p k_i^3 a^2}{LC_0\omega_i^2}, \;\; \kappa_i = \frac{\kappa_p (2k_p - k_s) k_s k_i a^2}{LC_0\omega_i^2}. \tag{5.49}$$

The coupling terms $\alpha_p, \alpha_s, \alpha_i$ are associated with changes of the pump wavevectors, signal, and idler due to self-phase and cross-phase modulations dependent upon the strength of the pump field. We will demonstrate this effect experimentally in Chapter 6. These are more specific descriptions of the nonlinear optical effects in Eq. (2.38) in the context of a JTWPA. As expected, the strength of the coupling terms depend on the pump amplitude, and they can alter the phase-matching conditions. Reaching the end of the derivation, the solutions are analogous to those for an optical parametric amplifier [2]:

$$a_s(x) = \Big[a_s(0)\Big(\cosh(gx) - \frac{i\Delta k}{2g}\sinh(gx)\Big) + \frac{i\kappa_s}{g}a_i^*(0)\sinh(gx)\Big]e^{i\Delta kx/2} \tag{5.50}$$

$$a_i(x) = \Big[a_i(0)\Big(\cosh(gx) - \frac{i\Delta k}{2g}\sinh(gx)\Big) + \frac{i\kappa_i}{g}a_s^*(0)\sinh(gx)\Big]e^{i\Delta kx/2}, \tag{5.51}$$

where the gain coefficient g is defined as $\sqrt{\kappa_s\kappa_i^* - (\Delta k/2)^2}$, with a phase mismatch of

$$\Delta k = 2k_p - k_s - k_i + 2\alpha_p - \alpha_s - \alpha_i. \tag{5.52}$$

As one can notice from the above solutions (Eq. (5.50) and Eq. (5.51)) for signal and idler amplitudes, if the phase-matching condition is achieved, i.e., $\Delta k = 0$, the gain becomes exponentially dependent on g, $a_s(x) \approx a_s(0)e^{gx}/2$. Otherwise, the gain is oscillatory and does not build to a large magnitude over the device length. Moreover, as pump

power is proportional to $A_{p,0}A_{p,0}^*$ (its value at the JTWPA input), so are the κ's and α's defined from Eq. (5.47) to Eq. (5.49), which scale according to the square of the pump current I_p. Therefore, the phase matching condition in Eq. (5.52) changes as a function of pump power, and we will observe this effect experimentally in Chapter 6.

5.6.2 JTWPA Phase-Sensitive Amplification

Parametric amplification can lead to squeezed state generation. More specifically, phase-sensitive gain is a necessary condition for single-mode squeezing. In this section, we are going to demonstrate phase-sensitive amplification from the same nonlinear wave equation Eq. (5.39) under different pump configurations.

Single-Pump Scheme

First of all, let us make a few simplifications. The signal and pump are degenerate in frequency, therefore, $\omega = \omega_s = \omega_p$, and $k = k_s = k_p$ follow. Assuming no idler input, we propose a modified ansatz of the solutions

$$\phi = \frac{1}{2}\left[A_p(x)e^{i(k_p x+\omega_p t)} + A_s(x)e^{i(k_s x+\omega_s t)} + c.c.\right]. \tag{5.53}$$

Following the same procedure as illustrated in the previous section, we substitute Eq. (5.53) into Eq. (5.39) and obtain the same expression as Eq. (5.41) for the propagation of the pump by making the same slowly-varying wave approximations. This is expected because nothing on the pump side has been changed. On the other hand, the propagation equation for the signal is modified:

$$\frac{\partial A_s}{\partial x} + \frac{ia^4k^5}{16C_oI_o^2L^3\omega^2}\left(-2A_pA_sA_s^* - A_p^2A_s^* - A_s^2A_s^* - A_p^*A_s^2 - 2A_pA_p^*A_s\right) = 0. \tag{5.54}$$

Since $A_s \ll A_p$, the terms that are quadratic in the signal amplitudes are neglected. The equation reduces to

$$\frac{\partial A_s}{\partial x} - i2\alpha_pA_s - i\alpha_pA_s^*e^{i2\alpha_p x} = 0, \tag{5.55}$$

in which Eq. (5.44) and the expression for α_p are substituted. Let $A_s(x) = a_s(x)e^{i\alpha_p x}$, the equation is further simplified to

$$\frac{\partial a_s}{\partial x} - i\alpha_p a_s - i\alpha_p a_s^* = 0. \tag{5.56}$$

The solution to this ordinary differential equation of the signal amplitude is

$$a_s(x) = A_{s,0}\cos\theta + iA_{s,0}(\sin\theta + 2\alpha_p x\cos\theta), \tag{5.57}$$

where $a_s(0) = A_{s,0}e^{i\theta}$, with $\theta \equiv \theta_{p,0} - \theta_{s,0}$ being the phase difference between the signal and the pump at the input of a JTWPA. The phase-sensitive gain G_{PSA} is:

$$G_{\mathrm{PSA}} = \frac{a_s(x)a_s^*(x)}{a_s(0)a_s^*(0)} = 1 + 4\alpha_p x\sin\theta\cos\theta + 4\alpha_p^2 x^2\cos^2\theta. \tag{5.58}$$

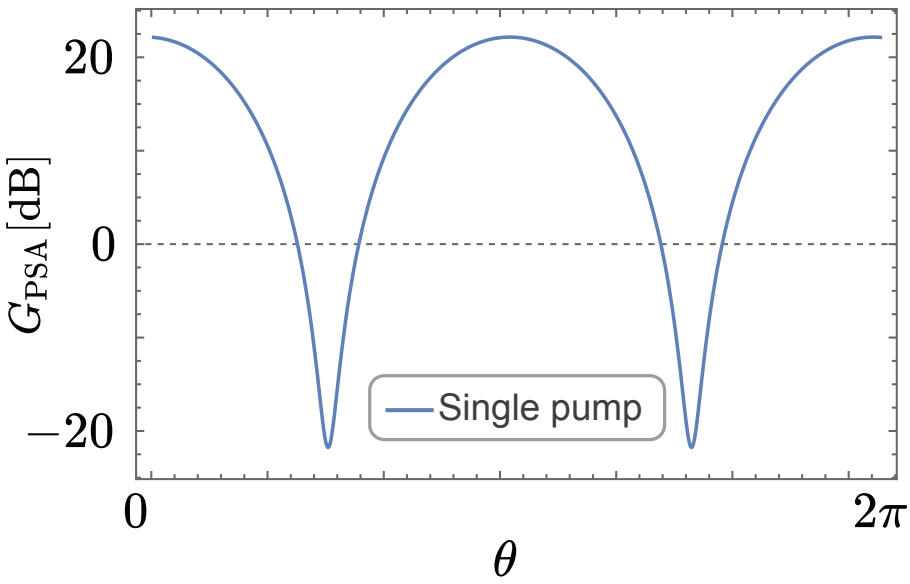

Figure 5-10. | **Single-pump phase-sensitive amplification.** Numerically simulated phase-sensitive amplification on a log scale of a JTWPA as a function of signal phase relative to the pump. For simplicity, parameters are set to $\alpha_p \to 0.00056$ and $x \to 3000$.

As displayed in Fig. 5-10, the gain changes as a function of the relative phase θ, a qualitative behavior that gives its name — phase-sensitive amplification. Here we assume the signal and pump are frequency-degenerate, which is not an ideal choice to operate the

JTWPA in practice. From Eq. (5.58), we can see the gain scales only quadratically instead of exponentially, because of phase mismatch due to the self-phase modulation effect caused by the strong pump. With the signal and pump at the same frequency, it is difficult to use dispersion engineering to mitigate such effects.

Dual-Pump Scheme

To address the fundamental phase-matching challenge due to the pump self-phase modulation, as we have seen in the single-pump case, a second pump tone is introduced, with both detuned from the signal frequency. As a result, it gives more degrees of freedom to set the phase-matching condition, as we will explore in Chapter 6. Here we will demonstrate from a mathematical perspective that a dual pump scheme can lead to an exponential phase-sensitive parametric amplification.

To begin with, a new ansatz of the solutions is:

$$\phi = \frac{1}{2}\left[A_{p1}(x)e^{i(k_{p1}x+\omega_{p1}t)} + A_{p2}(x)e^{i(k_{p2}x+\omega_{p2}t)} + A_s(x)e^{i(k_sx+\omega_st)} + c.c.\right], \tag{5.59}$$

where we assume no idler, but an additional pump field denoted with subscript p_2. Overall, the ansatz allows us to neglect the effect of degenerate four-wave mixing due to a single pump and focus on the dual-pump non-degenerate four-wave mixing instead. Nevertheless, the strategy in solving the differential equation does not change, since the nonlinear wave equation Eq. (5.39) remains the same, but now we have many more terms due to the additional pump.

After careful examination of different terms, we can group the ones for the signal, and its equation of propagation becomes:

$$\begin{aligned}\frac{\partial A_s}{\partial x} - \frac{ia^4}{8C_oI_o^2L^3\omega_s^2}\Big[&k_s^3\left(k_{p1}^2A_{p1}A_{p1}^* + k_{p2}^2A_{p2}A_{p2}^*\right)A_s \\ &+ k_s^2k_{p1}k_{p2}A_{p1}A_{p2}\left(k_{p1}+k_{p2}-k_s\right)A_s^*e^{i(k_{p1}+k_{p2}-2k_s)x}\Big] = 0.\end{aligned} \tag{5.60}$$

We define

$$\alpha_s^{\mathrm{DP}} = \frac{a^4 k_s^3}{8C_0 I_0^2 L^3 \omega_s^2} \left(k_{p1}^2 A_{p1} A_{p1}^* + k_{p2}^2 A_{p2} A_{p2}^* \right), \tag{5.61a}$$

$$\kappa_s^{\mathrm{DP}} = \frac{a^4 k_s^2}{8C_0 I_0^2 L^3 \omega_s^2} k_{p1} k_{p2} A_{p1,0} A_{p2,0} (k_{p1} + k_{p2} - k_s), \tag{5.61b}$$

where $A_{p1,0}$, $A_{p2,0}$ are pump amplitudes at the input of a JTWPA. We then rewrite Eq. (5.60) as

$$\frac{\partial A_s}{\partial x} - i\alpha_s^{\mathrm{DP}} A_s - i\kappa_s^{\mathrm{DP}} A_s^* e^{i(k_{p1}+k_{p2}-2k_s+\alpha_{p1}+\alpha_{p2})x} = 0, \tag{5.62}$$

where α_{p1}, α_{p2} are the respective phase modulation terms caused by pumps, similar to Eq. (5.47). Again, by making the substitution $A_s = a_s e^{i\alpha_s^{\mathrm{DP}} x}$, the equation of propagation is simplified to

$$\frac{\partial a_s}{\partial x} - i\kappa_s^{\mathrm{DP}} a_s^* e^{i(k_{p1}+k_{p2}-2k_s+\alpha_{p1}+\alpha_{p2}-2\alpha_s^{\mathrm{DP}})x} = 0. \tag{5.63}$$

Phase matching $\Delta k^{\mathrm{DP}} = k_{p1} + k_{p2} - 2k_s + \alpha_{p1} + \alpha_{p2} - 2\alpha_s^{\mathrm{DP}} = 0$ is achieved through dispersion engineering, and the solution to the signal propagation equation becomes:

$$a_s(x) = a_{s,0}\Big[\cos\theta \cosh(\kappa_s^{\mathrm{DP}} x) + \sin\theta \sinh(\kappa_s^{\mathrm{DP}} x) + i \left(\sin\theta \cosh(\kappa_s^{\mathrm{DP}} x) + \cos\theta \sinh(\kappa_s^{\mathrm{DP}} x) \right) \Big]. \tag{5.64}$$

The phase-sensitive gain $G_{\mathrm{PSA}}^{\mathrm{DP}}$ becomes:

$$G_{\mathrm{PSA}}^{\mathrm{DP}} = \frac{a_s(x) a_s(x)^*}{a_s(0) a_s(0)^*} = \cosh(\kappa_s^{\mathrm{DP}} x) + \sin(2\theta) \sinh(\kappa_s^{\mathrm{DP}} x) \tag{5.65}$$

Notice that the solution Eq. (5.64) now has an exponential dependence on the pump powers under the perfect phase matching condition. For phase mismatching, the solution will exhibit an oscillatory behavior, as we witnessed for the single-pump scheme. The $\theta \equiv \theta_{p,0} - \theta_{s,0}$ term is again the relative phase difference between the signal and the two pumps at the input of the JTWPA assuming no phase difference between the latter. The phase sensitive gain exhibits a similar trend with respect to the phase difference θ as shown in Fig. 5-10. As we can see, the gain is a function of the quadrature phase, which we will

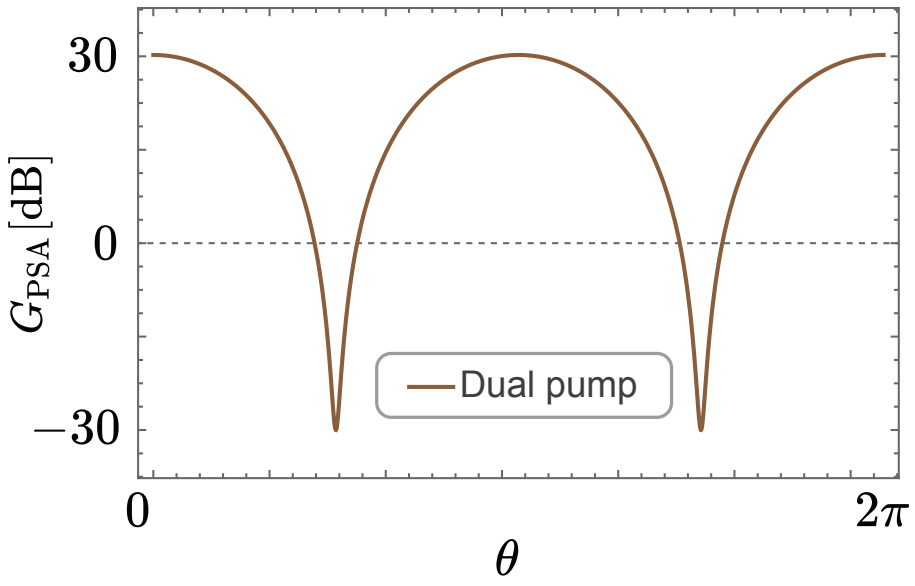

Figure 5-11. | **Dual-pump phase-sensitive amplification.** Numerically simulated phase-sensitive gain on a log scale of a JTWPA as a function of signal phase relative to the pump. For simplicity, parameters are set to $\kappa_s^{\mathrm{DP}} \to 0.00056$ and $x \to 3000$.

demonstrate experimentally in Chapter 6. More importantly, the unique capability of a phase-sensitive amplifier to amplify one quadrature while de-amplifying the other leads to anti-squeezing and squeezing as we discussed earlier in Sec. 5.2.2.

So far, we have presented the fundamental concepts behind using nonlinearity to generate parametric amplification. An important aspect of engineering a nonlinear device like the JTWPA is phase matching, especially in the presence of strong pump fields. In this chapter, we assumed phase matching without describing how it is experimentally achieved. In Chapter 6, we shall discuss the experimental realization of dispersion engineering to phase match different nonlinear processes selectively that will ultimately lead to the generation of interesting non-classical light — squeezed states.

Chapter 6

Development of Josephson Parametric Amplifiers

Dispersion engineering is a technique to create different desired phase-matching conditions. Phase matching is an essential concept in constructing a nonlinear system, especially in the presence of strong pump fields that can lead to unwanted nonlinear effects such as self-phase and cross-phase modulations discussed earlier in Chapter 2. This chapter will begin by illustrating the resonant phase-matching technique to counter these unwanted nonlinear effects, followed by highlights of two major single-pump JTWPA projects. The last part of this chapter will introduce non-degenerate four-wave mixing, which is used to generate phase-sensitive amplification and squeezing in Chapter 7. We will discuss the circuit design used to engineer the JTWPA dispersion and analyze the corresponding amplifier performance, including gain profile, bandwidth, 1-dB compression point, phase-sensitive amplification, etc. These are important metrics of a quantum amplifier that can affect the squeezing performance.

6.1 Phase Matching in a JTWPA

Let's first examine the simple case of a nonlinear transmission line consisting of Josephson junctions with a monochromatic pump. Below the plasma frequency (typically around 30 GHz) of the junction, the dispersion relation is approximately linear [78]. Ideally, with-

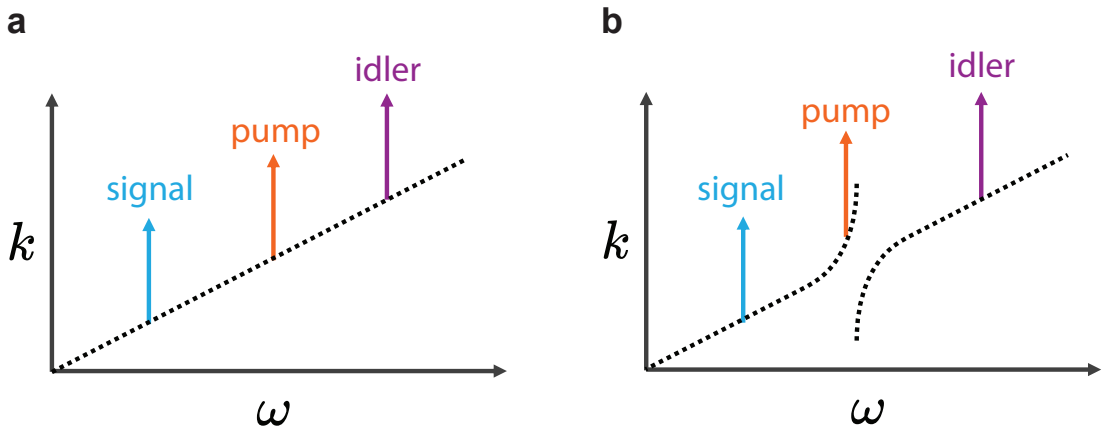

Figure 6-1. | **Dispersion engineering illustration. a.** Linear dispersion relation. **b.** Dispersion modification with phase-matching resonators opens up a stop band at their resonant frequency.

out a power dependence [negligible α's in Eq. (5.52)], the phase mismatch condition is $\Delta k = 2k_p - k_s - k_i$, where k_p, k_s and k_i are wavevectors of the pump, signal and idler, respectively. Shown in Fig. 6-1, a single pump tone creates an amplified signal and an idler, and the process is naturally phase-matched due to the linear dispersion relation. However, this depiction is only valid at zero pump power, as pump-power-dependent SPM and XPM processes would modify the phase-matching condition as the α's become larger. The resonant phase-matching technique is introduced to address these additional effects [78]. Fig. 6-2(b) shows the addition of phase-matching resonators, comprising a coupling capacitance C_c, resonator capacitance C_r and inductance L_r, the technique creates a dispersion feature, manifested as resonance at frequency $\omega_r = \sqrt{L_r C_r}$ in the JTWPA transmission profile; it alters the original, approximately linear wavevector near the resonance frequency of the phase-matching resonators as shown in Fig. 6-1(b). Adjusting the pump frequency around this dispersion feature can offset the additional SPM and XPM terms to the phase to achieve phase-matching. We will demonstrate the technique can be translated when adding a secondary pump field and discuss the performance of a dual-dispersion JTWPA in Sec. 6.4.

A typical way to operate a JTWPA is through a degenerate four-wave mixing (DFWM) process, which converts two pump photons into a pair of signal and idler photons that are equally spaced around the pump in frequency, as shown in Fig. 6-2(a). The DFWM process — $2\omega_\mathrm{p} = \omega_\mathrm{s} + \omega_\mathrm{i}$ — converts two frequency-degenerate pump photons (ω_p) into

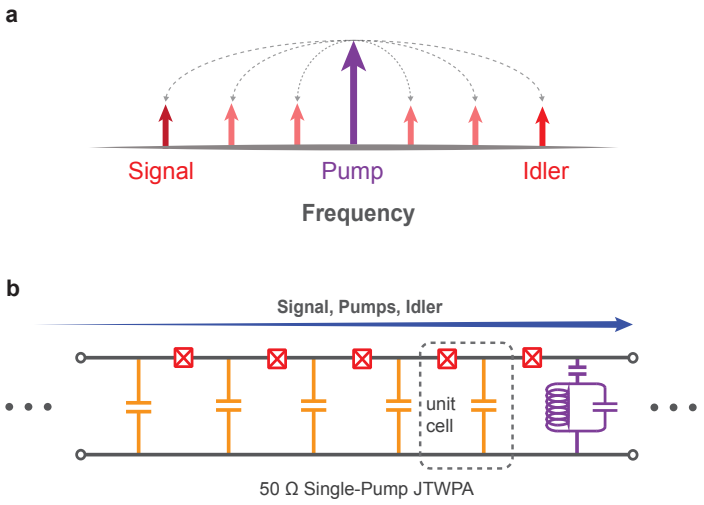

Figure 6-2. | **JTWPA nonlinear wave-mixing process and circuit schematic. a.** Degenerate Four-Wave Mixing (DFWM) process, where a pair of signal and idler photons are created symmetrically around the pump in frequency. **b.** Single-pump JTWPA circuit schematic. A repeating section of the single-pump JTWPA showing the L-C ladder that forms a 50 Ω transmission line from lumped elements and a phase-matching resonator.

an entangled pair of signal (ω_s) and idler (ω_i) photons. When $\omega_s \neq \omega_p$, energy conservation places the idler photon at a different frequency than the signal photon. This leads to two-mode squeezed photons and entanglement.

As first introduced in Chapter 5, the single-pump JTWPAs have been commonly deployed as near-quantum-limited amplifiers in the microwave C band (4-8 GHz) [61] and have been pushing the limit in multiqubit readout in quantum computing.

6.2 Low-Frequency (LF) JTWPA

Broadband amplifiers are essential in signal processing outside the C band in quantum computing, astrophysics and condensed matter physics. They can greatly reduce measurement time and enhance the signal-to-noise ratio. Several design considerations must be made before designing a JTWPA in a different frequency spectrum. First, the phase-matching resonators need to be redesigned to resonate in the hundreds of MHz range. Their frequency is given by $\omega_{LF} = 1/\sqrt{L_{LF}C_{LF}}$. Since ω_{LF} is now ten times smaller than a typical JTWPA operating at 7 GHz, for instance, the product $L_{LF}C_{LF}$ needs to increase by a factor 100 to achieve such a goal. Given that the chip layout is confined within

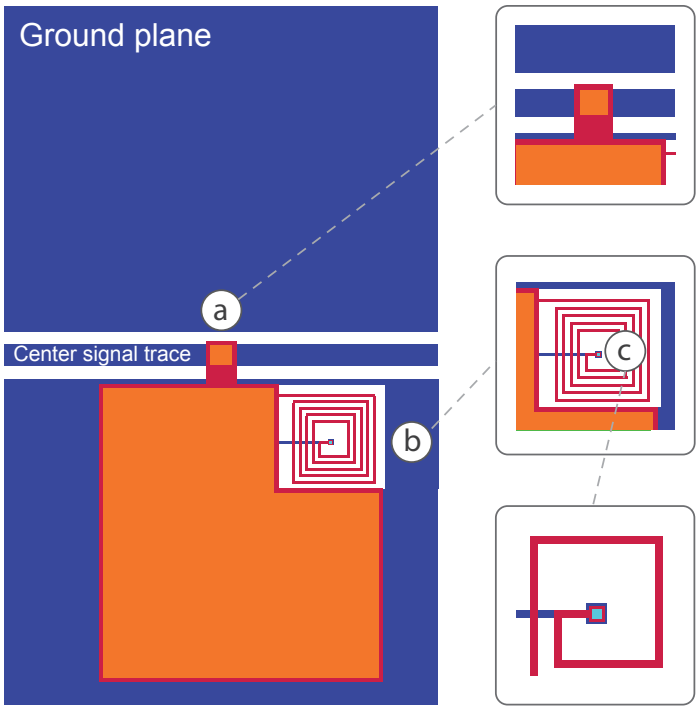

Figure 6-3. | **Low-frequency JTWPA phase matching resonator layout.** The blue region represents the ground plane, the red trace is the upper niobium plane, and the orange is the dielectric layer. **a.** Coupling capacitor C_c. **b.** Ground plane cutout for the spiral inductor with a spacing $3 \sim 5\,\mu\mathrm{m}$ to the ground plane. **c.** Via and underpass routing the circuit line from the top plane to the bottom.

a 5 mm by 5 mm area, we increase the capacitor pad of the phase-matching resonator and turn the inductor into a dense spiral shape to increase its geometric inductance. As a side effect, the self-capacitance of the spiral inductor also increases, leading to a red shift to its self-resonance condition. This phenomenon happens due to the parasitic capacitance of a realistic inductor (there is a finite capacitance between the inductor leads and between the spiral center traces). One can typically model it as a parallel capacitor across the inductor itself, as shown in Fig. 6-4(a). Sometimes, one includes an additional serial resistor as the loss channel for the inductor, which we can ignore since the inductor wire is made out of superconducting niobium. As the frequency increases, the parasitic reactance $X^C_{\mathrm{parasitic}} = 1/\omega C_{\mathrm{parasitic}}$ drops until it equals the inductive reactance $X^L_{\mathrm{LF}} = \omega L_{\mathrm{LF}}$, where $C_{\mathrm{parasitic}}$ is the parasitic capacitance of the inductor L_{LF}. The parallel capacitance and the inductor form a tuned circuit, leading to the so-called "self-resonance" condition. An EM simulation is performed to ensure the spiral inductor does not self-resonate within the

operating frequency band of the LF JTWPA. The simulation result can be seen in Fig. 6-4(b), where the self-resonant frequency occurs around 40 GHz, well above the operating frequency band.

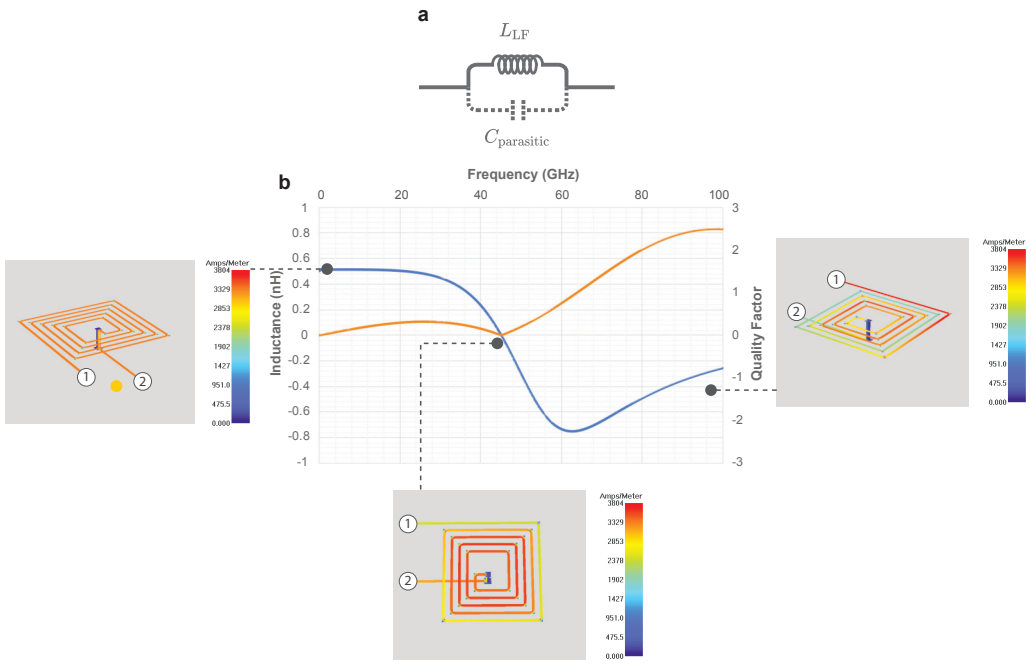

Figure 6-4. | EM simulation of self-resonant frequency of the spiral inductor inside the LF JTWPA. a. Circuit model for an inductor with the addition of its parasitic capacitance. Here we are ignoring the internal loss of the inductor. **b.** EM simulation of self-resonant frequency of the spiral inductor design (3D current density view — color bar represents current density). Labels 1 and 2 denote the simulation ports.

We adjust the design geometry through a iterative process to target the phase-matching resonator frequency ω_{LF} at $2\pi \times 700\,\mathrm{MHz}$. Fig. 6-5 displays a transmission profile of a phase-matching resonator capacitively coupled to a $50\,\Omega$ coplanar waveguide. Because a JTWPA's operability and gain performance depend on the dispersion feature, EM simulation drastically reduces the risk of design mistakes. In practice, the dispersion feature (Fig. 6-7) yields well and comes out very close to the design. Moreover, the LF JTWPA has low insertion loss of around -0.7 dB at 700 MHz, which has the potential of being a quantum-limited amplifier in comparison with the C-band JTWPA ($> -3\,\mathrm{dB}$ loss in comparison). A compatible set of microwave hardware is necessary to characterize and operate an LF JTWPA, such as its noise temperature. Unfortunately, there were no readily available off-the-shelf cryogenic isolators that would support the broadband operation of the LF

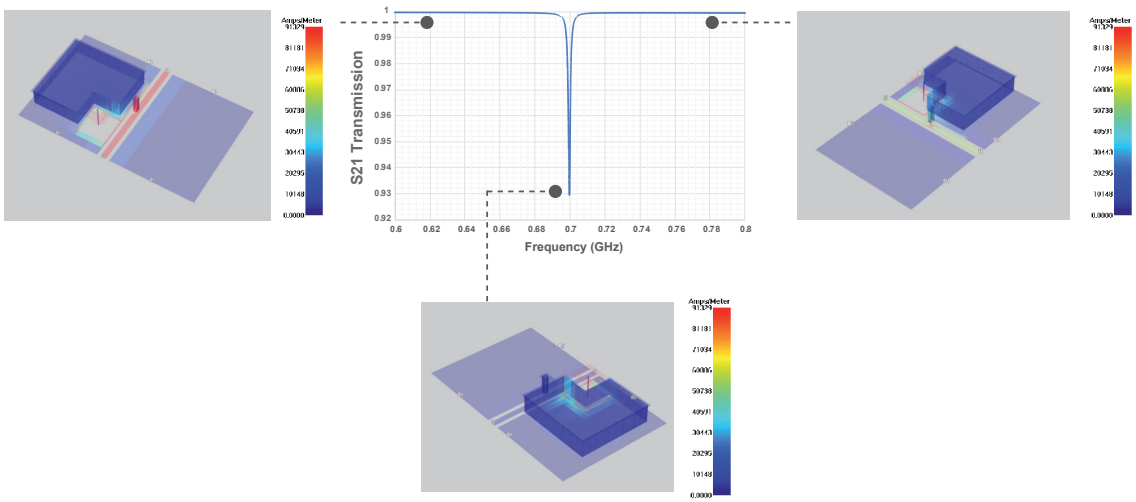

Figure 6-5. | **Dispersion feature EM simulation.** Simulation of a single phase matching resonator coupled to the a CPW transmission line (3D current density view — color bar represents current density).

JTWPA at the time of the experiment. Most of the measurement is done with a setup that involves at least two 20 dB cryogenic attenuators placed before and after the LF JTWPA to minimize any standing waves due to impedance mismatch. Developing the necessary microwave components for the LF JTWPA would be a crucial next step.

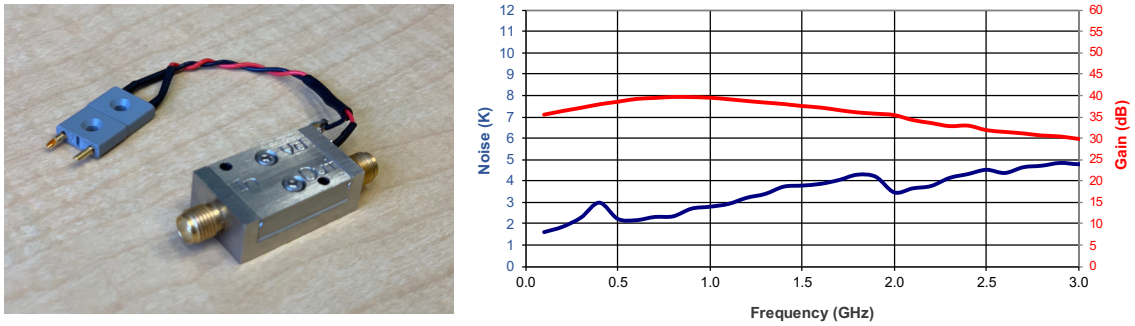

Figure 6-6. | **Low-frequency HEMT.** A sub-gigahertz HEMT shown to the left. Its gain and noise performance characterized at 4 K are shown to the right.

The LF JTWPA operating principle is similar to the C-band single-pump design [61]. In the end, the JTWPA successfully demonstrates greater than 20 dB parametric amplification and achieves an overall broadband gain from 500 MHz to 900 MHz (Fig. 6-8). The performance is many orders of magnitude higher than a resonator-based JPA within this frequency band [113]. Engineering a first-of-its-kind sub-gigahertz broadband super-

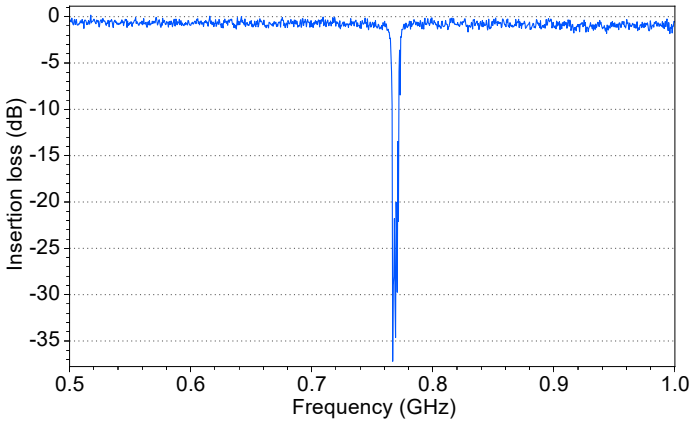

Figure 6-7. | **LF JTWPA transmission.** Experimental S21 of an LF JTWPA (pump off) normalized with respect to a microwave thru line. The plot shows the frequency of the dispersion feature and the LF JTWPA insertion loss from 500 MHz to 1 GHz.

conducting parametric amplifier enables many exciting quantum metrological applications below 1 GHz such as cryogenic sensing and spin qubit quantum computing.

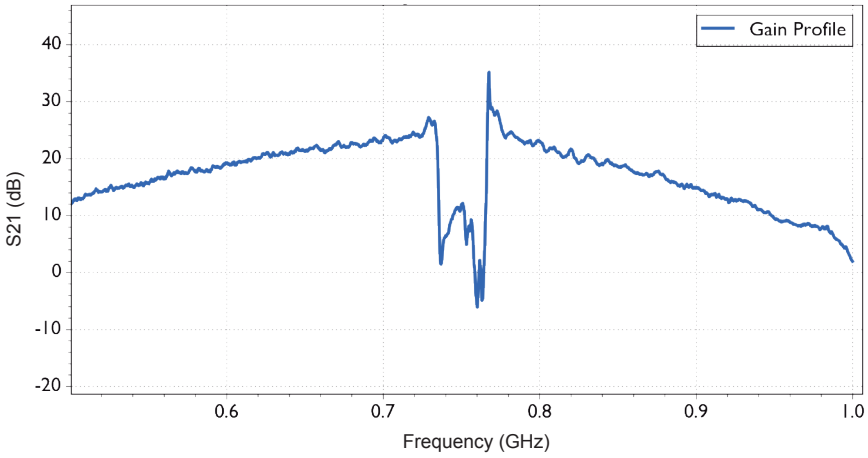

Figure 6-8. | **Parametric gain of an LF JTWPA.** Experimental on-off parametric gain of an LF JTWPA displaying broadband gain from 500 MHz to 1 GHz.

6.3 Aluminum (Al) JTWPA

The quantum efficiency (QE) of a JTWPA is greatly affected by the intrinsic loss of the device and coupling to higher frequency idler modes. Currently, most of the loss comes from defects in the dielectric material of a niobium-based, tri-layer JTWPA [95]. Theoretically, a smaller loss tangent can lead to a higher QE than existing designs. We aim to

improve QE by switching the fabrication to a planar aluminum process instead of a niobium tri-layer architecture. Note the higher QE is not related to the material property of aluminum or niobium as both metals become superconducting at the operating temperature of the JTWPA, but rather their associated fabrication process (planar or 3D) and oxide layer made of SiO_2 or Nb_2O_5.

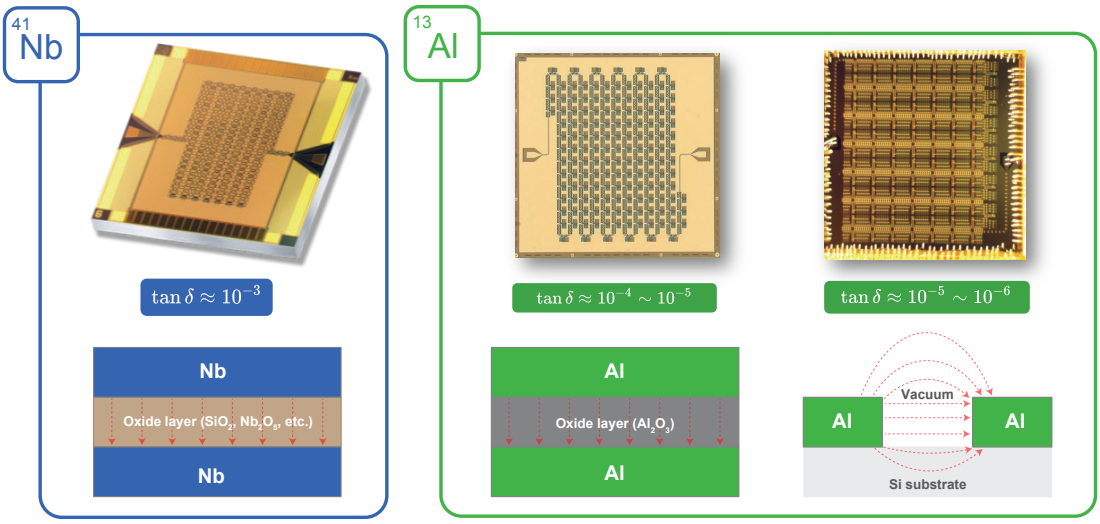

Figure 6-9. | **Nb vs. Al JTWPAs.** An illustration of Nb-based JTWPA (left) and its parallel-plate capacitors. The loss tangent associated with this process is characterized by the loss tangent $\tan\delta$. The red arrows portray the electric field in the capacitor. In contrast, the two Al-based JTWPA (middle: parallel-plate; right: CPW stub) design variants are shown with their respective capacitor structures.

To this end, we design and fabricate various aluminum-based, planar JTWPAs Fig. 6-9 using a qubit-compatible aluminum process to reduce insertion loss. We work closely with Kaidong Peng and Prof. Kevin O'Brien, who performed the design and simulation; MIT Lincoln Lab fabricated and packaged the devices. We primarily study the overall improved dielectric loss and broadband amplification in Al JTWPAs. There are two variants of the new Al JTWPAs. The first kind is the coplanar waveguide (CPW) stub design utilizing CPW stubs as the capacitor to ground (C_g) throughout the JTWPA. The second one is the parallel-plate capacitor (PPC) using aluminum oxide as its dielectric material. The CPW design helps understand the dielectric loss in the PPC, considering its loss tangent is about an order of magnitude lower than the latter. This is due to the higher electric participation ratio (higher concentration of the electric field) inside the aluminum oxide dielectric layer

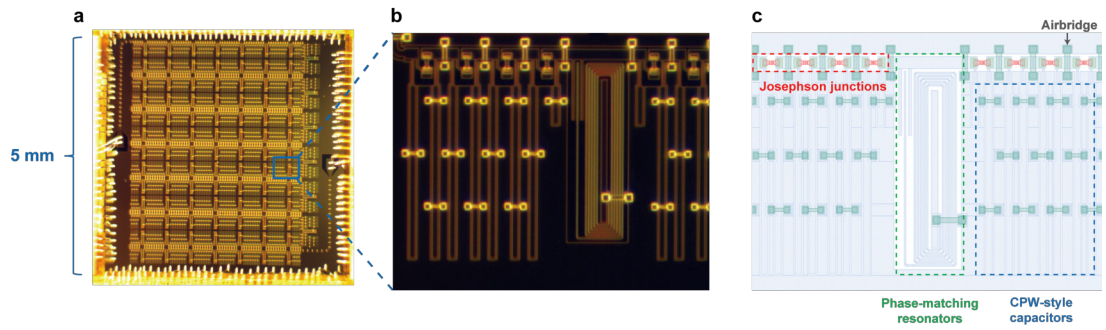

Figure 6-10. | **Al JTWPA with CPW stub design. a.** Microscopic image of the chip wire-bonded around the edges. **b.** A zoomed-in view of the JTWPA unit cell. **c.** GDS design schematic of the JTWPA unit cell showing various components.

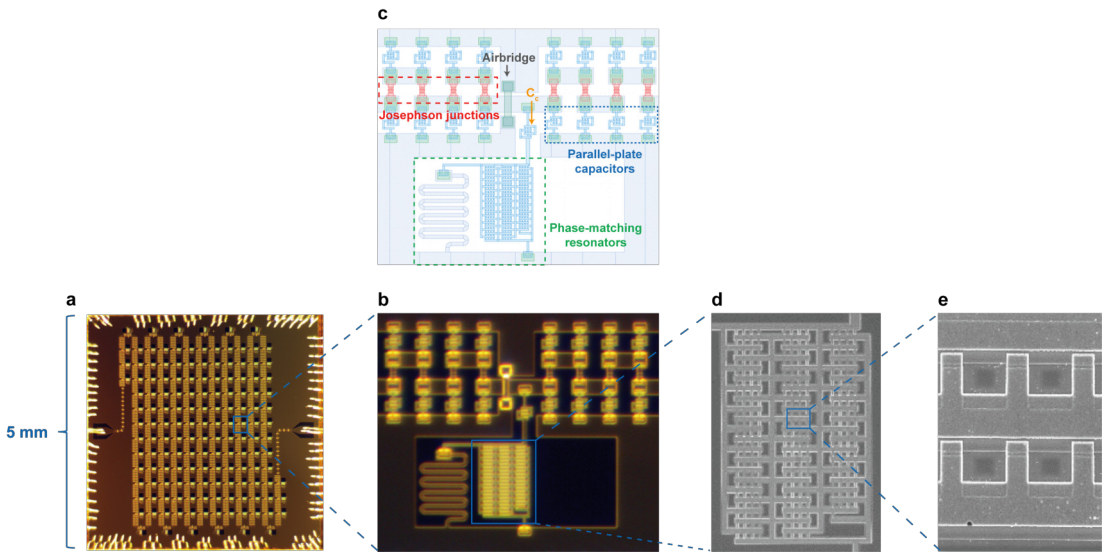

Figure 6-11. | **Al JTWPA with parallel-plate design. a.** Microscopic image of the chip wire-bonded around the edges. **b.** A zoomed-in view of the JTWPA unit cell. **c.** GDS design schematic of the JTWPA unit cell showing various components. **d.** SEM image of the capacitor arrays inside a phase-matching resonator. **e.** A zoomed-in view of some individual capacitors in (d).

in the PPC instead of media such as the vacuum or a pristine Si substrate. As shown in Fig. 6-10, one drawback of the CPW design is that it occupies a larger footprint, which limits the device lengths in the current fabrication run, given the chip size. However, this is not a hard limit as we can enlarge the chip size from 5 by 5 mm to 10 by 10mm or even larger.

Fig. 6-11 shows the second variant of the Al JTWPA using PPC with a few design highlights. The primary concern is the uniformity of the oxide layer in the PPC across the

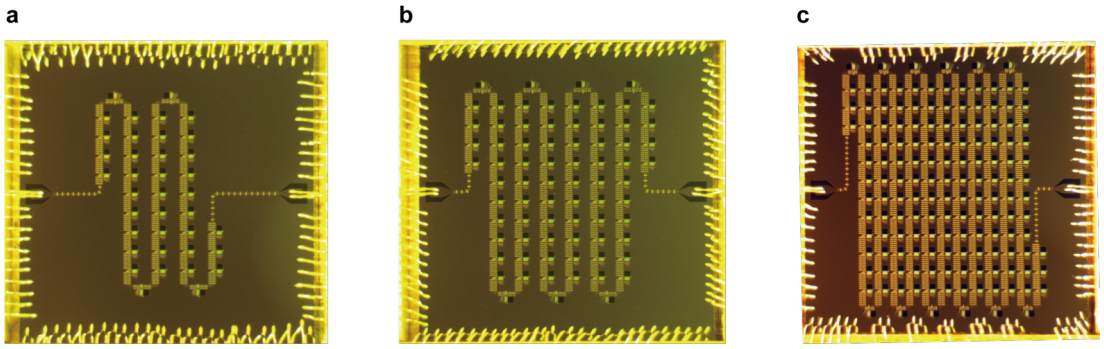

Figure 6-12. | **Al JTWPA with different lengths. a.** JTWPA with 300 unit cells. **b.** JTWPA with 600 unit cells. **c.** JTWPA with 1200 unit cells.

device and its impact on phase matching. The size of the coupling capacitor (C_c) is crucial, as too small of its value could not compensate for the phase mismatch, while too large of C_c would distort the band structure and reduces gain. Therefore, we design a variety of C_c sizes to compensate for the spread of capacitance up to 5% deviation from its nominal value.

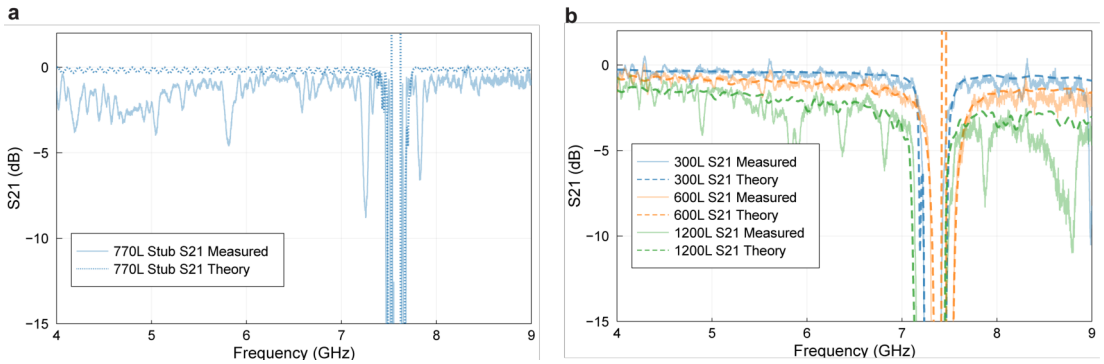

Figure 6-13. | **Transmission profiles of the two Al JTWPA designs. a.** S21 of the stub design. **b.** S21 of three parallel-plate designs with different number of unit cells.

To optimize the JTWPA gain performance, we vary the device length with a total number of 300 (300L device), 600 (600L device), and 1200 (1200L device) unit cells (Fig. 6-12) in addition to a combination of different characteristic impedance and coupling capacitance. The goal is to examine the tradeoff between device length (associated with gain) and density (related to crosstalk and other unwanted EM interactions).

We characterize and optimize the gain profiles of 300L, 600L, and 1200L devices shown in Fig. 6-14. The gain profiles demonstrate a maximum parametric amplification over

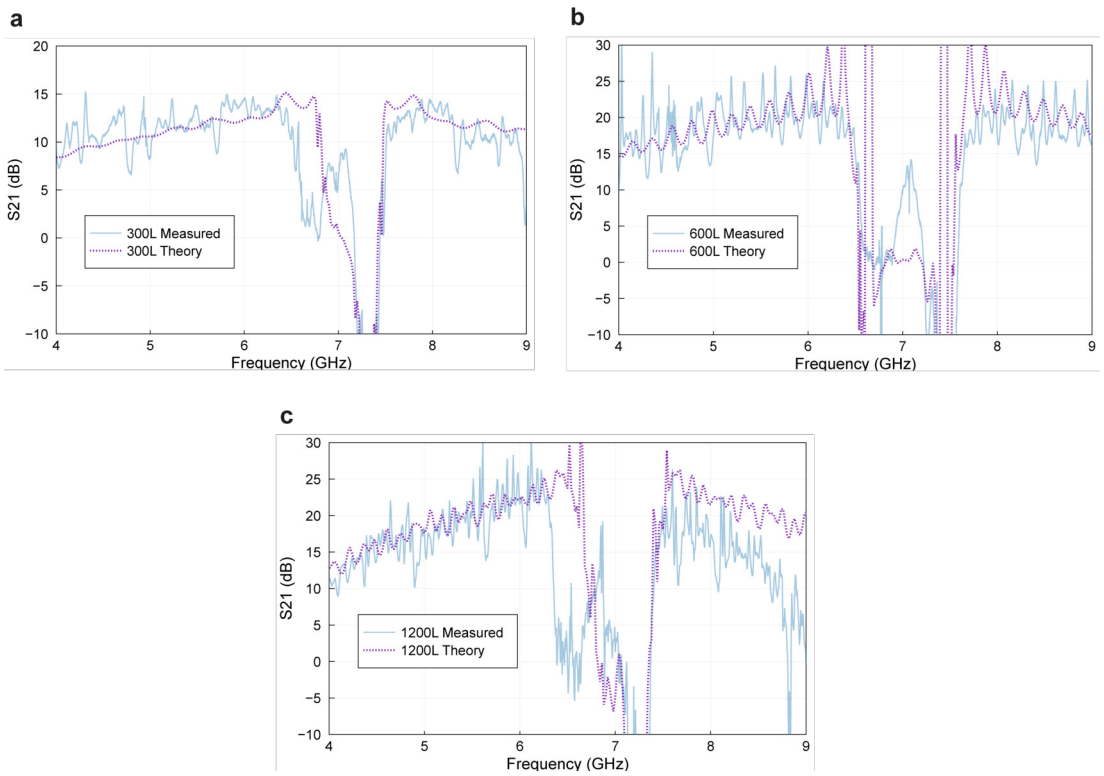

Figure 6-14. | Gain profiles of parallel-plate style Al JTWPAs. a. Optimized gain profile for the 300L device with a numerical simulation plotted together. **b.** Optimized gain profile for the 600L device with a numerical simulation plotted together. **c.** Optimized gain profile for a 1200L device with a numerical simulation plotted together.

20 dB and a broad bandwidth from 4-9 GHz, on par with the Nb version JTWPAs. Their respective insertion loss is displayed in Fig. 6-13. As we can see, the average loss below 7 GHz for the 600L is less than 2 dB — a significant improvement over the Nb JTWPA, which typically has more than 4 dB with a similar gain performance.

The work validates design and fabrication in the process of reducing intrinsic loss. It is an ongoing project at the time of writing this thesis, as we have seen issues such as unwanted EM coupling between adjacent signal lines, but the preliminary characterization helps guide future design iterations of Al JTWPAs in resolving these problems.

6.4 Dual-Dispersion JTWPA

Like a centrosymmetric crystal, the JTWPA junction nonlinearity features a spatial-inversion symmetry (in the absence of a DC current) that results in $\chi^{(3)}$-type nonlinear elec-

tromagnetic interactions. These support both degenerate-pump four-wave mixing (DFWM) and non-degenerate-pump four-wave mixing (NDFWM).

However, DFWM has two drawbacks when considering single-mode squeezing, $\omega_s = \omega_p$. First, the signal and idler frequencies coincide with the strong pump, resulting in self-phase modulation that leads to unwanted phase mismatch, which cannot be compensated through dispersion engineering [78]. Second, it is challenging to later separate the signal and idler photons from the "background" pump photons. These issues motivate us to consider a NDFWM process (Fig. 6-15) – $\omega_1 + \omega_2 = \omega_s + \omega_i$ — that generates both single-mode and two-mode squeezed states far from the pump frequencies ω_1 and ω_2. To do this, we introduce a JTWPA that uses two pumps and dispersion engineering to achieve the desired NDFWM interaction.

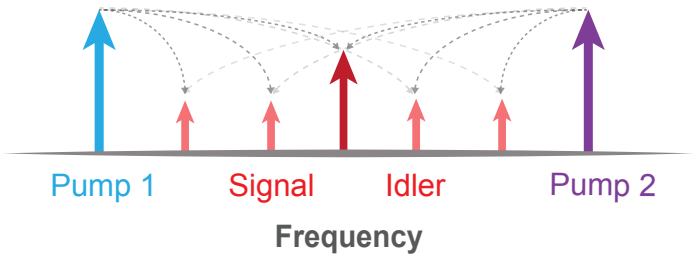

Figure 6-15. | Non-degenerate four-wave mixing (NDFWM) process. For NDFWM, the picture shows the special case when the signal and idler are at the same frequency ω_c at the center between the two pumps. In general, the signal and idler can be detuned from each other.

6.4.1 Chip Design

The dual-pump JTWPA is fabricated in a niobium trilayer process on 200-mm silicon wafers. This meandering nonlinear transmission line has 3141 Josephson junctions and shunt capacitors (Fig. 6-16b). These are parallel-plate capacitors with silicon dioxide as their dielectric material. In addition, the JTWPA features two sets of interleaved phase-matching resonators, one (purple) at $\omega_{r1} = 2\pi \times 5.2$ GHz and the other (blue) at $\omega_{r2} = 2\pi \times 8.2$ GHz (Fig. 6-16d). The phase-matching resonators comprise lumped-element parallel-plate capacitors with niobium pentoxide dielectric and meandering geometric inductors.

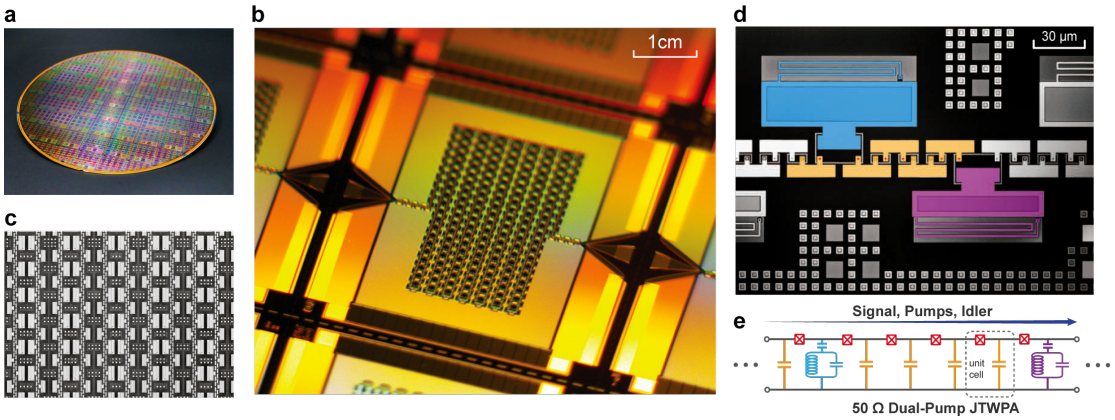

Figure 6-16. | Josephson traveling wave parametric amplifier dispersion engineered for a bichromatic pump. a. Multiple JTWPA chips fabricated on an 8-inch silicon wafer using a niobium trilayer process at MIT Lincoln Laboratory. **b.** Micrograph of a 5 mm $\times$ 5 mm JTWPA chip. **c.** Top-view confocal image of arrays of phase-matching resonators, capacitors to ground, and Josephson junctions (light gray). **d.** Zoomed-in view of the structure showing the low-frequency lumped-element phase matching resonator (blue), capacitors to ground C_g (orange), high-frequency lumped-element phase matching resonator (purple), and Josephson junctions (red). The color-coded elements correspond to the circuit schematic in panel (e). **e.** A repeating section of the dual-pump JTWPA. We can identify the L-C ladder that forms a 50 Ω transmission line from lumped elements and the two phase-matching resonators for dispersion engineering.

6.4.2 Wavevector

To characterize the phase-matching condition of a nonlinear process, we need to characterize the JTWPA dispersion as a function of frequency. The wavevector of a JTWPA can be extracted relative to that of a SMA coaxial through-line shown in Fig. 6-17. This measurement scheme aims to single out only the phase change induced by the JTWPA itself. To be more specific, the real part of the wavevector is measured via the phase of the transmitted field. However, due to the presence of other microwave components, the phase response incorporates an additional frequency-dependent phase ϕ_0, such that

$$\phi_{\mathrm{JTWPA}} + \phi_0 = k(\omega)L, \tag{6.1}$$

where k and L are the wavevector and length of the device. In contrast, the phase response from the through-line is:

$$\phi_{\mathrm{thru}} + \phi_0 = k_{\mathrm{thru}} L_{\mathrm{thru}} \tag{6.2}$$

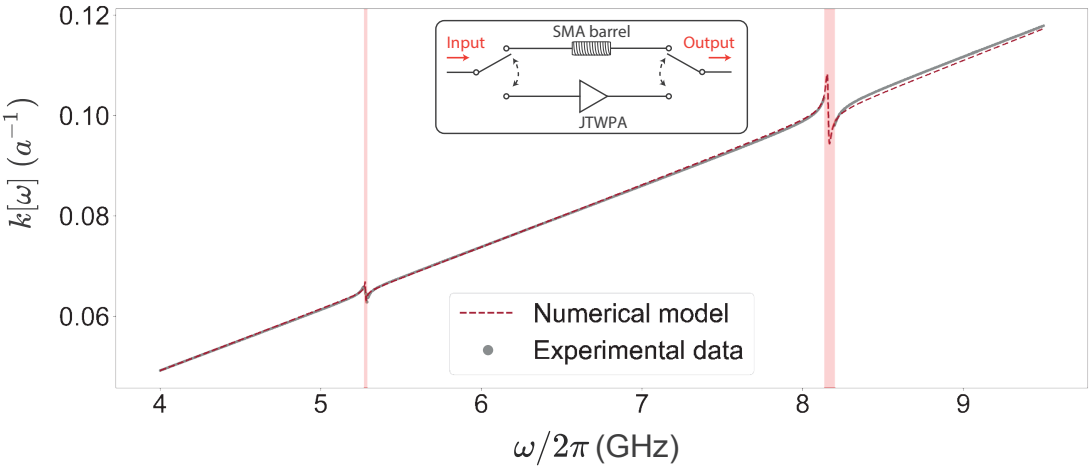

Figure 6-17. | Experimental data and numerical model for the JTWPA wavevector. The wavevector is experimentally characterized by measuring the phase of the transmission through the JTWPA when the pumps are turned off. The numerical model is calculated from the dispersion relation (see Eq. (A.5)) using fitted circuit parameters to match the experimental data. Crimson-shaded areas are regions where the phase inside the JTWPA cannot be fully resolved because the phase-matching resonators act as stop-band filters and reflect the probe back; the transmission is dominated by instrumental noise within the stopband. The inset shows the measurement schematic using a switch to calibrate the wavevector of a JTWPA.

By subtracting Eq. (6.1) from Eq. (6.2), we can ideally eliminate the offset ϕ_0. Furthermore, we can back out ϕ_{JTWPA} (which includes the effects from wirebonds, coplanar waveguide boards, etc.) given the through-line phase at DC is zero and the phase is approximately linear in our frequency range of interest [61].

6.4.3 JTWPA Insertion Loss

Circuit parameters for a dual-dispersion Josephson metamaterial

N(unit cells)	3141
C_0	28.616 fF
I_c	3.14 μA
Phase-matching LC resonator 1	
ω_{r1}	$5.2815 \times 2\pi$ GHz
C_{r1}	6.653 pF
C_{c1}	28.616 fF
Phase-matching LC resonator 2	
ω_{r2}	$8.169 \times 2\pi$ GHz
C_{r1}	2.441 pF
C_{c1}	28.616 fF
Pumps	
Ω_1	$5.2984 \times 2\pi$ GHz
Ω_2	$8.109 \times 2\pi$ GHz

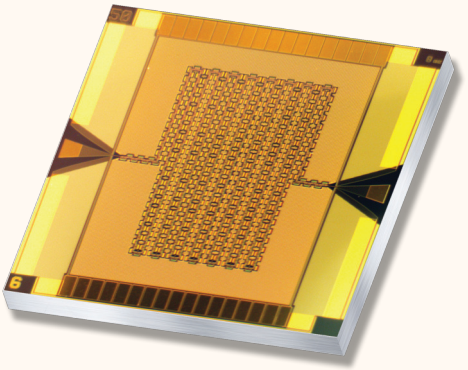

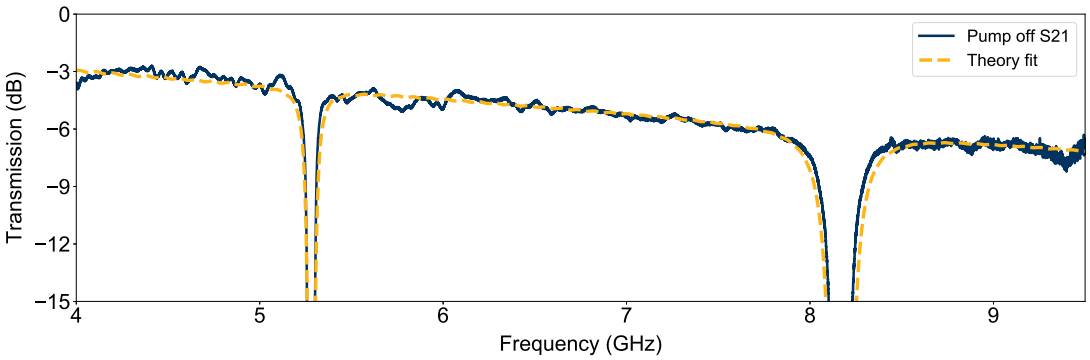

Figure 6-18. | **JTWPA insertion loss and theory fit.**

Utilizing the JTWPA circuit parameters obtained from modeling the measured wavevector in Fig. 6-17, we fit the measured insertion loss $|e^{i\tilde{k}(\omega)L}|$ using a single parameter of loss tangent $\tan\delta$ of 4.9×10^{-3}

$$\tilde{k}(\omega) = \frac{\omega\sqrt{L_g C_g(1 - i\tan\delta)}}{\sqrt{1 - \omega^2 L_J C_J}}\xi, \tag{6.3}$$

where

$$\xi = \Bigg[1 - \frac{C_{c1}+C_{c2}}{10C_g} + \frac{C_{c1}}{10C_g}\frac{1-\omega^2 L_{r1}C_{r1}(1-i\tan\delta)}{1-\omega^2 L_{r1}(C_{r1}+C_{c1})(1-i\tan\delta)} + \frac{C_{c2}}{10C_g}\frac{1-\omega^2 L_{r2}C_{r2}(1-i\tan\delta)}{1-\omega^2 L_{r2}(C_{r2}+C_{c2})(1-i\tan\delta)}\Bigg]^{1/2}, \tag{6.4}$$

ω is the frequency, L_J is the junction inductance, and L_r is the phase-matching resonator inductance. The expression of $\tilde{k}(\omega)$ above is obtained from the lossless formula Eq. (A.5) by replacing every capacitor term $C \rightarrow C(1 - i\tan\delta)$ to account for the dielectric loss tangent of the capacitors using a parallel RC model. In addition, the 1/10 factors appearing in the resonance terms account for the fact that each set of phase-matching resonators is only inserted once every ten unit cells.

Phase Mismatch for Different Processes

Pumping the JTWPA at two angular frequencies $\omega_{1,2}$ generates parametric amplification that satisfies the energy conservation relation $\omega_\mathrm{s} + \omega_\mathrm{i} = \omega_1 + \omega_2$ and leads to the desired single-mode and two-mode squeezing. However, NDFWM also creates unwanted photons through the frequency conversion process $|\omega_\mathrm{s} - \omega_{\mathrm{i}'}| = |\omega_1 - \omega_2|$, where $\omega_{\mathrm{i}'}$ is an extraneous idler angular frequency. This unwanted by-product does not participate in the desired two-mode squeezing, but rather, it is effectively noise that undermines squeezing performance. Fortunately, these unfavorable conversion processes are susceptible to phase mismatch and can be effectively reduced through dispersion engineering for a wide range of pump powers.

To understand the phase mismatch quantitatively as a function of pump power P_1 and P_2, we define an effective power-dependent phase mismatch for the parametric amplification (PA) process,

$$\begin{aligned}\Delta k(P_1, P_2) = (2k_{\omega_s} - k_{\Omega_1} - k_{\Omega_2}) &+ [2k_{\omega_s}(P_1) - k_{\Omega_1}(P_1) - k_{\Omega_2}(P_1)] \\ &+ [2k_{\omega_s}(P_2) - k_{\Omega_1}(P_2) - k_{\Omega_2}(P_2)]\,,\end{aligned} \tag{6.5}$$

where the quantity in the first parentheses is the "bare" (linear) phase mismatch due to the

linear dispersion of the JTWPA measured at low probe power (below single-photon level), the second group of terms in the bracket represents the pump 1 induced Kerr modulation, and the third set is the pump 2 power induced phase shifts. We need to account for all of these terms as we operate the device in the dual-pump scheme.

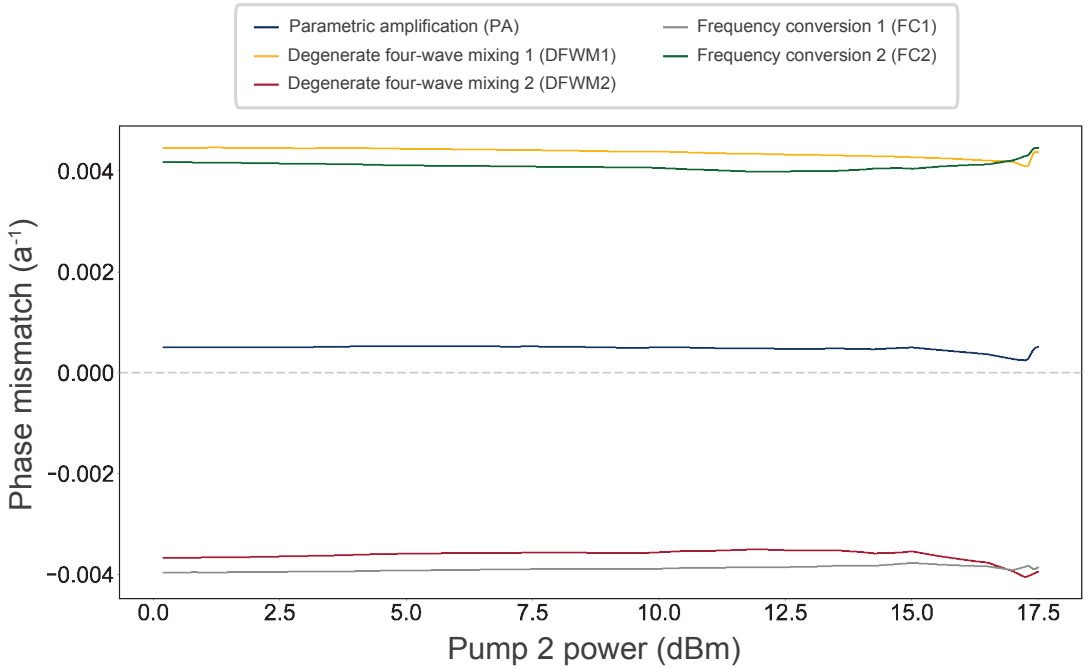

Figure 6-19. | Phase mismatch for different nonlinear processes. The phase mismatch is characterized as a function of pump 2 power with a fixed pump 1 power (the same power sweep performed in the squeezing measurement). The unwanted processes are highly phase-mismatched compared to the desired parametric amplification process (blue).

Similarly, we consider other two-pump-photon nonlinear processes that could lead to degradation in squeezing performance [83]. There are four major parasitic processes, and their corresponding phase mismatch are power-dependent as well and expressed as the following:

- Degenerate four-wave mixing 1 (DFWM1): $\Delta k_{\mathrm{DFWM1}}(P_1, P_2) = k_{\omega_s}(P_1, P_2) + k_{\omega_{i1}}(P_1, P_2) - 2k_{\Omega_1}(P_1, P_2)$
- Degenerate four-wave mixing 2 (DFWM2): $\Delta k_{\mathrm{DFWM2}}(P_1, P_2) = k_{\omega_s}(P_1, P_2) + k_{\omega_{i2}}(P_1, P_2) - 2k_{\Omega_2}(P_1, P_2)$
- Frequency conversion 1 (FC1): $\Delta k_{\mathrm{FC1}}(P_1, P_2) = k_{\omega_s}(P_1, P_2) - k_{\omega_{i1}}(P_1, P_2) - k_{\Omega_2}(P_1, P_2) + k_{\Omega_1}(P_1, P_2)$

- Frequency conversion 2 (FC2): $\Delta k_{\mathrm{FC2}}(P_1, P_2) = k_{\omega_s}(P_1, P_2) - k_{\omega_{i2}}(P_1, P_2) - k_{\Omega_1}(P_1, P_2) + k_{\Omega_2}(P_1, P_2)$

  with frequencies:

  - Ω_1: pump 1 frequency
  - Ω_2: pump 2 frequency
  - $\omega_s = (\Omega_1 + \Omega_2)/2$
  - $\omega_{i1} = 2\Omega_1 - \omega_s$
  - $\omega_{i2} = 2\Omega_2 - \omega_s$

Here k_ω represents the measured wavevector that accounts for both the linear dispersion and the nonlinear phase modulations from the pumps. It is related to a measurement of a phase $\Delta\phi(\omega)$ using $\Delta\phi(\omega) \sim k(\omega) \times L$. We perform a measurement as shown in Fig. 6-19, demonstrating the effectiveness of our dispersion engineering technique to suppress undesirable processes while achieving a large dual-pump gain. As an example shown in Fig. 6-20, we suppress (i.e. highly phase-mismatch) the unwanted DFWM processes (DFWM1 and DFWM2), leading to minimum gain. The results are illustrated by the blue and purple curves, representing the phase-preserving-parametric gain when only a single pump is turned on. They starkly contrast the broadband gain, as demonstrated in the next section, with the same pump parameters.

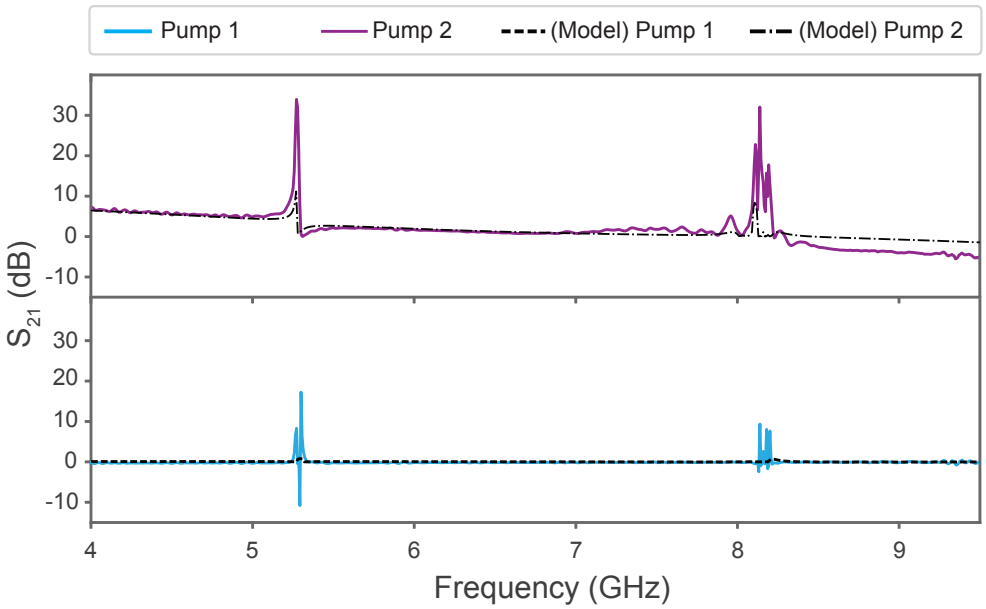

Figure 6-20. | **Single pump gain profiles.** Single pump gain and numerical simulations that fit and predict the gain profiles. The deviation between the model and the experimental data is expected to be caused by the bandwidth constraint of cryogenic components such as the isolator/circulator.

6.4.4 Gain Profiles

This section will present the experimental and simulated results of JTWPA gain with monochromatic and bichromatic pumps. The validated simulation is useful when designing future generations of amplifiers and squeezers and gives a quantitative description of the gain performance as a function of circuit parameters.

Experimental and Simulated Results of Single-Pump Gain

For this part of the measurement, we use a VNA as the pump. The basic procedure is to set the probe tone at the frequency of interest, strengthen the probe tone and observe the self-phase modulation (SPM) of the pump. By fitting the SPM data to the analytical equations solved in reference [78] as shown in Fig. 6-21, we can obtain a calibration factor β_{I_p} for the pump power at the device. A shown in Chapter 2, we expect a quadratic relation between the pump phase and the pump current, which is used as the fit model in the plot.

Moreover, we obtain the pump attenuation from the loss coefficients extraction based on the experimental data shown in Fig. 6-18. The attenuation is further used in solving the coupled differential equations for the parametric amplifier, as detailed in reference [78],

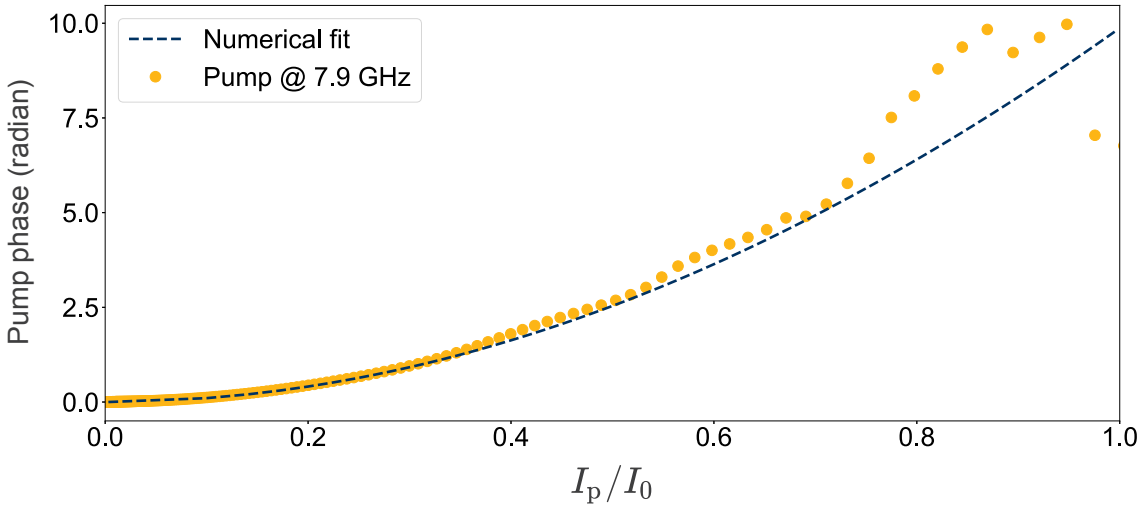

Figure 6-21. | Self-phase modulation data for a single pump at 7.9 GHz**.** The pump phase data is numerically fit as a function of pump current I_p in units of junction critical current I_0. The discrepancy between the fit and the data near the junction critical current can be observed by the gain degradation in Fig. 6-22, similar to the behavior reported in reference [62] as well.

with results shown in Fig. 6-22. The normalized gain is characterized at the signal frequency at 7 GHz for all four pump frequencies, and they are chosen without loss of generality to show the difference in JTWPA behavior. Overall, the experimental data follow the theoretical predictions (dashed line). The reason behind the less ideal amplification performance for pump frequencies at 7.4 GHz and 7.5 GHz is likely that the image of the dispersion feature around 8.169 GHz starts to influence the signal. In other words, we are pumping the JTWPA in a non-ideal regime for maximum parametric amplification at those pump frequencies.

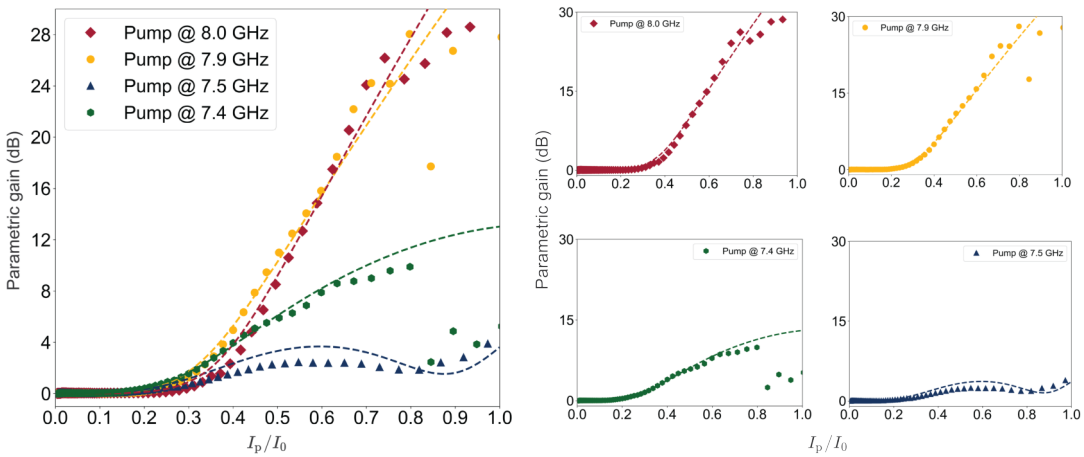

Figure 6-22. | Experimental and theoretical parametric gain with different pump frequencies. Solid markers represent experimental values while dashed lines represent the theoretical predictions.

Experimental & Simulated Results of Dual-Pump Gain

The efficiency of parametric amplification is determined by momentum conservation, i.e., phase matching [61]. To achieve this, we adopt the dispersion-engineering approach of Ref. [61] and extend it to two phase-matching resonators placed periodically throughout the amplifier. The resonator frequencies are chosen to be near-resonant with the desired pump frequencies. The modified admittance of the transmission line about these resonances leads to a rapid change in phase with frequency. Tuning the pump frequencies across the resonances thereby enables us to retune the pump phases periodically along the device and control the degree of phase matching.

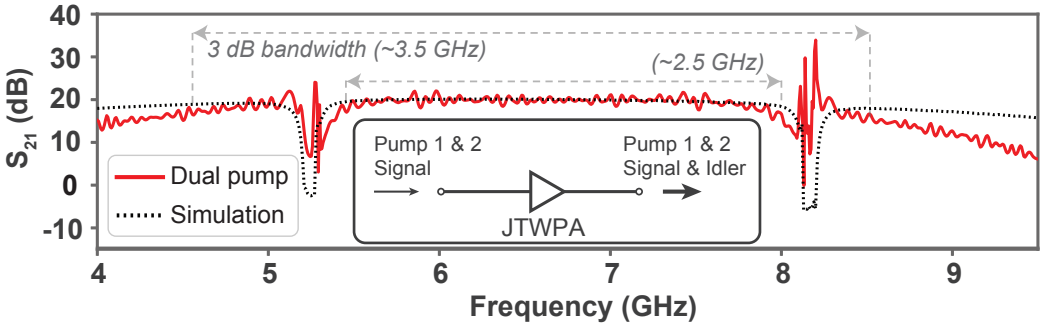

Figure 6-23. | Dual-pump phase-preserving gain. Phase-preserving gain measured using a microwave vector network analyzer (red line) and a numerical simulation of the gain profile (black dotted line). The total bandwidth between the two pumps is around 2.5 GHz, and the total 3 dB bandwidth across the entire gain spectrum is more than 3.5 GHz.

The precise selection of pump frequencies determines the phase matching condition and thereby enhances and suppresses different nonlinear processes. We preferentially phase match the parametric amplification process, $\omega_1 + \omega_2 = \omega_s + \omega_i$. This is achieved if $\Delta k_{12}^{PA} \simeq 0$, while all other processes are highly phase-mismatched as shown in Fig. 6-19. Experimentally, we sweep pump powers and frequencies in order to identify pump parameters that simultaneously maximize the dual-pump gain and minimize the single-pump gain. As shown in Fig. 6-23, with both pumps on, we obtain more than 20 dB phase-preserving gain over more than 3.5 GHz total bandwidth – comparable with the single-pump JTWPA [61] and significantly broader than JPAs [109, 65, 16, 127, 128]. The amplification metrics and the flat gain profile between the dispersion features are useful for applications such as multiqubit readout with frequency-multiplexed resonators.

6.4.5 1-dB Compression Point

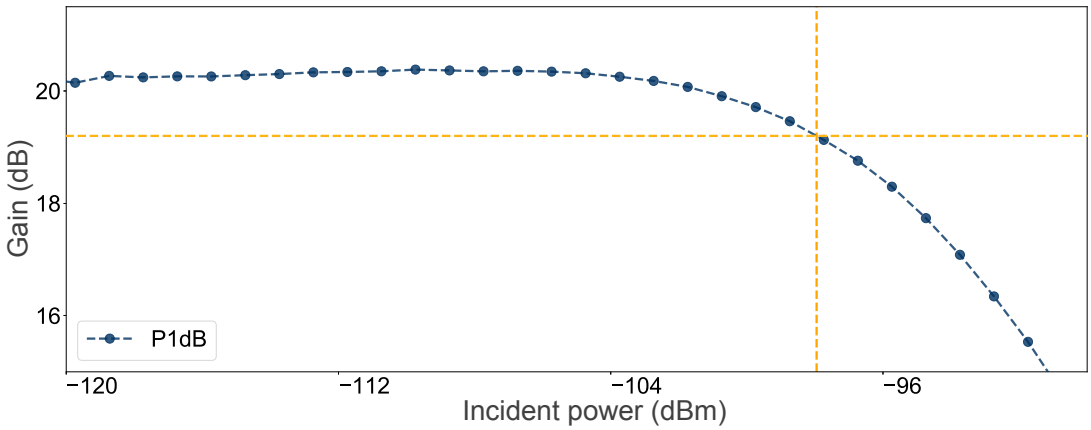

Figure 6-24. | **1-dB compression point.** JTWPA gain at 6.37 GHz as a function of incident power. The yellow crosshair indicates the 1-dB compression point.

The 1-dB compression point (P1dB) refers to the incident signal power level that causes the amplifier gain to deviate (decrease) by 1 dB from a perfectly linear device. Beyond this point, the linear amplifier might exhibit nonlinear effects such as frequency conversion to higher harmonics and signal distortion. Fig. 6-24 is measured at the signal frequency at 6.70 GHz. The input signal power is swept while the pump powers are fixed. We extract a P1dB value of -98 dBm, on par with the value reported for a single-pump JTWPA [61]. The

large dynamic range enables the JTWPA to be a bright source of squeezed microwave photons. This power level is capable of amplifying more than 35000 photons per microsecond ($P_{1\mathrm{dB}}/\hbar\omega$) within the microwave C-band (4-8 GHz) and 20 to 30 dB higher compared to a cavity-based amplifier [32, 9, 127]. JTWPA has the potential to generate bright squeezed microwaves for quantum teleportation experiments [91] and to enhance resonator-induced phase gate fidelity [87].

6.4.6 Phase-Sensitive Amplification (PSA)

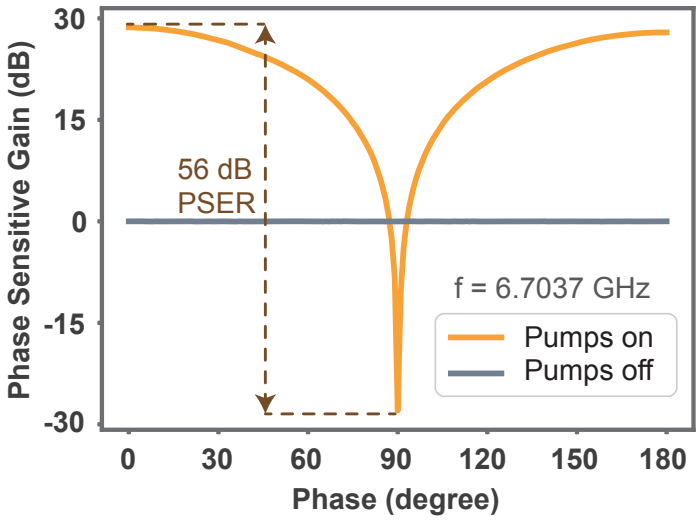

Figure 6-25. | Experimental data on phase-sensitive amplification. Experimental phase-sensitive amplification at $\omega_c = 2\pi \times 6.7037\,\mathrm{GHz}$. The phase-sensitive extinction ratio (PSER) is approximately 56 dB.

The JTWPA can also generate phase-sensitive interactions using a bichromatic pump, as has been previously shown in JPAs [14]. At the center of the two pump frequencies, $\omega_c = (\omega_1 + \omega_2)/2$, the signal and idler interfere constructively or destructively, depending on their relative phase, leading to phase sensitive amplification and deamplification. We characterize such interference by injecting a probe tone at frequency ω_c and measuring the amplifier output as a function of the probe phase θ_{probe}. Fig. 6-25 shows the JTWPA output phase-sensitive gain with pumps on (orange) normalized to the case with pumps off (gray). The phase-sensitive extinction ratio (PSER), defined as the difference between the maximum phase-sensitive amplification and de-amplification, is measured to be $56\,\mathrm{dB}$, which as

far as we know, the largest value reported to date with superconducting Josephson-junction circuits [109, 9, 127]. It is the first experimental demonstration of phase-sensitive amplification in a JTWPA, with the unique characteristic of providing amplification/deamplification to input signals at selective phases. Such a phase-sensitive amplifier is a valuable piece of readout technology in quantum computing — low-noise or even potentially noiseless amplification can boost the speed in qubit readout before the quantum state decays away [117, 29, 28]. Furthermore, phase-sensitive amplifiers can improve receiver sensitivity when using a quadrature phase-shift keying protocol — a modulation technique that enables faster data rates and longer reach in both space [53] and quantum communications [103, 110]. The large phase-sensitive gain we have achieved can be utilized for low-noise or even potentially noiseless amplification for applications such as high-fidelity qubit readout in quantum computing.

Chapter 7

Squeezed Microwaves Generation

Generating squeezed microwaves has been of particular interest in research fields such as dark matter detection and optomechanical superconducting circuits, typically with cavity-based Josephson parametric amplifiers (JPAs). In comparison with a JTWPA, JPAs have relatively low insertion loss and can be frequency-tunable. However, they have constrained squeezing performance due, in part, to higher-order nonlinearities when the system is strongly-driven [14, 65, 76, 69, 9, 57]. Moreover, their resonant nature limits the instantaneous bandwidth of the device and, thus, the bandwidth of two-mode squeezed microwaves. The technique of impedance engineering can achieve larger bandwidth [94, 77], but the inherent dynamic range and bandwidth constraints are still present within cavity-based JPAs.

Several alternative approaches have been developed that address some of these limitations. For example, the impedance engineering of resonator-based JPAs has increased the bandwidth to the 0.5-0.8 GHz range [94, 77], but these devices still have a dynamic range limited to -110 to -100 dBm and sub-gigahertz bandwidth. Alternative approaches using superconducting nonlinear asymmetric inductive elements (SNAILs) for both resonant [102, 40, 101] and traveling-wave [34, 84] parametric amplification feature a higher dynamic range in the -100 to -90 dBm range. However, both architectures require a magnetic field bias, making them subject to magnetic field noise. Furthermore, the resonant version remains narrowband, and one traveling-wave approach [84] requires additional shunt resistors, which introduce dissipation and unwanted noise. To date, both approaches have been limited to 2-3 dB single-mode and two-mode squeezing.

High kinetic inductance wiring has been used in place of Josephson junctions to realize the nonlinearity needed for both resonant [82] and traveling wave parametric amplification [66, 12] with higher dynamic range. However, the relatively weak nonlinearity of the wiring translates to a much larger requisite pump power to operate the devices, and the traveling wave paramps have larger gain ripple due to impedance variations on the long (up to 2 m) lines. Furthermore, although a single-mode quadrature noise (variance) reduction has been demonstrated in narrowband resonant nanowire devices, their degree of squeezing in dB has yet to be quantified using a calibrated noise source [82].

In this chapter, we demonstrate a broadband single-mode and two-mode microwave squeezer using a dispersion-engineered, dual-pump Josephson traveling-wave parametric amplifier (JTWPA). As discussed in Chapter 6, the high saturation power and large bandwidth of our dispersion-engineered JTWPA will make it a promising candidate for generating highly-squeezed single-mode squeezed vacuum as well as broadband two-mode squeezed vacuum states. This chapter will present the experimental results on squeezed microwaves generation using a JTWPA and explain the measurement procedure, data acquisition, and analytical methods.

7.1 Single-Mode Squeezed Vacuum

Single-mode squeezed states have a variety of applications. As a quantum engineer, I focus on exploring the single-mode squeezing performance of a traveling-wave amplifier compared to a cavity-based squeezer.

7.1.1 Measurement Protocol

We first characterize the single-mode squeezed vacuum of the dual-pump JTWPA. To do this, we apply vacuum to the JTWPA input using a cold 50 Ω resistive load. We measure and compare the output field of the JTWPA for two cases: 1) the output with both pumps off – i.e., vacuum, and 2) the output with both pumps on, i.e., squeezed vacuum. In both cases, the JTWPA output field propagates up the measurement chain to a room-temperature heterodyne detector comprising an IQ mixer that downconverts the signal into

its in-phase (I) and quadrature (Q) components at 50 MHz. These two components are then sampled using a field-programmable gate array (FPGA)-based digitizer with a sampling rate 500 MS/s. The components are then digitally demodulated to obtain an I-Q pair from which one can derive the amplitude and phase of the output field.

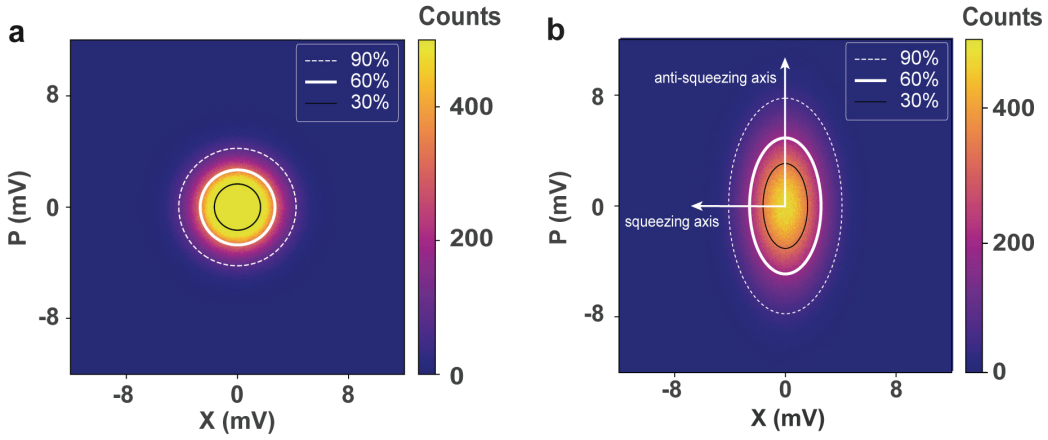

Figure 7-1. | **Output field imaging. a.** 2-D histogram of the vacuum state from a JTWPA when the pumps are off. The legend shows different confidence circles. **b.** Output field histogram of squeezed vacuum state with different confidence ellipses. Both histograms comprise 6×10^6 data points.

To acquire I-Q pairs, the pumps – and thus the squeezing – are periodically switched on and off with a duration of 10 µs each. For each 10 µs acquisition, only the inner 8 µs is digitally demodulated to eliminate sensitivity to any turn-on and turn-off transients. The 8 µs signal is integrated, corresponding to a measurement bandwidth $B_{\text{meas}} \approx 125\,\text{kHz}$ and yields a single I-Q pair. We interleave the squeezer-on and squeezer-off acquisitions to reduce sensitivity to experimental drift between the measurements. When the squeezer is off, we extract an isotropic Gaussian noise distribution for the vacuum state (Fig. 7-1a) with variance $\Delta X^2_{\text{SQZ, off}}$. When the squeezer is on, the squeezed vacuum state exhibits an elliptical Gaussian noise distribution as shown in Fig. 7-1(b). In total, we acquire 6 million I-Q pairs to reconstruct each histogram. We then extract the variance along the squeezing axis $\Delta X^2_{\text{SQZ, min}}$ and along the anti-squeezing axis $\Delta X^2_{\text{SQZ, max}}$. Comparing the values $\Delta X^2_{\text{SQZ, min}}$ and $\Delta X^2_{\text{SQZ, max}}$ to the vacuum level $\Delta X^2_{\text{SQZ, off}}$ along with the measurement gain and efficiency enables us to determine the degree of squeezing and anti-squeezing, respectively.

7.1.2 Output Field Data Analysis

We measure the output fields from the JTWPA using a room-temperature digitizer and demodulation scheme. An example of such a measurement is shown in Fig. 7-3(a). This corresponds to pump 1 power $P_1 = 1.57\,\text{nW}$ and pump 2 power $P_2 = 0.665\,\text{nW}$ in Fig. 7-4(d). The measured distributions for squeezing (blue) and vacuum (red) are plotted independently in the insets, and then also together by subtracting the vacuum distribution from the squeezing distribution. Although this bias point corresponds to a high-degree of squeezing, the room-temperature measurement result is somewhat ameliorated due to several factors [e.g., see probability densities, right-hand side of Fig. 7-3(a)]. The reason is that we are measuring the quadratures at room temperature, rather than at the JTWPA output. Our measurement incorporates all of the loss, gain, and added amplifier noise in the measurement chain from the JTWPA output to the room temperature digitizer, and we must account for these to obtain the degree of squeezing at the JTWPA output. In addition, the digitizer measures the distributions in the voltage basis, and while this is sufficient for relative measurements between squeezing and vacuum, we also convert to the photon basis to make a standardized assessment in the photon basis.

We use the procedure following Mallet *et al.* in Ref. [63] to go from the room temperature measurement in the voltage basis to the degree of squeezing at the JTWPA output in the photon basis. The procedure is summarized in table 7.1 and goes as follows:

- We first determine the vacuum state variance in the photon basis at the output of the JTWPA to be $\Delta X^2_{\text{SQZ, off}} = 1/2 + \bar{n}$. To begin, the variance of the vacuum state in the photon basis $\Delta X^{2\,\text{(input)}}_{\text{SQZ, off}}$ at the JTWPA input is $1/2 + \bar{n}$, where $\bar{n} = \sum_i \bar{n}_i$ is the sum of average residual thermal photons arriving at the JTWPA from different temperature stages stages i in the refrigerator. For each temperature stage i, the residual photon number is given by the Bose-Einstein distribution, $\bar{n}_i = A_{\text{i}}/(e^{\hbar\omega/k_{\text{B}}T_{\text{i}}} - 1)$, where T_{i} is the temperature of stage i, and the net average photon number is reduced by the collective attenuation A_{i} from stage i to the JTWPA input.

- Next, we determine the measurement efficiency η_{meas} from the system noise temperature T_{sys} determined using the noise calibration methods described in more detail in the next

Quantity	Definition	Value
$\boldsymbol{\Delta X^2_{\mathrm{SQZ,\ off}}}$	Vacuum variance, photon basis, stage 1	$\frac{1}{2} + \bar{n}$
$\boldsymbol{T_{\mathrm{sys}}}$	System noise temperature, stage 2	measured quantity (noise temperature calibration)
$\boldsymbol{\eta_{\mathrm{meas}}}$	Measurement efficiency, stage 2	$\hbar\omega / 2k_{\mathrm{B}}T_{\mathrm{sys}}$
$\boldsymbol{\alpha}$	Transfer function, stage 2	$\Delta x^2_{\mathrm{SQZ,\ off}} / \Delta V^2_{\mathrm{SQZ,\ off}}$
$\boldsymbol{\Delta V^2_{\mathrm{SQZ,\ min/max}}}$	Field variance, voltage basis, stage 3	measured quantity
$\boldsymbol{\Delta x^2_{\mathrm{SQZ,\ min/max}}}$	Field variance, photon basis, stage 2	$\alpha\ \Delta V^2_{\mathrm{SQZ,\ min/max}}$
$\boldsymbol{\Delta X^2_{\mathrm{SQZ,\ min/max}}}$	Field variance, photon basis, stage 1	$\dfrac{\Delta x^2_{\mathrm{SQZ,\ min/max}} - (1-\eta_{\mathrm{meas}})/2}{\eta_{\mathrm{meas}}}$

Table 7.1. | Definition of quantities used to convert measured fields to squeezed fields at the JTWPA output. These quantities are used to convert the measured fields in the voltage basis to the desired squeezing and anti-squeezing fields at the output of the JTWPA in the photon basis. Stages refer to the modeling of the measurement chain shown in Fig. 7-2.

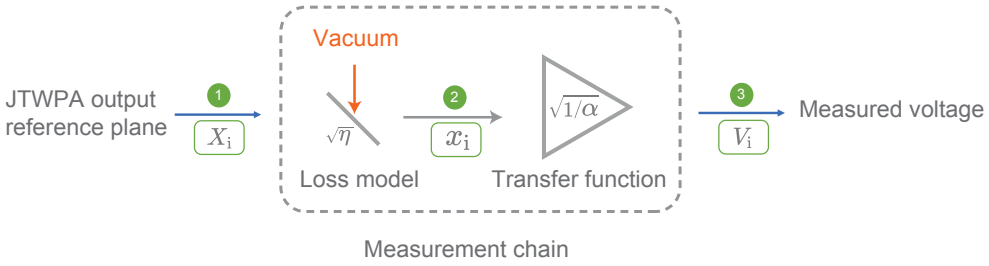

Figure 7-2. | Physical model connecting the field at the JTWPA output to the measured voltage. Due to non-negligible loss and noise in the microwave setup, the output field measured by the room-temperature digitizer is different from that at the output of the JTWPA at milliKevin temperature. Therefore, to infer the squeezing levels at the JTWPA output, we use a model for the measurement chain from the output of the JTWPA (input of the model with quadrature field amplitude X_{i} in the photon basis) to the digitizer (output of the model with quadrature field amplitude V_{i} in the voltage basis). The model uses a fictitious beamsplitter that accounts for noise (loss) in the measurement chain followed by a lossless transfer function that accounts for amplifier gain and the conversion between the photon basis and the voltage basis. The losses and other Gaussian noise sources [63] are captured by the beamsplitter with transmissivity η, after which the quadrature field amplitude in the photon basis is denoted as x_{i}. The transfer function α with a field conversion factor $\sqrt{1/\alpha}$ encompasses any linear scaling in the measurement chain, including amplifier gain (linear) and analog-to-digital conversion process of the digitizer. Green label 1, 2, and 3 mark the relative position in the model as referenced in our discussion.

section. The efficiency is primarily affected by the HEMT, which we use as our first-stage amplifier with a large dynamic range, chosen to prevent gain saturation that would otherwise affect the measurement outcome. The efficiency is also affected by distributed loss in the measurement chain between the JTWPA and room-temperature digitizer. For the case shown in Fig. 7-3 and Fig. 7-12, $\eta_{\mathrm{meas}} = 6.53^{+0.23}_{-0.22}\%$ at measurement frequency 6.70 GHz. For our specific setup, we estimate an effective temperature $T < 40\,\mathrm{mK}$ (or $\bar{n} < 0.00014$) at 6.70 GHz, which has a negligible effect on the output field from the squeezer [122, 51]. This is further validated by the noise characterization experiment using a shot noise tunnel junction (SNTJ), where we extract an average temperature T = 30.4 mK of the tunnel junction. The JTWPA input vacuum state is nearly ideal, with only a negligible thermal background, that is, $\bar{n} \ll 1/2$. Therefore, we could safely take $\Delta X^{2\,\text{(input)}}_{\text{SQZ, off}} = \bar{n} + 1/2 \approx 1/2$. Nonetheless, although negligible, for completeness, we carry forward the small $\bar{n}$ to the JTWPA output. We note that this is an overestimate (worst-case), since the non-equilibrium thermal-photon portion of $\bar{n}$ – the portion arriving from higher temperature stages in the refrigerator – is further attenuated by the JTWPA itself. Therefore $\bar{n}_{\text{output}} < \bar{n}_{\text{input}}$. Since the JTWPA attenuation changes with the bias point, we simply use the worst-case estimate $\bar{n}_{\mathrm{output}} = \bar{n}_{\mathrm{input}} \equiv \bar{n}$. This means we take $\Delta X^2_{\text{SQZ, off}} \equiv \Delta X^{2\,\text{(output)}}_{\text{SQZ, off}} = \Delta X^{2\,\text{(input)}}_{\text{SQZ, off}} = (1/2 + \bar{n})$. Again, we have confirmed that $\bar{n}$ at this level has no discernible impact on our results.

- We next determine the factor α that converts between the voltage basis and photon basis, $\alpha = \Delta x^2_{\text{SQZ, off}}/\Delta V^2_{\text{SQZ, off}} = 0.129052\,\mathrm{quanta/mV^2}$, obtained from the calculated value for $\Delta x^2_{\text{SQZ, off}}$ and the measured value of $\Delta V^2_{\text{SQZ, off}}$ for the vacuum state in the voltage basis [63]. This conversion factor enables us to utilize a beamsplitter model as shown in Fig. 7-2 that accounts for the measurement efficiency, which for the variances we consider here, leads to:

$$\Delta x_i^2 = \eta_{\mathrm{meas}} \Delta X_i^2 + (1 - \eta_{\mathrm{meas}}) \frac{1}{2}, \tag{7.1}$$

where ΔX_i^2 is the variance of the X quadrature field at the beamsplitter input (i.e., the JTWPA output, the quantity we want to extract), Δx_i^2 is the variance of the x quadra-

ture field at the beamsplitter output that accounts for measurement efficiency, the factor (1/2) is the variance of vacuum introduced by the vacuum port of the beamsplitter, and i corresponds to "SQZ, off" (vacuum), "SQZ, min" (squeezing), and "SQZ, max" (anti-squeezing). The same holds for the P quadrature field.

We then use α in this equation to calculate the desired quadratures from the measured voltage variance [63]:

$$\Delta x_i^2 = \alpha \Delta V_i^2 = \eta_{\text{meas}} \Delta X_i^2 + (1 - \eta_{\text{meas}}) \frac{1}{2}$$
$$\left(\frac{\Delta V_i^2}{\Delta V_{\text{SQZ, off}}^2} \right) \Delta x_{\text{SQZ, off}}^2 = \eta_{\text{meas}} \Delta X_i^2 + (1 - \eta_{\text{meas}}) \frac{1}{2}$$

which takes the decrease (increase) of the squeezed (anti-squeezed) voltage variance relative to the voltage variance obtained for vacuum, and uses it to scale the variance of vacuum in the photon basis.

$$\begin{aligned} \Delta x_{\text{SQZ, off}}^2 &= \eta_{\text{meas}} \Delta X_{\text{SQZ, off}}^2 + (1 - \eta_{\text{meas}}) \frac{1}{2} \\ &= \eta_{\text{meas}} (\frac{1}{2} + \bar{n}) + (1 - \eta_{\text{meas}}) \frac{1}{2} = \frac{1}{2} + \eta_{\text{meas}} \bar{n} \end{aligned}$$

- Finally, we obtain the desired variance at the JTWPA output by inverting Eq. (7.1), which in turn accounts for the measurement efficiency, leading to the final entry in table 7.1:

$$\Delta X_{\text{SQZ, min/max}}^2 = \frac{\Delta x_{\text{SQZ, min/max}}^2 - (1 - \eta_{\text{meas}}) \frac{1}{2}}{\eta_{\text{meas}}}. \tag{7.2}$$

This converts from $\Delta x_{\text{SQZ, min/max}}^2$ to $\Delta X_{\text{SQZ, min/max}}^2$, that is, the (anti-)squeezed quadratures at the JTWPA output. The same is done for the P quadrature.

Using this procedure, we can convert from the measured distributions in the voltage basis in Fig. 7-3(a) to distributions in the photon basis Fig. 7-3(b). For the particular bias point in Fig. 7-3, we provide a few numbers. We process the output field data using the *GaussianMixture* module within the *sklearn.mixture* package in Python to compute the

output field variance. The extracted variances for vacuum and squeezed states are denoted $\Delta V^2_{\mathrm{SQZ,\ off}}$ and $\Delta V^2_{\mathrm{SQZ,\ min/max}}$ respectively. The corresponding standard deviations for the squeezed output field distributions shown in Fig. 7-3(a) are $\sigma^{\mathrm{sqz}}_{\mathrm{min}} = 1.90805 \times \pm 4.63 \times 10^{-4}$ mV and $\sigma^{\mathrm{sqz}}_{\mathrm{max}} = 3.62295 \pm 7.64 \times 10^{-4}$ mV when the squeezer is turned on. When it is off, the measured minimum and maximum standard deviations of the vacuum are identical within the fitting error bar $\sigma^{\mathrm{vac}}_{\mathrm{min}} = 1.96837 \pm 4.65 \times 10^{-4}$ mV and $\sigma^{\mathrm{vac}}_{\mathrm{max}} = 1.96837 \pm 4.04 \times 10^{-4}$ mV, which is expected for vacuum output field. The transfer function α is calculated as the ratio $\Delta x^2_{\mathrm{SQZ,\ off}} / \Delta V^2_{\mathrm{SQZ,\ off}} = 0.129052 \pm 5.2 \times 10^{-5}\,\mathrm{quanta/mV^2}$.

Stage	Parameter	Value	Error
3	$\sigma^{\mathrm{off}}_{\mathrm{min}}$	$1.96837\,\mathrm{mV}$	$\pm 4.65 \times 10^{-4}\,\mathrm{mV}$
3	$\sigma^{\mathrm{off}}_{\mathrm{max}}$	$1.96837\,\mathrm{mV}$	$\pm 4.04 \times 10^{-4}\,\mathrm{mV}$
3	$\sigma^{\mathrm{sqz}}_{\mathrm{min}}$	$1.90805\,\mathrm{mV}$	$\pm 4.63 \times 10^{-4}\,\mathrm{mV}$
3	$\sigma^{\mathrm{sqz}}_{\mathrm{max}}$	$3.62295\,\mathrm{mV}$	$\pm 7.64 \times 10^{-4}\,\mathrm{mV}$
3	$\Delta V^2_{\mathrm{SQZ,min}}$	$3.64065\,\mathrm{mV^2}$	$\pm 1.77 \times 10^{-3}\,\mathrm{mV^2}$
3	$\Delta V^2_{\mathrm{SQZ,max}}$	$13.1258\,\mathrm{mV^2}$	$\pm 5.54 \times 10^{-3}\,\mathrm{mV^2}$
3	$\Delta V^2_{\mathrm{SQZ,off}}$	$3.87448\,\mathrm{mV^2}$	$\pm 1.83 \times 10^{-3}\,\mathrm{mV^2}$
2	$\Delta x^2_{\mathrm{SQZ,\ min}}$	0.469833 quanta	$\pm 2.28 \times 10^{-4}\,\mathrm{quanta}$
2	$\Delta x^2_{\mathrm{SQZ,\ max}}$	1.69391 quanta	$\pm 7.15 \times 10^{-4}\,\mathrm{quanta}$
2	$\Delta x^2_{\mathrm{SQZ,\ off}}$	0.500009 quanta	$+5 \times 10^{-6} / -2 \times 10^{-7}\,\mathrm{quanta}$
2	α	$0.129052\,\mathrm{quanta/mV^2}$	$\pm 5.2 \times 10^{-5}\,\mathrm{quanta/mV^2}$
2	$\eta_{\mathrm{meas}}(6.70\,\mathrm{GHz})$	6.534 %	$+0.234 / -0.218\,\%$
1	$\Delta X^2_{\mathrm{SQZ,\ min}}$	0.0383 quanta	$+0.0160 / -0.0159\,\mathrm{quanta}$
1	$\Delta X^2_{\mathrm{SQZ,\ max}}$	18.77 quanta	$\pm 0.63\,\mathrm{quanta}$
1	$\Delta X^2_{\mathrm{SQZ,\ off}}$	0.50014 quanta	$+1.3 \times 10^{-4} / -1.0 \times 10^{-4}\,\mathrm{quanta}$
1	$\mathrm{dB_{SQZ}}$	-11.16 dB	$+1.51 / -2.33\,\mathrm{dB}$
1	$\mathrm{dB_{ANTI}}$	15.74 dB	$+0.14 / -0.15\,\mathrm{dB}$

Table 7.2. A list of experimental parameter values and errors and their corresponding stage in the physical model in Fig. 7-2.

Individual parameter errors lead to different variations in the overall squeezing and anti-squeezing levels. For example, errors in $\sigma^{\mathrm{off}}_{\mathrm{min}}$, $\sigma^{\mathrm{off}}_{\mathrm{max}}$, $\sigma^{\mathrm{sqz}}_{\mathrm{min}}$, $\sigma^{\mathrm{sqz}}_{\mathrm{max}}$ and α lead to a maximum of $\sim 0.4\,\mathrm{dB}$ change in the squeezing level and $\sim 0.01\,\mathrm{dB}$ in the anti-squeezing level. In con-

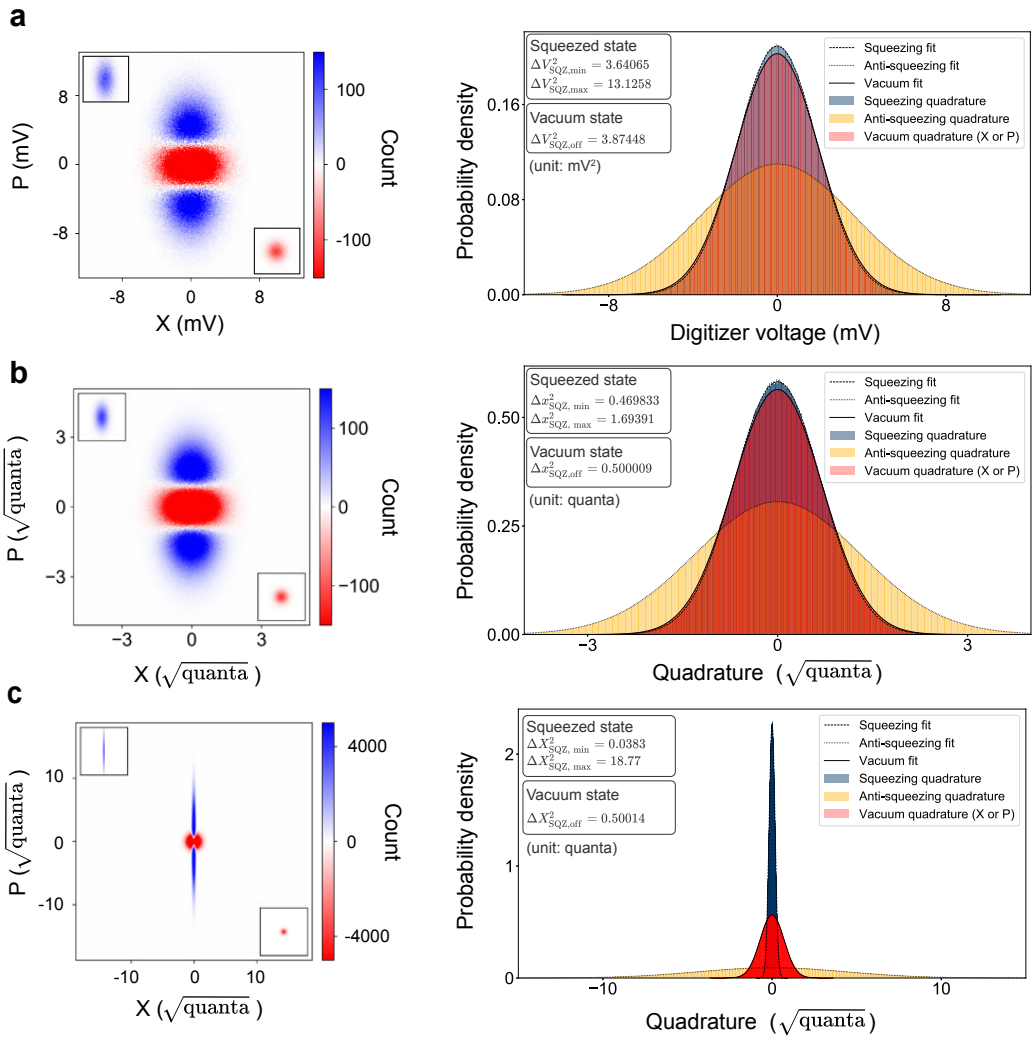

Figure 7-3. | **Gaussian fits to quadrature data in voltage and photon bases. a.** Left: the histograms display the X and P quadratures for the single-mode squeezed vacuum (blue) and vacuum (red) states in the digitizer voltage basis (position 3 in Fig. 7-2). Their output fields are shown individually in the insets. Right: probability density distribution of the X and P quadratures for the vacuum and squeezed states plotted together with Gaussian fits. **b.** Histograms and probability density distribution for the same vacuum and squeezed vacuum states are plotted in photon basis before the converter but after the beamsplitter (position 2 in Fig. 7-2). **c.** Histograms and probability density distribution for the same vacuum and squeezed vacuum states are plotted in photon basis before the beamsplitter (position 1 in Fig. 7-2). The measurement is taken at the pump configuration (pump 1 power $P_1 = 1.57$ nW and pump 2 power $P_2 = 0.665$ nW in Fig. 7-6.

trast, errors in the measurement efficiency η_{meas} amount to $\sim 2\,\mathrm{dB}$ and $\sim 0.15\,\mathrm{dB}$ change in the squeezing and anti-squeezing level, respectively. Fast FPGA demodulation enables efficient collection of large quadrature datasets and thus results in small variations while η_{meas} is limited by microwave measurement losses and noises. Therefore, we primarily consider the errors associated with measurement efficiency η_{meas}, the most significant error source, to estimate variations in squeezing and anti-squeezing levels.

For the output fields in Fig. 7-3(b), accounting for measurement efficiency, the squeezed variance $\Delta X^2_{\mathrm{SQZ,\ min}} = 0.0383^{+0.0160}_{-0.0159}\,\mathrm{quanta}$ and the anti-squeezing variance $\Delta X^2_{\mathrm{SQZ,\ max}} = 18.77 \pm 0.63\,\mathrm{quanta}$ give $-11.16^{+1.51}_{-2.33}\,\mathrm{dB}$ squeezing and $15.74^{+0.14}_{-0.16}\,\mathrm{dB}$ anti-squeezing, relative to the vacuum state with a variance $\Delta X^2_{\mathrm{SQZ,\ off}} = 0.5001\,\mathrm{quanta}$. The conversion to decibels, $\mathrm{dB_{SQZ}}$, is:

$$\mathrm{dB_{SQZ}} = 10\log_{10}\frac{\Delta \mathrm{X}^2_{\mathrm{SQZ,\ min}}}{\Delta \mathrm{X}^2_{\mathrm{SQZ,\ off}}}, \tag{7.3}$$

while the anti-squeezing level $\mathrm{dB_{ANTI}}$ is

$$\mathrm{dB_{ANTI}} = 10\log_{10}\frac{\Delta \mathrm{X}^2_{\mathrm{SQZ,\ max}}}{\Delta \mathrm{X}^2_{\mathrm{SQZ,\ off}}}. \tag{7.4}$$

7.1.3 Optimizing Single-Mode Squeezing

The squeezing process is sensitive to the power of both pumps due to the desired phase-matching condition for parametric amplification (e.g., $\Delta k^{\mathrm{PA}} \simeq 0$ in Eq. (6.5)) and also residual parasitic processes such as frequency conversion. As displayed in Fig. 7-4(b), we perform a coarse measurement of the $\Delta X^2_{\mathrm{SQZ,\ min}}$ (plotted relative to vacuum) as a function of pump powers to maximize the degree of squeezing. This enables us to identify empirically the pump powers P_1 and P_2 that correspond to higher squeezing levels. For six such near-optimal values, the six different colors in Fig. 7-4(d), we carry out finer scans of squeezing, anti-squeezing, and parametric gain as a function of P_2 for fixed P_1. Accounting for the measurement efficiency η_{meas} at the output, we extract a squeezing level of $-11.35^{+1.57}_{-2.49}\,\mathrm{dB}$ and an anti-squeezing level of $15.71^{+0.14}_{-0.15}\,\mathrm{dB}$ at the optimal pump conditions, comparable with the best performance demonstrated by resonator-based squeezers in superconducting circuits [14, 9, 69, 65, 63, 16, 74, 21, 127].

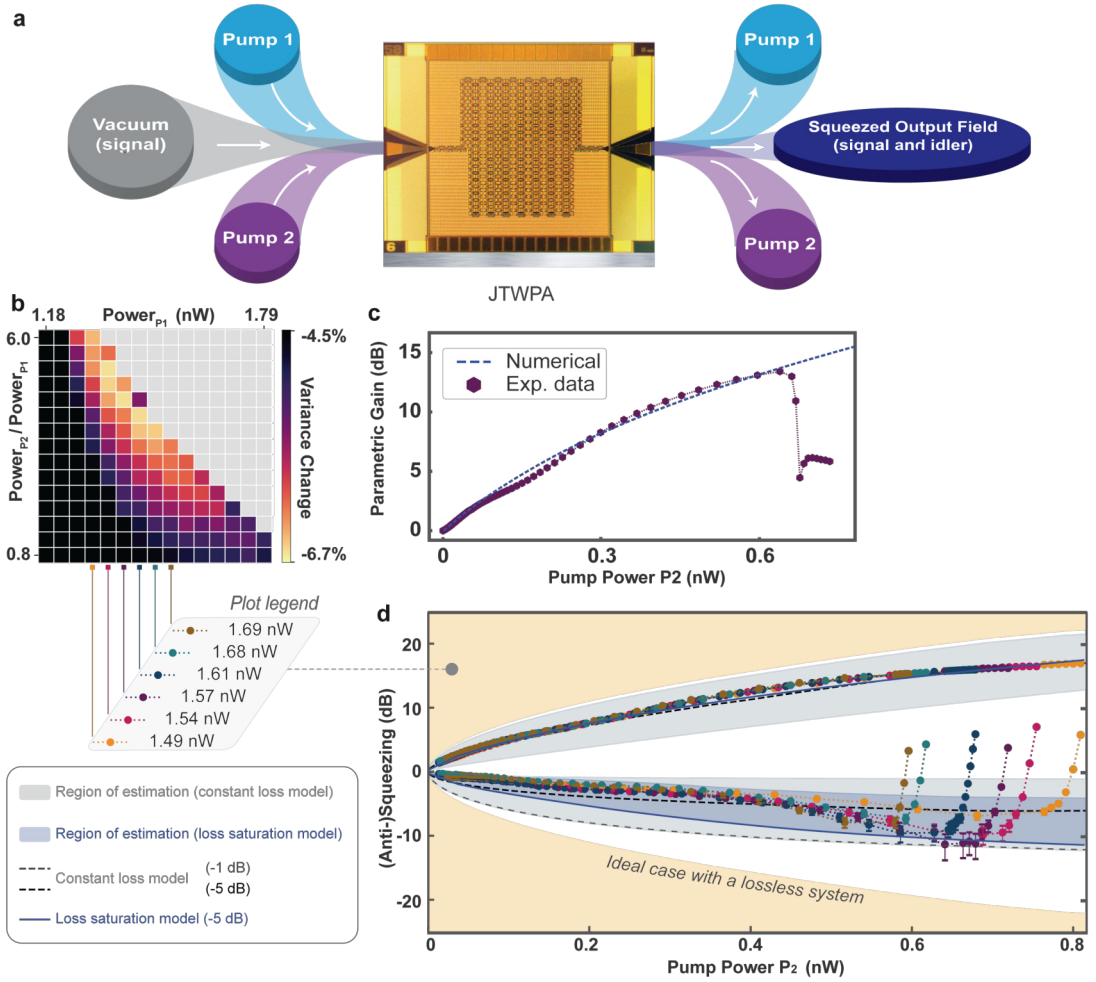

Figure 7-4. | **Single-mode squeezed vacuum. a.** The JTWPA in the presence of a bichromatic pump transforms the vacuum field at the input into a squeezed field at the output through non-degenerate four-wave mixing. **b.** At 6.7037 GHz, measurement of the change in squeezing variance (relative to vacuum) versus asymmetry in the pump powers P_1 and P_2. Colored vertical lines indicate six different values of P_1 in units of nW, used in the 1D measurement in panel (d). The power is referred at the input of the squeezer. **c.** Experimental data of the parametric gain as a function of P_2 with P_1 fixed at 1.57 nW (at the input of the squeezer). **d.** Measurement of squeezing and anti-squeezing versus P_2 with six different P_1 configurations (colored data). The data are presented as mean values of 3 sets of repeated measurement (each with 6×10^6 sample points. Their statistical variation is almost entirely due to the uncertainty in estimating the noise temperature, which dominates the error bars shown in the plot as an estimation range for the squeezing/anti-squeezing levels. We confirm there is no squeezing when pumps are turned off. The squeezing level increases as a function of P_2 as gain increases, but eventually degrades as the pumps become too strong and gain decreases. The shaded regions and trend lines corresponding to constant-loss and loss-saturation models. The observed squeezing levels are consistent with a saturated loss of approximately -1 dB at high gain.

7.1.4 Effects of Microwave Loss on JTWPA Squeezing Performance

We include several numerical simulations of squeezer performance reduction due to distributed dielectric loss along the JTWPA. The numerical models are developed by our theory collaborator Arne Grimsmo and described in more detail in appendix A. In essence, the models attempt to capture the effects of loss saturation in a distributed system like the JTWPA on its output squeezing levels.

Squeezing performance is sensitive to dissipation (loss), which acts as a noise channel. Within our JTWPA, loss primarily originates from defects — modelled as two-level systems (TLSs) — within the plasma-enhanced chemical-vapor-deposited (PE-CVD) $\mathrm{SiO_2}$ dielectric used in the parallel-plate shunt capacitors. Previous studies have shown a quality factor Q $\sim 10^3$ associated with this dielectric in the single-photon regime, observed at low-power and low-temperature. In this limit, the TLSs readily absorb photons from the JTWPA and cause relatively high loss.

We observe high levels of squeezing despite the use of such lossy materials in the JTWPA. We conjecture the reason is due to TLS saturation. At sufficiently high powers (large photon numbers), the TLSs saturate and the loss is reduced [95]. We can understand the net impact of TLSs on squeezing performance by considering the JTWPA to be a cascade of individual squeezers. The amount of added squeezing becomes position-dependent and increases with the increased gain at the output end. The TLSs are also distributed along the JTWPA, and they become saturated towards the output end due to the larger number of photons associated with the higher gain. Therefore, the impact of loss on squeezing performance is reduced towards the output where the marginal squeezing is the largest [49]. As a result, we expect loss saturation at large signal gain to improve squeezing performance, as we observe in our experiment [see Fig. 7-4(d) at higher pump power P_2]. To verify this conjecture, we independently measure the JTWPA loss as a function of photon number by varying the JTWPA temperature. The loss at small thermal photon numbers (<50 mK) is around -5 dB. We have observed that the loss becomes saturated as the temperature increases — it reduces to -1 dB for large photon numbers (>800 mK). Fig. 7-5(a) is a plot of the empirical characterization of the saturation behavior of our device. The temperature is

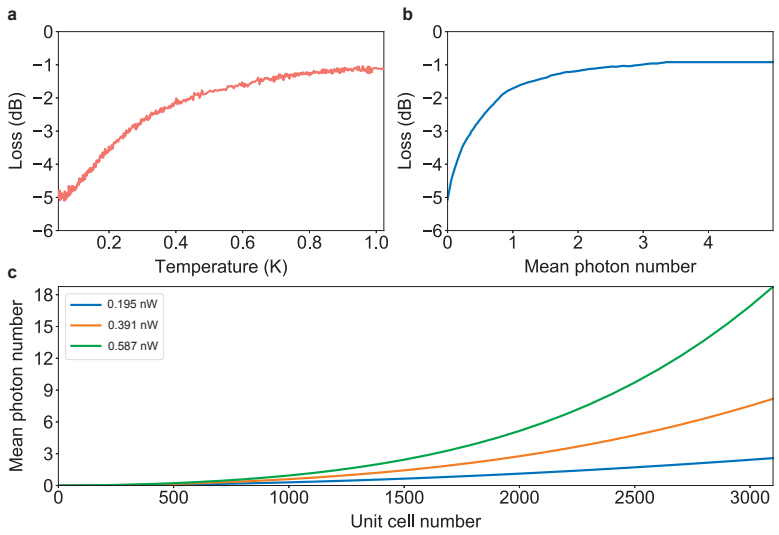

Figure 7-5. | **JTWPA loss saturation. a.** JTWPA insertion loss at 6.7 GHz as a function of temperature controlled using a heater at the mixing chamber. **b.** JTWPA insertion loss plotted versus thermal photon number n_s associated with the temperatures T_s, based on Bose-Einstein statistics $n_s = 1/(e^{hf/k_{\mathrm{B}}T_{\mathrm{s}}} - 1)$. **c.** The amplification process of the JTWPA produces an effective thermal state, and its photon number depends on the gain and the position inside the amplifier, as shown in the simulation plot. Each curve corresponds to a specific pump 2 power. Pump 1 power is always fixed at 1.57 nW.

controlled by adjusting the current through a heating element on the mixing chamber of the dilution refrigerator.

Bounding the Squeezing Levels

We start with the basic models. The boundary of the beige region in Fig. 7-6 corresponds to the ideal-case squeezing achievable for a lossless JTWPA. The gray-shaded areas represent regions of estimation for squeezing and anti-squeezing levels; we define a lower bound that corresponds to numerical results assuming all of the loss (-5 dB) is at the end of the device (worst case), while the upper bounds are obtained using Caves and Crouch's distributed beamsplitter loss model [20] with -1 dB distributed loss (best case). The black dashed lines represent the numerical model with a uniformly distributed -5 dB-loss across the device. These numerical models confine the possible squeezing and anti-squeezing levels given the loss of the JTWPA.

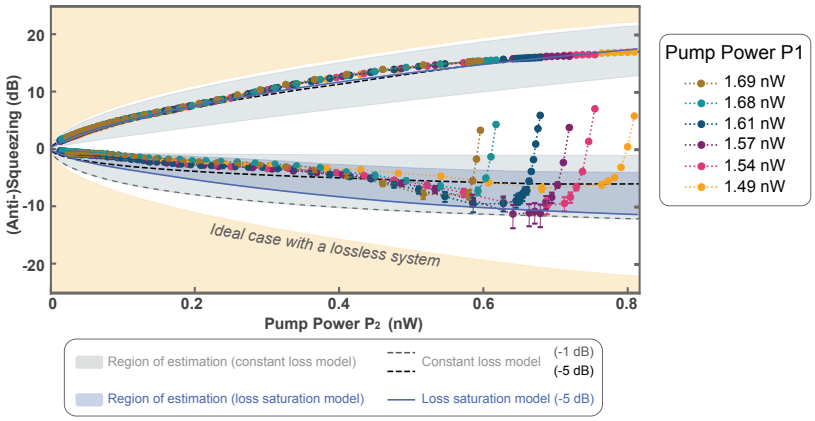

Figure 7-6. | Measurement of squeezing and anti-squeezing versus P_2 with six different P_1 configurations. Single pump gain and numerical simulations that fit and predict the gain profiles. The deviation between the model and the experimental data is expected to be caused by the bandwidth constraint of cryogenic components. Pump power P_1 corresponds to the output of its RF source at room temperature.

Estimating the Squeezing Level: Constant Loss Model

Given our knowledge of the JTWPA design and the characterization results, we can model squeezing levels as a function of pump power. First, two limits are shown as dashed lines using a constant loss model. For low pump power P_2, our data are closer to the -5 dB line. At higher powers, where we see maximal squeezing, the data are more consistent with the -1 dB line corresponding to saturated TLSs. We then use numerical simulations to calculate the photon number in the JTWPA from its input to its output. The photon number is converted to loss from the independent loss-temperature measurement, and we plot the corresponding squeezing due to this distributed loss (solid line). It starts at -5 dB for low powers and reduces toward -1 dB at high powers due to loss saturation. The high degree of squeezing observed in this device is consistent with the loss saturation model to within about 1-2 dB at high powers.

Estimating the Squeezing Level: Loss Saturation Model

We estimate the loss saturation effect on squeezing at intermediate powers using a distributed loss saturation model plotted as a blue line in Fig. 7-6. In this model, the loss rate $\gamma(x)$ at position x is determined by an effective temperature T_e extracted from the instantaneous photon number in the numerical simulation shown in Fig. 7-5(c). $\gamma(x)$ is

then taken to be the measured loss rate $\gamma'(T_e)$ at temperature T_e in Fig. 7-5(b). The loss saturation model gives the lower bound with all the loss towards the end of the device, while the same model provides the upper bound with a more realistic distributed 5 dB loss model. Together, they form a refined estimation region displayed in the blue-shade area. At intermediate pump powers before saturation, there is a discrepancy between the measured behavior of the squeezing and the numerical simulation. This is likely due to our optimizing for maximum squeezing at high pump powers. Parasitic processes that are largely absent at high powers may not be completely suppressed at intermediate powers. More complicated pump dynamics and multimode interactions could mix in vacuum noise, which is not captured by the input-output model used here (more details can be found in appendix A). There is ongoing research to understand better and suppress these unwanted modes [83].

7.2 Two-Mode Squeezed Vacuum

7.2.1 Phase calibration

Broadband two-mode squeezing is expected from the JTWPA given its broadband parametric amplification. To observe two-mode squeezing, we need to construct collective quadrature operators of the signal and idler defined as

$$\begin{aligned} \hat{X}_{\pm} &= \hat{X}_{\mathrm{s}} \pm e^{i\phi_{\mathrm{m}}} \hat{X}_{\mathrm{i}}, \\ \hat{P}_{\pm} &= \hat{P}_{\mathrm{s}} \pm e^{i\phi_{\mathrm{m}}} \hat{P}_{\mathrm{i}}, \end{aligned} \tag{7.5}$$

where $\hat{X}_{\mathrm{s}}$, $\hat{P}_{\mathrm{s}}$ and $\hat{X}_{\mathrm{i}}$, $\hat{P}_{\mathrm{i}}$ are quadrature components of the signal and the idler; ϕ_{m} is the phase difference between the signal and the idler. In the ideal case where the signal and idler have the same phase, i.e., $\phi_{\mathrm{m}} = 0$ and $e^{i\phi_{\mathrm{m}}} = 1$, we can find the maximum squeezing. However, in practice the relative phase might not be zero due to the frequency dependency of the output line at the individual modes. Therefore, after acquiring the quadrature components of the two modes, we sweep ϕ_{m}, construct new histograms for $\hat{X}_{\pm}$ and $\hat{P}_{\pm}$ for each ϕ_{m} as shown in Fig. 7-7, and extract the variance of the squeezed quadrature in the voltage basis $\Delta V_{\pm}^2$. to find the the minimum variance corresponding to the maximum two-mode

squeezing.

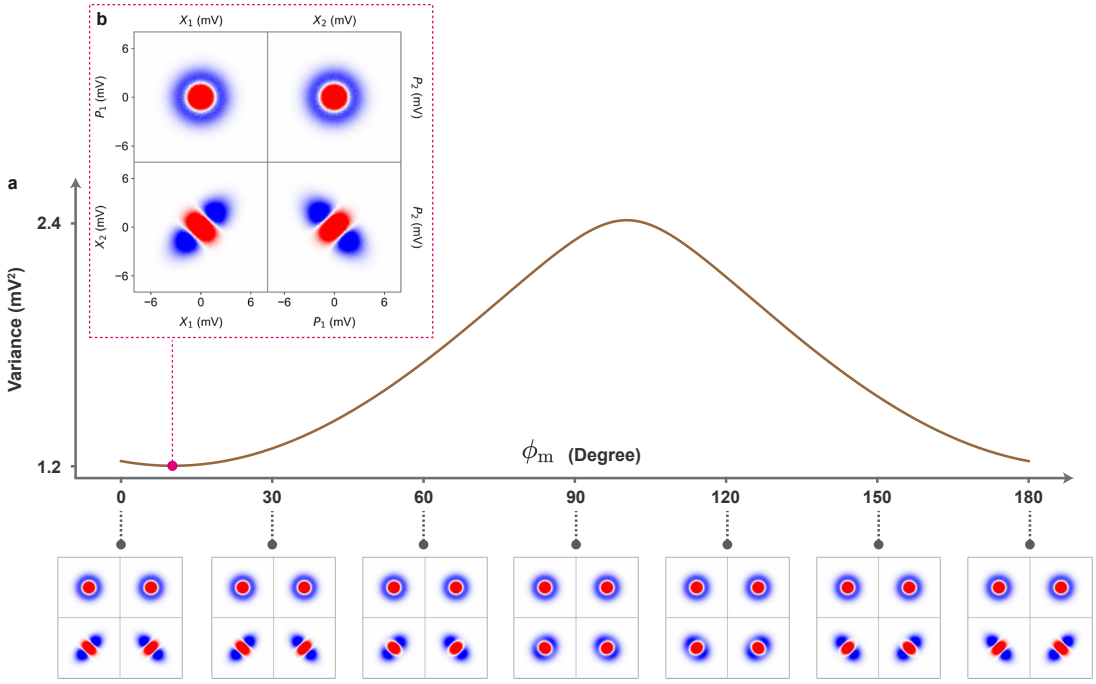

Figure 7-7. | Two-mode squeezing signal-idler phase calibration at 187 MHz mode separation. a. Variance of the squeezed quadrature X_1X_2 or P_1P_2 as a function of relative phase ϕ_m, which we vary in data analysis. In addition, we display different output field histograms with different ϕ_m. Difference in the output field histograms between vacuum (red) and two-mode squeezed vacuum (blue). The histograms show the X and P quadratures (equivalently, the in-phase and quadrature components) of the squeezed and vacuum states. **b.** Output field histograms for optimal two-mode squeezing with $\phi_m = 0.17\,\mathrm{rad}(10^\circ)$.

For example, at mode separation of 187 MHz, we first set up the dual readout scheme as shown in Fig. 7-8. We then simultaneously demodulate the output signal at the two modes $\omega_s/2\pi = 6.6102\,\mathrm{GHz}$ and $\omega_i/2\pi = 6.7972\,\mathrm{GHz}$. The demodulation frequency $\omega_{\mathrm{demod}}/2\pi = 47\,\mathrm{MHz}$ is the same for both, and we use two frequency-locked signal generators as local oscillators at frequencies $\omega_s^{\mathrm{LO}}/2\pi = \omega_s/2\pi + \omega_{\mathrm{demod}}/2\pi = 6.6572\,\mathrm{GHz}$ and $\omega_i^{\mathrm{LO}}/2\pi = \omega_s/2\pi + \omega_{\mathrm{demod}}/2\pi = 6.8442\,\mathrm{GHz}$, respectively. After the demodulation, we obtain pairs of I-Q data for the two modes. We also correct for the power difference between the signal and idler mode that could lead to asymmetry in the output field due to any discrepancy such as attenuation between the two RF paths in the dual readout setup. To compensate for this effect, we measure the ratio ν_{TMS} in vacuum state (JTWPA off) variance of the two modes and normalize that of the idler mode

$\Delta V^2_{\mathrm{i,off}} = 1.424\,\mathrm{mV}^2$ with respect to that of the signal $\Delta V^2_{\mathrm{s,off}} = 1.119\,\mathrm{mV}^2$ — $\nu_{\mathrm{TMS}} = \sqrt{\Delta V^2_{\mathrm{s,off}}/\Delta V^2_{\mathrm{i,off}}} = 0.8865$. As a result, we achieve normalized I-Q pairs with variances $\Delta \tilde{V}^2_{\mathrm{s,off}} = 1.119(3)\,\mathrm{mV}^2$ and $\Delta \tilde{V}^2_{\mathrm{i,off}} = 1.118(8)\,\mathrm{mV}^2$, now with an asymmetry of 0.04% ($\Delta \tilde{V}^2_{\mathrm{s,off}}/\Delta \tilde{V}^2_{\mathrm{i,off}} = 1.0004$) in vacuum state variance between the two modes; the asymmetry in the squeezed state variance of normalized data is also negligible at 0.03 % — $\Delta \tilde{V}^2_{+}/\Delta \tilde{V}^2_{-} = 1.064(7)\,\mathrm{mV}^2/1.065(0)\,\mathrm{mV}^2 = 0.9997$. This procedure accounts for the frequency dependence of the output line without amplification but does not compensate for asymmetry in the squeezer when it is turned on, e.g., the small ripples in the gain. Similar to the single-mode analysis, the variances of output fields are extracted using the *GaussianMixture* module within the *sklearn.mixture* package in Python. The histograms are plotted in Fig. 7-7 (b). In the same plot, we have also calibrated the relative phase $\phi_{\mathrm{m}} = 0.17\,\mathrm{rad}(10^\circ)$ and achieved a maximum squeezing for this dataset. Fig. 7-7 (b) shows the signature of two-mode squeezing, in which the individual modes are in a "thermal-like" state with an increased variance (blue histograms in the X_1P_1 and X_2P_2 quadrants) while we have squeezing and anti-squeezing in the collective quadratures (blue histograms in the X_1X_2 and P_1P_2 quadrants).

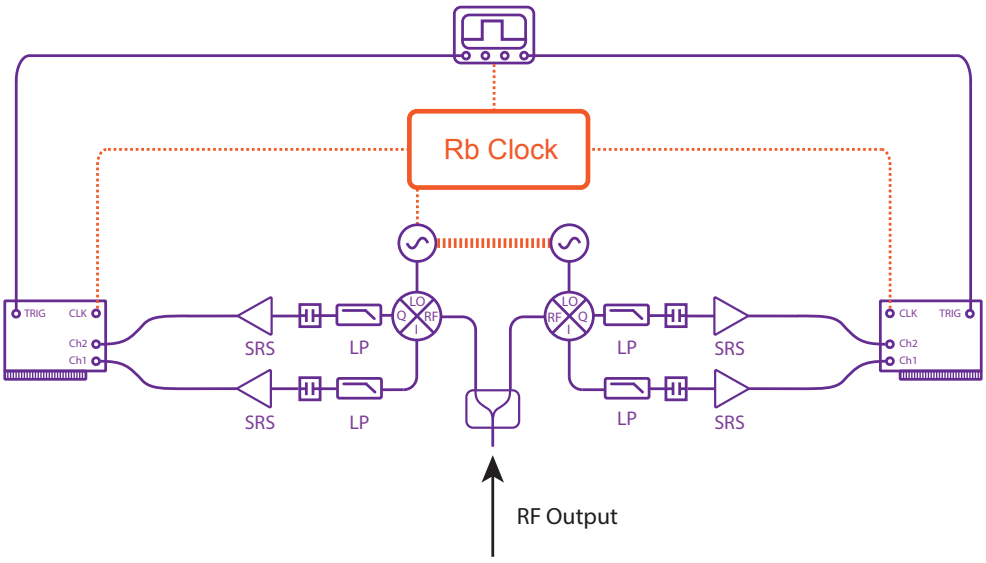

Figure 7-8. | Dual readout setup schematic diagram for two-mode squeezing data acquisition. The RF output from the dilution fridge gets divided by a power splitter into two identical branches of IQ down-conversion circuits, where the signal at the two modes can be simultaneously demodulated.

7.2.2 Characterization

Using the same optimized pump configuration for the single-mode squeezing, we generate and characterize two-mode squeezed vacuum as a function of the frequency separation $\omega_\mathrm{s} - \omega_\mathrm{i}$ between the two modes. As shown in Fig. 7-8, we switch to a dual-readout configuration [127] that simultaneously demodulates the signal and idler using two separate FPGA-based digitizers, circumventing bandwidth limitations of the digitizer and other components in the experiment, such as IQ-mixers, low-frequency amplifiers, etc. We directly measure up to a separation of 373 MHz with the maximum squeezing of $-9.54^{+1.11}_{-1.63}\,\mathrm{dB}$, an average squeezing of -6.71 dB, and an average anti-squeezing of 16.12 dB, as displayed in Fig. 7-9(c).

To extract the squeezing level, we collect the joint distribution in the X_1X_2 or P_1P_2 quadrant (analogous to the single-mode squeezed state statistics) and perform the same analytical procedure Eq. (7.1) - Eq. (7.4) as detailed in Sec. 7.1.2 using the measured system noise temperatures (details of system noise characterization can be found in Chapter 4). The results are shown in Fig. 7-9(c) up to a frequency range $\sim 500\,\mathrm{MHz}$, constrained by the bandwidth of our noise calibration device.

Therefore, we cannot directly calibrate the degree of squeezing beyond this range. Nonetheless, squeezing is expected to continue beyond 500 MHz [44]. Outside that bandwidth, we perform the same two-mode squeezing analysis except without the system noise temperature and report variance change between the squeezed and vacuum states as $1 - \Delta\tilde{V}_+^2/\Delta\tilde{V}_{+,\mathrm{off}}^2$, where $\tilde{V}_{+,\mathrm{off}}^2$ is the variance for the two-mode vacuum state in the voltage basis. In the case of no squeezing, we have $\Delta\tilde{V}_+^2 = \Delta\tilde{V}_{+,\mathrm{off}}^2$ and variance change would be 0; in the case of squeezing, the squeezing variance drops below that of the vacuum, i.e., $\Delta\tilde{V}_+^2 < \Delta\tilde{V}_{+,\mathrm{off}}^2$, and variance change would be < 1. As shown in Fig. 7-9(d), we characterize the variance change between the squeezed and the vacuum quadratures. Below 373 MHz, the results are consistent with the squeezing measured in Fig. 7-9(c). Above 373 MHz, the JTWPA exhibits a consistently low variance out to 1500 MHz, beyond which we are again limited for technical reasons, in this case, by the onset of a filter roll-off. Because the signal and idler photons propagate at different frequencies, frequency-dependent

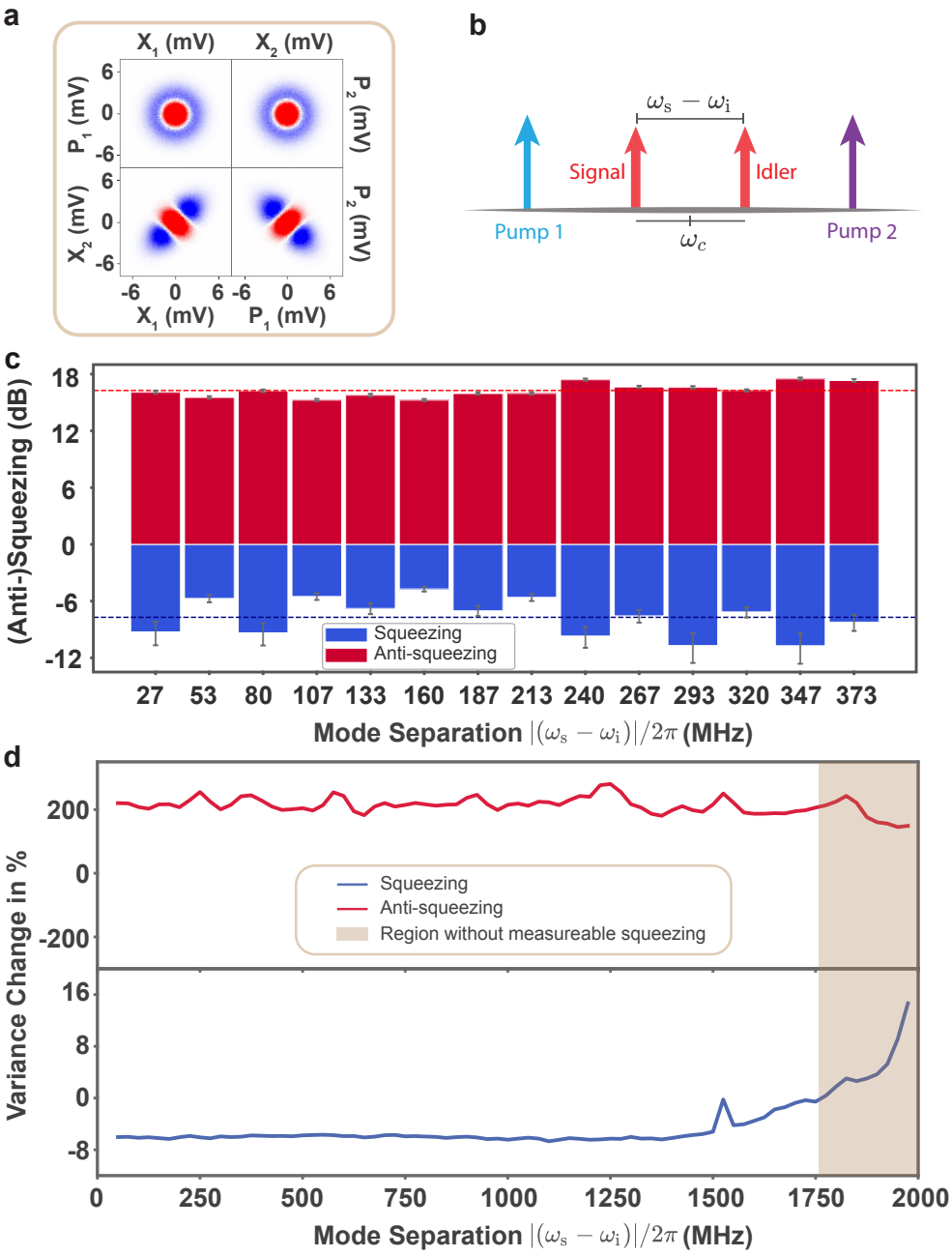

Figure 7-9. Broadband two-mode squeezed vacuum. a. Difference in the output field histograms between vacuum (red) and two-mode squeezed vacuum (blue). The histograms show the X and P quadratures (equivalently, the in-phase and quadrature components) of the squeezed and vacuum states with signal and idler 320 MHz detuned from each other and centered at ω_c. The histograms are collected at room temperature. **b.** Illustration of the frequency spectrum for the two-mode squeezing process. **c.** Measurement of two-mode squeezing versus frequency separation $|\omega_s - \omega_i|/2\pi$ between the signal and the idler. The dashed lines indicate average values for the measured squeezing/anti-squeezing levels. **d.** Percent change in variance measured at room temperature between squeezed vacuum and vacuum for the X_1X_2 (or P_1P_2) quadrature as measured using two digitizers (see text). The beige-colored shading indicates the region where there is no measureable squeezing. The spike in the blue line plot (squeezing quadrature) around 1500 MHz correspond to the extra mode generated by the JTWPA.

variations of the loss and nonlinear processes can lead to frequency-dependent two-mode squeezing performance [49]. However, based on the flat and broadband gain profile observed in our JTWPA, we infer consistent squeezing levels out to 1.5 GHz total signal-to-idler bandwidth, and net squeezing out to 1.75 GHz total signal-to-idler bandwidth.[1] These results represent almost two-orders-of-magnitude increase in two-mode squeezing bandwidth compared to conventional resonator-based squeezers [31, 32, 69, 65, 39, 97].

Further Discussion

7.2.3 Squeezing Purity

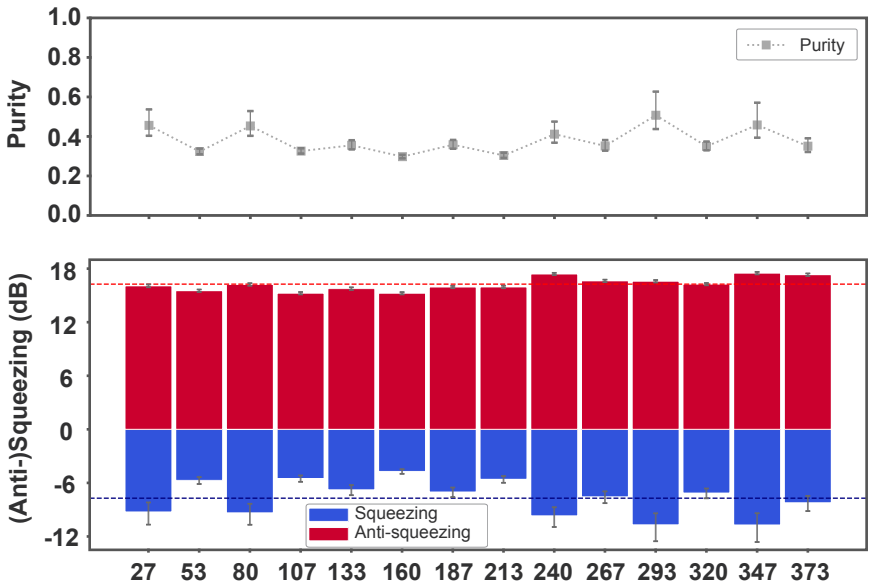

Figure 7-10. | Squeezing level and purity of two-mode squeezed vacuum state. The top panel displays the corresponding squeezing purity associated with the squeezing levels shown at the bottom. Similar to the single-mode squeezing results, the data are presented as mean values of 3 sets of repeated measurement (each with 6×10^6 sample points). Their statistical variation is almost entirely due to the uncertainty in estimating the noise temperature, which dominates the error bars shown in the plot as an estimation range for the squeezing/anti-squeezing levels.

In both Fig. 7-12(g) and Fig. 7-10, we have shown the purity of the squeezed states as a

[1] We note that although our noise calibration device was limited to 500 MHz bandwidth, the system noise temperature likely remains similar outside of this frequency range, as there is no apparent reason why it would suddenly change value. Therefore, we expect similar reductions in measured variance outside the calibrated band to correspond to similar levels of inferred squeezing measured within the band. However, since we did not explicitly calibrate the system noise at those frequencies, we report the measured reduction in variance.

function of pump power and mode separation, respectively. Following the definition used in Ref. [25], purity of the squeezed state can be expressed as $\mathcal{P} = 1/\sqrt{S_- S_+}$ for a Gaussian state, where S_- and S_+ denote squeezing and anti-squeezing factors. For single-mode squeezing, we extract the purity around the maximum squeezing level to be $0.605^{+0.201}_{-0.100}$. Similarly, for two-mode squeezing, the average purity is 0.379 and a maximum purity of $0.507^{+0.120}_{-0.070}$ at 293 MHz mode separation. The two-mode squeezing is measured under the same pump configuration for the maximal single-mode squeezing and can be further optimized. In comparison with cavity-based squeezers, the purity values have more room for improvement. The remarkably high levels of squeezing (as high as -11.3 dB for single-mode squeezing and -9.5 dB for two-mode squeezing) with only 40%-50% purity suggests that the JTWPA is capable of achieving even better squeezing performance, e.g., if we reduce the internal loss that likely limits the purity in this Nb-based version of the JTWPA. As discussed in Chapter 6, we are currently developing a new generation of Al-JTWPAs with a much lower internal loss and further suppression of spurious nonlinear processes [83].

7.2.4 Squeezing Degradation

Fig. 7-12 shows the evolution of squeezing as a function of pump powers for 6 of the points shown in Fig. 7-4. The vacuum and squeezed states from Fig. 7-3 are the middle panels (top and bottom) in Fig. 7-12 and correspond approximately to the maximal degree of squeezing observed. The leftmost panel(a) correspond to vacuum states with the pumps off. Panel(b) shows a moderate degree of squeezing. As mentioned, panel(c) is from Fig. 7-3. For even higher pump powers, squeezing becomes distorted in panel(d) and even disappears in panel(f) as the junctions in the JTWPA become overpowered, the gain starts to saturate and degrade as shown in Fig. 7-11, and higher-order nonlinearities [14] and even losses manifest. The histograms give a different perspective on squeezing degradation shown in Fig. 7-4 and indicate different higher-order nonlinearities compared to a JPA that exhibits a distorted output field [14]. After the junctions become saturated, they can generate excessive noise due to their dynamic resistance. The output field shows more intense fluctuations from the blue enlarged circular “blob” in panel(e) and more so

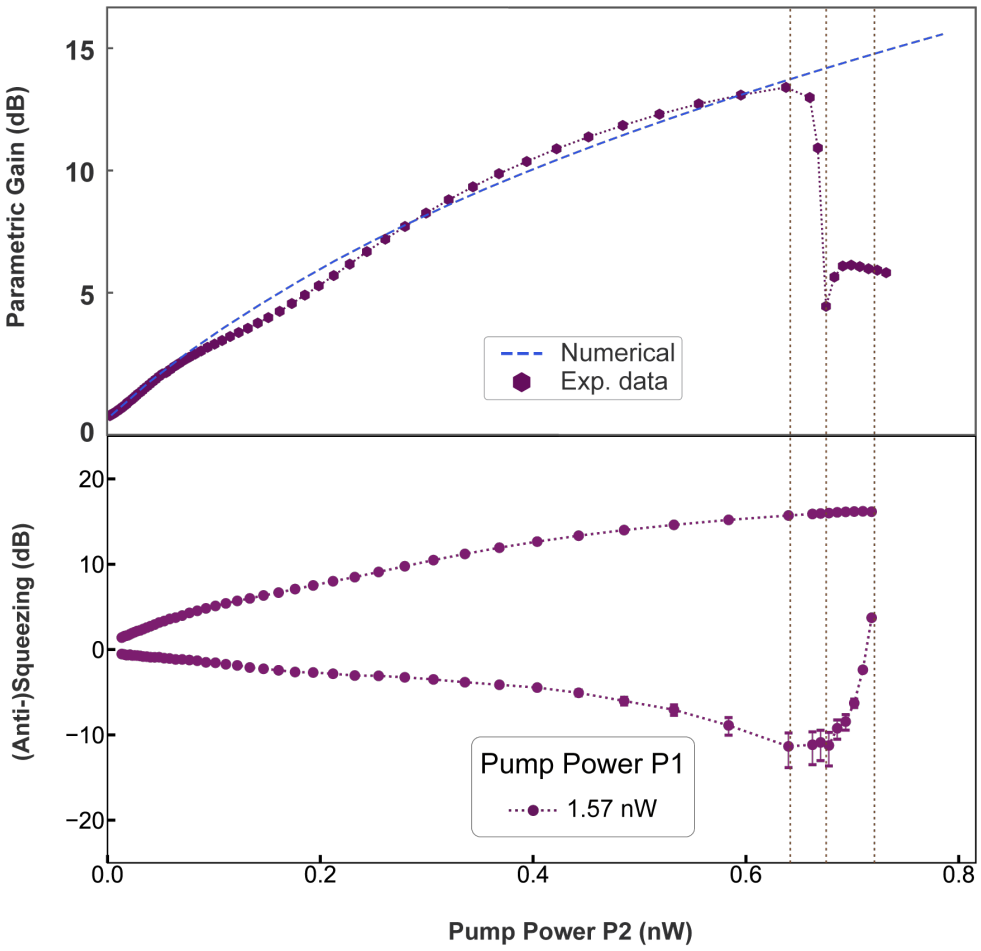

Figure 7-11. | **Squeezing and parametric gain as a function of pump power.** The top panel shows the parametric gain as function pump 2 power while fixing the pump 1 power at 1.57 nW. The gain is measured by normalizing the JTWPA transmission profile when both pumps are on with respect to that when both pumps are off. The bottom panel shows the squeezing (upper data trace) and anti-squeezing (lower data trace) as a function of pump powers.

in panel(f). As the pump power continues to increase, the power dissipation leads to an increasing quadrature variance as seen in Fig. 7-4, and Fig. 7-12(g) shows more details towards the high-pump-power region.

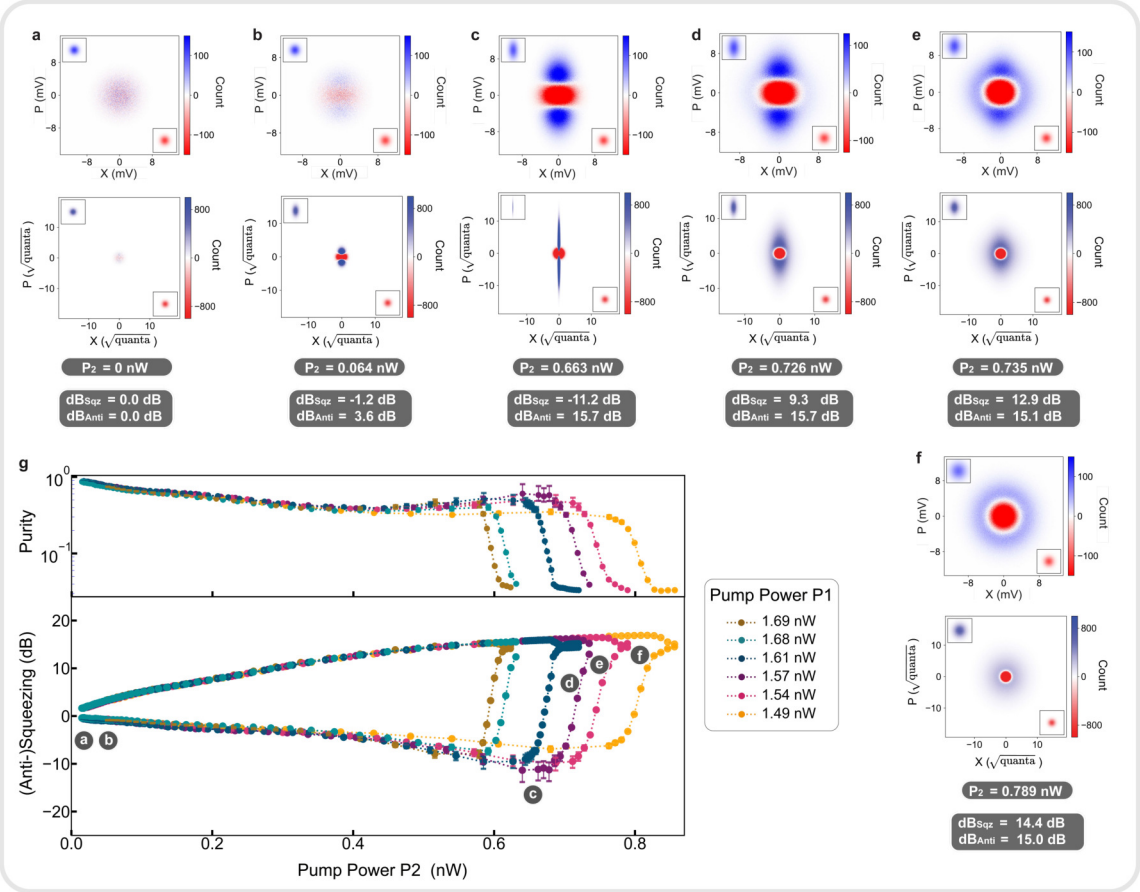

Figure 7-12. | Output field imaging of squeezed state evolution as pump power increases. The top row demonstrates the output fields in voltage basis measured at room temperature, and the bottom row shows the same state in photon basis at the JTWPA. The histograms show the X and P quadratures of the squeezed and vacuum states. Panels **a** - **f** display the difference in the output field histograms between vacuum (red) and single-mode squeezed vacuum (blue), which are shown individually in the insets. The top panel in **g** shows the purity of the squeezed states as a function of pump power.

7.2.5 JTWPA Multimode Behavior

Because of its traveling-wave nature, the JTWPA permits a broad frequency spectrum of modes to propagate and to be converted from/to various modes through the $\chi^{(3)}$ non-linearity. We assume the pumps to be classical and effective delta functions in the fre-

quency spectrum in the analysis. However, a collection of frequency products of a single or both pumps exist in reality and can gradually become significant at increased pump power. Furthermore, depending on the phase mismatch, any two-pump-photon nonlinear process could, in principle, exert non-negligible and often adverse effects on the signal.

The deviation between the simulation and experimental data on single-mode squeezing indicates that the multimode behavior cannot be captured by the two-mode input-output model developed within the scope of the thesis work. This section will demonstrate preliminary experimental observations to illuminate the multimode dynamics within a JTWPA further.

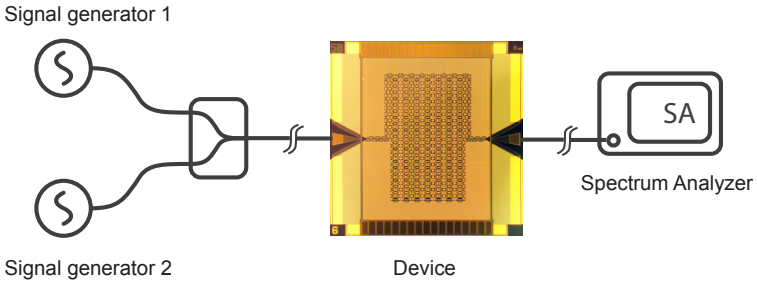

Figure 7-13. | Simplified measurement schematic to probe the multimode behavior. Two signal generators send pump tones into the device, of which the output is measured using a spectrum analyzer.

To understand the multimode behavior and quantify their relative levels at the output, we performed a spectral analysis of the JTWPA pumped by two frequency-locked signal generators at 5.2984 GHz and 8.109 GHz, respectively. The simplified experimental setup for the multimode is illustrated in Fig. 7-13.

Shown in Fig. 7-15, as pump 2 power is increased, we observe a notable increase in the mode at frequencies $f_4 = 5.9447$ GHz, which is related to the two pumps by $f_4 = 4f_{p2} - 5f_{p1}$. This and the other visible modes can be understood as the by-products of both pumps under strong field dynamics [79]. These modes can only reach the signal of interest at $f_s = (f_{p1} + f_{p2})/2$ through higher-order nonlinear processes that are mediated by the two major pump tones. Their direct interactions with the signal are thus significantly weaker and neglected.

Instead, these pump products indirectly affect the squeezing performance; they effectively modulate the spatial profile of the two primary pump tones, as indicated by the cor-

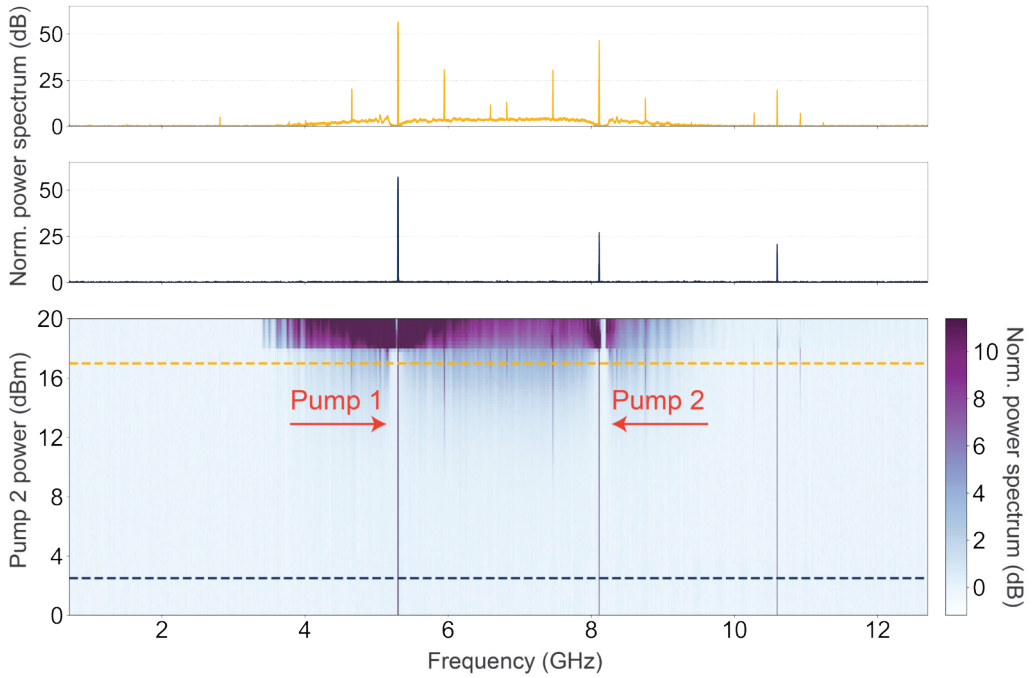

Figure 7-14. | **Power spectrum with dual pumps.** The 2D plot displays a normalized power spectrum with the background (pumps off) subtracted from the data. The X-axis is the frequency range scanned, and Y-axis represents the pump power value at the signal generator in dBm. The top two panels correspond to a slice of 2D data at a specific pump power.

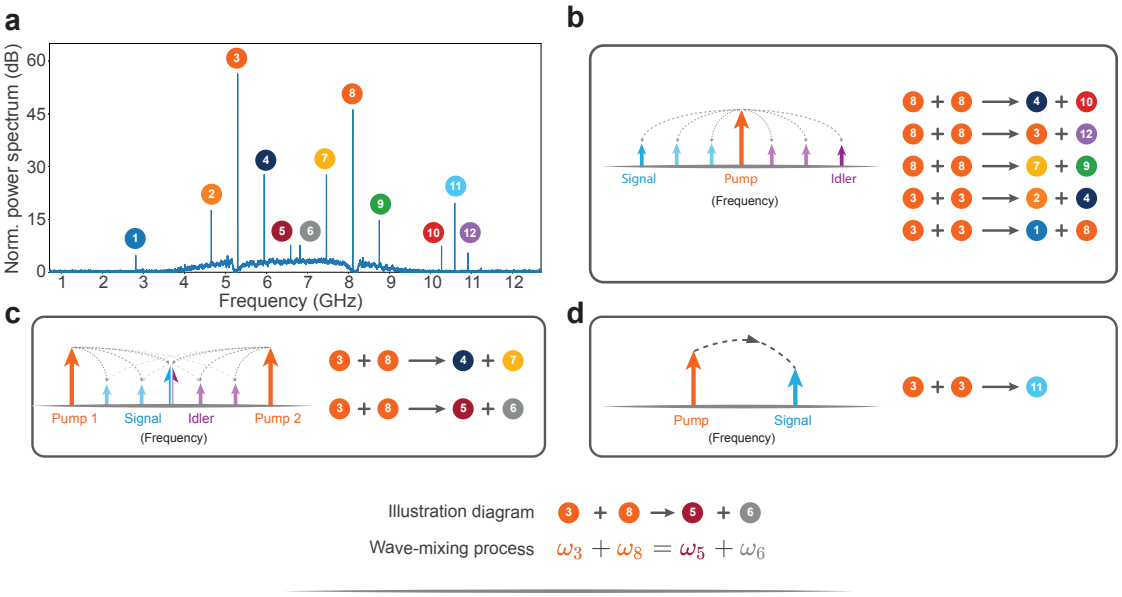

Figure 7-15. | **Mode spectrum and associated wave mixing processes. a.** A spectrum of modes shows up after both pumps are turned on. It is the same plot as the top panel in Fig. 7-14, but with labels for each of the dominant 12 modes (pumps included). **b.** Degenerate four-wave mixing. **c.** Non-degenerate four-wave mixing. **d.** Second-harmonic generation.

relations between the measured pump phase data and the increase of their intensities. The modes correlate to the qualitative change in the measured phase data of the two pumps. Although too weak to act as a pump to the signal, the pump products are coupled to the pump tones and lead to an effective modulation. We can account for their effects to a good approximation by extracting the loaded wave vector and amplitude of the pump tones from measurements and then applying them in the updated numerical model, explained in appendix A. It remains an interesting open research topic to simulate the multimode behavior involving multi-pump photon processes and ways to mitigate or enhance them through dispersion engineering, for instance.

There are two major approaches to improving the JTWPA squeezing performance based on our current architecture. The squeezing level is expected to approach the performance dominated by loss through Floquet engineering and its potential benefit of suppressing spurious nonlinear processes such as sideband generation. The squeezing purity will improve in the low-to-mid power region. Moreover, we can further decrease the JTWPA loss from the dielectrics by using a high-Q fabrication process. In the limit of near-lossless performance, the maximum squeezing level limit will approach -20 dB — an almost 10 dB improvement — assuming the device performance is solely constrained by loss at this point.

Chapter 8

Conclusion and Outlook

This thesis illustrates a new application of dispersion engineering for a JTWPA to produce broadband amplification. We design and demonstrate a dual-pump Josephson traveling-wave parametric amplifier that exhibits both phase-preserving and phase-sensitive amplification and both single-mode and two-mode squeezing. We measured 20 dB parametric gain over more than 3.5 GHz total instantaneous bandwidth (1.75 GHz for each the signal and the idler) with a 1 dB compression point of -98 dBm. This gain performance is comparable with the single-pump JTWPA, yet it features minimal gain ripple and gain roll-off within the frequency band of interest. This advance alone holds the promise to improve the readout of frequency-multiplexed signals [46].

In addition, it is also the first demonstration of phase-sensitive amplification and the production of squeezed vacuum states in a JTWPA. The favorable performance of this device enabled us to measure a 56 dB phase-sensitive extinction ratio, useful for qubit readout in quantum computing and phase regeneration in quantum communications. The phase-sensitive amplification can be used in near-noiseless amplification, for instance, qubit readout. Directly embedding a JTWPA within a qubit system using 3D integration techniques [93] can improve the overall measurement efficiency by mitigating the effects of off-chip losses. This configuration can minimize backaction to the qubit dispersive measurement by squeezing the quantum noise [29].

This work explores different noise characterization methods using various platforms (a shot-noise tunnel junction and a qubit-waveguide system) and analyzes their merits and

drawbacks. The noise calibration is crucial to squeezed states characterization. The measurement protocols and the setup schematics developed comprehensively throughout the project help with future experiments that require a deeper understanding of measurement efficiency, particularly on quantum amplifiers and squeezer characterization.

We have observed high squeezing levels, despite dielectric loss from the $\mathrm{SiO_2}$ capacitors, which we attribute predominantly to distributed TLS saturation in the high-gain regions of our JTWPA. Nonetheless, squeezing performance can be further improved by introducing a lower-loss capacitor dielectric. Performance can also be improved by exploring distributed geometries and Floquet-engineered JTWPAs that reduce the impact of unwanted parasitic processes [83].

We also achieve a single-mode squeezing level of $-11.35^{+1.57}_{-2.49}\,\mathrm{dB}$, and two-mode squeezing levels averaging -6.71 dB with a maximum value of $-9.54^{+1.11}_{-1.63}\,\mathrm{dB}$ measured directly over approximately 400 MHz and extending to over more than 1.5 GHz total bandwidth (signal to idler frequency separation). The results enable direct applications of the JTWPA in superconducting circuits, such as suppressing radiative spontaneous emission from a superconducting qubit [76] and enhancing the search for dark matter axions [5].

The broad bandwidth and high degree of squeezing demonstrated in our device represent a resource-efficient means to generate multimode, non-classical states of light with applications spanning qubit-state readout [8, 26], quantum illumination [7, 58], teleportation [63, 127, 36], and quantum state preparation for continuous-variable quantum computing in the microwave regime [44, 37]. In addition, the technique of using dispersion engineering to phase match different nonlinear processes can be extended to explore dynamics within superconducting Josephson metamaterials with engineered properties not otherwise found in nature.

In this thesis, we develop sub-gigahertz JTWPAs and demonstrate first-of-its-kind broadband superconducting amplifiers with significant gain and broadband amplification performance. Moreover, we explore fabricating JTWPAs using a high-Q aluminum process and achieve promising preliminary results with broadband gain and low insertion loss. This work will continue here at MIT, and I believe we will see outstanding performance from aluminum JTWPA in the near future.

Future Outlook

The end of the thesis does not represent the end of the work but rather a demonstration of engineering Josephson traveling-wave amplifiers to generate squeezing. As a step forward, the goal is to utilize squeezing to interact with different quantum systems. We will discuss a few ideas here.

Heisenberg-Limited Readout

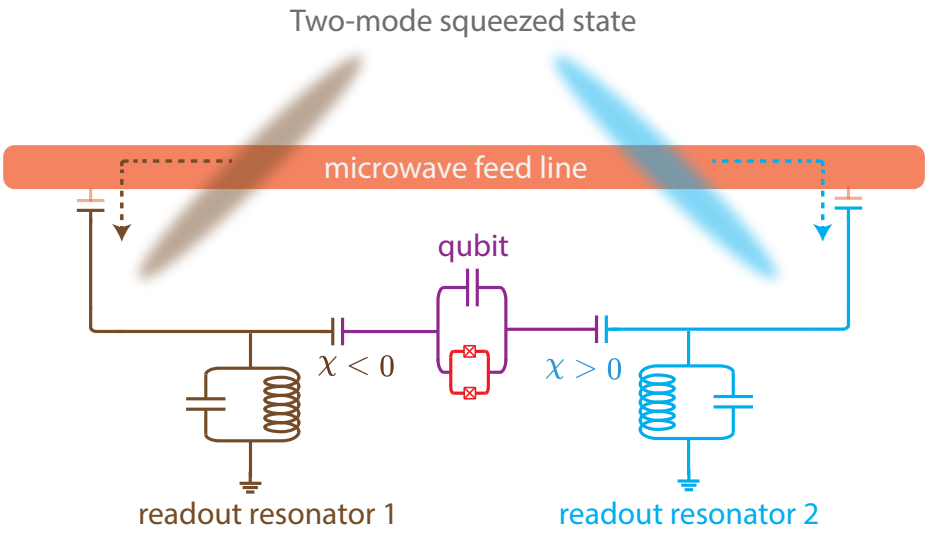

Figure 8-1. | cQED implementation of Heisenberg-limited readout with two-mode squeezed states produced by a JTWPA. The qubit is coupled to two resonators with equal and opposite dispersive shifts. The two-mode squeezed state generated by a JTWPA will shine onto these two resonator modes to create a QMFS.

Increasing the device length is expected to improve the squeezing and gain further [61]. The performance can also benefit from TLS loss reduction. An interesting direction we have explored is to design and benchmark aluminum-base JTWPAs with higher-Q than the niobium process for enhancing both amplification and squeezing performances. So far, we have reached promising preliminary results, and the project is expected to continue. Overall, this work demonstrates a scalable dispersion engineering approach to achieve multimode squeezing, which has the potential to generate large cluster states [44], to be utilized in continuous-variable quantum computing [68], and to assist Heisenberg-limited readout

of superconducting qubits [26]. As shown in Fig. 8-1, by shining two-mode squeezed microwave generated by a JTWPA in a two-cavity-plus-qubit system, one can construct a "quantum-mechanics-free subspace" (QMFS), a subsystem that evades the measurement backaction of quantum mechanics [112] that can have both quadratures squeezed simultaneously, and therefore, achieve Heisenberg-limited SNR scaling.

Qubits Entanglement with Two-Mode Squeezed State

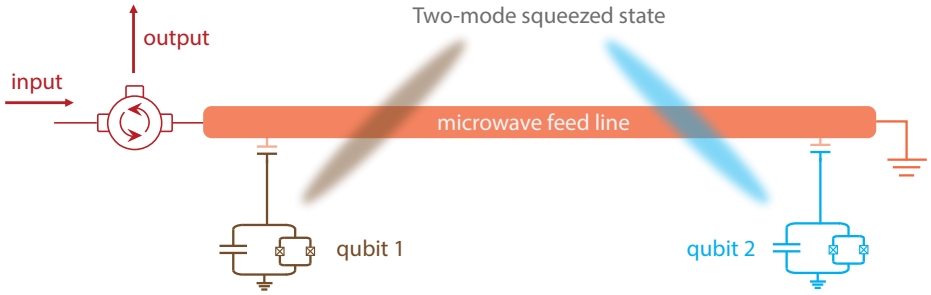

Figure 8-2. | **Entangling qubits via dissipation with two-mode squeezed state.** The qubit system is similar to the OTL device with qubits coupled to a waveguide in reflection mode. A higher degree of entanglement can be achieved by avoiding vacuum noise into the waveguide; the two-mode squeezed state is injected through the input.

The work has also inspired us to utilize qubits to detect and measure two-mode squeezed microwaves. JTWPA can become a source of entanglement for the qubits coupled to a waveguide [44]. The entanglement can be achieved by addressing a pair of qubits resonant with each of the squeezed modes in a two-mode squeezed state. Moreover, multiple pairs of qubits can be entangled simultaneously using a single squeezer, which can benefit from the broadband squeezing performance we have demonstrated with a JTWPA.

Enhancing RIP Gate Fidelity with Squeezed Coherent State

The RIP gate has an inherent tradeoff between measurement-induced dephasing and gate time. During the adiabatic gate evolution, photons "encoded" with qubit state ('which-path') information can leak through different channels, such as cavity losses, and cause dephasing [14]. One remedy is to drive the cavity far detuned (many linewidths) away

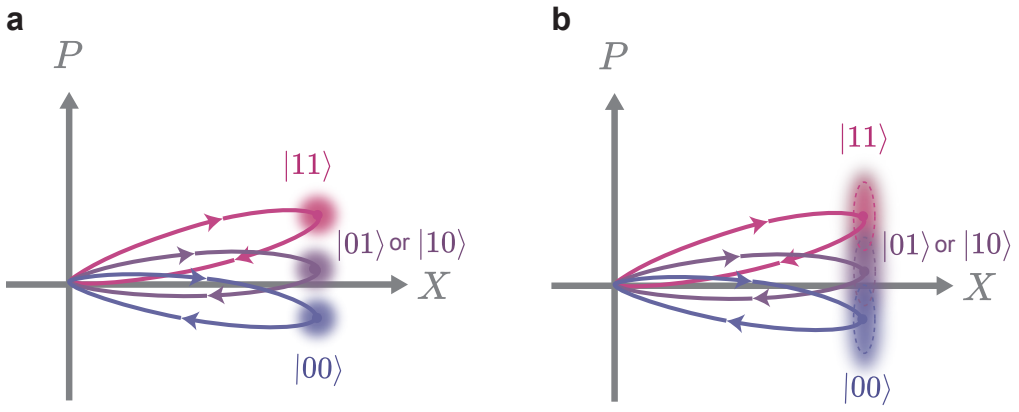

Figure 8-3. | Evolution of qubit-state-dependent resonator field. a. Qubit-state dependent trajectories of the outgoing resonator field under a coherent-state drive. The states are displayed in phase space (solid lines) in the rotating frame of the drive. **b.** Qubit-state dependent trajectories with squeezed-coherent-state drive.

from its resonance so that it is only virtually populated. The drawback with this remedy is the prolonged gate time detrimental to achieving high gate fidelity. On the other hand, if we decrease this drive detuning, so will the gate time, but dephasing will deteriorate further.

Pulse-shaping techniques can be utilized to mitigate this problem partially [15]. Single-mode squeezing has been proposed to directly address the challenge of improving RIP gate fidelity by lowering the dephasing rate while shortening the gate time [14]. In the previous realization of the RIP gate, residual qubit-cavity entanglement creates an unwanted leakage channel of qubit state information to the environment via cavity photon loss and degrades gate fidelity [13]. To address this problem, we engineer the light-mediated interaction by driving the resonator using squeezed coherent state.

Quantum erasure

The benefit of radiating the resonator with squeezed light can be understood as enhancing the fluctuation in the appropriate quadrature to erase the "which-path" information while leaving the area enclosed by the path — accumulated phase unchanged. A cartoon illustration can be seen in Fig.8-3. Intuitively, measurement-induced dephasing is caused by the ac-Stark shift from photon shot noise in the resonator. Even when we (as observers)

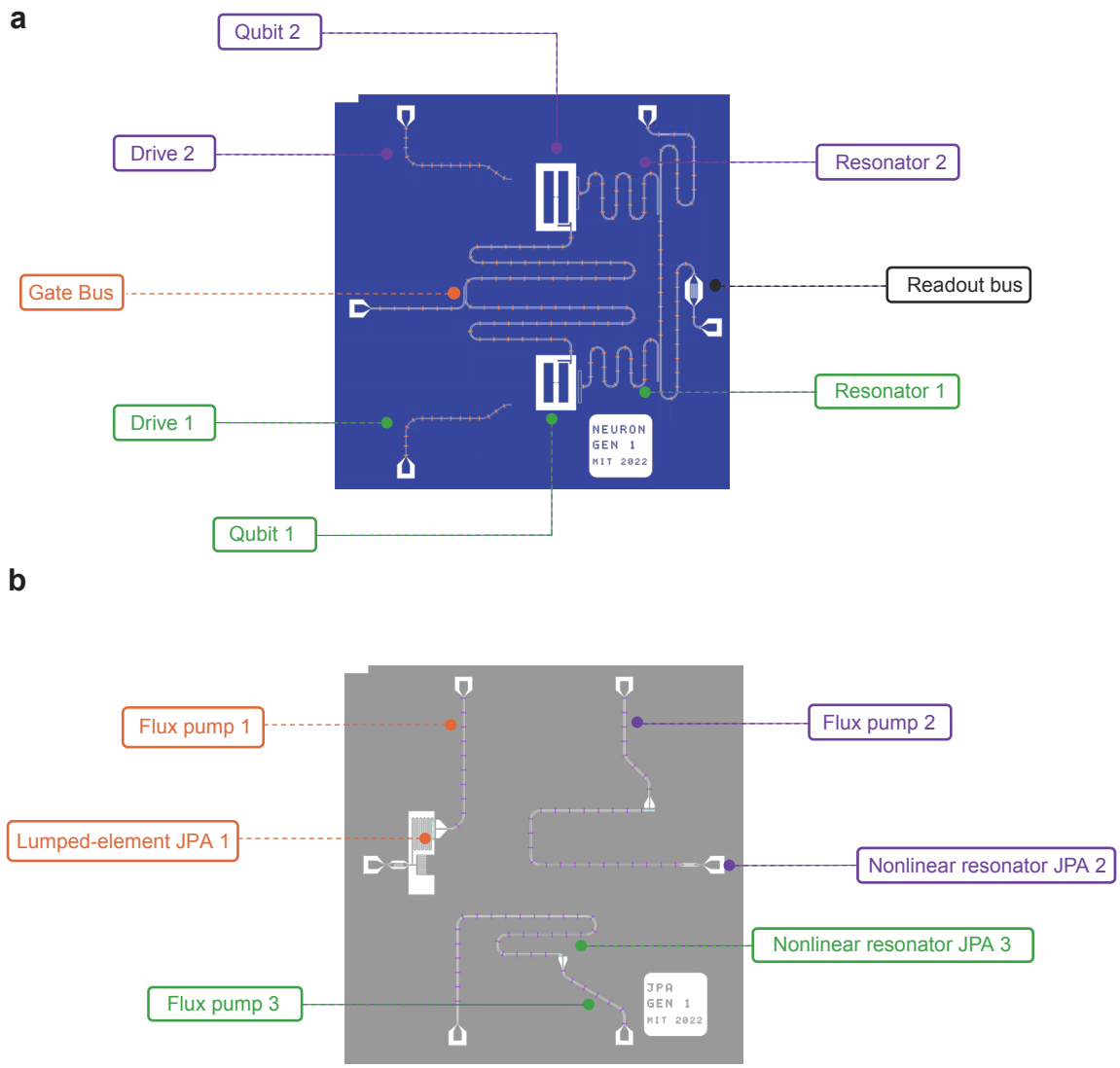

Figure 8-4. | **Chip designs. a.** 2D chip layout for two-qubit RIP gate. **b.** 2D chip layout for a trio-JPA device.

are not actively measuring the quantum system, there is still quantum backaction from the environment upon the qubits during the phase evolution. In other words, the environment is "measuring" the quantum system. The enlarged fluctuation in the anti-squeezing quadrature "smears" qubit state trajectories, thereby countering environmental quantum backaction. This technique can erase qubit "which-path" information for different qubit states, thereby reducing qubit dephasing during the RIP gate operation.

For this project, a preliminary set of qubit chips have been designed, simulated, and ready for fabrication. The designs are shown in Fig. 8-4. The qubit chip consists of two

fixed-frequency transmons, both coupled to a quarter-wave resonator for readout and a Purcell filter to minimize the Purcell decay. The JPAs are preferred in this specific experiment due to their narrow-band output spectrum, which could be beneficial in reducing the thermal contribution. The chip consists of three lumped-element SQUID-based JPAs. These would be the legacy device that future students can test and improve. The goal is to build a multiqubit system with all-to-all connectivity, advantageous and unique for quantum computing and analog quantum simulation purposes. The thesis focuses on amplification and squeezed photon generation using Josephson parametric amplifiers. As a major source of non-classical light, squeezed light plays an important role in light-matter physics. The JTWPA developed in this thesis demonstrates the versatility of traveling-wave-based architecture in dispersion engineering and the capability of extending the broadband amplification performance beyond the existing frequency spectrum. Furthermore, the design approach presented is extensible to more complex Josephson metamaterials with the potential to generate different types of non-classical light. The last part of the thesis draws a blueprint for a specific interaction between squeezed microwave photons and superconducting qubits. The utilization of squeezing can mitigate errors and protect the fragile quantum states in the path of achieving a robust quantum computer.

Appendix A

Linearized Input-Output Theory for Squeezing Simulation

The numerical models have been primarily developed by our theory collaborator Arne Grimsmo, which allow us to simulate the squeezing effect based as illustrated in Chapter 7. In this appendix, we describe the numerical models of JTWPA squeezing. Note that some of the notations may appear slightly different.

Following the approach from Ref. [44], we derive a Hamiltonian for the JTWPA in the continuum limit where the unit cell distance $a \to 0$ such that the total length $z = Na$ is held constant

$$\hat{H} = \hat{H}_0 + \hat{H}_1, \tag{A.1}$$

where to fourth order in the Josephson junction potential we have

$$\hat{H}_0 = \int_0^\infty d\omega \hbar\omega \hat{a}_\omega^\dagger \hat{a}_\omega, \tag{A.2}$$

$$\hat{H}_1 = -\frac{\gamma}{2}\int_0^z dx[\partial_x \hat{\phi}(x)]^4. \tag{A.3}$$

Here $\hat{a}_\omega^\dagger$ creates a delocalized right-moving photon of energy $\hbar\omega$, $\gamma = a^3 E_J \left(\frac{2\pi}{\Phi_0}\right)^4 /12$ is a parameter that describes the strength of the non-linearity, and

$$\hat{\phi}(x) = \int_0^\infty d\omega \sqrt{\frac{\hbar Z_0}{4\pi k_\omega v}} e^{ik_\omega x}\hat{a}_\omega + \text{H.c.}, \tag{A.4}$$

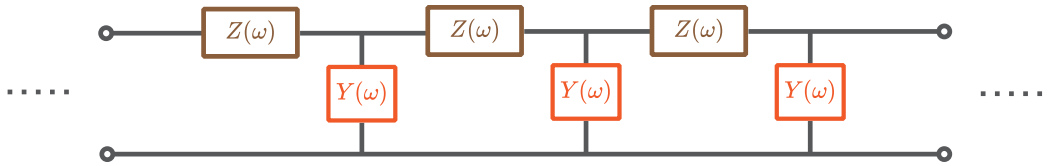

Figure A-1. | Illustration of linear impedance $Z(\omega)$ and admittance $Y(\omega)$ for an arbitrary linear transmission line.

is the flux field along the JTWPA. For simplicity, we only consider the right-moving part of the field, under the assumption the input/output transmission lines are well impedance matched and that back-scattering is negligible. We have moreover introduced a characteristic impedance $Z_0 = \sqrt{l/c}$ and nominal speed of light $v = 1/\sqrt{lc}$, with $c = C_0/a$ and $l = \Phi_0/(2\pi I_c a)$, the capacitance to ground and inductance per unit length, respectively. The dispersion relation for the wavenumber k_ω is given by the series impedance $Z(\omega)$ and parallel admittance to ground $Y(\omega)$ of each unit cell [78, 44] (see A-1).

$$k_\omega a = -i\sqrt{Z(\omega)Y(\omega)}. \tag{A.5}$$

We linearize the problem by assuming a strong right-moving classical pump and replace $\hat{a}_\omega \to \hat{a}_\omega + b(\omega)$, with $b(\omega)$ the pump amplitude, and neglect terms higher than second order in $\hat{a}_\omega^{(\dagger)}$, as well as the influence of the quantum fields on the pump. Moreover, dropping fast rotating terms, we have a Hamiltonian

$$\hat{H} = \hat{H}_0 + \hat{H}_{\text{fc}} + \hat{H}_{\text{sq}}, \tag{A.6}$$

where

$$\hat{H}_{\text{fc}} = -\frac{\hbar}{2\pi}\int_0^\infty d\omega_1 d\omega_2 \Phi_{\text{fc}}(\omega_1,\omega_2)\hat{a}^\dagger_{\omega_1}\hat{a}_{\omega_2} + \text{H.c.}, \tag{A.7}$$

$$\hat{H}_{\text{sq}} = -\frac{\hbar}{4\pi}\int_0^\infty d\omega_1 d\omega_2 \Phi_{\text{sq}}(\omega_1,\omega_2)\hat{a}^\dagger_{\omega_1}\hat{a}^\dagger_{\omega_2} + \text{H.c.} \tag{A.8}$$

describes frequency conversion and photon pair creation, respectively. For notational con-

venience, we have defined phase matching functions

$$\Phi_{\text{fc}}(\omega_1,\omega_2)=\sqrt{k_{\omega_1}k_{\omega_2}}\int_0^\infty d\Omega_1 d\Omega_2\times\int_0^z dx\beta(\Omega_1)^*\beta(\Omega_2)e^{i\left(k_{\omega_1}-k_{\omega_2}+k_{\Omega_1}-k_{\Omega_2}\right)x} \tag{A.9}$$

$$\Phi_{\text{sq}}(\omega_1,\omega_2)=\sqrt{k_{\omega_1}k_{\omega_2}}\int_0^\infty d\Omega_1 d\Omega_2\times\int_0^z dx\beta(\Omega_1)\beta(\Omega_2)e^{i\left(k_{\omega_1}+k_{\omega_2}-k_{\Omega_1}-k_{\Omega_2}\right)x}, \tag{A.10}$$

where $\beta(\omega)=\sqrt{3\gamma l}\sqrt{\hbar Z_0 k_\omega/4\pi v}b(\omega)$ is a rescaled pump amplitude with units of inverse frequency. The pump amplitude can be related to the pump current as [44]

$$\beta(\omega)=\frac{I_p(\omega)}{4I_c}, \tag{A.11}$$

where the current is defined as $I_p(\omega)=\sqrt{\hbar Z_0/4\pi k_\omega v}b(\omega)/l$ and we used that $\gamma l^3=1/12I_c$.

Similarly, the classical pump Hamiltonian can be written

$$H_p=H_{p0}+H_{p1} \tag{A.12}$$

with

$$H_{p0}=\frac{16\pi E_J}{a}\int_0^\infty\frac{d\omega\omega}{k_\omega}\beta(\omega)^*\beta(\omega), \tag{A.13}$$

$$H_{p1}=-\frac{4E_J}{a}\int_0^\infty\frac{d\omega_1 d\omega_2\Phi_{\text{fc}}(\omega_1,\omega_2)}{\sqrt{k_{\omega_1}k_{\omega_2}}}\beta(\omega_1)^*\beta(\omega_2)+\text{c.c.} \tag{A.14}$$

To simplify the problem, we consider the steady-state solution by going to an interaction picture with respect to $\hat{H}_0+H_{p0}$ and integrating from an initial time $t_0=-\infty$ to final time $t_1=\infty$ [44, 90]. Moreover, we take the pump to be a sum of two delta functions in frequency $\beta(\omega)=\sum_{p=1}^2\beta_p\delta(\omega-\Omega_p)$, with β_p a dimensionless pump amplitude.

In the scattering limit, we find position-dependent equations of motion for the pump

and the quantum fields [44]. Specifically,

$$\frac{d\beta_p}{dx} = ik_p\left(|\beta_p|^2 + 2|\beta_q|^2\right)\beta_p, \tag{A.15}$$

with $p = 1, 2$, $q \neq p$ $k_p \equiv k_{\Omega_p}$ and

$$\begin{aligned}\frac{d\hat{a}_\omega}{dx} = 2i\sum_{p=1}^{2}\lambda_{pp}^{\text{fc}}(\omega)e^{-i\Delta k_{pp}^{\text{fc}}(\omega)x}\hat{a}_\omega + 2i\sum_{p\neq q}\lambda_{pq}^{\text{fc}}(\omega)e^{-i\Delta k_{pq}^{\text{fc}}(\omega)x}\hat{a}_{\omega+\Omega_p-\Omega_q} \\ + i\sum_{p,q=1}^{2}\lambda_{pq}^{\text{sq}}(\omega)e^{-i\Delta k_{pq}^{\text{sq}}(\omega)x}\hat{a}^\dagger_{\Omega_p+\Omega_q-\omega},\end{aligned} \tag{A.16}$$

where

$$\lambda_{pq}^{\text{fc}}(\omega) = \beta_p^*\beta_q\sqrt{k_\omega k_{\omega+\Omega_p-\Omega_q}}, \tag{A.17a}$$

$$\lambda_{pq}^{\text{sq}}(\omega) = \beta_p\beta_q\sqrt{k_\omega k_{\Omega_p+\Omega_q-\omega}}, \tag{A.17b}$$

$$\Delta k_{pq}^{\text{fc}}(\omega) = -k_\omega + k_{\omega+\Omega_p-\Omega_q} - k_p + k_q, \tag{A.17c}$$

$$\Delta k_{pq}^{\text{sq}}(\omega) = -k_\omega - k_{\Omega_p+\Omega_q-\omega} + k_p + k_q. \tag{A.17d}$$

The first term in Eq. (A.16) describes cross-phase modulation, which contributes to the phase mismatch. It is convenient to transform to a rotating frame with respect to this process by defining $\hat{c}_\omega = \hat{a}_\omega e^{-2i\sum_p|\beta_p|^2k_\omega x}$, such that we have an equation of motion

$$\frac{d\hat{c}_\omega}{dx} = 2i\sum_{p\neq q}\lambda_{pq}^{\text{fc}}(\omega)e^{-i\tilde{\Delta}k_{pq}^{\text{fc}}(\omega)x}\hat{c}_{\omega+\Omega_p-\Omega_q} + i\sum_{p,q=1}^{2}\lambda_{pq}^{\text{sq}}(\omega)e^{-i\tilde{\Delta}k_{pq}^{\text{sq}}(\omega)x}\hat{c}^\dagger_{\Omega_p+\Omega_q-\omega}, \tag{A.18}$$

with a non-linear modification to the phase mismatch

$$\tilde{\Delta}k_{pq}^{\text{fc}}(\omega) = -\tilde{k}_\omega + \tilde{k}_{\omega+\Omega_p-\Omega_q} - \tilde{k}_p + \tilde{k}_q, \tag{A.19}$$

$$\tilde{\Delta}k_{pq}^{\text{sq}}(\omega) = -\tilde{k}_\omega - \tilde{k}_{\Omega_p+\Omega_q-\omega} + \tilde{k}_p + \tilde{k}_q, \tag{A.20}$$

where

$$\tilde{k}_\omega = \left(1 + 2\sum_p |\beta_p|^2\right) k_\omega, \tag{A.21a}$$

$$\tilde{k}_p = \left(1 + |\beta_p|^2 + 2|\beta_q|^2\right) k_p \quad (p \neq q). \tag{A.21b}$$

Quantum Loss Model

We introduce a phenomenological distributed loss model by adding loss terms to Eq. (A.18)

$$\begin{aligned}\frac{d\hat{c}_\omega}{dx}(x) = 2i\sum_{p\neq q} \lambda_{pq}^{\text{fc}}(\omega) e^{-i\tilde{\Delta}k_{pq}^{\text{fc}}(\omega)x} \hat{c}_{\omega+\Omega_p-\Omega_q}(x) + i\sum_{p,q=1}^{2} \lambda_{pq}^{\text{sq}}(\omega) e^{-i\tilde{\Delta}k_{pq}^{\text{sq}}(\omega)x} \hat{c}^\dagger_{\Omega_p+\Omega_q-\omega}(x) \\ - \frac{\gamma(\omega)}{2}\hat{c}_\omega(x) + \sqrt{\gamma(\omega)}\hat{c}_{\text{in}}(x),\end{aligned} \tag{A.22}$$

where the loss rate $\gamma(\omega)$ has units of inverse length and $\hat{c}_{\text{in}}(x)$ describes vacuum input noise coupled to the JTWPA at each position x [20]. Similarly, the pump equation of motion is modified to

$$\frac{d\beta_p}{dx}(x) = ik_p\left(|\beta_p(x)|^2 + 2|\beta_q(x)|^2\right)\beta_p(x) - \frac{\gamma_p}{2}\beta_p(x). \tag{A.23}$$

The JTWPA output field is found by integrating the spatial differential equations from $x = 0$ to $x = z$, with $\hat{c}_\omega(0)$ taken to be vacuum input. The pump amplitudes can be solved independently and substituted into Eq. (A.22). We have the following solution to the pump equation:

$$\beta_p(x) = \beta_p(0) e^{-\frac{\gamma_p x}{2} - ik_p\left\{\frac{1}{\gamma_p}\left[|\beta_p(x)|^2 - |\beta_p(0)|^2\right] + \frac{2}{\gamma_q}\left[|\beta_q(x)|^2 - |\beta_q(0)|^2\right]\right\}}. \tag{A.24}$$

Note that with this solution, we have

$$|\beta_p(x)|^2 = |\beta_p(0)|^2 e^{-\gamma_p x} \Rightarrow \frac{d|\beta_p(x)|^2}{dx} = -\gamma_p|\beta_p(x)|^2, \tag{A.25}$$

such that we can write

$$\beta_p(x) = \beta_p(0) e^{-\frac{\gamma_p x}{2} + ik_p\left\{\frac{1}{\gamma_p}(1-e^{-\gamma_p x})|\beta_p(0)|^2 + \frac{2}{\gamma_q}\left(1-e^{-\gamma_q x}\right)|\beta_q(0)|^2\right\}}. \tag{A.26}$$

Differentiating Eq. (A.26) gives Eq. (A.23). Note that in the limit $\gamma_p \to 0$ Eq. (A.26) gives

$$\beta_p(x) = \beta_p(0) e^{ik_p x \left\{ |\beta_p(0)|^2 + 2|\beta_q(0)|^2 \right\}}. \tag{A.27}$$

Equation (A.22) can now be solved by inserting the solution for $\beta_p(x)$ into the coupling constants $\lambda_{pq}^{\mathrm{fc,sq}}(\omega)$ and phase mismatch $\Delta k_{pq}^{\mathrm{fc,sq}}(\omega)$.

Numerical method

To solve for the output fields numerically, we first have to choose a finite set of frequencies

$$\mathbb{K} \equiv \{\omega_0, \omega_1, \ldots, \omega_n\}, \tag{A.28}$$

and set $\hat{c}_\omega = 0$ for $\omega \notin \mathbb{K}$ in Eq. (A.22). For a given "signal" frequency ω_0 we construct the set $\mathbb{K}$ in an iterative manner. For the first "level" we add the two frequencies

$$\mathbb{K}_0 = \{\omega_0, \Omega_1 + \Omega_2 - \omega_0\}. \tag{A.29}$$

Then we construct the next level as follows:

$$\mathbb{K}_{l+1} = \{\Omega_p + \Omega_q - \omega_l, \omega_l \pm (\Omega_2 - \Omega_1) \mid \omega_l \in \mathbb{K}_l, p, q \in \{1, 2\}\}, \tag{A.30}$$

but remove from $\mathbb{K}_{l+1}$ any $\omega_l < 0$, any $\omega_l \simeq \Omega_1, \Omega_2$ and any ω_l already in $\mathbb{K}_l$. Finally, $\mathbb{K} = \cup_{l=0}^{k} \mathbb{K}_l$ up to some truncation k. The first two levels thus include

$$\mathbb{K}_0 = \{\omega_0, \Omega_1 + \Omega_2 - \omega_0\}, \tag{A.31a}$$

$$\mathbb{K}_1 = \{2\Omega_1 - \omega_0, 2\Omega_2 - \omega_0, \omega_0 + \Omega_1 - \Omega_2, \omega_0 + \Omega_2 - \Omega_1\}. \tag{A.31b}$$

In practice, we have found after extensive numerical testing that including frequencies beyond the first level $\mathbb{K}_0$ does not improve the fit to the experimental squeezing data.

Once a finite set of frequencies has been chosen, we can use Eq. (A.22) to compute expectation values. For numerical purposes, it is convenient to introduce a matrix-vector

notation

$$\vec{c} = [\hat{c}_1, \ldots, \hat{c}_n, \hat{c}_1^\dagger, \ldots, \hat{c}_n^\dagger]^T, \tag{A.32}$$

and write

$$\frac{d}{dx} \langle \vec{c} \rangle = iKH \langle \vec{c} \rangle - \frac{\Gamma}{2} \langle \vec{c} \rangle , \tag{A.33}$$

where K, H and Γ are $2n \times 2n$ matrices, with $K = \text{diag}[I_n, -I_n]$,

$$\Gamma = \text{diag}[\gamma_1, \ldots, \gamma_n, \gamma_1, \ldots, \gamma_n],$$

and H is a Hermitian matrix that can be written in the block form

$$H = \begin{bmatrix} \Lambda_1 & \Lambda_2 \\ \Lambda_2^* & \Lambda_1^* \end{bmatrix}, \tag{A.34}$$

with $\Lambda_1^\dagger = \Lambda_1$ Hermitian and $\Lambda_2^T = \Lambda_2$ symmetric.

From Eq. (A.33) we can compute the gain using as initial condition

$$\langle \vec{c}(0) \rangle = [\alpha, 0, \ldots, 0, \alpha^*, 0, \ldots, 0]^T,$$

and define the gain to be $g = \langle \hat{c}_0 \rangle / \alpha$, and power gain $G = |g|^2$.

To compute squeezing, we also need to solve for all second order moments, $\left\langle \hat{c}_i \hat{c}_j \right\rangle$, $\left\langle \hat{c}_i \hat{c}_j^\dagger \right\rangle$, etc. For this purpose it is convenient to define a "correlation matrix"

$$C = [\langle \vec{c}_i \vec{c}_j \rangle] = \begin{bmatrix} \left\langle \hat{c}_i \hat{c}_j \right\rangle & \left\langle \hat{c}_i \hat{c}_j^\dagger \right\rangle \\ \left\langle \hat{c}_i^\dagger \hat{c}_j \right\rangle & \left\langle \hat{c}_i^\dagger \hat{c}_j^\dagger \right\rangle \end{bmatrix}, \tag{A.35}$$

where each block is $n \times n$. An equation of motion can be derived from Eq. (A.24) by using that

$$\frac{d}{dx} \langle \hat{c}_i \hat{c}_j \rangle = \langle (\partial_x \hat{c}_i) \hat{c}_j \rangle + \langle \hat{c}_i (\partial_x \hat{c}_j) \rangle , \tag{A.36}$$

etc. We find

$$\frac{d}{dx}C = iKHC + iC(KH)^T + \begin{pmatrix} 0 & \Gamma \\ 0 & 0 \end{pmatrix}, \tag{A.37}$$

where we have assumed a vacuum input field $\hat{c}_{\text{in}}(x)$.

To compute squeezing we first define a "squeezing matrix"

$$\begin{aligned} \Delta Y_{ij}^2(\theta) &= \frac{1}{2}\left\langle \left(\hat{Y}_i^\theta + \hat{Y}_j^\theta\right)^2 \right\rangle - \frac{1}{4}\left\langle \hat{Y}_i + \hat{Y}_j \right\rangle^2 \\ &= \frac{1}{4}\sum_{\substack{i'=i,j \\ j'=i,j}} \left(\left\langle \hat{c}_{i'}^\dagger \hat{c}_{j'} \right\rangle + \left\langle \hat{c}_{i'} \hat{c}_{j'}^\dagger \right\rangle - e^{i\theta}\left\langle \hat{c}_{i'}^\dagger \hat{c}_{j'}^\dagger \right\rangle - e^{-i\theta}\left\langle \hat{c}_{i'} \hat{c}_{j'} \right\rangle \right), \end{aligned} \tag{A.38}$$

where $\hat{Y}_i^\theta = \frac{i}{\sqrt{2}}\left(e^{i\theta/2}\hat{c}_i^\dagger - e^{-i\theta/2}\hat{c}_i\right)$, and in the second line we have used $\left\langle \hat{Y}_i + \hat{Y}_j \right\rangle = 0$ for vacuum input.

The squeezing matrix is here defined such that high squeezing level means that $\Delta Y_{ij}^2(\theta)$ is small. Squeezing is thus maximized between modes i and j ($i = j$ for single-mode squeezing) by choosing θ such that $e^{i\theta}\left\langle \hat{c}_i^\dagger \hat{c}_j^\dagger \right\rangle = \left|\left\langle \hat{c}_i^\dagger \hat{c}_j^\dagger \right\rangle\right|$. Note that the θ that maximizes squeezing might in general be different for different ij.

The squeezing in dB is defined as

$$\mathcal{S}_{ij} = 10\log_{10}\left(\frac{\Delta Y_{ij}^2}{1/2}\right), \tag{A.39}$$

where the $1/2$ is the vacuum fluctuations. To compute the squeezing, Eq. (A.37) is integrated numerically with initial condition

$$C(0) = \begin{pmatrix} 0 & I_n \\ 0 & 0 \end{pmatrix}, \tag{A.40}$$

corresponding to vacuum input.

Calibrating pump power at the device

Matching the numerical results to experimental data requires knowing the dimensionless pump strength $\beta_p = I_p/4I_c$ at the device for a given input power P. One approach to determine β_p is to measure the power dependent phase shift $\Delta\phi_p$ at the pump frequency in the presence of a single pump. From Eq. (A.24) we have that

$$|\beta_p(x=0)|^2 = \frac{1}{k_p}\frac{\gamma_p(P)}{1-e^{-\gamma_p(P)z}}\Delta\phi_p(P), \tag{A.41}$$

where we have included the power dependence of the pump loss rate $\gamma_p(P)$. This procedure is, however, complicated by the fact that we do not observe a linear relationship between $\Delta\phi_p$ and P in the experiment. This could be, amongst other factors, due to the non-trivial dependence of the dispersion feature on power: As the pump power increases, the dispersion feature is observed to become significantly more narrow in frequency, likely due to saturation of two-level systems in the LC oscillators.

Nevertheless, we have found reasonable agreement with experiments by assuming a power dependence of the form

$$|\beta_p(0)|^2 = \frac{1}{k_p}\frac{\gamma_p(P)}{1-e^{-\gamma_p(P)z}} \times c_p P, \tag{A.42}$$

where c_p is a power-independent fit parameter. In practice, we first vary c_p to fit the numerical results to the gain curve and subsequently use the same value of c_p to extract squeezing and anti-squeezing.

Since the gain curve has been fitted, the theory does not directly predict the gain at a given input power P. Nevertheless, it is noteworthy that an excellent fit to the overall shape of the gain curve can be found using this method, as shown in Fig. 3c in the main text. Most importantly, this method allows us to predict the squeezing and anti-squeezing at a given gain.

Bibliography

[1] G. P. Agrawal. *Nonlinear Fiber Optics*. Academic Press, 5 edition, 2012.

[2] J. A. Armstrong, N. Bloembergen, J. Ducuing, and P. S. Pershan. Interactions between light waves in a nonlinear dielectric. *Phys. Rev.*, 127:1918–1939, Sep 1962.

[3] Frank Arute, Kunal Arya, Ryan Babbush, Dave Bacon, Joseph C. Bardin, Rami Barends, Rupak Biswas, Sergio Boixo, Fernando G. S. L. Brandao, David A. Buell, Brian Burkett, Yu Chen, Zijun Chen, Ben Chiaro, Roberto Collins, William Courtney, Andrew Dunsworth, Edward Farhi, Brooks Foxen, Austin Fowler, Craig Gidney, Marissa Giustina, Rob Graff, Keith Guerin, Steve Habegger, Matthew P. Harrigan, Michael J. Hartmann, Alan Ho, Markus Hoffmann, Trent Huang, Travis S. Humble, Sergei V. Isakov, Evan Jeffrey, Zhang Jiang, Dvir Kafri, Kostyantyn Kechedzhi, Julian Kelly, Paul V. Klimov, Sergey Knysh, Alexander Korotkov, Fedor Kostritsa, David Landhuis, Mike Lindmark, Erik Lucero, Dmitry Lyakh, Salvatore Mandrà, Jarrod R. McClean, Matthew McEwen, Anthony Megrant, Xiao Mi, Kristel Michielsen, Masoud Mohseni, Josh Mutus, Ofer Naaman, Matthew Neeley, Charles Neill, Murphy Yuezhen Niu, Eric Ostby, Andre Petukhov, John C. Platt, Chris Quintana, Eleanor G. Rieffel, Pedram Roushan, Nicholas C. Rubin, Daniel Sank, Kevin J. Satzinger, Vadim Smelyanskiy, Kevin J. Sung, Matthew D. Trevithick, Amit Vainsencher, Benjamin Villalonga, Theodore White, Z. Jamie Yao, Ping Yeh, Adam Zalcman, Hartmut Neven, and John M. Martinis. Quantum supremacy using a programmable superconducting processor. *Nature*, 574(7779):505–510, Oct 2019.

[4] Alain Aspect, Philippe Grangier, and Gérard Roger. Experimental realization of einstein-podolsky-rosen-bohm gedankenexperiment: A new violation of bell's inequalities. *Phys. Rev. Lett.*, 49:91–94, Jul 1982.

[5] K. M. Backes, D. A. Palken, S. Al Kenany, B. M. Brubaker, S. B. Cahn, A. Droster, Gene C. Hilton, Sumita Ghosh, H. Jackson, S. K. Lamoreaux, A. F. Leder, K. W. Lehnert, S. M. Lewis, M. Malnou, R. H. Maruyama, N. M. Rapidis, M. Simanovskaia, Sukhman Singh, D. H. Speller, I. Urdinaran, Leila R. Vale, E. C. van Assendelft, K. van Bibber, and H. Wang. A quantum enhanced search for dark matter axions. *Nature*, 590(7845):238–242, Feb 2021.

[6] R. Barends, J. Kelly, A. Megrant, A. Veitia, D. Sank, E. Jeffrey, T. C. White, J. Mutus, A. G. Fowler, B. Campbell, Y. Chen, Z. Chen, B. Chiaro, A. Dunsworth, C. Neill, P. O'Malley, P. Roushan, A. Vainsencher, J. Wenner, A. N. Korotkov, A. N. Cleland, and John M. Martinis. Superconducting quantum circuits at the surface code threshold for fault tolerance. *Nature*, 508(7497):500–503, Apr 2014.

[7] S. Barzanjeh, S. Pirandola, D. Vitali, and J. M. Fink. Microwave quantum illumination using a digital receiver. *Science Advances*, 6(19), 2020.

[8] Sh. Barzanjeh, D. P. DiVincenzo, and B. M. Terhal. Dispersive qubit measurement by interferometry with parametric amplifiers. *Phys. Rev. B*, 90:134515, Oct 2014.

[9] A. Bienfait, P. Campagne-Ibarcq, A. H. Kiilerich, X. Zhou, S. Probst, J. J. Pla, T. Schenkel, D. Vion, D. Esteve, J. J. L. Morton, K. Moelmer, and P. Bertet. Magnetic resonance with squeezed microwaves. *Phys. Rev. X*, 7:041011, Oct 2017.

[10] A. Bienfait, J. J. Pla, Y. Kubo, M. Stern, X. Zhou, C. C. Lo, C. D. Weis, T. Schenkel, M. L. W. Thewalt, D. Vion, D. Esteve, B. Julsgaard, K. Mølmer, J. J. L. Morton, and P. Bertet. Reaching the quantum limit of sensitivity in electron spin resonance. *Nature Nanotechnology*, 11(3):253–257, Mar 2016.

[11] Alexandre Blais, Ren-Shou Huang, Andreas Wallraff, S. M. Girvin, and R. J. Schoelkopf. Cavity quantum electrodynamics for superconducting electrical circuits: An architecture for quantum computation. *Phys. Rev. A*, 69:062320, Jun 2004.

[12] C. Bockstiegel, J. Gao, M. R. Vissers, M. Sandberg, S. Chaudhuri, A. Sanders, L. R. Vale, K. D. Irwin, and D. P. Pappas. Development of a broadband nbtin traveling wave parametric amplifier for mkid readout. *Journal of Low Temperature Physics*, 176(3):476–482, Aug 2014.

[13] V. Bouchiat, D. Vion, P. Joyez, D. Esteve, and M. H. Devoret. Quantum coherence with a single cooper pair. *Physica Scripta*, T76(1):165, 1998.

[14] Samuel Boutin, David M. Toyli, Aditya V. Venkatramani, Andrew W. Eddins, Irfan Siddiqi, and Alexandre Blais. Effect of higher-order nonlinearities on amplification and squeezing in Josephson parametric amplifiers. *Phys. Rev. Applied*, 8:054030, Nov 2017.

[15] M. Castellanos-Beltran. *Development of a Josephson Parametric Amplifier for the Preparation and Detection of Nonclassical States of Microwave Fields*. PhD thesis, Boulder, 2010.

[16] M. A. Castellanos-Beltran, K. Irwin, G. Hilton, L. Vale, and K. Lehnert. Amplification and squeezing of quantum noise with a tunable Josephson metamaterial. *Nature Physics*, 4:929–931, 2008.

[17] M. A. Castellanos-Beltran and K. W. Lehnert. Widely tunable parametric amplifier based on a superconducting quantum interference device array resonator. *Applied Physics Letters*, 91(8):083509, 2007.

[18] C. M. Caves. Quantum-mechanical noise in an interferometer. *Phys. Rev. D*, 23:1693–1708, Apr 1981.

[19] Carlton M. Caves. Quantum limits on noise in linear amplifiers. *Phys. Rev. D*, 26:1817–1839, Oct 1982.

[20] Carlton M Caves and David D Crouch. Quantum wideband traveling-wave analysis of a degenerate parametric amplifier. *JOSA B*, 4(10):1535–1545, 1987.

[21] J. B. Clark, F. Lecocq, R. Simmonds, J. Aumentado, and J. Teufel. Sideband cooling beyond the quantum backaction limit with squeezed light. *Nature*, 541:191–195, 2017.

[22] John Clarke. The Josephson effect and e/h. *American Journal of Physics*, 38(9):1071–1095, 1970.

[23] John Clarke and Frank K. Wilhelm. Superconducting quantum bits. *Nature*, 453(7198):1031–1042, Jun 2008.

[24] A. A. Clerk, M. H. Devoret, S. M. Girvin, Florian Marquardt, and R. J. Schoelkopf. Introduction to quantum noise, measurement, and amplification. *Rev. Mod. Phys.*, 82:1155–1208, Apr 2010.

[25] R. Dassonneville, R. Assouly, T. Peronnin, A.A. Clerk, A. Bienfait, and B. Huard. Dissipative stabilization of squeezing beyond 3 db in a microwave mode. *PRX Quantum*, 2:020323, May 2021. doi:10.1103/PRXQuantum.2.020323.

[26] Nicolas Didier, Archana Kamal, William D. Oliver, Alexandre Blais, and Aashish A. Clerk. Heisenberg-limited qubit read-out with two-mode squeezed light. *Phys. Rev. Lett.*, 115:093604, Aug 2015.

[27] Duke University. Making quantum computers useful and usable, 2020. [Online; accessed Oct 6, 2022]. URL: https://staq.pratt.duke.edu.

[28] A. Eddins, J. M. Kreikebaum, D. M. Toyli, E. M. Levenson-Falk, A. Dove, W. P. Livingston, B. A. Levitan, L. C. G. Govia, A. A. Clerk, and I. Siddiqi. High-efficiency measurement of an artificial atom embedded in a parametric amplifier. *Phys. Rev. X*, 9:011004, Jan 2019.

[29] A. Eddins, S. Schreppler, D. M. Toyli, L. S. Martin, S. Hacohen-Gourgy, L. C. G. Govia, H. Ribeiro, A. A. Clerk, and I. Siddiqi. Stroboscopic qubit measurement with squeezed illumination. *Phys. Rev. Lett.*, 120:040505, Jan 2018.

[30] Andrew W. Eddins. *Superconducting Circuits for Quantum Metrology with Nonclassical Light*. PhD thesis, University of California, Berkeley, 2017.

[31] C. Eichler, D. Bozyigit, C. Lang, M. Baur, L. Steffen, J. M. Fink, S. Filipp, and A. Wallraff. Observation of two-mode squeezing in the microwave frequency domain. *Phys. Rev. Lett.*, 107:113601, Sep 2011.

[32] C. Eichler, Y. Salathe, J. Mlynek, S. Schmidt, and A. Wallraff. Quantum-limited amplification and entanglement in coupled nonlinear resonators. *Phys. Rev. Lett.*, 113:110502, Sep 2014.

[33] Christopher Eichler. *Experimental characterization of quantum microwave radiation and its entanglement with a superconducting qubit*. Doctoral thesis, ETH Zurich, Zurich, 2013.

[34] Martina Esposito, Arpit Ranadive, Luca Planat, Sébastien Leger, Dorian Fraudet, Vincent Jouanny, Olivier Buisson, Wiebke Guichard, Cécile Naud, José Aumentado, Florent Lecocq, and Nicolas Roch. Observation of two-mode squeezing in a traveling wave parametric amplifier. *Phys. Rev. Lett.*, 128:153603, Apr 2022.

[35] K. G. Fedorov, S. Pogorzalek, U. Las Heras, M. Sanz, P. Yard, P. Eder, M. Fischer, J. Goetz, E. Xie, K. Inomata, Y. Nakamura, R. Di Candia, E. Solano, A. Marx, F. Deppe, and R. Gross. Finite-time quantum entanglement in propagating squeezed microwaves. *Scientific Reports*, 8(1):6416, Apr 2018.

[36] Kirill G. Fedorov, Michael Renger, Stefan Pogorzalek, Roberto Di Candia, Qiming Chen, Yuki Nojiri, Kunihiro Inomata, Yasunobu Nakamura, Matti Partanen, Achim Marx, Rudolf Gross, and Frank Deppe. Experimental quantum teleportation of propagating microwaves. *Science Advances*, 7(52):eabk0891, 2021. doi:10.1126/sciadv.abk0891.

[37] Kirill G. Fedorov, L. Zhong, S. Pogorzalek, P. Eder, M. Fischer, J. Goetz, E. Xie, F. Wulschner, K. Inomata, T. Yamamoto, Y. Nakamura, R. Di Candia, U. Las Heras, M. Sanz, E. Solano, E. P. Menzel, F. Deppe, A. Marx, and R. Gross. Displacement of propagating squeezed microwave states. *Phys. Rev. Lett.*, 117:020502, Jul 2016.

[38] J. E. Fernandez. A noise-temperature measurement system using a cryogenic attenuator. *TMO Progress Report*, 10:034040, 1998.

[39] E. Flurin, N. Roch, F. Mallet, M. H. Devoret, and B. Huard. Generating entangled microwave radiation over two transmission lines. *Phys. Rev. Lett.*, 109:183901, Oct 2012.

[40] N. E. Frattini, V. V. Sivak, A. Lingenfelter, S. Shankar, and M. H. Devoret. Optimizing the nonlinearity and dissipation of a snail parametric amplifier for dynamic range. *Phys. Rev. Applied*, 10:054020, Nov 2018.

[41] Jay Gambetta, Alexandre Blais, M. Boissonneault, A. A. Houck, D. I. Schuster, and S. M. Girvin. Quantum trajectory approach to circuit qed: Quantum jumps and the zeno effect. *Phys. Rev. A*, 77:012112, Jan 2008.

[42] Jay Gambetta, Alexandre Blais, D. I. Schuster, A. Wallraff, L. Frunzio, J. Majer, M. H. Devoret, S. M. Girvin, and R. J. Schoelkopf. Qubit-photon interactions in a cavity: Measurement-induced dephasing and number splitting. *Phys. Rev. A*, 74:042318, Oct 2006.

[43] C. C. Gerry and P. L. Knight. *Introductory Quantum Optics*. Cambridge University Press, 2005.

[44] Arne L. Grimsmo and Alexandre Blais. Squeezing and quantum state engineering with Josephson travelling wave amplifiers. *npj Quantum Information*, 3(1):20, 2017.

[45] H. A. Haus and J. A. Mullen. Quantum noise in linear amplifiers. *Phys. Rev.*, 128:2407–2413, Dec 1962.

[46] Johannes Heinsoo, Christian Kraglund Andersen, Ants Remm, Sebastian Krinner, Theodore Walter, Yves Salathé, Simone Gasparinetti, Jean-Claude Besse, Anton Potočnik, Andreas Wallraff, and Christopher Eichler. Rapid high-fidelity multiplexed readout of superconducting qubits. *Phys. Rev. Applied*, 10:034040, Sep 2018.

[47] Byeong Ho Eom, Peter K. Day, Henry G. LeDuc, and Jonas Zmuidzinas. A wideband, low-noise superconducting amplifier with high dynamic range. *Nature Physics*, 8(8):623–627, Aug 2012.

[48] J. M. Hornibrook, J. I. Colless, A. C. Mahoney, X. G. Croot, S. Blanvillain, H. Lu, A. C. Gossard, and D. J. Reilly. Frequency multiplexing for readout of spin qubits. *Applied Physics Letters*, 104(10):103108, 2014. doi:10.1063/1.4868107.

[49] M. Houde, L.C.G. Govia, and A.A. Clerk. Loss asymmetries in quantum traveling-wave parametric amplifiers. *Phys. Rev. Applied*, 12:034054, Sep 2019.

[50] G. Ithier, E. Collin, P. Joyez, P. J. Meeson, D. Vion, D. Esteve, F. Chiarello, A. Shnirman, Y. Makhlin, J. Schriefl, and G. Schön. Decoherence in a superconducting quantum bit circuit. *Phys. Rev. B*, 72:134519, Oct 2005.

[51] X. Y. Jin, A. Kamal, A. P. Sears, T. Gudmundsen, D. Hover, J. Miloshi, R. Slattery, F. Yan, J. Yoder, T. P. Orlando, S. Gustavsson, and W. D. Oliver. Thermal and residual excited-state population in a 3d transmon qubit. *Phys. Rev. Lett.*, 114:240501, Jun 2015.

[52] B. D. Josephson. Possible new effects in superconductive tunnelling. *Phys. Lett.*, page 79, 1962.

[53] Ravikiran Kakarla, Jochen Schröder, and Peter A. Andrekson. One photon-per-bit receiver using near-noiseless phase-sensitive amplification. *Light: Science & Applications*, 9(1):153, Sep 2020.

[54] B. Kannan, D. L. Campbell, F. Vasconcelos, R. Winik, D. K. Kim, M. Kjaergaard, P. Krantz, A. Melville, B. M. Niedzielski, J. L. Yoder, T. P. Orlando, S. Gustavsson, and W. D. Oliver. Generating spatially entangled itinerant photons with waveguide quantum electrodynamics. *Science Advances*, 6(41), 2020.

[55] Jens Koch, Terri M. Yu, Jay Gambetta, A. A. Houck, D. I. Schuster, J. Majer, Alexandre Blais, M. H. Devoret, S. M. Girvin, and R. J. Schoelkopf. Charge-insensitive qubit design derived from the cooper pair box. *Phys. Rev. A*, 76:042319, Oct 2007.

[56] P. Krantz, M. Kjaergaard, F. Yan, T. P. Orlando, S. Gustavsson, and W. D. Oliver. A quantum engineer's guide to superconducting qubits. *Applied Physics Reviews*, 6(2):021318, 2019.

[57] Philip Krantz, Yarema Reshitnyk, Waltraut Wustmann, Jonas Bylander, Simon Gustavsson, William D Oliver, Timothy Duty, Vitaly Shumeiko, and Per Delsing. Investigation of nonlinear effects in Josephson parametric oscillators used in circuit quantum electrodynamics. *New Journal of Physics*, 15(10):105002, oct 2013.

[58] U. Las Heras, R. Di Candia, K. G. Fedorov, F. Deppe, M. Sanz, and E. Solano. Quantum illumination reveals phase-shift inducing cloaking. *Scientific Reports*, 7(1):9333, Aug 2017.

[59] F. Lecocq, L. Ranzani, G. A. Peterson, K. Cicak, R. W. Simmonds, J. D. Teufel, and J. Aumentado. Nonreciprocal microwave signal processing with a field-programmable Josephson amplifier. *Phys. Rev. Applied*, 7:024028, Feb 2017.

[60] A. I. Lvovsky. *Squeezed Light*, chapter 5, pages 121–163. John Wiley & Sons, Ltd, 2015.

[61] C. Macklin, K. O'Brien, D. Hover, M. E. Schwartz, V. Bolkhovsky, X. Zhang, W. D. Oliver, and I. Siddiqi. A near–quantum-limited Josephson traveling-wave parametric amplifier. *Science*, 350(6258):307–310, 2015.

[62] Christopher S. Macklin. *Quantum Feedback and Traveling-wave Parametric Amplification in Superconducting Circuits*. PhD thesis, University of California, Berkeley, 2015.

[63] F. Mallet, M. A. Castellanos-Beltran, H. S. Ku, S. Glancy, E. Knill, K. D. Irwin, G. C. Hilton, L. R. Vale, and K. W. Lehnert. Quantum state tomography of an itinerant squeezed microwave field. *Phys. Rev. Lett.*, 106:220502, Jun 2011.

[64] M. Malnou, D. A. Palken, B. M. Brubaker, Leila R. Vale, Gene C. Hilton, and K. W. Lehnert. Squeezed vacuum used to accelerate the search for a weak classical signal. *Phys. Rev. X*, 9:021023, May 2019.

[65] M. Malnou, D. A. Palken, Leila R. Vale, Gene C. Hilton, and K. W. Lehnert. Optimal operation of a Josephson parametric amplifier for vacuum squeezing. *Phys. Rev. Applied*, 9:044023, Apr 2018.

[66] M. Malnou, M.R. Vissers, J.D. Wheeler, J. Aumentado, J. Hubmayr, J.N. Ullom, and J. Gao. Three-wave mixing kinetic inductance traveling-wave amplifier with near-quantum-limited noise performance. *PRX Quantum*, 2:010302, Jan 2021.

[67] V. E. Manucharyan, E. Boaknin, M. Metcalfe, R. Vijay, I. Siddiqi, and M. Devoret. Microwave bifurcation of a Josephson junction: Embedding-circuit requirements. *Phys. Rev. B*, 76:014524, Jul 2007.

[68] Nicolas C. Menicucci, Peter van Loock, Mile Gu, Christian Weedbrook, Timothy C. Ralph, and Michael A. Nielsen. Universal quantum computation with continuous-variable cluster states. *Phys. Rev. Lett.*, 97:110501, Sep 2006.

[69] E. P. Menzel, R. Di Candia, F. Deppe, P. Eder, L. Zhong, M. Ihmig, M. Haeberlein, A. Baust, E. Hoffmann, D. Ballester, K. Inomata, T. Yamamoto, Y. Nakamura, E. Solano, A. Marx, and R. Gross. Path entanglement of continuous-variable quantum microwaves. *Phys. Rev. Lett.*, 109:250502, Dec 2012.

[70] A. Metelmann and A. A. Clerk. Nonreciprocal photon transmission and amplification via reservoir engineering. *Phys. Rev. X*, 5:021025, Jun 2015.

[71] Yoshinari Minami. Extraction of thrust from quantum vacuum using squeezed light. *AIP Conference Proceedings*, 880:1034–1044, 01 2007.

[72] Mohammad Mirhosseini, Eunjong Kim, Xueyue Zhang, Alp Sipahigil, Paul B. Dieterle, Andrew J. Keller, Ana Asenjo-Garcia, Darrick E. Chang, and Oskar Painter. Cavity quantum electrodynamics with atom-like mirrors. *Nature*, 569(7758):692–697, May 2019.

[73] J. E. Mooij, T. P. Orlando, L. Levitov, Lin Tian, Caspar H. van der Wal, and Seth Lloyd. Josephson persistent-current qubit. *Science*, 285(5430):1036–1039, 1999.

[74] R. Movshovich, B. Yurke, P. G. Kaminsky, A. D. Smith, A. H. Silver, R. W. Simon, and M. V. Schneider. Observation of zero-point noise squeezing via a Josephson-parametric amplifier. *Phys. Rev. Lett.*, 65:1419–1422, Sep 1990.

[75] R. Movshovich, B. Yurke, A. D. Smith, and A. H. Silver. Subharmonic pumping of a Josephson-parametric amplifier and the pitchfork instability. *Phys. Rev. Lett.*, 67:1411–1414, Sep 1991.

[76] K. W. Murch, S. J. Weber, K. M. Beck, E. Ginossar, and I. Siddiqi. Reduction of the radiative decay of atomic coherence in squeezed vacuum. *Nature*, 499:62 – 65, 2013.

[77] J. Y. Mutus, T. C. White, R. Barends, Yu Chen, Z. Chen, B. Chiaro, A. Dunsworth, E. Jeffrey, J. Kelly, A. Megrant, C. Neill, P. J. J. O'Malley, P. Roushan, D. Sank, A. Vainsencher, J. Wenner, K. M. Sundqvist, A. N. Cleland, and John M. Martinis. Strong environmental coupling in a Josephson parametric amplifier. *Applied Physics Letters*, 104(26):263513, 2014.

[78] Kevin O'Brien, Chris Macklin, Irfan Siddiqi, and Xiang Zhang. Resonant phase matching of Josephson junction traveling wave parametric amplifiers. *Phys. Rev. Lett.*, 113:157001, Oct 2014.

[79] Kevin Patrick O'Brien. *Nonlinear Light-Matter Interactions in Metamaterials*. PhD thesis, UC Berkeley, 2016.

[80] T. P. Orlando, J. E. Mooij, Lin Tian, Caspar H. van der Wal, L. S. Levitov, Seth Lloyd, and J. J. Mazo. Superconducting persistent-current qubit. *Phys. Rev. B*, 60:15398–15413, Dec 1999.

[81] Hanhee Paik, A. Mezzacapo, Martin Sandberg, D. T. McClure, B. Abdo, A. D. Córcoles, O. Dial, D. F. Bogorin, B. L. T. Plourde, M. Steffen, A. W. Cross, J. M. Gambetta, and Jerry M. Chow. Experimental demonstration of a resonator-induced phase gate in a multiqubit circuit-qed system. *Phys. Rev. Lett.*, 117:250502, Dec 2016.

[82] Daniel J. Parker, Mykhailo Savytskyi, Wyatt Vine, Arne Laucht, Timothy Duty, Andrea Morello, Arne L. Grimsmo, and Jarryd J. Pla. Degenerate parametric amplification via three-wave mixing using kinetic inductance. *Phys. Rev. Appl.*, 17:034064, Mar 2022.

[83] Kaidong Peng, Mahdi Naghiloo, Jennifer Wang, Gregory D. Cunningham, Yufeng Ye, and Kevin P. O'Brien. Floquet-mode traveling-wave parametric amplifiers. *PRX Quantum*, 3:020306, Apr 2022.

[84] M.R. Perelshtein, K.V. Petrovnin, V. Vesterinen, S. Hamedani Raja, I. Lilja, M. Will, A. Savin, S. Simbierowicz, R.N. Jabdaraghi, J.S. Lehtinen, L. Grönberg, J. Hassel, M.P. Prunnila, J. Govenius, G.S. Paraoanu, and P.J. Hakonen. Broadband continuous-variable entanglement generation using a kerr-free josephson metamaterial. *Phys. Rev. Appl.*, 18:024063, Aug 2022.

[85] Luca Planat, Rémy Dassonneville, Javier Puertas Martínez, Farshad Foroughi, Olivier Buisson, Wiebke Hasch-Guichard, Cécile Naud, R. Vijay, Kater Murch, and Nicolas Roch. Understanding the saturation power of Josephson parametric amplifiers made from squid arrays. *Phys. Rev. Applied*, 11:034014, Mar 2019.

[86] David M Pozar. *Microwave engineering; 3rd ed.* Wiley, Hoboken, NJ, 2005.

[87] Shruti Puri and Alexandre Blais. High-fidelity resonator-induced phase gate with single-mode squeezing. *Phys. Rev. Lett.*, 116:180501, May 2016.

[88] Xiaogang Qiang. Building quantum computers with photons – silicon chip creates two-qubit processor, 2018. [Online; accessed Oct 6, 2022]. URL: `https://spectrum.ieee.org/building-quantum-computers-with-photons`.

[89] Jack Y. Qiu, Arne Grimsmo, Kaidong Peng, Bharath Kannan, Benjamin Lienhard, Youngkyu Sung, Philip Krantz, Vladimir Bolkhovsky, Greg Calusine, David Kim, Alex Melville, Bethany M. Niedzielski, Jonilyn Yoder, Mollie E. Schwartz, Terry P. Orlando, Irfan Siddiqi, Simon Gustavsson, Kevin P. O'Brien, and William D. Oliver. Broadband squeezed microwaves and amplification with a Josephson traveling-wave parametric amplifier. *ArXiv e-prints*, 2022. arXiv:2201.11261.

[90] Nicolás Quesada and J. E. Sipe. Effects of time ordering in quantum nonlinear optics. *Phys. Rev. A*, 90:063840, 2014.

[91] T. C. Ralph and P. K. Lam. Teleportation with bright squeezed light. *Phys. Rev. Lett.*, 81:5668–5671, Dec 1998.

[92] N. Roch, E. Flurin, F. Nguyen, P. Morfin, P. Campagne-Ibarcq, M. H. Devoret, and B. Huard. Widely tunable, nondegenerate three-wave mixing microwave device operating near the quantum limit. *Phys. Rev. Lett.*, 108:147701, Apr 2012.

[93] D. Rosenberg, S. J. Weber, D. Conway, D. W. Yost, J. Mallek, G. Calusine, R. Das, D. Kim, M. E. Schwartz, W. Woods, J. L. Yoder, and W. D. Oliver. Solid-state qubits: 3d integration and packaging. *IEEE Microwave Magazine*, 21(8):72–85, 2020.

[94] Tanay Roy, Suman Kundu, Madhavi Chand, A. M. Vadiraj, A. Ranadive, N. Nehra, Meghan P. Patankar, J. Aumentado, A. A. Clerk, and R. Vijay. Broadband parametric amplification with impedance engineering: Beyond the gain-bandwidth product. *Applied Physics Letters*, 107(26):262601, 2015.

[95] Jeremy M. Sage, Vladimir Bolkhovsky, William D. Oliver, Benjamin Turek, and Paul B. Welander. Study of loss in superconducting coplanar waveguide resonators. *Journal of Applied Physics*, 109(6):063915, 2011.

[96] Roman Schnabel. Squeezed states of light and their applications in laser interferometers. *Physics Reports*, 684:1–51, 2017. Squeezed states of light and their applications in laser interferometers.

[97] B. H. Schneider, A. Bengtsson, I. M. Svensson, T. Aref, G. Johansson, Jonas Bylander, and P. Delsing. Observation of broadband entanglement in microwave radiation from a single time-varying boundary condition. *Phys. Rev. Lett.*, 124:140503, Apr 2020.

[98] Carsten Schulte. Spin with a new twist, 2014. [Online; accessed Oct 6, 2022]. URL: https://www.cam.ac.uk/research/news/spin-with-a-new-twist.

[99] D. I. Schuster, A. Wallraff, A. Blais, L. Frunzio, R.-S. Huang, J. Majer, S. M. Girvin, and R. J. Schoelkopf. ac stark shift and dephasing of a superconducting qubit strongly coupled to a cavity field. *Phys. Rev. Lett.*, 94:123602, Mar 2005.

[100] I. Siddiqi, R. Vijay, F. Pierre, C. M. Wilson, M. Metcalfe, C. Rigetti, L. Frunzio, and M. H. Devoret. Rf-driven Josephson bifurcation amplifier for quantum measurement. *Phys. Rev. Lett.*, 93:207002, Nov 2004.

[101] V. V. Sivak, S. Shankar, G. Liu, J. Aumentado, and M. H. Devoret. Josephson array-mode parametric amplifier. *Phys. Rev. Applied*, 13:024014, Feb 2020.

[102] V.V. Sivak, N.E. Frattini, V.R. Joshi, A. Lingenfelter, S. Shankar, and M.H. Devoret. Kerr-free three-wave mixing in superconducting quantum circuits. *Phys. Rev. Applied*, 11:054060, May 2019.

[103] Radan Slavík, Francesca Parmigiani, Joseph Kakande, Carl Lundström, Martin Sjödin, Peter A. Andrekson, Ruwan Weerasuriya, Stylianos Sygletos, Andrew D. Ellis, Lars Grüner-Nielsen, Dan Jakobsen, Søren Herstrøm, Richard Phelan, James O'Gorman, Adonis Bogris, Dimitris Syvridis, Sonali Dasgupta, Periklis Petropoulos, and David J. Richardson. All-optical phase and amplitude regenerator for next-generation telecommunications systems. *Nature Photonics*, 4(10):690–695, Oct 2010.

[104] Daniel H. Slichter. *Quantum Jumps and Measurement Backaction in a Superconducting Qubit*. PhD thesis, University of California, Berkeley, 2011.

[105] R. E. Slusher, L. W. Hollberg, B. Yurke, J. C. Mertz, and J. F. Valley. Observation of squeezed states generated by four-wave mixing in an optical cavity. *Phys. Rev. Lett.*, 55:2409–2412, Nov 1985.

[106] Lafe Spietz, K. W. Lehnert, I. Siddiqi, and R. J. Schoelkopf. Primary electronic thermometry using the shot noise of a tunnel junction. *Science*, 300(5627):1929–1932, 2003.

[107] M. A. Taylor, J. Janousek, V. Daria, J. Knittel, B. Hage, Hans-A. Bachor, and W. P. Bowen. Biological measurement beyond the quantum limit. *Nature Photonics*, pages 229 – 233, 2013.

[108] The LIGO Scientific Collaboration. A gravitational wave observatory operating beyond the quantum shot-noise limit. *Nature Physics*, pages 962 – 965, 2011.

[109] E A Tholén, A Ergül, K Stannigel, C Hutter, and D B Haviland. Parametric amplification with weak-link nonlinearity in superconducting microresonators. *Physica Scripta*, T137:014019, dec 2009.

[110] Z. Tong, C. Lundström, P. A. Andrekson, M. Karlsson, and A. Bogris. Ultralow noise, broadband phase-sensitive optical amplifiers, and their applications. *IEEE Journal of Selected Topics in Quantum Electronics*, 18(2):1016–1032, 2012.

[111] D. M. Toyli, A. W. Eddins, S. Boutin, S. Puri, D. Hover, V. Bolkhovsky, W. D. Oliver, A. Blais, and I. Siddiqi. Resonance fluorescence from an artificial atom in squeezed vacuum. *Phys. Rev. X*, 6:031004, Jul 2016.

[112] Mankei Tsang and Carlton M. Caves. Evading quantum mechanics: Engineering a classical subsystem within a quantum environment. *Phys. Rev. X*, 2:031016, Sep 2012.

[113] Visa Vesterinen, Slawomir Simbierowicz, Robab Najafi Jabdaraghi, Leif Grönberg, Janne S. Lehtinen, Mika Prunnila, and Joonas Govenius. A sub-ghz impedance-engineered parametric amplifier for the readout of sensors and quantum dots. *IEEE Transactions on Applied Superconductivity*, 32(4):1–6, 2022.

[114] D. Vion, A. Aassime, A. Cottet, P. Joyez, H. Pothier, C. Urbina, D. Esteve, and M. H. Devoret. Manipulating the quantum state of an electrical circuit. *Science*, 296(5569):886–889, 2002.

[115] Benedikt Vogel. Qubits – the building blocks of the quantum computer, 2017. [Online; accessed Oct 6, 2022]. URL: `https://www.unibas.ch/en/News-Events/Uni-Nova/Uni-Nova-130/Uni-Nova-130-Qubits-the-building-blocks-of-the-quantum-computer.html`.

[116] A. Wallraff, D. I. Schuster, A. Blais, L. Frunzio, R.-S. Huang, J. Majer, S. Kumar, S. M. Girvin, and R. J. Schoelkopf. Strong coupling of a single photon to a superconducting qubit using circuit quantum electrodynamics. *Nature*, 431(7005):162–167, September 2004.

[117] T. Walter, P. Kurpiers, S. Gasparinetti, P. Magnard, A. Potočnik, Y. Salathé, M. Pechal, M. Mondal, M. Oppliger, C. Eichler, and A. Wallraff. Rapid high-fidelity single-shot dispersive readout of superconducting qubits. *Phys. Rev. Applied*, 7:054020, May 2017.

[118] David S. Weiss and Mark Saffman. Quantum computing with neutral atoms. *Physics Today*, 70(7):44–50, 2017.

[119] S. Wood and Annette Cowie. *A Review of Greenhouse Gas Emission Factors for Fertiliser Production*, volume 38. 01 2004.

[120] O. Yaakobi, L. Friedland, C. Macklin, and I. Siddiqi. Parametric amplification in Josephson junction embedded transmission lines. *Phys. Rev. B*, 87:144301, Apr 2013.

[121] T. Yamamoto, K. Inomata, M. Watanabe, K. Matsuba, T. Miyazaki, W. D. Oliver, Y. Nakamura, and J. S. Tsai. Flux-driven Josephson parametric amplifier. *Applied Physics Letters*, 93(4):042510, 2008.

[122] Fei Yan, Dan Campbell, Philip Krantz, Morten Kjaergaard, David Kim, Jonilyn L. Yoder, David Hover, Adam Sears, Andrew J. Kerman, Terry P. Orlando, Simon Gustavsson, and William D. Oliver. Distinguishing coherent and thermal photon noise in a circuit quantum electrodynamical system. *Phys. Rev. Lett.*, 120:260504, Jun 2018.

[123] Fei Yan, Simon Gustavsson, Archana Kamal, Jeffrey Birenbaum, Adam P. Sears, David Hover, Ted J. Gudmundsen, Danna Rosenberg, Gabriel Samach, S. Weber, Jonilyn L. Yoder, Terry P. Orlando, John Clarke, Andrew J. Kerman, and William D. Oliver. The flux qubit revisited to enhance coherence and reproducibility. *Nature Communications*, 7(1):12964, Nov 2016.

[124] J. Q. You, Xuedong Hu, S. Ashhab, and Franco Nori. Low-decoherence flux qubit. *Phys. Rev. B*, 75:140515, Apr 2007.

[125] B. Yurke, L. R. Corruccini, P. G. Kaminsky, L. W. Rupp, A. D. Smith, A. H. Silver, R. W. Simon, and E. A. Whittaker. Observation of parametric amplification and deamplification in a Josephson parametric amplifier. *Phys. Rev. A*, 39:2519–2533, Mar 1989.

[126] B. Yurke, P. G. Kaminsky, R. E. Miller, E. A. Whittaker, A. D. Smith, A. H. Silver, and R. W. Simon. Observation of 4.2-k equilibrium-noise squeezing via a Josephson-parametric amplifier. *Phys. Rev. Lett.*, 60:764–767, Feb 1988.

[127] L Zhong, E P Menzel, R Di Candia, P Eder, M Ihmig, A Baust, M Haeberlein, E Hoffmann, K Inomata, T Yamamoto, Y Nakamura, E Solano, F Deppe, A Marx, and R Gross. Squeezing with a flux-driven Josephson parametric amplifier. *New Journal of Physics*, 15(12):125013, dec 2013.

[128] A. B. Zorin, M. Khabipov, J. Dietel, and R. Dolata. Traveling-wave parametric amplifier based on three-wave mixing in a Josephson metamaterial. In *2017 16th International Superconductive Electronics Conference (ISEC)*, pages 1–3, 2017.